Molecular modeling of physico-chemical properties in microporous solids

Romain Gaillac

THÈSE DE DOCTORAT

de l'Université de recherche Paris Sciences et Lettres
PSL Research University

Préparée à Chimie ParisTech

Modélisation moléculaire des propriétés physico-chimiques de matériaux microporeux

École doctorale n°388

CHIMIE PHYSIQUE ET CHIMIE ANALYTIQUE DE PARIS-CENTRE

Spécialité CHIMIE PHYSIQUE

COMPOSITION DU JURY :

Mme Anne Boutin
ENS, Présidente

M Jean-Marc Simon
Université de Bourgogne, Rapporteur

Mme Élise Dumont
ENS Lyon, Rapporteur

M Thomas D. Bennett
Cambridge University, Membre du jury

M Pluton Pullumbi
Air Liquide, Membre du jury

M François-Xavier Coudert
Chimie ParisTech, Membre du jury

Soutenue par **Romain GAILLAC**
le 19 juin 2018

Dirigée par **François-Xavier Coudert**

Chimie Paris ParisTech | PSL RESEARCH UNIVERSITY PARIS

Thèse de doctorat de
l'Université de recherche Paris Sciences et Lettres

Spécialité: Chimie Physique

Molecular modeling of physico-chemical properties in microporous solids

---

présentée par

Romain Gaillac

afin d'obtenir le grade de
Docteur de l'Université Paris Sciences et Lettres

dirigée par
François-Xavier COUDERT et Pluton PULLUMBI

Soutenance prévue le 19/06/2018 devant le Jury composé de

Dr. Thomas D. Bennett
Dr. Anne Boutin
Dr. François-Xavier Coudert
Pr. Élise Dumont
Dr. Pluton Pullumbi
Dr. Jean-Marc Simon

« La recherche de la vérité doit être le but de notre activité ; c'est la seule fin qui soit digne d'elle »

Henri Poincaré, La valeur de la science

Remerciements

Je souhaiterais en premier lieu remercier les rapporteurs de ma thèse, Élise Dumont et Jean-Marc Simon, pour leur présence lors de ma soutenance et leurs remarques constructives exprimées dans leur rapport. Je remercie aussi Anne Boutin et Thomas Bennett pour avoir accepté de participer à mon jury de thèse. Je remercie aussi Thomas Bennett pour la collaboration très fructueuse que nous avons mené sur l'étude de la fusion des MOFs grâce à de magnifiques résultats expérimentaux et des discussions passionnantes.

Je tiens à remercier Pluton Pullumbi qui m'a fait découvrir la recherche industrielle au sein d'Air Liquide et avec qui nous avons toujours des échanges fructueux sur la science et son lien avec le business.

Je remercie très chaleureusement François-Xavier Coudert qui a dirigé ma thèse pendant ces trois années. Ses conseils précieux et les discussions régulières que nous avons eu m'ont permis d'avancer avec plaisir tout le long de ce travail de recherche. Outre ses apports scientifique et technique j'ai découvert grâce à lui l'escalade de bloc, excellent moyen de se défouler après une journée de simulations infructueuses. Sa bienveillance a fait de ces trois années passionnantes de thèse une expérience très agréable.

Je tiens également à remercier David Keen, Kevin Beyer et Karena Chapman pour leurs contributions à l'étude de la fusion de ZIF-4 qui nous ont permis d'écrire un bel article reliant expériences et simulations pour expliquer ce phénomène. Je remercie aussi Rodolphe Vuilleumier pour ses conseils toujours pertinents quand il s'agit de simulation moléculaire.

Ces trois années n'auraient pas été aussi intéressantes sans tous les membres de l'équipe : Guillaume, pour ses outils indispensables à l'analyse de simulations moléculaires et ses conseils avisés en matière d'informatique, Jean-Mathieu, pour sa bonne humeur et ses réponses à mes questions sur la fin de thèse, Clarisse, pour sa joie de vivre qui a bien égayé mon bureau pendant quelques mois, Elsa, pour sa contribution à me faire découvrir l'escalade et les modèles gros-grains, Dani, pour ses bons conseils sur les présentations et sa chaleur humaine argentine dont j'ai bénéficié pendant ma première année de thèse, Fabien, pour nos discussions scientifiques toujours posées, Liam, pour sa thèse sur les états excités en phase condensée qui m'a permis d'entrevoir les méthodes d'étude de ces systèmes, Jack, pour la bonne ambiance australienne qu'il a amenée dans l'équipe pendant deux ans, Laura, pour

m'avoir fait découvrir les imogolites et également Adrian, Johaness et Dominicka pour leur sympathique passage dans l'équipe pour quelques mois.

Je remercie Michel Mortier, directeur de l'IRCP, pour nos discussions. Mes remerciements vont aussi à Alain Fuchs, qui apporte à l'équipe une vision expérimentée dans les moments où il arrive à se libérer de ses obligations de président (du CNRS puis de PSL).

Un grand merci à Francine, Ali et Djamel qui m'ont accueillis pendant trois ans à l'accueil de Chimie Paris, toujours avec le sourire, et leur collaboration à l'organisation de nos conférences sur place. Elisabeth et Nathalie contribuent (ou ont contribué) énormément au fonctionnement quotidien du laboratoire avec efficacité, qu'elles en soient remerciées.

Je tiens à remercier Christine Dervin, gestionnaire au centre de recherche Paris-Saclay d'Air Liquide, qui m'a apporté un grand soutien logistique, souvent à distance, avec promptitude et bienveillance.

Je remercie aussi tous mes amis venus assister à ma soutenance (et ceux qui n'ont pas pu) : Quentin (très bon conseiller sur le vin après l'escalade), Amaury (les thèses de maths ça donne des discussions formidables), Maxence (toujours prêt à faire le zouave avec Quentin pour mettre l'ambiance), William et Mathilde (les thésariums et les mariages c'est vraiment génial !), Sylvain et Sophie (la raclette de décembre c'est encore mieux avec un petit), Léa (lumineuse et toujours prête à rendre service), Sylvain (précieux soutien, malgré les obligations militaires), Mathieu, Ariane et Édouard, Lauriane et Timothée, Marylou, Danijela, Paul-Hervé, Margaux et tous mes collègues du MBA du Collège des ingénieurs, Adrien, Agathe, Ferdinand, Delphine et Charlotte.

Je veux aussi remercier Bruno Morel et Jean-Paul Beynier qui ont été respectivement mes professeurs de mathématiques et de chimie en première année de classes préparatoires pour avoir renforcé mon goût pour les sciences et m'avoir fait apprécier leur beauté.

Je voudrais également remercier mes parents qui m'ont toujours soutenu tout au long de mes études et qui sont toujours ouverts et attentifs à la vulgarisation plus ou moins approximative de mes travaux. Je remercie également ma sœur, Victoria, et mon frère, Jean-Baptiste, pour leur affection et leur soutien constant.

Enfin, je remercie l'amour de ma vie, Sophie, qui m'a soutenu au quotidien durant toute ma thèse et qui m'a apporté son regard de physicienne sur mes problématiques de recherche. Je me réjouis par avance de nos futurs discussions scientifiques dans notre vie à venir.

Acknowledgements

I would like to acknowledge first and foremost the reviewers of this thesis, Élise Dumont and Jean-Marc Simon, for their presence at my defense and their quite relevant comments and questions. I also thank Anne Boutin and Thomas Bennett for accepting to be on my PhD committee. I would also like to thank Thomas Bennett for the very prolific collaboration we had on the study of melting MOFs, thanks to great experimental results and many interesting discussions.

I wish to thank Pluton Pullumbi who made me discover industrial research at Air Liquide and with whom I had plenty of exciting exchanges on science and its interactions with the business.

My warmest acknowledgments go to my PhD advisor, François-Xavier Coudert, who supervised me during three years. His precious advice and our regular discussions allowed me to happily go forward all along these research projects. Besides its scientific and technical contributions, he also made me discover boulder climbing, which is a nice way to release the tensions after a day of unsuccessful simulations. His kindness also made these three years a very enjoyable experience.

I would like to thank David Keen, Kevin Beyer and Karena Chapman for their contributions to the study of the melting of ZIF-4 which allowed us to write a beautiful article linking experiments and simulations to explain this phenomenon. I also thank Rodolphe Vuilleumier for his relevant advice about molecular simulations.

These three years would not have been the same without all my colleagues : Guillaume, for his necessary tools for the analysis of molecular simulations and his advice on computing, Jean-Mathieu, for his cheerfulness and his answers to my questions about the end of my PhD, Clarisse, for her happiness which lightened up my office during a few months, Elsa, for her contribution to my discovery of climbing and coarse-grained models, Dani, for her advice on presentations and her Argentinian human warmth from which I benefited during my first year of PhD, Fabien, for our nice and quiet scientific discussions, Liam, for his thesis on excited states in condensed matter which allowed me to perceive the methods used to study such systems, Jack, for the very nice Australian atmosphere he brought to the team during two years, Laura, to have made me discover imogolites and also Adrian, Johaness and Dominicka

for their nice stay in the team for a few months.

I thank Michel Mortier, director of the lab, for our discussions. My acknowledgments also go towards Alain Fuchs, who brings an experienced vision to the team when he manages to free himself from his presidential obligations (of the CNRS and now of PSL).

A great thanks to Francine, Ali and Djamel who always welcomed me with a smile at the entry of Chimie Paris and for their collaboration on the logistics of our local conferences. Elisabeth and Nathalie contribute (or have contributed) enormously to the daily operation of the lab with efficiency and they shall be warmly thanked for it.

I would like to thank Christine Dervin, administrative assistant at the Paris-Saclay Research Center of Air Liquide, who helped me a lot with all sorts of details with a great kindness.

I also thank all my friends who came to my defense (and those who could not make it): Quentin (always of good advice on the wine after climbing), Amaury (PhD in maths give rise to incredible discussions), Maxence (always ready to have fun with Quentin), William and Mathilde (the "thésariums" and weddings are great!), Sylvain and Sophie (the annual raclette is even better with a child), Léa (always here to help), Sylvain (precious support despite his military obligations), Mathieu, Ariane and Édouard, Lauriane and Timothée, Marylou, Danijela, Paul-Hervé, Margaux and all my colleagues from the MBA of the Collège des ingénieurs, Adrien, Agathe, Ferdinand, Delphine and Charlotte.

I also wish to thank Bruno Morel and Jean-Paul Beynier who were respectively my mathematics and chemistry teachers in first year of "classes préparatoires" to have strengthened my taste for sciences and made me appreciate their beauty.

I would like to thank my parents who supported me all along my studies and who are always open to my explanations of my research studies. I also thank my sister, Victoria, and my brother, Jean-Baptiste, for their affection and constant support.

Finally, I thank the love of my life, Sophie, who supported me every day during my PhD and brought her physics point of view on my research. I am already looking forward to our futur scientific discussions in our life to come.

Main table of contents

Detailed table of contents

Main introduction

During my PhD I conducted studies based on molecular simulation methods on two types of materials: zeolites, already used industrially and in a lot of applications in daily life and Metal-Organic Frameworks (MOFs), which present a lot of potential for applications, with promising commercial developments currently developed.

Zeolites are natural and artificial porous aluminosilicates, known since 1756 and artificially synthesized since the 1940s. They have been thoroughly studied for their properties linked to adsorption and catalysis for more than 50 years. However, their mechanical behaviour really began to get some interest less than 15 years ago, especially on the theoretical standpoint. Yet, thanks to their complex structures, some of these porous aluminosilicates have fascinating mechanical properties, called anomalous properties, such as negative linear compressibility or auxeticity (negativity of the Poisson's ratio). Using a large structural database of hypothetical zeolites and thanks to quantum level calculations, I investigated the links between structural descriptors and mechanical properties in all silica zeolitic structures. With the data generated by quantum calculations I used machine learning techniques to develop a methodology allowing to screen this type of materials looking for auxeticity and capable of efficiently predicting their Poisson's ratio at a small computational cost.

MOFs constitute a new class of porous materials that has been studied for about 25 years, with an exponentially growing number of reported structures. Until very recently, they have essentially been considered as crystalline materials. Yet their amorphization, by increase of temperature, mechanical stress or increase of pressure, is of great interest whether to study its mechanism or for potential applications of the amorphous phases obtained. I have been interested in characterizing the melting and quenching of some of these materials, especially from the family of zeolitic imidazolate frameworks (ZIFs). ZIFs are a subgroup of MOFs, topologically isomorphic to zeolites, with particularly good thermal stability, making them good candidates for thermal-induced amorphization. In particular, using quantum molecular dynamics simulations, I unraveled the mechanism behind the melting and characterized the nature of the liquid phase obtained. I also shed light on the links existing between the initial topology, the melting behaviour and the resulting glass-like phase. Finally, I modelled a situation that has not yet been studied experimentally: the forced filling of one of these materials with carbon dioxide before and during melting. I could infer the influence of putting carbon dioxide inside this specific ZIF on the melting behaviour and I found a possible way

through which it could be trapped inside the amorphous phase.

This thesis is composed of three parts. In the first part, I describe the classes of materials I studied, namely microporous materials in general and zeolites and MOFs in particular. In the second chapter of this first part I detail the numerical methods I used during my PhD.

In a second part, I detail the work I carried out on the mechanical properties of zeolites. I first remind the theory of elasticity and how elastic constants are computed before analyzing the database I based my work on and describing the results of my investigations on auxeticity in these materials.

Finally, the third part treats the melting and quenching of MOFs. The first chapter gives an overview of the amorphization of MOFs in the literature. The second chapter investigates the melting itself, its mechanism, its thermodynamics implications and the nature of the liquid obtained. The third chapter aims at describing the quenching of three different ZIFs from liquid phases obtained earlier, focusing on the structural implications of the initial topology on the final glass. The last chapter presents the study I conducted on the filling of one of these ZIFs with CO_2 before melting it.

Part I

Materials and methods

Chapter 1

Microporous materials studied

1.1 Presentation of porous materials

1.1.1 Generalities

Porous materials are materials which possess voids, or cavities, of various shapes, sizes and regularities inside their three-dimensional structure. [1] There are many natural examples of porous materials as well as a lot of synthesized ones. [2] The network formed by the pores can be percolated, meaning the pores are all connected, or not. The chemical nature of these materials can be very different, from purely inorganic materials to purely organic, through mixed metallo-organic structures. Their complex internal structure is often characterized by their specific surface area, which is the area by unit of mass where a liquid-solid or a gas-solid interface can be formed.

The large specific surface areas they often exhibit makes them interesting for industrial applications that rely on the physico-chemical phenomena of adsorption or catalysis. They can be used as insulating materials, with a insulating fluid, such as air, inside their pores. They are also widely used in gas separation, purification and storage, for sieving oil products in refineries, in heterogeneous catalysis, as substrate for ionic exchange, as dielectric coating and to trap chemically harmful and radioactive substances. [3–5] For instance zeolites and activated carbons are used to produce medical oxygen from air by using those materials as molecular sieves. To give an idea of the industrial importance of those materials, I give in Table 1.1 the amounts produced per year for some of them.

As the pore size influences the properties of these materials, they are classified in three categories by the IUPAC (International Union of Pure and Applied Chemistry):

- Microporous solids, with pores of dimensions smaller than 2 nm

	annual production (tons)	example of use	Reference
Natural zeolites	3.2 M	water purification	[6]
Synthetic zeolites	1.8 M	detergent industries	[6]
Metal-Organic Frameworks	*	carbon capture	[7]
Activated carbons	1.7 M	gas separation	[8]
Resins and fibers	380 M	for reference	[9]

Table 1.1: Annual amounts produced for different kinds of porous materials and example of use. * Though Metal-Organic Frameworks are produced at the ton scale by two companies (BASF, MOF Technologies), the total amount produced annually remains low and uncertain.

- Mesoporous solids, with pores having sizes between 2 nm and 50 nm
- Macroporous solids, with pores larger than 50 nm

Microporous and mesoporous solids are grouped together to be called nanoporous solids, with pores smaller than 50 nm. Three examples of such materials are shown in Figure 1.1.

The chemical composition is also a discriminant to classify porous materials. The main difference is between organic and inorganic porous materials, with many more representatives for the latter than the former. The purely organic materials are composed of carbon-based frameworks such as polymers, activated carbons or Covalent-Organic Frameworks (COFs). Among inorganic materials there are many oxides (from silica, titanium, zirconium) such as zeolites, or binary compounds such as sulfates and aluminophosphates (based on $AlPO_4$).

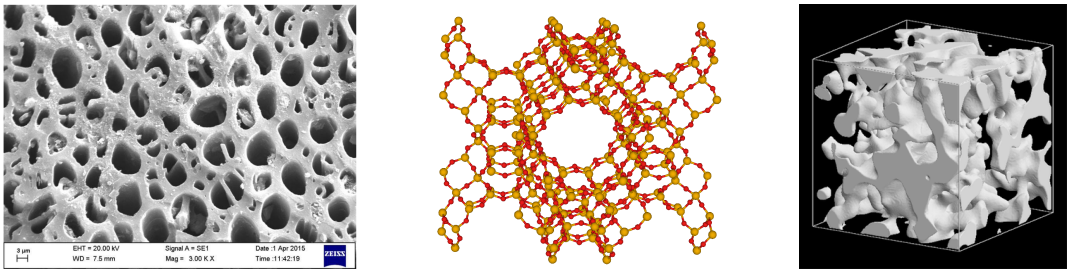

Figure 1.1: Three examples of different porous materials. On the left a scanning electron microscopic image of an activated carbon is shown [10] (ordered but non crystalline), in the middle the crystalline molecular structure of the zeolite faujasite (made with VESTA [11]) and on the right an amorphous vycor glass is represented (disordered). [12]

Finally, another important distinction to characterize porous materials lies in the regularity of their structure. There are crystalline materials, like zeolites and Metal-Organic Frameworks, in which atoms form a three-dimensional motif periodically repeated to form a periodic network (see Figure 1.1 for an example of a zeolite unit cell). By symmetry, the

porous network in crystalline materials is regular and periodic. Other materials are regular, but not crystalline, such as clays or carbon nanotubes. For the latter, the pores have well defined characteristics, but there is no three-dimensional periodic arrangement. The third type is the amorphous type, which represents the majority of materials. Examples of amorphous porous materials span from activated carbons to Vycor glass through aerogels or amorphous silica. Their pores have a great polydispersity with irregular shapes (see Figure 1.1 for an example of Vycor glass).

During my PhD, I have been interested in zeolites as well as Metal-Organic Frameworks, so I will describe them in more details afterwards. For a large part I have studied amorphous Metal-Organic Frameworks and the transition from a crystalline to an amorphous phase in these systems. For that reason, I introduce hereafter the characteristics of crystalline and amorphous materials.

1.1.2 Crystalline materials

As previously written, crystalline materials are composed of periodic arrangements of ordered atoms in three dimensions. This property of periodicity makes them rather easy to analyze from an experimental point of view. For instance, one can determine to which space group the material belongs by X-ray diffraction, either on a full mono-crystal or on a powder, retrieving the structure by Rietveld refinement. [13] This is useful when one looks at symmetry-dependent properties, such as mechanical properties, piezoelectric, ferroelectric or dielectric properties. For instance, a centrosymmetric crystal cannot exhibit piezoelectricity as the elements of the piezoelectric tensor would vanish by symmetry.

It is also of importance when we want to predict the mechanical properties from the second order elastic tensor. In fact, according to the crystal class to which it belongs, the material studied may have coefficients either identical with each other or equal to zero (described extensively in [14]). There are 230 symmetry space groups to which a crystal can belong. However, these can be regrouped into 14 Bravais lattices belonging to only 7 crystal systems as shown in Figure 1.2. These symmetries can be leveraged when one wants to simulate crystalline systems. Within each crystal system, point groups are grouped into different Laue classes as presented in Table 1.2.

The periodicity of the crystals makes it easy to simulate a single unit cell and virtually extend the size of the system by periodic boundary conditions. It means that can we simulate what happens only in one unit cell, assuming that this cell is infinitely repeated in space as exemplified in Figure 1.3. In quantum chemistry, we simulate the infinite spatial repetition by going to the reciprocal space, where it is enough to sample the first Brillouin zone to have a good representation of the electrons in the system. Theoretically, there needs to be an infinite number of k-points to perfectly sample the first Brillouin zone. However, this is overcome by choosing a discrete number of specific k-points according to the Monkhorst-Pack method. [15] The coordinates of the k-points chosen correspond to nodes of the reciprocal

Crystal system	Laue class	Point groups
Triclinic	$\bar{1}$	$1, \bar{1}$
Monoclinic	$2/m$	$2, m, 2/m$
Orthorhombic	mmm	$222, 2mm, mmm$
Tetragonal (II)	$4/m$	$4, \bar{4}, 4/m$
Tetragonal (I)	$4/mmm$	$4mm, 422, \bar{4}2m, 4/mmm$
Rhombohedral (II)	$\bar{3}$	$3, \bar{3}$
Rhombohedral (I)	$\bar{3}m$	$32, 3m, \bar{3}m$
Hexagonal (II)	$6/m$	$6, \bar{6}, 6/m$
Hexagonal (I)	$6/mmm$	$6mm, 622, \bar{6}2m, 6/mmm$
Cubic (II)	$m\bar{3}$	$23, m\bar{3}$
Cubic (I)	$m\bar{3}m$	$432, \bar{4}3m, m\bar{3}m$

Table 1.2: Crystal systems with corresponding Laue classes and point groups. Table extracted from [14].

lattice. Depending on the size of the unit cell considered in the real space, we sample the reciprocal space with more or less k-points: the bigger the unit cell, the less k-points are needed.

1.1.3 Amorphous materials

On the contrary to crystalline materials, amorphous materials have a long-range disordered structure. It does not mean that no local organization is possible, but rather than there is no spatial periodicity in the system. For instance, Metal-Organic Frameworks, usually known as crystalline materials, can sometimes be amorphized to form glass-like materials (Figure 1.4) with the same chemical composition, but a different spatial organization. In an amorphous material, the range over which the atoms can be considered ordered is usually limited to a few covalent bonds, up to 10 Å. In Figure 1.4, along with the two chemical structures, we can see the results of X-ray diffraction patterns for both materials. This is a way to realize the difficulty posed by amorphous materials: while the crystal gives sharp, easily recognizable peaks, the amorphous MOF is associated with a very wide signal, characteristic of an absence of long-range order.

This lack of periodicity and symmetry in amorphous systems creates a challenge for simulation and characterization, but can also be useful for applications. In fact, amorphous phases are thus much more isotropic which is a great advantage for industrial applications in particular for shaping the actual material.

In the next section, I present one of the most studied class of crystalline nanoporous materials: the zeolites.

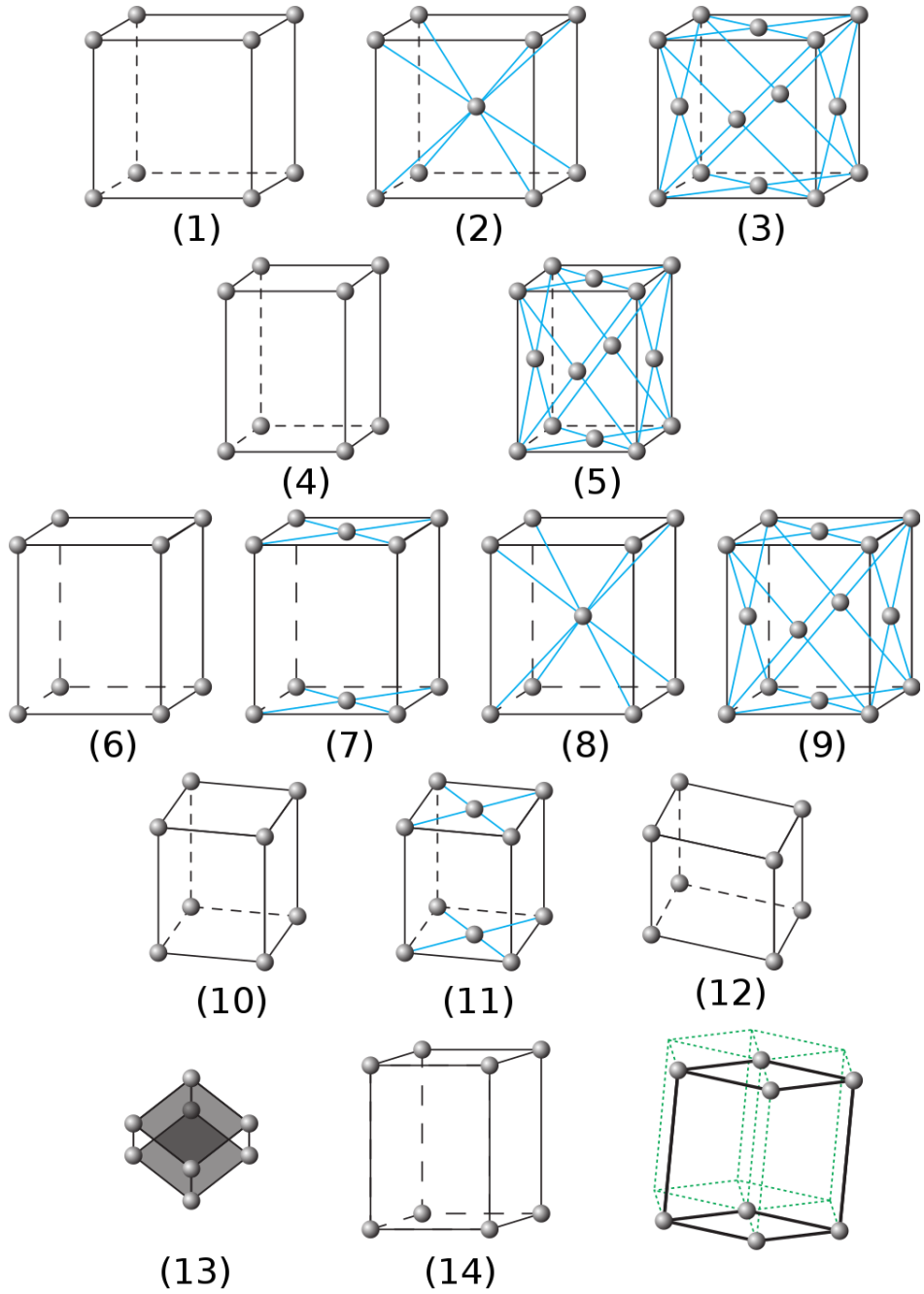

Figure 1.2: The 14 Bravais lattices are represented. With the following conventions : Primitive centering ↔ P; C ↔ Centered on a single face; I ↔ Body centered; F ↔ Face centered. (1) is Cubic P, (2) is Cubic I, (3) is Cubic F, (4) is Tetragonal P, (5) is Tetragonal I, (6) is Orthorhombic P, (7) is Orthorhombic C, (8) is Orthorhombic I, (9) is Orthorhombic F, (10) is Monoclinic P, (11) is Monoclinic C, (12) is Triclinic, (13) is Rhomboedral, (14) is Hexagonal.

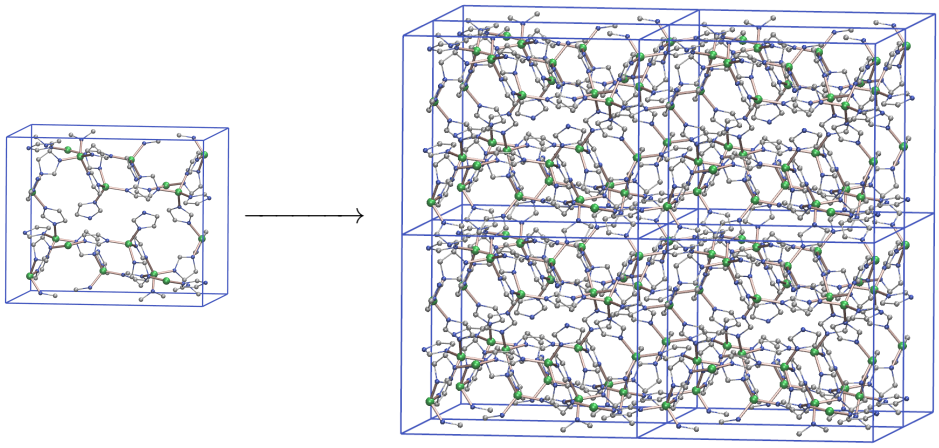

Figure 1.3: Example of a system studied with periodic boundary conditions (a MOF called ZIF-4). Here, 8 (2x2x2) unit cells are shown while only 1 is really considered in the simulation. Zn, green; C, grey; N, blue; coordination bonds, flesh.

1.2 Zeolites: porous aluminosilicates

The term zeolite comes from the greek words $\zeta\varepsilon\omega$, meaning "to boil" and $\lambda\iota\vartheta o\sigma$, meaning "stone". This term was originally coined by Axel Frederik Cronstedt in 1756 as he observed that a lot of steam from water, previously adsorbed in the material, would come out of it as he heated it. [17] Zeolites belong to the class of nanoporous materials and are composed of oxygen, silicon and aluminium, hence their denomination as aluminosilicates. At the molecular scale, they are constituted of tetrahedra made of a central T atom (T = Al or Si) and four oxygen atoms sharing one corner with each other (Figure 1.5). It is mathematically possible to create an infinite number of such crystalline structures and there are databases of hypothetical zeolitic structures containing up to 2 million different frameworks. [18] However, today only 228 different frameworks have been reported experimentally, among which 67 are natural zeolites (according to the International Zeolite Association). Each zeolite is identified by a 3 letters code such as FAU, for the faujasite framework, or LTA for Linde Type A (Figure 1.5).

Zeolites are aluminosilicates with a generic chemical formula $M_{x/m}Al_xSi_{1-x}O_2$. The ratio between the number of silicon atoms and aluminium atoms ($\frac{1-x}{x}$) called the Si/Al ratio is an important parameter that varies between 1 (as many Al than Si) and infinity (no Al). Most zeolites only exist for this ratio within a specific range. In the case where there is no aluminium, the zeolite is said to be pure silica. In all other cases, when some silicon atoms are substituted by aluminium atoms, the difference of oxidation degree (+IV for Si, +III for Al) creates a delocalized charge imbalance in the structure. These defects are compensated by extra-framework cations that don't belong to the crystalline arrangement, hence the *extra-framework* denomination. The most common cation is Na^+, but Li^+, K^+, Ba^{2+}, Ca^{2+} as well as others are commonly used. These delocalized cations create local electrostatic gradients,

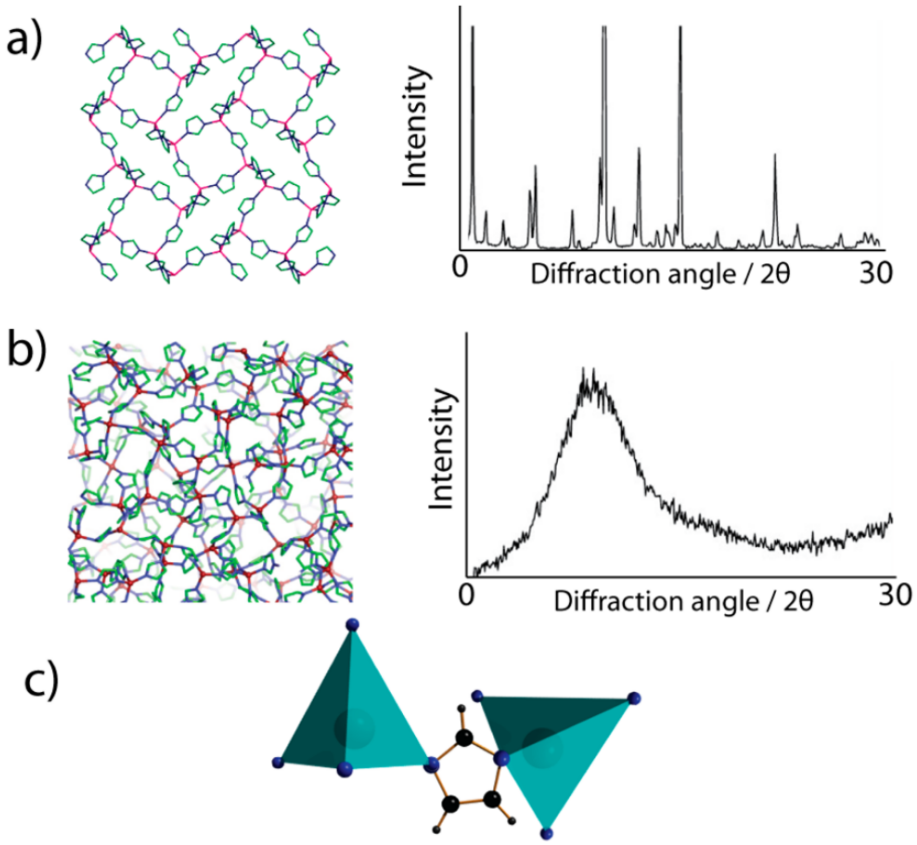

Figure 1.4: Figure showing the difference between crystalline (a) and amorphous (b) ZIF-1, even though they are both composed of the same basic unit, a zinc tetrahedra linked by an imidazolate cycle (c) (taken from [16]).

thus improving the adsorption properties of zeolites towards molecules with dipolar and quadrupolar moments. Their accessibility to adsorbed molecules also serves the catalytic use of zeolites, as they can act as catalytically active sites (for example with proton for heterogeneous acid catalysis).

The term zeolite is often extended to describe four-connected nets of porous structures with other atoms such as aluminophosphates or germanium and gallium oxides. As evidenced in Table 1.1, these materials are widely used in many industries worldwide. For example the zeolite A (LTA) substituted with different cations is used to remove carbon dioxide from natural gas, as dehydrating agent or to selectively extract linear alkanes in refining processes. Other zeolites are used in the production of medical oxygen from air or to trap carbon dioxide during cement production, or even to decontaminate nuclear sites from radioactive nuclides. They are also used in domestic applications such as water softening or in detergents to replace phosphates.

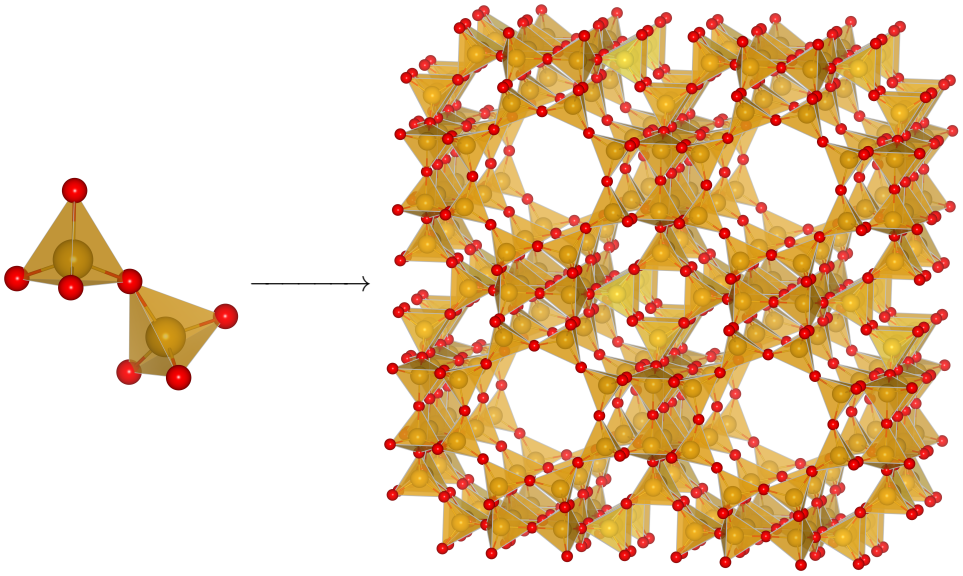

Figure 1.5: Two tetrahedra connected by a corner on the left and the molecular structure of the zeolite LTA (Linde Type A) on the right (made with VESTA [11]). Si, yellow; O, red.

1.3 Metal-Organic Frameworks: crystalline and amorphous nanoporous materials

The concept of Metal-Organic Frameworks (MOFs) appeared almost 30 years ago in the literature [19] to designate a class of materials composed of inorganic nodes linked by organic ligands. In this seminal article, Hoskins and Robson use the term "Infinite Polymeric Frameworks" and they emphasize the large cavities created by such 3D arrangements leading to potential applications as "molecular sieve", for "ion exchange" or in "heterogeneous catalysis". Ten years later, the first use of the term "MOF" is reported by Omar Yaghi's team at UCLA for the synthesis of a material called MOF-5. [20] Since then, the field of MOF has been developing exponentially, in terms of publications and in terms of number of structures reported in the literature. For instance, Yaghi *et al.*'s paper is cited more than 5000 times and more than 400 times per year in the last 5 years. Figure 1.6 shows the growth of the number of structures reported in the Cambridge Structural Database with a doubling time of 3.9 years for three-dimensional MOFs. Academic studies are also sustained by a growing industrial interest for MOFs. In fact, the great versatility and the extremely large specific surface area accessible through these materials make them very good candidates as a new generation to follow zeolites in catalysis and adsorption-related applications.

However, the presence of organic ligands in MOFs and the bonds they are based on being weaker than the Si-O covalent bond make them thermally stable up to 300 °C to 500 °C, while zeolites can stand temperatures over 1000 °C. MOFs also tend to have difficulties fitting

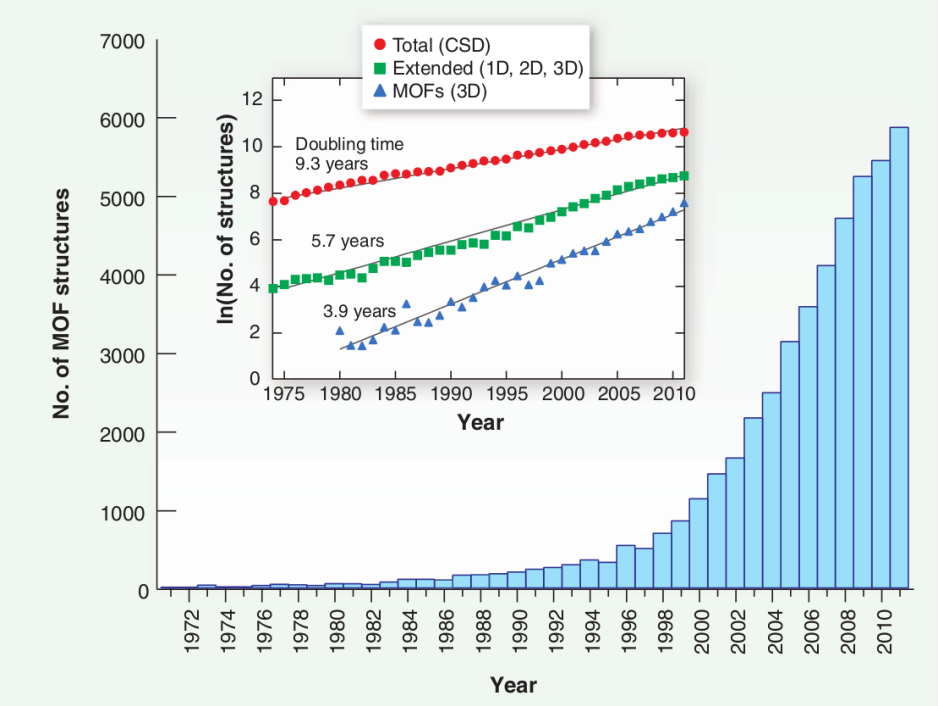

Figure 1.6: Figure showing the exponential growth of the number of MOF structures reported in the Cambridge Structural Datadabase (CSD) (taken from [21]).

in industrial processes due to their smaller stiffness as compared to inorganic zeolites. [22] Nonetheless MOFs have been produced at the ton scale by some industrial companies, namely BASF and MOF Technologies. The latter introduced the first commercially viable MOF in 2016, integrated in a system aiming at keeping fruit and vegetables fresh by controlled release of 1-methylcyclepropene, initially contained in the MOF. [23]

The MOF field is very wide and carries many different aspects. I am going to evoke some of these aspects, namely the variety which makes MOFs so promising, write a word on synthesis and characterization techniques and finally an introduction to the world of amorphous MOFs, that shall be more detailed in the dedicated part (see chapter 1 of Part III). For further details, many reviews are available, to cite a few: [21] for a general presentation of MOFs, [22] focuses on mechanical properties in MOFs, [24] reviews the responsive behaviours of MOFs to different stimuli (pressure, temperature, adsorption, light), [25] describes the interesting aspects that disorder, flexibility and defects bring to the MOF field, [26] and [27] present the different ways MOFs and their properties are simulated, with a focus on the simulation of flexibility in [27].

1.3.1 The great versatility of MOFs

One of the main advantages of MOFs over zeolites or activated carbons is the diversity of structures that can be built from the different inorganic clusters and organic linkers available. Figure 1.7 shows only part of the available secondary building units, the name given to the inorganic clusters, and organic linkers. With all the diversity provided by coordination chemistry and organic chemistry, the number of structures is only limited by the thermodynamic stability of the phases obtained. One must also be able to direct the synthesis towards a porous polymorph, while the corresponding dense phase might be more thermodynamically stable.

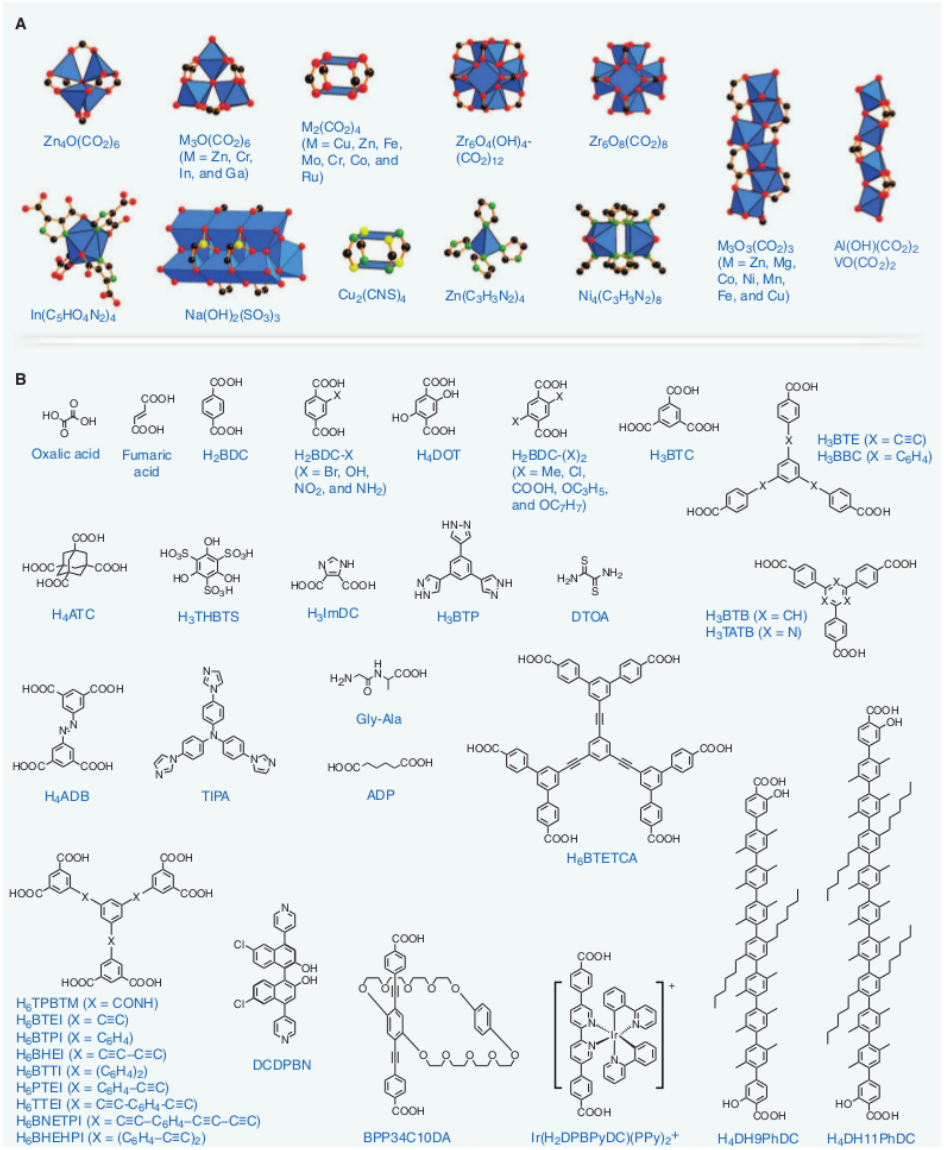

Figure 1.7: Figure exhibiting examples of inorganic clusters (A) and organic linkers (B) (taken from [21]).

This diversity of structures gave rise to a *design to applications* approach, where one aims at producing the best structure for a given functionality. For instance, the MOF with the highest methane uptake to date has been reported [28] as well as another MOF with the highest hydrogen uptake for now. [29] Sometimes, different aims are combined, such as in the study reported in [30] where hydrogen uptake, carbon dioxide against water selectivity and economic cost are taken into account.

Most organic ligands used in MOFs are either polycarboxylates or polynitrogens. As demonstrated in Figure 1.8, the carboxylate functional group has three different coordination modes, that can be used to create structures with the same chemistry and a different topology. The other approach can be to create structures with the same connectivity and different organic linkers. These structures are then called isoreticular, meaning that they share the same net.

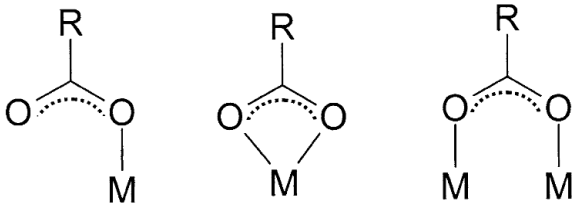

Figure 1.8: Figure showing the different coordination modes of a carboxylate ligand: monodentate (left), bidentate chelate (center), bidentate bridging (right) (taken from [31]).

For example all the MOFs in the IRMOF family, beginning with MOF-5 (IRMOF-1), have bidentate bridging carboxylate ligand. [32] In this case, the length of the ligand linking two Zn-O-C clusters varies to go from a pore size of 3.8 Å for IRMOF-1 to 28.8 Å for IRMOF-16 (Figure 1.9).

To rationalize the design process, the inorganic nodes and the organic linkers are represented as polyhedra with more or less simple geometries, as shown in Figure 1.10. [33] 131 SBUs have been identified, from simple tetrahedra to geometric configurations with 66 points of extension through cuboctahedra, icosahedra or simple cubes. [34]

In the case of organic ligands containing nitrogen, the lone pair of the nitrogen atoms forms a coordination bond with the metal ion. Usually the ligand creates a bridge between two metallic clusters. It is the case for the bipyridine ligand, especially used to obtain MOFs with catalytic activity. [35, 36] Another widely used nitrogen-containing ligand is the imidazolate cycles, functionalized or not. These ligands are the basis of the family of MOFs called Zeolitic Imidazolate Frameworks (ZIFs). Their name comes from the topologic similarity with zeolites, meaning that the angle metal-imidazolate-metal has the same value of 145 ° than the angle Si-O-Si in zeolites. [37] The metal center is usually a Zn(II) or Co(II) with a tetrahedral coordination. This family of MOFs is particularly studied for their chemical and thermal stability, much better than most other MOFs.

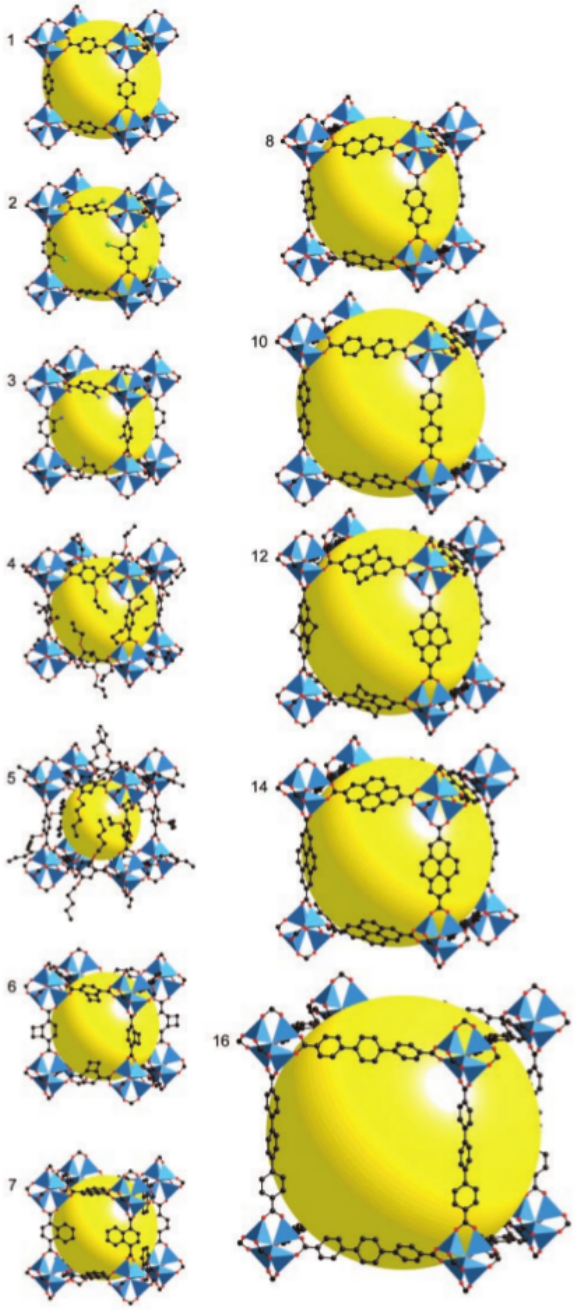

Figure 1.9: All the non-interpenetrated MOF of the IRMOF family are shown, with number n being IRMOF-n (extracted from [32]).

1.3.2 Synthesis and characterization

MOF synthesis is usually a solvothermal synthesis from a salt containing the metallic ion (e.g. nitrates, sulfates) disolved in a polar organic solution which contains a precursor for the organic ligand (carboxylic acid for example). [38, 39] The auto-assembly takes place as the

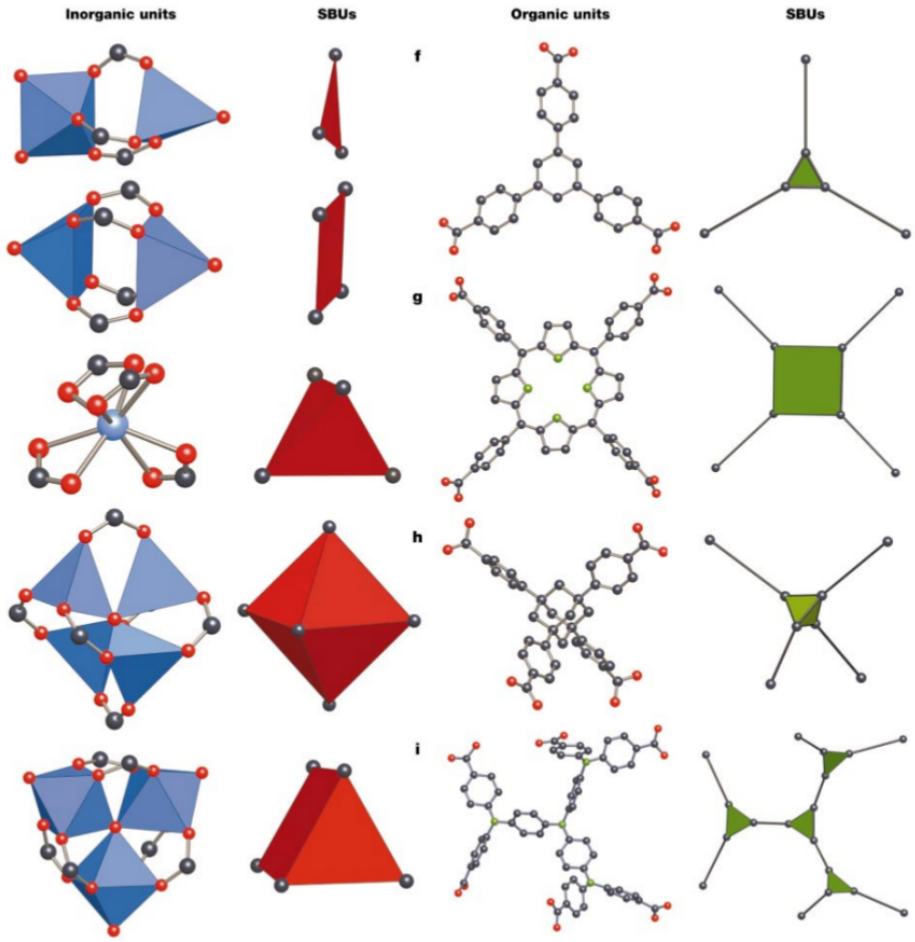

Figure 1.10: Figure demonstrating the reduction from chemical structures to geometric secondary building units (SBU) (taken from [33]).

temperature is elevated up to 250 °C. The purification and drying steps after precipitation and crystallisation have to be carried out carefully as MOFs can retain a lot of impurities in their pores. The stability of the MOF and its final characteristics depend very much on the pH of the initial solution and the right conditions have to be determined for each new structure. Other synthesis methods have been developed: microwave-assisted synthesis, electrochemical synthesis, mechanochemical synthesis and sonochemical synthesis. Microwave radiations are an energy efficient way to heat the system and can be used to speed up the synthesis. [38] Sonochemical synthesis uses high-energy ultrasound to give energy to the system and has not been studied extensively. Electrochemical synthesis, first reported by BASF in 2005 [40], has been developed to avoid using nitrates at the industrial scale for safety reasons. In this case, the metal ions are introduced through anodic dissolution to the main solution. Finally, mechanochemical synthesis uses mechanical force to activate chemical reactions and is important for environmental issues. In fact, this kind of synthesis can be carried out at room temperature without any solvent. For example, this method had to be used for the first commercial application of MOFs, because of the contacts with food afterwards. [23] As a

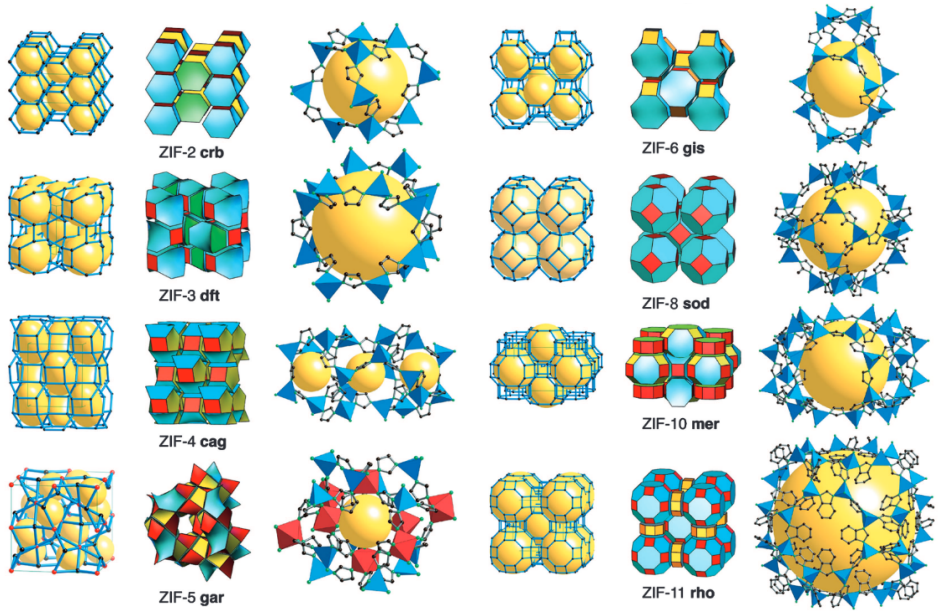

Figure 1.11: Examples of Zeolitic Imidazolate Frameworks (built from Figure 1 in [37]).

matter of fact this technique is gaining a lot of traction for MOF production at larger scales.

After the synthesis, the MOF can be modified by so-called post-synthetic modifications (PSM), which created a whole field of research on how to exchange, insert, polymerize or functionalize ligands post-synthesis. [41] For example, MIL-101 has been synthesized as nanoparticles and submitted to covalent post-synthetic modificiations to be able to efficiently deliver imaging contrast agents and anticancer drugs. [42] ZIF-8 is one of the most studied structure for its large cavities and its thermal and water stability. It is composed of Zn^{2+} tetrahedral ions with methyldimidazolate cycles as ligands arranged in a sodalite topology. The methyl functional groups prevent from taking full advantage of the large cavities as they reduce the aperture size (Figure 1.12). In 2012, Karagiaridi *et al.* reported the exchange of methylimidazolate ligands for unsubstituted imidazolate ligands up to 85% to synthesize a MOF called SALEM-2. [43] As depicted in Figure 1.12, this post-synthetically modified structure has a better solvent uptake than ZIF-8 and exhibits a Brønsted base catalytic activity upon application of n-butyllithium, which is unreachable with the parent material ZIF-8.

As the vast majority of MOFs are crystalline, the main characterization technique used to determine the crystallinity and the structure is X-ray diffraction. It can be done on a single crystal if the synthesis allows to have large enough crystals or on powder. Scanning electron microscopy is used to study the size and regularity of the synthesized crystals. [44] Transmission electron microscopy, electron diffraction and high-resolution electron microscopy can be combined to direcly image larger pores in MOF, like the ones in MIL-101. [45] In order to determine the specific surface area and the porous volume, nitrogen adsorption measurements at 77 K are done after every synthesis. The adsorption properties of important gas for applications, such as CO_2, H_2 or CH_4, are also routinely studied at low pressure. [46] Adsorption

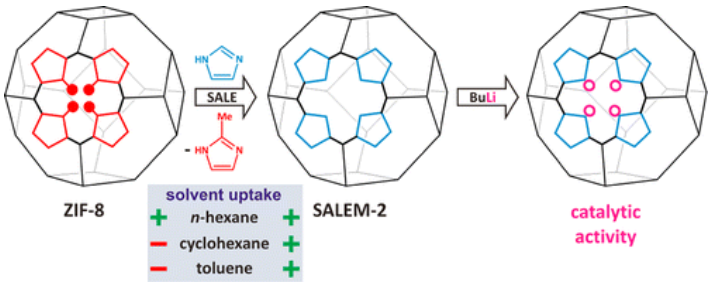

Figure 1.12: Post-synthetic modifications of ZIF-8 to synthesize SALEM-2 in order to obtain catalytic activity (taken from [43]).

isotherms at higher pressures or characterization by neutron diffusion are less frequent due to the necessary equipments. [47] Advanced spectroscopic methods such as EXAFS or XPS can be useful to determine the chemical environment of the metal centers, but classical spectroscopic techniques such as IR, UV and Raman are also used, partly to study the properties of adsorbed molecules inside the pores. [48]

1.3.3 Amorphous MOFs: new phases, new applications

Although most studies on MOFs focus on crystalline structures, there has been a recent shift, with increasingly more examples of MOFs that show defects and disorder, and the realization that this is not always detrimental to their physical or chemical properties — and thus, to their performance in potential applications. There are even studies that focus on "defective by design" strategies to explore further the configurational space of organometallic structures. [25] In particular, several amorphous MOFs have been studied in the last few years and proposed as candidates for applications such as controlled release, irreversible trapping of harmful substances, or creating new optically active glass-like materials. [16] There are several ways to obtain amorphous MOFs, ranging from direct synthesis [49] to the amorphization of crystalline MOFs by melting and quenching, [50] application of mechanical pressure, [24] or ball-milling. [51] The conditions under which a MOF can undergo amorphization vary very much depending on the topology and the chemistry of the framework. Actually, most MOFs cannot amorphize at all, but would rather decompose when heated or submitted to high pressures. Most MOFs structures found to be able to undergo amorphization belong to the ZIF family, [50–55] even though there are examples of MOFs from other families, such as MIL-140 or UiO-66. [56]

For instance, Orellana-Tavra *et al.* [57] reported, in 2015, the controlled release of calcein, used as a model drug, thanks to the amorphization of UiO-66 by ball-milling. They used the idea reported by Bennett *et al.* to irreversibly trap iodine in ZIFs amorphized by ball-milling [51, 58] to hinder the diffusion of calcein inside UiO-66. Another example of the enhancement of properties by amorphization is the transition from a crystalline insulator to an amorphous semiconductor reported by Tominaka *et al.* in 2015. [59] It is important to notice

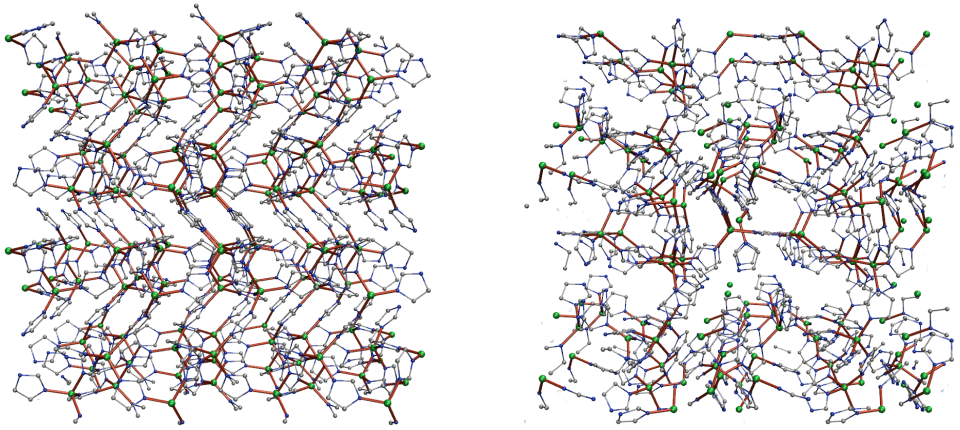

Figure 1.13: ZIF-4 structure as simulated: crystalline structure (left) and snapshot of a glass-like configuration (right). The Zn–N nitrogen coordination bonds are represented in red.

that the local coordination environment is conserved during these amorphization processes (as represented in Figure 1.13), which underlines the importance of the flexibility of MOFs. The potential of these new phases is huge, but a lot of aspects in the process of amorphization are to be understood in order to control it to design new functional materials. Experimental characterization being very difficult on these systems, molecular simulation methods offer a way to get further insights on the amorphization process. In 2017, we reported a mixed computational/experimental study on the melting of ZIF-4, especially about the mechanism and the thermodynamics involved. [60]

In chapter 1 of Part III, I give a more precise view of the different amorphization strategies in MOFs and in chapter 2 of Part III I detail the specific frameworks I studied during my PhD.

Chapter 2

Molecular simulations methods

Numerical simulation, and in particular molecular simulation, began in the 50s after the second world war, especially in the field of neutron dynamics for nuclear reactions. It started with the Monte Carlo algorithm, presented by Metropolis *et al.* in 1953 [61], followed by a simulation of an anharmonic 1D crystal by Fermi *et al.* in 1955 [62] and a molecular dynamics simulation of a hard sphere system by Alder and Wainwright reported in 1957. [63] Since these seminal studies, with the improvement of the algorithms and the exponential increase of computational power, numerical simulation to study physical and chemical systems has become a whole research domain. Numerical simulations are complementary with experiments and analytical theories and are sometimes called *in silico* experiments. [64–66] In fact, experimental measurements often give global information on the system and the phenomena and are often unable to tell anything about the microscopic mechanisms leading to the macroscopic observation. On the other hand, analytical theories, although very elegant, represent the system studied with many simplifications to make calculations tractable, which can hinder their capacity to actually predict how the *real* system would behave.

These *in silico* experiments also allow to go beyond the realm of experimental conditions. It can be very useful to study systems in extreme conditions, such as radioactive matter in the case of a nuclear incident [67] or systems under very high pressure, temperature or electric field. [68] It can also be used to study systems in conditions that are difficult to reproduce, as in the domain of cosmochemistry. Finally numerical simulations can help to bring insights on either very fast or very slow phenomena, impossible to observe in real time. Molecular simulations in particular give a microscopic view on the system, thus helping us to provide mechanistic explanations of macroscopic phenomena.

In this chapter, I will present the methods I used during my PhD. I start by the ones I used the most, which are approaches based on quantum physics to study molecular systems, and then I briefly present classical methods that I did use a little and offer a point of comparison with the former.

2.1 Quantum calculations

There are many different simulation methods relying a quantum level of theories. I present here only the density functional theory (DFT) method, as it is the most widely used and the only one — among quantum methods — which is tractable for systems with hundreds of atoms and periodic boundary conditions.

2.1.1 Principles of Density Functional Theory

In order to study the structure, energetics, electronic states and other physico-chemical properties of nanoporous materials with a high level of accuracy, we routinely use calculations based on density functional theory (DFT). [69]

Fundamentally, in quantum simulations of electronic ground-state properties, the wave function has to be found (ψ) so that it satisfies the Schrödinger equation to give the energy (E) of the system. An example of the Schrödinger equation for multiple electrons interacting with multiple fixed nuclei is given in Equation 2.1, Equation 2.2 and Equation 2.3. In these equations m is the electron mass and the Hamiltonian ($\hat{H}$) is composed of the kinetic energy of each electron ($\hat{T}$), the interaction energy between the atomic nuclei and each electron ($\hat{V}$) and finally the interaction energy between different electrons (i and j) for N electrons ($\hat{U}$).

$$\hat{H}\psi = E\psi \tag{2.1}$$

$$\left[\hat{T}+\hat{V}+\hat{U}\right]\psi = E\psi \tag{2.2}$$

$$\left[-\frac{\hbar^2}{2m}\sum_{i=1}^{N}\nabla_i^2+\sum_{i=1}^{N}V(\boldsymbol{r}_i)+\sum_{i=1}^{N}\sum_{j<i}U(\boldsymbol{r}_i,\boldsymbol{r}_j)\right]\psi = E\psi \tag{2.3}$$

The complete electronic wave function is a very complicated mathematical function with $3N$ variables, even for a simple molecule, as each atom has several electrons. For instance, the full electronic wave function for H_2O is a 30-dimensional function. Furthermore, the interelectronic repulsion term of the Hamiltonian ($\sum_{i=1}^{N}\sum_{j<i}U(\boldsymbol{r}_i,\boldsymbol{r}_j)$) is crucial and requires considering the correlations of each individual electron with all the other electrons. Therefore, an analytical treatment of the Schrödinger equation is vain. Furthermore wave functions cannot be directly observed, only real observables that are wave-function weighted averages of a hermitian operator can be. For example, Equation 2.4 illustrates how the density of electrons ($n(\boldsymbol{r})$) is determined from the individual electron wave functions, ψ_i.

$$n(\boldsymbol{r}) = 2\sum_i \psi_i^*(\boldsymbol{r})\psi_i(\boldsymbol{r}) \tag{2.4}$$

To circumvent the complexity of the wave function, DFT methods rely on two Hohenberg–Kohn theorems that allow to reduce the dimensionality of the problem greatly. [70] The first states that there is a unique electron density for which the energy is the ground-state energy. As a result, finding the right electron density — a scalar 3 variables function — is enough to uniquely determine a solution to the Schrödinger equation. The second states that the ground-state electron density minimizes the overall energy functional and subsequently corresponds to the solution of the Schrödinger equation. The latter shows that the electron density can be determined through a variational process. Kohn and Sham applied these theorems to build a set of single electron equations, holding their names, illustrated in Equation 2.5 that can be solved to find the electron density. [71] The solution of these equations are straightforward single electron wave functions that depend on three spatial coordinates. Although one would appreciate to relate these single electron wave functions, called orbitals, to the different electrons of the system, the Kohn-Sham orbitals are merely mathematical tricks, but they cannot be directly physically interpreted.

$$\left[-\frac{\hbar^2}{2m}\nabla^2 + V(\boldsymbol{r}) + V_{\mathrm{H}}(\boldsymbol{r}) + V_{\mathrm{XC}}(\boldsymbol{r})\right]\psi_i(\boldsymbol{r}) = \varepsilon_i\psi_i(\boldsymbol{r}) \tag{2.5}$$

The Kohn-Sham equations contain three potentials V, V_{H} and V_{XC}. The first, V, describes the interaction between an electron and the collection of atomic nuclei, similar to $\hat{V}$. This potential has a simple analytical form. The second, V_{H}, describes the repulsion between the single-electron and the total electron density. It is named the Hartree potential and is defined by Equation 2.6, where the electron density is given by n.

$$V_{\mathrm{H}}(\boldsymbol{r}) = e^2 \int \frac{n(\boldsymbol{r}')}{|\boldsymbol{r} - \boldsymbol{r}'|}\mathrm{d}^3 r' \tag{2.6}$$

Importantly, this potential includes a self-interaction contribution as the electron described by the Kohn-Sham equation also contributes to the total electron density. Thus, V_{H} includes a nonphysical Coulombic interaction concerning an electron and itself which is corrected for in V_{XC}. This final potential, V_{XC}, characterizes the electron exchange and correlation interactions to the single-electron Kohn-Sham equations. The potential is formally defined as a "functional derivative" of the exchange–correlation energy (E_{XC}) which is not exactly known, except for a free electron gas. Nevertheless, many approximations exist, which permit the calculation of certain physical quantities accurately.

To solve the Kohn–Sham equations, the definition of Hartree potential (V_{H}) requires the electron density (n), which depends on the single-electron wave functions (ψ_i), which in turn requires the solution of the Kohn–Sham equations. As such, an iterative approach is applied to obtain a solution. [72] This is routinely achieved using the self-consistent field method, an example of a simplified algorithm for this approach is outlined below:

1. Define an initial trial electron density, $n(\boldsymbol{r})$

2. Calculate corresponding potentials, V, V_H and V_{XC}, for the electron density.

3. Solve the Kohn–Sham equations to find the single-electron wave functions, ψ_i.

4. Calculate the electron density, n_{KS}, from the constructed Kohn–Sham equations using the single-electron wave functions, ψ_i, from step 3.

5. Compare the calculated electron density, $n_{\mathrm{KS}}(\boldsymbol{r})$, with the electron density used in solving the Kohn–Sham equations, $n(\boldsymbol{r})$. If the two densities are the same, then this is the ground-state electron density and it can be used to compute the total energy. If the two densities are different, then a new trial electron density, $n(\boldsymbol{r})$, is used and the process begins again from step 2.

Reliable approximations for the exchange-correlation functional (E_{XC}) are required for the solution of the the Kohn–Sham equations. There are a number of approaches for treating exchange-correlation including LDA, GGA, meta-GGA and hybrid functionals. Each functional has particular strengths and weaknesses that must be considered for every new study. In particular, most functionals are fitted against experimental results on a finite set of systems, therefore their validity domain might be more or less narrow according to the size and diversity of the set.

Ultimately, the power of DFT is simplifying a $3N$-dimensional problem, where N is the number of electrons, into a 3-dimensional problem. Consequently DFT is a popular choice for electronic structure calculation, of both molecules and crystals, because of the accuracy obtained for relatively cheap computational cost. Moreover it is readily available and widely implemented in several open source, academic and commercial software packages. Recently, by comparing the equation of states for 71 elemental crystals with many DFT codes and methods a collection of the solid state community have demonstrated the reproducibility of DFT simulations. [73] The results for modern codes and methods agree very well exhibiting pairwise differences which are comparable to different experiments conducted with high-precision. In the following, I present the two main ways in which we have used DFT: it can be used for "static" calculations, where only the energy is computed or for molecular dynamics simulations where the forces and velocities are computed from the density to propagate the equations of motion.

2.1.2 Static calculations

The simplest type of DFT calculation on crystal structures are "static" DFT calculations used to explore local features of their energy landscape. This includes single-point energy calculations, energy minimization, harmonic vibration modes and more. The single electron wave functions presented are represented by a superposition of basis functions, gathered in basis sets. In practice, atomic basis sets are finite and their size (and parametrization), for each element in the system, is chosen as a compromise between computational cost and accuracy.

Depending on the accuracy needed, I have used either the DZVP (double-ζ valence polarized) or TZVP (triple-ζ valence polarized) basis sets, or alternatively basis sets parametrized for chemically similar compounds. To determine which type of basis set to use, I usually run single-point energy calculations with the various candidate basis sets, and check the quality of the description of the electronic states obtained. This is typically done by comparing values of electron density, atomic partial charges and band gap to our chemical knowledge of the system, or higher-level quantum chemical calculations.

For DFT calculations the level of detail contained in the electronic exchange and correlation functional (E_{XC}) is the main cause of approximation (or inaccuracy). Therefore, the choice of exchange–correlation functional has significant influence on how the energy depends on atomic positions, and thus on all calculated properties. While many options are available in the literature and implemented in popular software, the decision on exchange–correlation functional has to be guided by a compromise between accuracy and computational cost. [74] In fact, the more complex ingredients are considered to approximate the exchange-correlation functional, the more computationally expensive it is compute (Figure 2.1.2). Throughout my thesis, I used generalized-gradient approximation (GGA) functionals to take into account the non-local exchange and correlation effects, which is not possible with local density approximation (LDA) functionals. Furthermore, when computationally possible and relevant in terms of accuracy, I used hybrid functionals which provide a better description of the electronic exchange, but are more computationally expensive. This is achieved by adding exact Hartree–Fock exchange, mixed with exchange and correlation terms computed at the GGA level.

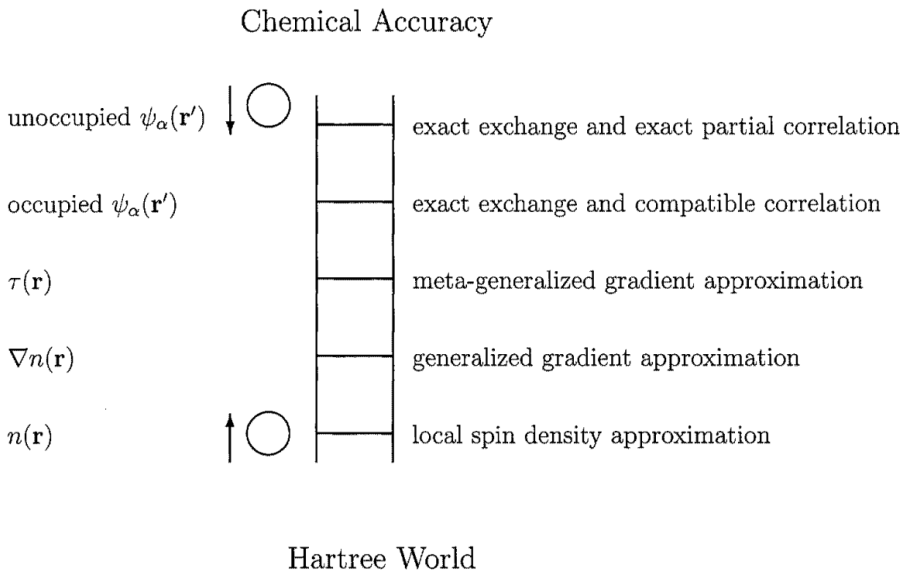

Figure 2.1: The Perdew ladder, showing that chemical accuracy comes closer as we lift approximations and satisfy more and more exact conditions by taking into account complex ingredients in the construction of the exchange-correlation functional (extracted from [74]).

Generally the appropriate functional is contingent on the property of interest. In practice previous work in my research group and others has shown that the PBE functional revised for solids (PBESOL) [75] in addition to a hybrid version, PBE0 (PBESOL0), produce consistent and physical results in many porous systems. [76, 77] Another common choice of hybrid functional in the literature is B3LYP [78]: although it is usually considered more appropriate for molecular calculations than in the solid state, it has been widely used in MOFs and appears to give reliable results overall. In cases of zeolites, which are built from stronger interactions than MOFs, it was noted that most properties (structure, energetics, mechanics) are well described already with GGA functionals such as PBESOL. However, for simulations of complex properties, such as band structures, the use of hybrid functionals is preferred. [79]

It is well known, and should be noted here, that DFT is quite poor at representing long-range correlation effects, typically including dispersion interactions. When required, in "static" calculations only, dispersion correction terms are added to the functional using the D2 correction scheme detailed by Grimme and coworkers. [80] The D2 correction is a relatively simple function of interatomic distances. This includes adjustable parameters fitted to interaction and conformational energies computed using high-level wave function methods. Subsequently this correction is added to the energy obtained by DFT and as such does not directly modify electron density (Equation 2.7). Equation 2.8 gives the formula used to compute the D2 correction.

$$E_{\text{Grimme}} = E_{\text{DFT}} + E_{\text{disp}} \ , \tag{2.7}$$

$$E_{\text{disp}} = -s_6 \sum_{i=1}^{N_{\text{at}}-1} \sum_{j=i+1}^{N_{\text{at}}} \frac{C_6^{ij}}{R_{ij}^6} f_{\text{damp}}(r_{ij}) \ , \tag{2.8}$$

where s_6 is a parameter adjusted according to the functional (equal to 0.75 for PBE), N_{at} is the number of atoms, $C_6^{ij} = \sqrt{C_6^i C_6^j}$ with C_6^i tabulated for each element, $R_{ij} = R_i + R_j$, r_{ij} is the distance between atoms i and j, and

$$f_{\text{damp}}(r_{ij}) = \begin{cases} \frac{1}{1+\exp\left[-d\left(\frac{r_{ij}}{R_{ij}}-1\right)\right]} & \text{if } r_{ij} \leq r_{\text{cutoff}} \\ 0 & \text{if } r_{ij} > r_{\text{cutoff}} \end{cases} \tag{2.9}$$

where d is a damping parameter (typically equal to 20) and r_{cutoff} is a cutoff radius that I took equal to 25Åin all the simulations where I used the D2 scheme.

Notably, there are a number of alternative dispersion correction methods [81] such as D3, that I used in *ab initio* molecular dynamics simulation (see subsection 2.1.3), and many-body-dispersion (MBD) scheme. [82, 83] Dispersion corrections are often essential as they can strongly influence energetic and mechanical properties, especially for porous structures.

Specifically, in MOF systems dispersion corrections often improve structural agreement with experimental crystal structures — although counter-examples can be found because Grimme's simple and empirical D2 correction scheme can lead to overestimation of the dispersive interactions at intermediate intermolecular distances (6–10 Å). Thus for each system, the good practice is to benchmark the performance of both approaches, without and with dispersion, to experimental data: in particular, the crystal density, unit cell parameters, and key intermolecular distances ($\pi - \pi$ stacking, hydrogen bonds, etc.) are considered, as these are crucial quantities typically affected by dispersive interactions.

Another important consideration for DFT calculations of crystals, especially for calculating mechanical properties, is the choice of reciprocal space sampling. In the CRYSTAL14 code, this is controlled by a shrinking factor, used to generate a corresponding grid of k-points in reciprocal space. For structures with very large unit cells reciprocal space sampling can be limited to the Γ point, in general it should be chosen so as to reach convergence on single-point energy. Recently, the importance of k-point convergence has been clearly described in simulations of MIL-47(V). [84] A rule of thumb I use, as a starting point, is to have the smallest lattice parameter multiplied by the value of the shrinking parameter be above 20 Å. In some structures with very asymmetric cells, for example MIL-47, [85] direction-dependent shrinking parameters are used, to refine the mesh in specific directions.

Finally, in order to supervise DFT calculations, a simple and useful is to examine, during the self-consistent field (SCF) iteration scheme for the calculation of the density and energy, the atomic partial charges (computed for instance via the Mulliken scheme). Because one has a reasonable chemical intuition of these quantities, they provide an initial and rapid feedback as to the quality of the density calculation: when the Si atoms in a zeolite acquire a net charge of 15, the simulation is certainly diverging! Subsequently if convergence seems unreachable, with standard minimization schemes and parameters, one can modify the initial population of orbitals for the first SCF cycle as to increase the damping of the SCF algorithm, to achieve self-consistence. Alternatively, the Broyden scheme for self-consistent field calculations is very robust. [86,87] Mulliken population analysis, commonly used to obtain atomic partial charges, has explicit basis set dependence [88] and may not display good accuracy. As atomic partial charges are nonphysical quantities there are complications and subjectivity to calculation of these values. Thus there are a number of alternative methods which are more suited to accurately describing porous systems. [89] However, to simply verify calculations the Mulliken method is adequate.

I give more details on how I computed mechanical properties of zeolites with static DFT calculations in Part II (chapter 1 for the detail of the theory for elastic constants and chapter 3 for the details of my use of CRYSTAL14).

2.1.3 Molecular dynamics with CP2K

In addition to the study of structures and "local" properties (often called "zero Kelvin" properties, because they do not account for thermal motions and entropic effects), the finite-temperature motion of condensed matter systems can be examined at the quantum chemical level using *ab initio* molecular dynamics (AIMD). Although much less frequent than local DFT calculations because of its much higher computational cost, AIMD is an essential tool to probe dynamical properties in situations where sub-nanosecond dynamics are relevant. It is applicable to all condensed matter systems, not limited to crystals but also including interfaces and complex liquids, as demonstrated in a recent study of transport mechanism of carbon dioxide in molten carbonates [90], or in our study on the melting mechanism of MOFs. [60] I present here the use of AIMD to study MOFs with or without adsorbates, using the CP2K simulation package — a general open source quantum chemistry and solid state physics simulation package, available at `https://www.cp2k.org`. There are several types of AIMD, the Ehrenfest dynamics, the Car-Parinello dynamics and the Born-Oppenheimer dynamics. During my PhD, I exclusively used Born-Oppenheimer AIMD, but I briefly present the two others for reference.

Ehrenfest dynamics

In Ehrenfest dynamics, the approximation employed is to write the full time-dependent wave-function of the system as a product of two time-dependent functions:

$$\Phi(\mathbf{r},\mathbf{R},t) = \Psi(\mathbf{r},t)\Xi(\mathbf{R},t)\exp\left(i\int_0^t dt' \left\langle \Psi_\Xi|\hat{H}_{\text{él}}|\Psi_\Xi\right\rangle\right) , \tag{2.10}$$

where Φ is the wave function of the system, Ψ its electronic part, Ξ its nuclear part, $\mathbf{r}$ the positions of all the electrons, $\mathbf{R}$ the positions of all the nuclei and $\hat{H}_{\text{él}}$ the electronic part of the Hamiltonian operator, without the kinetic energy of the nuclei and the nucleus-nucleus coulombic interaction. This approximation turns the Schrödinger equation into two coupled equations:

$$\begin{cases} i\dfrac{\partial\Psi}{\partial t} = -\displaystyle\sum_k \frac{1}{2}\nabla^2_{\mathbf{r}_k}\Psi + \left\langle \Xi|\hat{V}_{\text{n-el}}|\Xi\right\rangle\Psi & (2.11) \\ i\dfrac{\partial\Xi}{\partial t} = -\displaystyle\sum_k \frac{1}{2}\nabla^2_{\mathbf{R}_k}\Xi + \left\langle \Psi|\hat{H}_{\text{el}}|\Psi\right\rangle\Xi & (2.12) \end{cases}$$

One of the ways to solve these equations is by an iterative process called the Time-Dependent Self-Consistent Field (TDSCF). [91] Considering the nuclei as classical particles, Equation 2.12 becomes:

$$M_k \frac{d^2\mathbf{R}_k}{dt^2} = -\nabla_{\mathbf{R}_k} \left\langle \Psi | \hat{H}_{\text{el}} | \Psi \right\rangle \ , \tag{2.13}$$

with a condition on Ψ: $i\frac{\partial \Psi}{\partial t} = \hat{H}_{\text{el}}\Psi$.

The principle is to propagate these equations from the initial positions of the nuclei $\mathbf{R}(t=0)$ and the corresponding electronic wave function $\Psi(\mathbf{r}, \mathbf{R}(0), 0)$. As the wave function and the positions are simultaneously propagated the time step required is of the order of one hundredth of femtosecond to correctly account for the rearrangement of the electronic density around the nuclei.

Car-Parinello dynamics

The Car-Parinello dynamics, introduced in 1985 by Car and Parinello [92], allows to propagate the electronic wave function and the positions of the nuclei at the same time, similarly to the Ehrenfest dynamics, with timesteps of the order of 0.1 fs. The main idea behind this method is to look at a fictive slower dynamics of the electrons than the real one.

This method is based, unlike the former, on Lagrangian dynamics, as opposed to Hamiltonian dynamics. The Lagrangian operator $\mathcal{L}$ is such that the equation of the movements for the system are:

$$\frac{d}{dt}\frac{\partial \mathcal{L}}{\partial \dot{\mathbf{R}}_k} = \frac{\partial \mathcal{L}}{\partial \mathbf{R}_k} \ , \tag{2.14}$$

where $\dot{\mathbf{R}}_k = \frac{\partial \mathbf{R}_k}{\partial t}$. Usually, we have the relation: $\mathcal{L} = \mathcal{T} - \mathcal{V}$, where $\mathcal{T}$ and $\mathcal{V}$ are the kinetic and potential energies respectively.

Considering $\boldsymbol{\psi}_i$, the Kohn-Sham orbitals (Equation 2.5), $\mathbf{R}_k$, the nuclear positions and $\boldsymbol{\alpha}_v$, all the possible constraints on the system, Car and Parinello built the following Lagrangian:

$$\mathcal{L} = \sum_i \frac{1}{2}\mu \left\langle \dot{\psi}_i | \dot{\psi}_i \right\rangle + \sum_k \frac{1}{2} M_k \dot{R}_k^2 + \sum_v \frac{1}{2}\mu_v \dot{\alpha}_v^2 - E[\boldsymbol{\psi}_i, \mathbf{R}_k, \boldsymbol{\alpha}_v] \ , \tag{2.15}$$

where $\langle \psi_i | \psi_j \rangle = \delta_{ij}$. In Equation 2.15, M_k are the physical masses of the nuclei and μ and μ_v are arbitrary parameters. This Lagrangian generates a dynamics for $\boldsymbol{\psi}_i$, $\mathbf{R}_k$ and $\boldsymbol{\alpha}_v$:

$$\begin{cases} \mu\ddot{\psi}(\boldsymbol{r},t) = \dfrac{\delta E}{\delta\psi_i^*(\boldsymbol{r},t)} + \displaystyle\sum_k \Lambda_{ik}\psi_k(\boldsymbol{r},t) & (2.16) \\ \mu_v\ddot{\alpha}_v = -\dfrac{\partial E}{\partial\alpha_v} & (2.17) \\ M_k\ddot{R}_k = -\nabla_{R_k}E \ , & (2.18) \end{cases}$$

where Λ_{ik} are Lagrange multipliers introduced to satisfy the orthonormalization of the ψ_i's. Equation 2.16 and Equation 2.17 correspond to fictitious dynamics and are used as tools to perform the simulation of the real dynamics described in Equation 2.18. In Equation 2.15, one can recognize a new kinetic energy given by:

$$\mathcal{T} = \sum_i \frac{1}{2}\mu\left\langle\dot{\psi}_i|\dot{\psi}_i\right\rangle + \sum_k \frac{1}{2}M_k\dot{R}_k^2 + \sum_v \frac{1}{2}\mu_v\dot{\alpha}_v^2 \tag{2.19}$$

Thus, the Car-Parinello dynamics corresponds to a real dynamics when μ, acting as a fictitious mass for the electrons, and the time step are small enough so that $\sum_i \frac{1}{2}\mu\left\langle\dot{\psi}_i|\dot{\psi}_i\right\rangle$ is close to zero. Indeed, as μ increases the dynamics of the electrons get coupled to the dynamics of the nuclei and the system diverges from its Born-Oppenheimer surface. As this term measures the transfer of energy from the nuclei to the electrons, it corresponds to their coupling and should remain low during all the simulation.

Born-Oppenheimer dynamics

Owing to the great difference of mass between the electrons and the nuclei, the idea behind Born-Oppenheimer molecular dynamics (BOMD) is to consider the dynamics of the electrons and the nuclei decoupled. It allows to explore the dynamic motion of molecules by numerically solving Newton's equations of motion for the nuclei:

$$\boldsymbol{F}_i(\boldsymbol{r}^N) = -\nabla_i U(\boldsymbol{r}^N) = m_i\frac{\mathrm{d}^2\boldsymbol{r}_i}{\mathrm{d}t^2} \tag{2.20}$$

The force, $\boldsymbol{F}_i$ experienced by an atom i of mass m_i and position $\boldsymbol{r}_i$ is equal to the negative of the gradient, ∇_i, of the potential energy of the system defined by electron density, $U(\boldsymbol{r}^N)$. Subsequently, Newton's second law relates the force to the particle's mass multiplied by the second derivative of its position, $\boldsymbol{r}_i$, with respect to time, t, *i.e.* the particle's acceleration. In *ab initio* MD, the atomic forces are calculated at the quantum chemical level, typically using DFT. CP2K uses the Gaussian and plane wave (GPW) method or a Gaussian and augmented plane wave (GAPW) method to accurately describe the electronic density within the system. [93] Van de Vondele *et al.* have reported a complete and thorough description of these methods used by CP2K and other codes. [94, 95] The quantum character of these simulations lies only in the descriptions of the electrons, the nuclei are considered as classical

massive objects. It is important to keep in mind that other methods are being developed to take into account the quantum nature of the nuclei, which can be useful for specific cases. [96]

The motion of the nuclei follows Newton's equation, and is integrated numerically with a finite size time step Δt of the order of the femtosecond, i.e. the dynamics of the nuclei. At each time step the wavefunction is optimized in the DFT framework, thus combining the accuracy of *ab initio* calculations and the ability to study time dependent phenomena. This method is thus much more costly than static calculations, but can be used to study mechanisms where bond cleavage and bond formation are essential or where no classical approximation (force field) of the intra- and intermolecular interactions is available.

Simulations in several different thermodynamic ensembles can be performed: constant number of particles, volume and temperature (N, V, T), constant number of particles, pressure, and temperature (N, P, T). Moreover, the simulation of rare events such as chemical reactions and infrequent diffusion using AIMD is challenging. By combining AIMD with constrained dynamics and metadynamics methods researchers have been able to elucidate properties relating to rare events with high accuracy. [97, 98] The output from the simulations are typically the system's wavefunction — although it is costly to store on disk due to its large size — and population charges on each atom (and for each time step). AIMD simulations primarily result in the positions, the velocities and the forces on each atom of the system as well as the instantaneous temperature, stress tensor and , for (N, P, T) simulations, time-dependent cell parameters.

By analysis of the resulting trajectories a number of properties can be computed. Firstly, pair distribution functions (PDF) which, when all atoms are taken into account, can be compared with PDF from X-ray diffraction analyses. This is useful for validating simulations. By examining individual PDFs one is able to identify the relevant interactions, which is not possible from experimental data. Moreover, statistical analyses are used to quantify events such as bond cleavage and formation, specifically this was used to study the mechanism of pyrocarbonate formation and its separation into carbon dioxide and carbonate anion. [90] Additionally, computing coordination numbers aids in monitoring stability of coordination networks. [99] Vibrational modes within the framework or in the presence of a guest molecule can be obtained by effective normal mode analysis [100] and preferred sites of adsorption are found by simple analysis of the spatial distribution of adsorbates. Extraction of fundamental free energy profiles are achieved by identifying a potential of mean force or from more sophisticated approaches using constraint molecular dynamics such as the Blue Moon Ensemble approach. [101, 102] These methods are quite powerful, for example, they have recently been used to uncover the mechanism by which a carbon dioxide molecule can permeate a zeolite where cations block narrow pores for other gases (see Figure 2.1.3 extracted from [97]).

Importantly, these methods are quite costly in terms of computational power. For simulations in the (N, V, T) ensemble of MOFs with approximately 300 atoms, I can simulate between 2 000 and 6 000 fs in 10 hours using 256 cores on national high performance computing systems. Simulations in the (N, P, T) ensemble are often three times slower than (N, V, T)

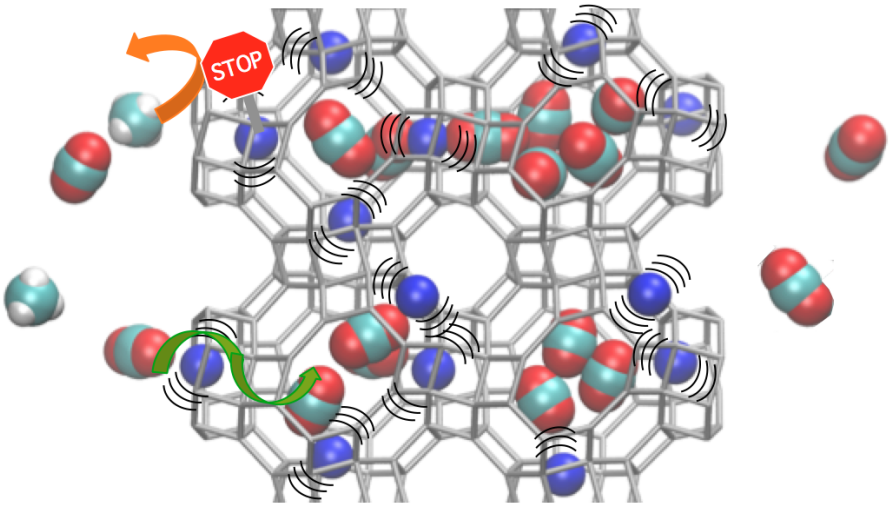

Figure 2.2: AIMD simulations was used to uncover the mechanism by which a carbon dioxide molecule can permeate a zeolite where cations block narrow pores for other gases by taking advantage of cations thermal motion. In gray: Na-RHO zeolitic framework; blue: Na^+ cations; CO_2 (cyan and red) guest molecules can bypass the sodium ions and diffuse through the zeolite's windows, while methane (cyan and white) cannot. This figure comes from [97].

simulations, as the temperature and pressure converge much slower. Despite this, Haigis *et al.* were able to accurately describe two structurally different phases of a very flexible MOF. [103] In particular, massive parallelization is not possible for this type of calculation, specifically, an increase from 64 to 128 cores has an efficiency of about 40%, from 128 to 256 cores about 50%, but increasing from 256 to 512 cores can even make the calculation 20% slower. Scaling studies are crucial before running simulations in order to be computationally efficient, or at least not to waste computational resources. Furthermore, simulations on supercells are often untractable, as DFT computational time scales approximately like N^3 where N is the number of electrons in the system.

During simulations, I check that the initially chosen parameters allow us to represent the system correctly. Conservation of energy and other conserved quantities are essential, in addition to convergence of temperature as it shows that the thermostat has the desired effect, and the same goes for the pressure (keeping in mind that pressure fluctuations on such small systems can be very large (∼10000 bars for a volume of 4000 $Å^3$)). I also check that the cell parameters and the charges remain plausible and they do not diverge or converge to obviously non-physical values. The number of self-consistent field steps needed to converge the energy at each time step is also a good hint of whether or not the input parameters, such as the time step, have been well-chosen. It is also crucial to check on the final trajectory that no unrealistic phenomena occur, such as a zeolite framework breaking covalent bonds in usual conditions of temperature and pressure.

2.2 Classical molecular mechanics

2.2.1 Main principles

Herein I have shown the wealth of information obtainable by quantum mechanical simulation, however, for longer time scales and larger systems classical molecular simulations are employed. Typically, classical simulations can be performed routinely on systems containing thousands of atoms, or in more extreme cases for systems up to 100,000 atoms [104] — although due to their periodic nature it is not common in simulation of crystalline materials. Simulation times in classical dynamics can also be much larger than in *ab initio* MD, ranging from a few nanoseconds to hundreds of nanoseconds. This allows molecular level insight into macroscopic material properties such as adsorption, diffusion and framework dynamics. [105–107]

Potential energy ($U(\boldsymbol{r}^N)$), in classical simulations is calculated from an interatomic potential energy function that is described by parameters from what is called the force field. The force field is the set that contains all the analytical expressions of the interactions between atoms and the corresponding parameters. The choice and implementation of force fields is crucial to the accuracy obtained by this method.

Force fields are parameterized such as to reproduce the molecular geometry or thermodynamic properties reported experimentally or described by higher level *ab initio* calculations. The general functional form of the potential energy function in classical molecular simulation includes bonded terms for interactions of atoms that are linked by covalent bonds (or metal-ligand bonds), and nonbonded or noncovalent terms that describe long-range electrostatic and van der Waals forces illustrated in Figure 2.3. The specific decomposition of the terms depends on the force field applied, but a general form for the total energy in an additive force field is illustrated in Equation 2.21, Equation 2.22 and Equation 2.23.

$$U_{\text{total}} = U_{\text{bonded}} + U_{\text{nonbonded}} \tag{2.21}$$

$$U_{\text{bonded}} = U_{\text{bond}} + U_{\text{angle}} + U_{\text{dihedral}} \tag{2.22}$$

$$U_{\text{nonbonded}} = U_{\text{electrostatic}} + U_{\text{van der Waals}} \tag{2.23}$$

There is a great variety of options for force fields with early examples developed to reproduce the geometry of small organic molecules and later adapted to treat more complex functionalized molecules. [109] Moreover, there are a number of general force fields that have been developed to treat all atoms in the periodic table, [110] biomolecules [111] and condensed matter. [112] Simulations employing these general force fields have shown to be applicable to many porous systems, in particular, universal force field (UFF) [110] parameters have been ubiquitous in calculating intermolecular energies ($U_{\text{van der Waals}}$) for gas adsorption simulations. [113]

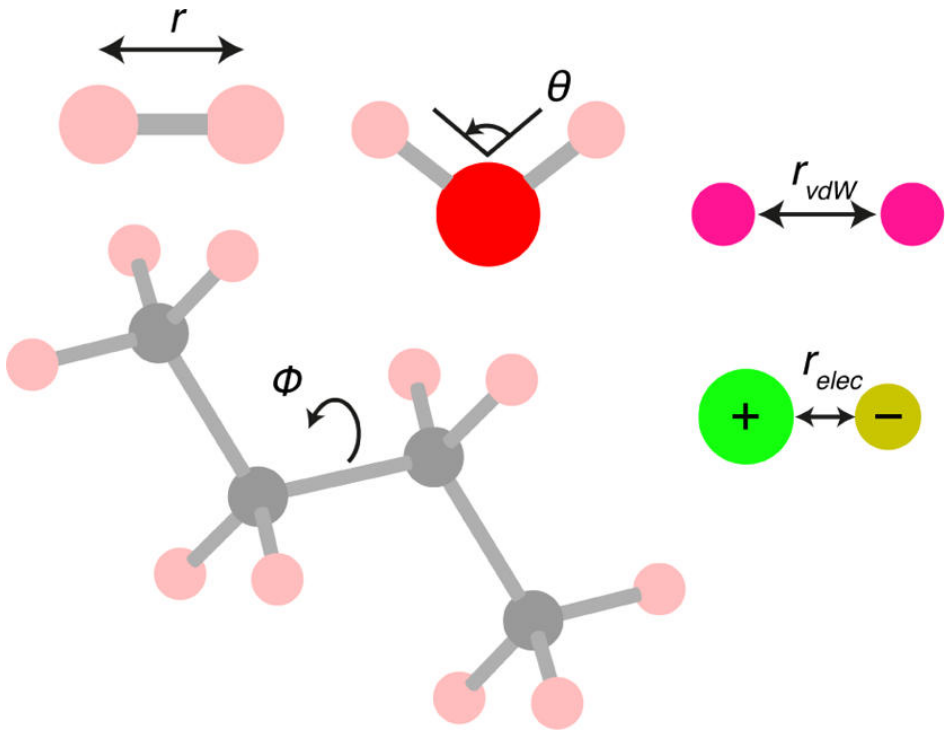

Figure 2.3: These are examples of the structural parameters explicitly described by force field models used in classical molecular simulations. This figure comes from [108].

Force fields for porous structures with a high degree of flexibility require good accuracy in the description of intramolecular interactions in the structure, in part due to the presence of low-frequency phonon modes, which is often not captured by generic force fields. To this end, researchers have used *ab initio* simulation to derive accurate system specific force fields. Van Speybroeck and coworkers have developed QuickFF for the easy derivation of new force fields from *ab initio* simulations [114] which has been used to describe a number of flexible MOFs and explore thermodynamics. [115] Alternatively Heine *et al.* have extended UFF for use in MOF systems by revising and adding parameters relating to common transition metal nodes. [116] In any case the choice of the force field applied in classical simulation must be initially tested against experimental or quantum chemistry methods to demonstrate the accuracy of the method.

Molecular dynamics is achieved by the same iterative process described previously for AIMD. However, owing to the cheaper computational costs of classical simulation, one can follow processes on a larger scale such as the dynamics of water molecules confined in zeolites. [117] In addition to the choice of the force field, as discussed previously, the options of time step and thermostat (or thermostat and barostat in the case of (N, P, T) simulations) are crucial. To optimize computational efficiency the time step should be chosen as large as possible in order to minimize the number of calculation steps for a given time period. However, the time step must be carefully checked, so that it does not result in drifts or large fluctuations in energy and other conserved quantities. [118] Notably, this is also true

for AIMD simulations.

Moreover, molecular dynamics explicitly represents the (N, V, E) ensemble; thus, to compare to experimental systems, dynamic constraints (thermostat and barostat), applied to the movement or particles or cell parameters, are added. These constraints are made so that the average over time of the temperature (and pressure for (N, P, T) simulations) converge to a given value. Many different approaches have been developed to implement these constraints, each having its advantages and disadvantages that must be considered before use. [119, 120] In particular, the Nosé–Hoover thermostat and barostat is routinely used. [121–123] When using this method there is choice in relaxation time which defines the timescale for the relaxation of temperature or pressure. Relaxation times of 1-5 ps are often chosen to ensure that the temperature and pressure do not fluctuate too much (more than expected in reality) and the equilibration time is not unnecessarily long.

2.2.2 Grand Canonical Monte Carlo calculations

Besides molecular dynamics simulations, another kind of simulations widely used are Monte Carlo simulations. It is particularly used to study the adsorption process as these simulations consist of trial displacement, insertion and removal of gas molecules in the framework structure. [124] The difference between molecular dynamics and Monte Carlo simulations in terms of exploration of the phase space is illustrated in Figure 2.4. The criterion for accepting a trial displacement is often described by the Metropolis algorithm. [125] In the Metropolis algorithm, for simulations in the canonical ensemble (constant volume, temperature and number of molecules) the below steps are followed until a move is accepted.

1. Calculate the potential energy (U_i) of the initial state.
2. Choose a trial displacement of a random molecule from a uniform random distribution.
3. Calculate the potential energy of the new state (U_f).
4. If $U_f \leq U_i$, accept the move.
5. If $U_f > U_i$, select a random number, w, where $w \in [0, 1]$ from a uniform distribution and if $\exp[-\beta(U_f - U_i)] > w$, accept the move.
6. Repeat steps 2-5.

For simulations in the grand-canonical ensemble (constant volume, temperature and chemical potential), the probability of acceptance also depends on the chemical potential. In these simulations the number of molecules adsorbed in the porous structure evolves over the course of the simulation, and after a period of equilibration it will fluctuate around an equilibrium value imitating the experimental system, in which the adsorbed phase is at equilibrium with

a gas reservoir. Conducting Monte Carlo simulations can be very straightforward, however there are a number of important options and analysis to consider before conducting a simulation including relative probability of different trial moves (rotation, displacement, reinsertion and more) and to ensure convergence in energy or the number of adsorbed particles. Dubbeldam *et al.* have produced an excellent resource for the applicaiton of Monte Carlo in this area. [124]

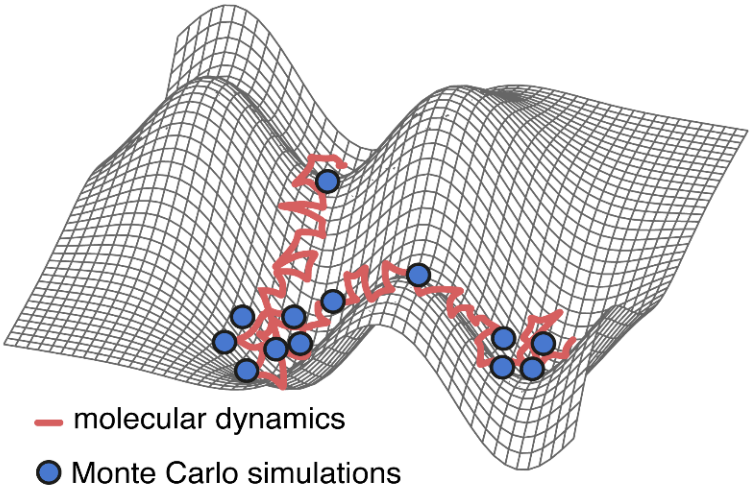

Figure 2.4: Representation of the way the potential energy surface is explored by molecular dynamics and Monte Carlo simulations.

GCMC simulations correspond to the (μ, V, T) where μ is the chemical potential of the adsorbate. This chemical potential is directly related to the partial pressure of the adsorbate. The number of trial steps necessary to reach convergence of the number of adsorbed molecules is usually very high, routinely about 1 million, as is the number of atoms to be simulated (framework and adsorbates). However, a way to reduce computational cost, assuming a rigid framework, is to precompute the value of the pair potentials on a grid. Then, the framework atoms are not explicitly simulated, the adsorbates molecules interact with the potential on the grid.

Monte Carlo simulations for adsorption are almost always carried out as classical simulations with analytical potentials, although a few studies tackle the issue of computational cost for *ab initio* simulations by describing the framework as a collection of lattice sites, but are still limited to smaller systems. [126] It is important to note though that *ab initio* Monte Carlo simulations have been carried out for years to study crystal structures and the stability of different phases. [127–129]

Part II

Anomalous mechanical properties in zeolites: the example of auxeticity

Although zeolites have been studied for more than 50 years by more and more researchers with always more advanced techniques, the question of the feasibility of zeolite remains a conundrum. Mathematically it is possible to create an infinite number of assemblies of tetrahedra linked by their corners forming periodic frameworks. [130] Even when considering the energetics of the system, as it has been done in numerous studies, the number of resulting frameworks is of the order of hundreds of thousands and up to few millions. [131–133] For that matter, energetic stabilities of zeolites has been studied both experimentally and theoretically for decades.

At the end of the 80's Derouane and Fripiat [134] reported on quantum calculations on small clusters with one or two T atoms to study the energetic landscape of zeolites. Then mechanical properties of molecular sieves in general, and zeolites in particular, have been studied at the macroscopic level in a chemical engineering context. [135, 136] The first theoretical study focusing specifically on the mechanical properties of zeolites was reported by Astala *et al.* in 2004. [137] They investigated the mechanical properties of 5 different pure silica zeolites via DFT calculations at the LDA level. Though this seminal study is very interesting, it was not able to extract any systematic structure-properties relations for zeolites as drawing correlations with 5 data points would have been unreliable. Sometimes in the literature the mechanical properties of zeolites are studied as a side property for a specific application. For instance, the study reported by Li *et al.* in 2006 [138] looks for low dielectric constant materials among pure silica zeolites in order to improve microprocessors. Besides dielectric properties, mechanical properties were investigated by experiments and force-field based simulations and compared with amorphous silica. In 2011, Coasne *et al.* showed a modification of mechanical properties via guest adsorption [139], which is of great importance owing to the adsorption-related applications of zeolites. Bryukhanov *et al.* published, in 2015 and 2017, two theoretical papers on the chemical reduction of mechanical properties by carbonate formation during dealumination [140] and on the influence of water presence on the elastic properties of zeolites. [141]

In 2013, F-X. Coudert published the first systematic study of the elastic properties of known zeolites at the quantum chemistry level. [142] Besides confirming known correlations, for example between the framework energy relative to α-quartz per Si atom (ΔE) and the specific volume, he suggested a feasibility criterion for zeolites based on their elastic anisotropy (see Figure 1) as defined in Equation 1:

$$\eta = max\left(\frac{E_{max}}{E_{min}}, \frac{G_{max}}{G_{min}}\right), \tag{1}$$

where $E_{min/max}$ are the minimum/maximum Young's moduli and $G_{min/max}$ are the minimum/maximum shear moduli. The criterion proposed is that feasible structures probably correspond to $\Delta E < 20\,\mathrm{kJ/mol}$ and $\eta < 4$ as almost all already synthesized structures respect it. Interestingly, this study is one of the first to mention an anomalous mechanical property in zeolites: negative linear compressibility, which is the fact that a material linearly expands in a specific direction while being submitted to an isotropic hydrostatic pressure. [143]

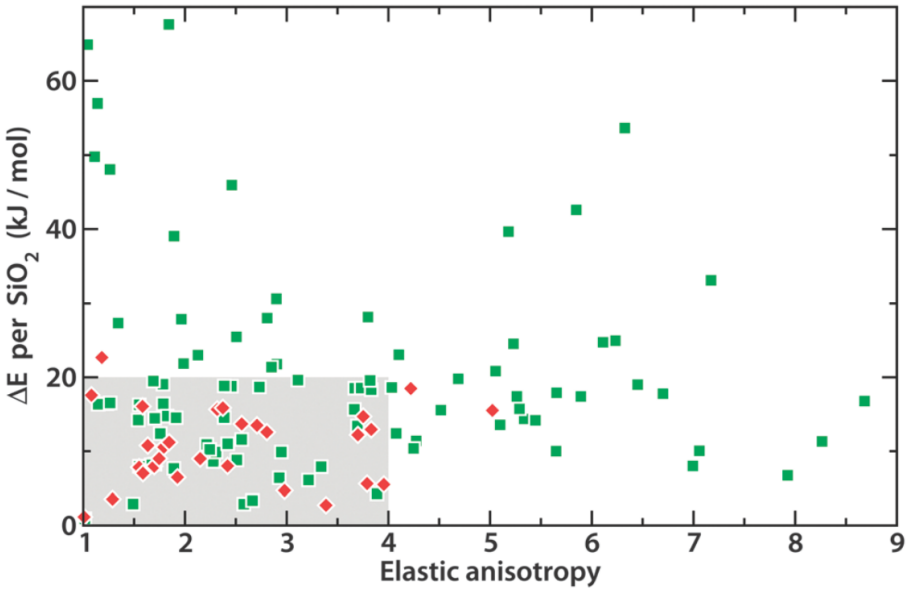

Figure 1: Plot of the elastic anisotropy of pure silica zeolites vs. lattice energy relative to α-quartz; red points correspond to synthesized pure silica zeolites. The gray area corresponds to the feasibility criterion proposed in [142]. Figure extracted from [142].

Another study, published in 2015 by Siddorn *et al.*, focuses on another anomalous mechanical property in all silica zeolites: auxeticity. [144] Auxeticity is the phenomenon, happening mainly in isotropic foams, corresponding to a linear expansion in one direction while a transverse direction is being submitted to a linear elongation. This phenomenon is characterized by the Poisson's ratio being negative. In subsection 1.2.5, I give more details on how this complex elastic constants is calculated and the typology proposed by the authors to classify auxetic materials.

In order to investigate the links between strutural properties and anomalous mechanical properties in zeolites, I used a database of hypothetical zeolitic structures generated and reported by Pophale *et al.*. [145] This database contains 590811 structures along with their mechanical properties computed at the force-field level. I detail its building principles and the analyses I made on it in chapter 2. I carried out density functional theory calculations on a specific set extracted from this database to unravel the mechanism behind complete auxeticity in all silica zeolites. I present all the results of this study in chapter 3. Before going through the details of the database and my study on complete auxeticity, I present hereafter the principles of mechanics in the elastic regime of materials.

Chapter 1

Elastic tensor and mechanical properties

1.1 Elasticity theory and averaging schemes

1.1.1 Mechanics of materials: the elastic regime

The principle of mechanics of materials is to study the behaviour of materials submitted to an external mechanical constraint. This mechanical constraint is called the stress (σ). The material usually reacts by changing its shape and size. These deformations, called strains (ε), are rank 2 tensors represented by a 3×3 symmetric matrix (Equation 1.1), as for the stress (Equation 1.2).

$$\varepsilon = \begin{pmatrix} \varepsilon_{xx} & \varepsilon_{xy} & \varepsilon_{xz} \\ \varepsilon_{yx} & \varepsilon_{yy} & \varepsilon_{yz} \\ \varepsilon_{zx} & \varepsilon_{zy} & \varepsilon_{zz} \end{pmatrix} \tag{1.1}$$

$$\sigma = \begin{pmatrix} \sigma_{xx} & \sigma_{xy} & \sigma_{xz} \\ \sigma_{yx} & \sigma_{yy} & \sigma_{yz} \\ \sigma_{zx} & \sigma_{zy} & \sigma_{zz} \end{pmatrix} \tag{1.2}$$

The relation between volumetric stress and strain can be schematically summed up by Figure 1.1: for small deformations, the response is called “elastic”, meaning it is reversible (and usually linear), then at higher strain the response is said to be “plastic”, meaning it is nonlinear and irreversible, before it reaches the fracture point.

Depending on the type of material, the elastic region might extend only to fraction of a percent (e.g. for steel) or up to 700% for some elastomers. In the following, we will only

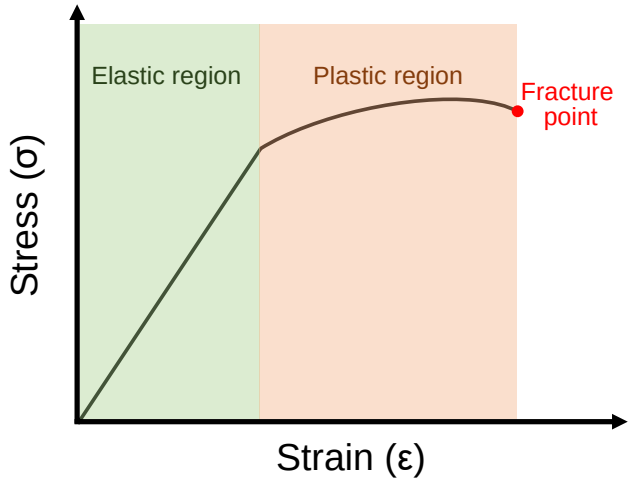

Figure 1.1: Schematic representation of the stress-strain relation in materials. It begins by a linear elastic region, then the material deforms irreversibly (plastic region) before eventually breaking apart.

focus on the linear elastic part of mechanical properties in materials, also called second-order elasticity (because the energy is quadratic as I will show).

1.1.2 Elasticity theory

In the linear elastic region, meaning in the limit of small deformations, the stress and strain second-rank tensors are linked through a generalized Hooke's law by a fourth-rank tensor called the stiffness tensor C as shown in Equation 1.3, and its inverse the compliance tensor S (Equation 1.4). The stiffness tensor is also named "second-order elastic tensor" and its components "elastic constants".

$$\sigma_{ij} = \sum_{kl} C_{ijkl}\varepsilon_{kl} \tag{1.3}$$

$$\varepsilon_{ij} = \sum_{kl} S_{ijkl}\sigma_{kl} \tag{1.4}$$

This is an anisotropic, 3D generalization of the well-known Hooke's law for a spring: $F = k \cdot L$.

As the indices range from 1 to 3 (the 3 directions of space), there are $3^4 = 81$ different C_{ijkl}. However, ε and σ being symmetric this number gets reduced to 36 components only (as $C_{ijkl} = C_{jikl} = C_{ijlk} = C_{jilk}$). This reduction to 36 components allows us to rewrite the stiffness tensor as a 6×6 matrix with C_{ij} components in Voigt notation. This notation

associates a couple of indices (n, m) to a single index p ($p \in [\![1:6]\!]$) as follows: $(1,1) \to 1$, $(2,2) \to 2$, $(3,3) \to 3$, $(2,3) \to 4$, $(1,3) \to 5$, $(1,2) \to 6$ (summed up in Figure 1.2).

$$\boldsymbol{\sigma} = \begin{bmatrix} \sigma_{xx} & \sigma_{xy} & \sigma_{xz} \\ & \sigma_{yy} & \sigma_{yz} \\ & & \sigma_{zz} \end{bmatrix}$$

Figure 1.2: In blue the indices in Voigt notation are given to replace the tensor indices. Figure by Nicoguaro (available at `https://commons.wikimedia.org/wiki/File:Voigt_notation_Mnemonic_rule.svg`).

With this notation, the stress and strain can be described by vectors of length 6. Furthemore, the mechanical energy density in differential form reads as:

$$dW = \sum_{ij} C_{ij} \varepsilon_i d\varepsilon_j, \tag{1.5}$$

hence,

$$\frac{\partial^2 W}{\partial \varepsilon_i \partial \varepsilon_j} = C_{ij} \tag{1.6}$$

$$\frac{\partial^2 W}{\partial \varepsilon_j \partial \varepsilon_i} = C_{ji}, \tag{1.7}$$

yielding $C_{ij} = Cji$. Thus, there are only 21 independent components for the second-order elastic tensor of a fully anisotropic material.

Thanks to the symmetry of crystalline materials, like zeolites, the number of independent components can even be lower, as demonstrated in [14]. For example, monoclinic crystals have 13 independent elastic constants, orthorhombic systems have 9 (Equation 1.8):

$$C_{\text{orthorhombic}} = \begin{pmatrix} C_{11} & C_{12} & C_{13} & & & \\ C_{12} & C_{22} & C_{23} & & & \\ C_{13} & C_{23} & C_{11} & & & \\ & & & C_{44} & & \\ & & & & C_{55} & \\ & & & & & C_{66} \end{pmatrix}, \tag{1.8}$$

hexagonal systems have 5 (Equation 1.9):

$$C_{\text{hexa}} = \begin{pmatrix} C_{11} & C_{12} & C_{13} & & & \\ C_{13} & C_{11} & C_{13} & & & \\ C_{13} & C_{13} & C_{33} & & & \\ & & & C_{44} & & \\ & & & & C_{44} & \\ & & & & & C_{66} \end{pmatrix} \quad \text{with} \quad C_{66} = \frac{C_{11} - C_{12}}{2} \quad , \tag{1.9}$$

and cubic systems only 3 (Equation 1.10) (coefficients equal to zero are omitted in matrices for clarity):

$$C_{\text{cubic}} = \begin{pmatrix} C_{11} & C_{12} & C_{12} & & & \\ C_{12} & C_{11} & C_{12} & & & \\ C_{12} & C_{12} & C_{11} & & & \\ & & & C_{44} & & \\ & & & & C_{44} & \\ & & & & & C_{44} \end{pmatrix} \tag{1.10}$$

1.2 Mechanical properties

1.2.1 Mechanical stability and directionality

For a crystalline system to be mechanically stable, the matrix C has to be positive-definite (i.e. all its eigenvalues must be strictly positive). This translates into a series of more or less simple inequalities involving the C_{ij} coefficients depending on the symmetry of the system named "Born stability criteria". [14] For instance, in the cubic case, the stability conditions read as follows:

$$C_{11} - C_{12} > 0, \quad C_{11} + 2C_{12} > 0, \quad C_{44} > 0 \tag{1.11}$$

and in the hexagonal case:

$$C_{11} > |C_{12}|, \quad 2C_{13}^2 < C_{33}(C_{11} + C_{12}), \quad C_{44} > 0 \text{ and } C_{66} > 0 \tag{1.12}$$

As we study anisotropic materials, we want to be able to represent their mechanical properties on a three-dimensional surface. A direction can be characterized by a unit vector $\mathbf{u}$. The shear modulus and the Poisson's ratio actually require a second, perpendicular, direction, which can be characterized by another unit vector $\mathbf{v}$. These vectors have the following coordinates:

$$\mathbf{u} = \begin{pmatrix} \sin(\theta)\cos(\varphi) \\ \sin(\theta)\sin(\varphi) \\ \cos(\theta) \end{pmatrix} \tag{1.13}$$

$$\mathbf{v} = \begin{pmatrix} \cos(\theta)\cos(\varphi)\cos(\chi) - \sin(\varphi)\sin(\chi) \\ \cos(\theta)\sin(\varphi)\cos(\chi) - \cos(\varphi)\sin(\chi) \\ -\sin(\theta)\cos(\chi) \end{pmatrix}, \tag{1.14}$$

where θ is in $(0, \pi)$ while φ and χ are in $(0, 2\pi)$. Thanks to tensor rotation formula [146], we can transform the stiffness or the compliance tensor to compute directional mechanical properties.

1.2.2 The bulk modulus and linear compressibility

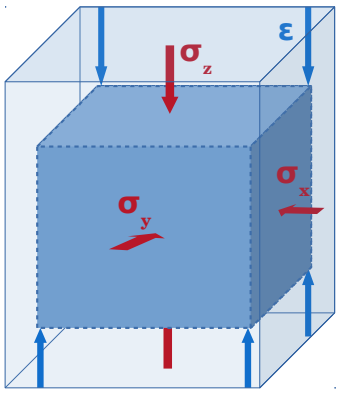

Figure 1.3: Representation of the stress-strain relation quantified by the linear compressibility. The stress is isotropic while the strain is characterized in one direction.

The bulk modulus K is the simplest mechanical property of a material, as it is volumetric and depends neither on the direction of the stress nor on the direction of the created strain. In fact, it quantifies the decrease in volume as a hydrostatic pressure is exerted on the material.

In order to treat properly materials composed of assemblies of randomly oriented crystalline grains, three main averaging schemes have been proposed: Voigt, [147] Reuss [148] and Hill. [149] The Voigt averaging scheme is based on the assumption of uniform strain while the Reuss averaging scheme assumes uniform stress. The Hill averaging scheme is the arithmetic average of the values computed with Voigt and Reuss schemes. With the Voigt average, the value of the bulk modulus from the C_{ij} is:

$$K_{\text{Voigt}} = \frac{C_{11} + C_{22} + C_{33}}{9} + 2 \times \frac{C_{23} + C_{13} + C_{12}}{9}. \tag{1.15}$$

With the Reuss average, its value from the S_{ij} is:

$$K_{\text{Reuss}} = \frac{1}{S_{11} + S_{22} + S_{33} + 2 \times (S_{23} + S_{13} + S_{12})}. \tag{1.16}$$

For zeolites, the bulk modulus is typically between 15 and 100 GPa.

The second most simple mechanical property is the linear compressibility β. It characterizes the linear strain associated with a hydrostatic pressure imposed on the material as illustrated in Figure 1.3, i.e. the individual response of each axis when a pressure σ is applied on all sides.

It can be computed from the compliance tensor:

$$\beta(\theta, \varphi) = \sum_{ijk} S_{ijkk} \mathbf{u}_i \mathbf{u}_j \tag{1.17}$$

The average over space of the linear compressibility is simply the compressibility, i.e. the inverse of the bulk modulus. For zeolites, the minimum linear compressibility is typically between -20 and 20 TPa^{-1} and the maximum linear compressiblity between 0 and 50 TPa^{-1}. Negative linear compressibility is called an anomalous mechanical property as it is quite unusual, though it has been quite reported in zeolites and MOFs recently. [150–152]

1.2.3 The Young's modulus

The Young's modulus E quantifies the longitudinal strain resulting from a longitudinal stress in the same direction as represented in Figure 1.4. It fundamentally is the slope of the linear part in the stress/strain diagram (Figure 1.1) of any given crystal axis.

For both, the Voigt average and the Reuss average it can be computed by:

$$E_{\text{Voigt/Reuss}} = \left(\frac{1}{3G_{\text{Voigt/Reuss}}} + \frac{1}{9K_{\text{Voigt/Reuss}}} \right), \tag{1.18}$$

where K is the bulk modulus and G is the shear modulus. For zeolites, it typically ranges from 20 to 100 GPa.

The direction-dependent value of the Young's modulus is computed from the S_{ij} as follows:

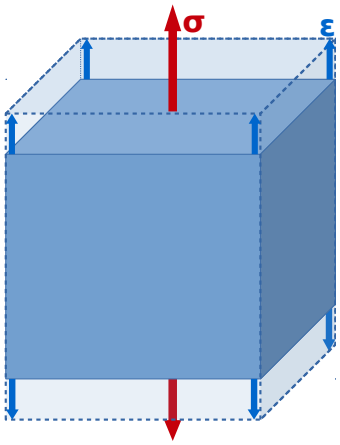

Figure 1.4: Representation of the stress-strain relation quantified by the Young's modulus.

$$E(\theta, \varphi) = \frac{1}{\sum_{ijkl} \mathbf{u}_i \mathbf{u}_j \mathbf{u}_k \mathbf{u}_l S_{ijkl}} \tag{1.19}$$

It is important to note that E is always positive, otherwise the stability criteria would not be met.

1.2.4 The shear modulus

The shear modulus G is the measure of the resistance of a material to a shearing stress (as imposed in ball-milling experiments for example [51]) as illustrated in Figure 1.5.

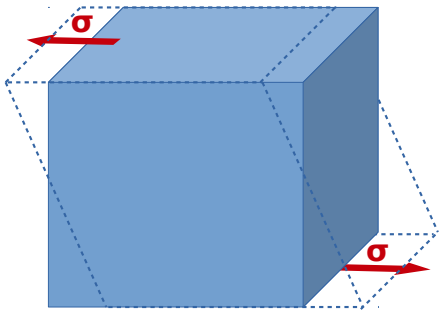

Figure 1.5: Representation of the stress-strain relation quantified by the shear modulus.

With the Voigt average, its value from the C_{ij} is:

$$G_{\text{Voigt}} = \frac{1}{5}\left(C_{44} + C_{55} + C_{66} + \frac{C_{11} + C_{22} + C_{33} - C_{23} - C_{13} - C_{12}}{3}\right). \tag{1.20}$$

With the Reuss average, its value from the S_{ij} is:

$$G_{\text{Reuss}} = \left[S_{44} + S_{55} + S_{66} + 4\left(\frac{S_{11} + S_{22} + S_{33} - S_{23} - S_{13} - S_{12}}{3}\right)\right]^{-1}. \tag{1.21}$$

For zeolites, the shear modulus is typically between 5 and 50 GPa.

The direction-dependent value of the Young's modulus is computed from the S_{ij} as follows:

$$G(\theta, \varphi, \chi) = \frac{1}{\sum_{ijkl} \mathbf{u}_i \mathbf{v}_j \mathbf{u}_k \mathbf{v}_l S_{ijkl}} \tag{1.22}$$

Contrary to the linear compressibility and the Young's modulus, which depend on 1 orientation, the shear modulus is a function of 2 perpendicular unit vectors and thus cannot be represented by a 3-dimensional surface. In practice, we usually represent the following quantities:

$$G_{\min}(\theta, \varphi) = \min_{\chi} G(\theta, \varphi, \chi) \quad \text{and} \quad G_{\max}(\theta, \varphi) = \max_{\chi} G(\theta, \varphi, \chi)\ , \tag{1.23}$$

i.e. the minimal and maximal response for a given direction of stress.

1.2.5 The Poisson's ratio: anepirretic and auxetic behaviours

The Poisson's ratio ν characterizes the strain resulting from a longitudinal stress in a transverse direction as illustrated in Figure 1.6. For this reason, it depends on two directions.

For both, the Voigt average and the Reuss average it can be computed from:

$$\nu_{\text{Voigt/Reuss}} = \frac{1}{2}\left(1 - \frac{3G_{\text{Voigt/Reuss}}}{3K_{\text{Voigt/Reuss}} + G_{\text{Voigt/Reuss}}}\right), \tag{1.24}$$

where K is the bulk modulus and G is the shear modulus. For zeolites, it typically ranges from -0.2 to 0.5.

The direction-dependent value of the Poisson's ratio is computed from the S_{ij} as follows:

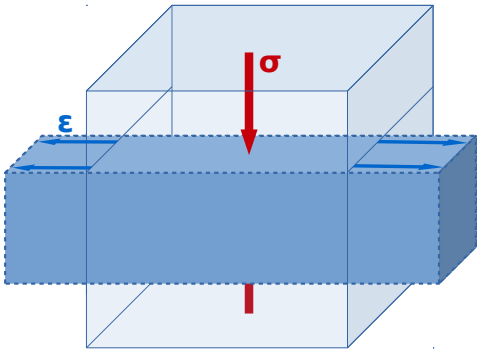

Figure 1.6: Representation of the stress-strain relation quantified by the Poisson's ratio. Here the scheme shows a material with a positive Poisson's ratio.

$$\nu(\theta,\varphi,\chi) = -\frac{\sum_{ijkl} \mathbf{u}_i\mathbf{u}_j\mathbf{v}_k\mathbf{v}_l S_{ijkl}}{\sum_{ijkl} \mathbf{u}_i\mathbf{u}_j\mathbf{u}_k\mathbf{u}_l S_{ijkl}} \tag{1.25}$$

As for the shear modulus, the dependence on two perpendicular directions force us to represent partially averaged quantities. In practice, we represent the following quantities:

$$\nu_{\min}(\theta,\varphi) = \min_{\chi} \nu(\theta,\varphi,\chi) \quad \text{and} \quad \nu_{\max}(\theta,\varphi) = \max_{\chi} \nu(\theta,\varphi,\chi) \tag{1.26}$$

ν can be negative, like β, without it implying that the material is unstable. In the case of negative values, $|\nu|$ is represented with a differently coloured surface.

ν is very often positive in average. Materials having a near-zero homogeneous Poisson's ratio are called "anepirretic" materials. [153] Some materials exhibit negative Poisson's ratio, making them "auxetic" materials. In [144], the authors propose a classification for auxetic materials, taking into account the 2-dimensional dependence, described in Table 1.1.

A material can belong to several classes of auxeticity, for instance it can fall into the categories 2B and 3A at the same time. The materials classified as 3C are called "completely auxetic" materials.

1.2.6 Practical calculations of C_{ij}

In practice, the calculation of the second order elastic tensor can be done with different methods. First, the energy and the forces can be calculated either at the quantum level or by classical force-field based methods. The first approach, developed by Nielsen and Martin [154, 155] in 1983 consists in solving the general system of six linear equations (six

Code	Poisson's ratio is negative
0	Never
1A	$\exists\ (\theta,\varphi,\chi),\ \nu(\theta,\varphi,\chi) < 0$
1B	$\exists(\theta,\varphi), \langle\nu(\theta,\varphi,\chi)\rangle_\chi < 0$
1C	$\exists(\theta,\varphi), \max_\chi \nu(\theta,\varphi,\chi) < 0$
2A	$\exists\ \chi,\ \langle\nu(\theta,\varphi,\chi)\rangle_{\theta,\varphi} < 0$
2B	$\langle\langle\nu(\theta,\varphi,\chi)\rangle_{\theta,\varphi}\rangle_\chi < 0$
2C	$\max_\chi\langle\nu(\theta,\varphi,\chi)\rangle_{\theta,\varphi} < 0$
3A	$\exists\ \chi,\ \max_{\theta,\varphi} \nu(\theta,\varphi,\chi) < 0$
3B	$\max_{\theta,\varphi}\langle\nu(\theta,\varphi,\chi)\rangle_\chi < 0$
3C	$\max_{\theta,\varphi,\chi} \nu(\theta,\varphi,\chi) < 0$

Table 1.1: Auxetic materials are classified in 3 groups (1, 2, 3) with 3 subgroups (A, B, C): 1 means auxeticity happens at least around one axis of loading, 2 means ν is negative when averaged over axes of loading and 3 means auxeticity happens independently from the axis of loading considered; A means auxeticity happens in at least one direction of strain, B means it is the case in average over the directions of strain and C means all directions of strain are affected.

components of the stress) with 21 variables (the elastic constants). This set of equations is built from the stress tensor computed for each deformation. In our approach, we use the second order Taylor development of the energy to write:

$$C_{ij} = \frac{1}{V}\left(\frac{\partial^2 E}{\partial\varepsilon_i\partial\varepsilon_j}\right) \tag{1.27}$$

The first step is to optimize the geometry (atomic positions and lattice parameters) of the system to relax to a reference geometry with $\varepsilon = 0$. Then the symmetry of the system is analyzed to determine how many independent deformation modes exist in the material. For each deformation mode, $2n$ deformed structures are generated with deformation amplitudes of $\varepsilon_k = k\delta\varepsilon_i$, with $-n \leq k \leq n$. The energy is then minimized for each deformed structure. The first derivatives $\left(\frac{\partial E}{\partial\varepsilon_j}\right)$ are analytically calculated at each point. Finally, knowing the $\left(\frac{\partial E}{\partial\varepsilon_j}\right)_{\varepsilon_k=k\delta\varepsilon_i}$ allows us to compute the second order derivatives by finite differences. Each deformation mode corresponds to one line of the second order elastic tensor, thus the symmetry of the obtained matrix allows us to validate (or not) this mixed analytical-numerical approach.

Our approach corresponds to the determination of the mechanical properties at 0 K, i.e. not taking into account the influence of thermal fluctuations. It is also possible to have access to the mechanical properties at a given temperature T by doing molecular dynamics

simulations. From these simulations the fluctuations of the ε_i lead to the C_ij through the following formula (with complete tensor notations):

$$\left(\frac{k_B T}{V}\right) C^{-1}_{ijkl} = \langle \varepsilon_{ij} \varepsilon_{kl} \rangle - \langle \varepsilon_{ij} \rangle \langle \varepsilon_{kl} \rangle \tag{1.28}$$

This method is called the strain-fluctuation method [156,157] and has for example been used in the investigation on the pressure-induced amorphization of ZIF-8. [158]

1.2.7 ELATE: an analysis and visualization tool

Many quantum chemistry software packages allow to compute second-order elastic tensors. Though the relations between this tensor and the different elastic moduli are straightforward, they are tedious to calculate. That is the reason why I (inspired by Arnaud Marmier's ElAM software [146]) developed ELATE, [159] which is both an open source Python module (available at `https://github.com/fxcoudert/elate`) for the manipulation of elastic tensors and a standalone online application (available at `http://progs.coudert.name/elate`) for the routine analysis of elastic tensors based on the module. In addition to being a user-friendly interface to the analysis code with no local installation required, the online application also provides a simple Application Programming Interface (API) to be called from other web-based tools. It can also import elastic data directly from the Materials Project database of elastic constants by interfacing with the Materials API (MAPI). This large database of materials contains more than 7000 elastic tensors computed at the DFT level.

The principle for using the online application is rather simple: given an elastic tensor (Figure 1.7) it returns a web page with a number of information (Figure 1.8):

- the average mechanical properties according to the 3 averaging schemes
- the eigenvalues of the elastic tensor (which have to be strictly positive for mechanical stability)
- if the material is mechanically stable:
  - Minima and maxima of the elastic moduli and associated axes (and directions for shear modulus and Poisson's ratio)
  - 2D projections of the spatial variations of the four elastic moduli
- 3D interactive graphs inside the user's browser

Finally, if needed, one can obtain 3-dimensional representations of the elastic moduli. Figure 1.9 shows the example of the Poisson's ratio of α-quartz and Figure 1.10 shows the

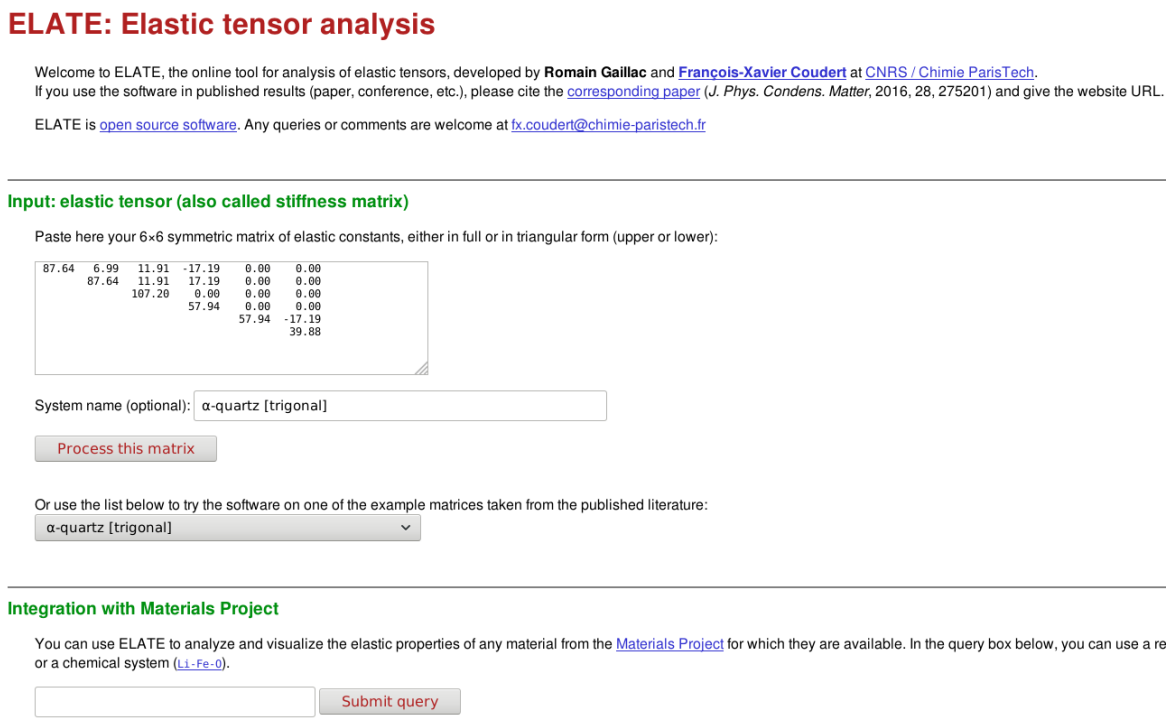

Figure 1.7: Home page of ELATE.

example of $Ag_3Co(CN)_6$. You can test it online with example data provided for 6 materials representing 6 of the 7 crystal systems: faujasite (cubic), α-quartz (trigonal), MIL-53(Al) (orthorhombic), ZnO (hexagonal), TiO_2 rutile (tetragonal), NSI zeolite (monoclinic). It seems to be quite useful to the community as it has already been used in 23 published papers since May 2016.

Average properties

Averaging scheme	Bulk modulus	Young's modulus	Shear modulus	Poisson's ratio
Voigt	K_V = 38.233 GPa	E_V = 101.41 GPa	G_V = 47.93 GPa	ν_V = 0.057923
Reuss	K_R = 37.724 GPa	E_R = 91.389 GPa	G_R = 41.683 GPa	ν_R = 0.096239
Hill	K_H = 37.979 GPa	E_H = 96.478 GPa	G_H = 44.806 GPa	ν_H = 0.076612

Eigenvalues of the stiffness matrix

λ_1	λ_2	λ_3	λ_4	λ_5	λ_6
29.493 GPa	42.464 GPa	68.327 GPa	82.937 GPa	96.126 GPa	118.89 GPa

Variations of the elastic moduli

	Young's modulus		Linear compressibility		Shear modulus		Poisson's ratio		
	E_{min}	E_{max}	β_{min}	β_{max}	G_{min}	G_{max}	ν_{min}	ν_{max}	
Value	70.591 GPa	129.53 GPa	7.1811 TPa^{-1}	9.6637 TPa^{-1}	29.493 GPa	68.417 GPa	-0.087201	0.31179	Value
Anisotropy	1.835		1.3457		2.32		∞		Anisotropy
Axis	0.8141 0.4768 0.3316	0.0000 0.7515 0.6598	0.0000 0.0000 1.0000	-0.9239 0.3827 0.0000	-1.0000 0.0000 -0.0000	0.4503 0.2610 0.8539	-0.0000 0.6823 0.7311	-0.5011 0.2905 0.8151	Axis
					-0.0000 -0.8559 -0.5172	-0.5014 0.8652 -0.0001	-1.0000 0.0000 -0.0000	-0.5047 -0.8633 -0.0026	Second axis

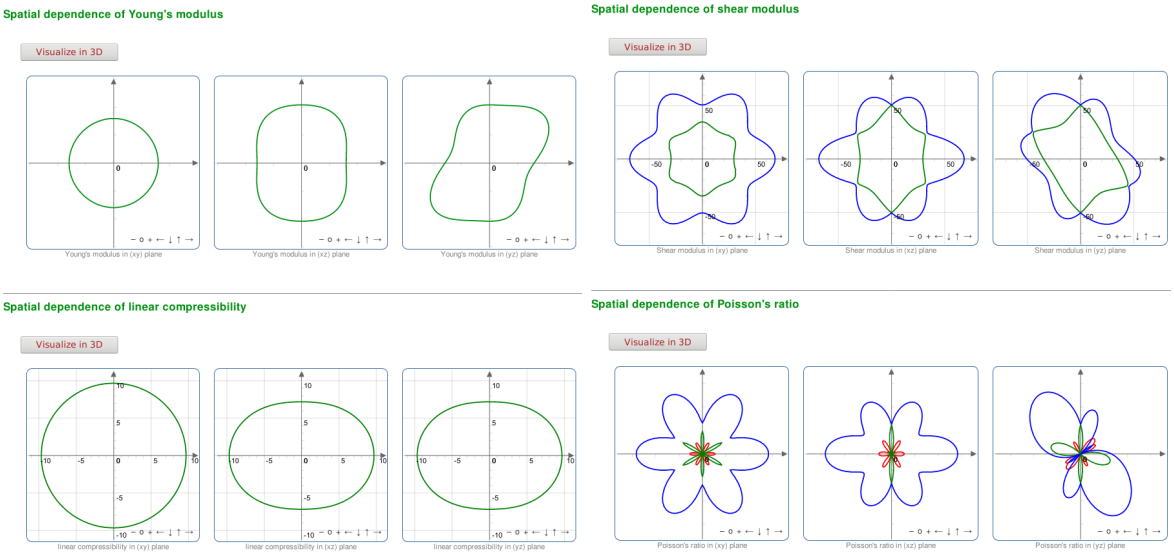

Figure 1.8: Example of the result page of ELATE for α-quartz.

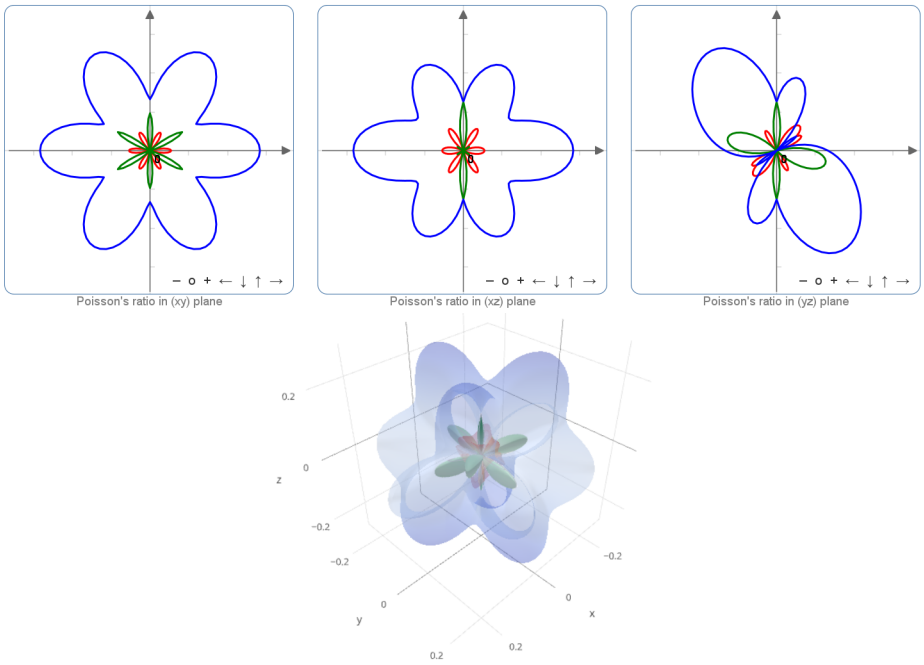

Figure 1.9: Spatial dependence of the Poisson's ratio of α-quartz (trigonal crystal system). The red and green surfaces correspond to the negative and positive part of $\min_\chi(\nu)$ respectively. The blue surface corresponds to $\max_\chi(\nu)$.

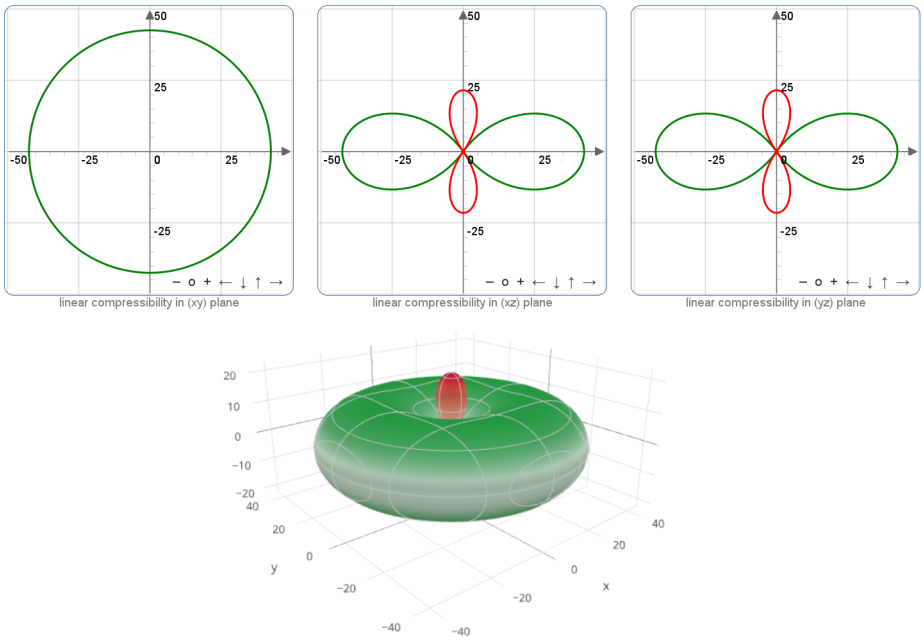

Figure 1.10: Spatial dependence of the linear compressibility of $Ag_3Co(CN)_6$, a material in the trigonal crystal system which exhibits very large negative linear compressibility (indicated by the red lobe).

Chapter 2

Mechanical properties of a classical database of zeolites

2.1 Building principles and first analyses

2.1.1 A force-field based database

In 2011, Pophale *et al.* published a paper describing two databases of zeolite-like materials. The two databases were created according to the same principles, but with different force-fields: the Sanders-Leslie-Catlow (SLC) potential [160] and the Beest–Kramer–van Santen (BKS) potential for silica based materials. [161] In the following, I will focus only on the database based on BKS, as it is the one I studied during my PhD.

The generation of the database involved several steps. Unit cells containing up to 8 independent Si atoms were generated by a Monte Carlo procedure specifically designed for zeolites. For each number of Si atoms, unit cell and symmetry space group, 100 simulated annealing runs were performed. The uniqueness of the obtained structures was guaranteed through a calculation of the coordination sequence to the 12th neighbor shell. Oxygen atoms were inserted into the structures, which were optimized again by use of the GULP molecular simulation software. [162] Constant pressure energy minimizations were carried out, or constant volume simulations when the previous one failed. Then, the mechanical properties were computed using the BKS potential for the 590811 different structures, yielding converged second-order elastic tensors for 590465 structures. These were published online as part of the database but have not been analyzed previously.

2.1.2 Main properties

Possessing the elastic tensors of all structures in the database, I first carried out a rapid analysis of the database with ELATE, focusing on the prevalence of mechanical stability and anomalous mechanical properties. The results are the following:

- 128563 mechanically unstable structures ($\simeq$ 22% of the database): they correspond to local minima that are very shallow and become unstable when perturbed by small strain ($\simeq$ 1%).
- 148974 structures exhibit negative linear compressibility, accounting for 32% of the mechanically stable structures.
- 368508 structures belong to the 1A class of auxeticity (Table 1.1) with $\nu_{\text{min}} < 0$ ($\simeq$ 80% of the mechanically stable structures), i.e. at least one direction exhibiting auxeticity around at least one axis of loading.
- 30342 structures belong to the 2B class of auxeticity (Table 1.1) with a negative Poisson's ratio in average ($\simeq$ 6.6% of the mechanically stable structures).
- 578 structures are completely auxetic (class 3C, Table 1.1) ($\simeq$ 0.1% of the mechanically stable structures).

The proportion of structures exhibiting negative linear compressibility or auxeticity seem to be quite large according to the force-field based data. A way to see how close the database is from the known space of zeolites is to compare with known zeolites included in the database. 134 known zeolitic structures are contained in the database, for which I performed the same analysis, which yields the following results:

- 14 mechanically unstable structures ($\simeq$ 10% of the known structures).
- 24 structures exhibit NLC, accounting for 20% of the mechanically stable known structures.
- 78 structures belong to the 1A class of auxeticity ($\simeq$ 65% of the mechanically stable known structures).
- 13 structures belong to the 2B class of auxeticity ($\simeq$ 11% of the mechanically stable known structures).
- 1 structure is completely auxetic (class 3C) ($\simeq$ 0.8% of the mechanically stable known structures).

For reference, the data computed at DFT level by Coudert [142] on 121 known structures yield the following results:

- 1 mechanically unstable structures.
- 16 structures exhibit NLC, accounting for 13% of the mechanically stable structures.
- 31 structures belong to the 1A class of auxeticity ($\simeq$ 26% of the mechanically stable structures).
- 1 structure belongs to the 2B and the 3C classes of auxeticity, the JST structure ($\simeq 0.8\%$ of the mechanically stable structures).

Statistically speaking, the force-field seems to overestimate the number of structures exhibiting anomalous properties. However, for simpler mechanical properties, like bulk and shear modulus, the force-field performs much better (Figure 2.1 from [163]). As depicted in Figure 2.1 the correlation between BKS and DFT values is correct for these two properties on known structures, even though the quantitative analysis leads to root mean square errors of 23 GPa and 36 GPa for bulk and shear moduli respectively.

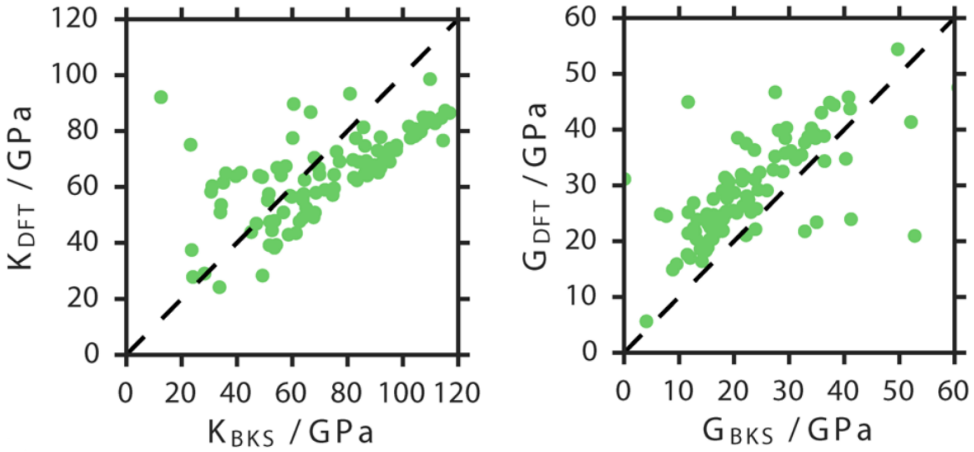

Figure 2.1: Left: Bulk modulus obtained by DFT compared to values obtained by using the BKS force-field. Right: Shear modulus obtained by DFT compared to values obtained by using the BKS force-field. Figure reproduced from [163].

In the next section, I look at the known structures included in the database to see how dispersed they are according to the different mechanical and structural properties examined.

2.2 Distributions of properties: comparison with known zeolites

Hereafter, I show to which extent the structures in the database are statistically similar to the known zeolitic structures, which represent only a small fraction (about 0.02%) of the database. Overall, I see that the hypothetical structures have similar properties, except for obvious outliers (less than 1% of the database), excluded by looking at reasonable ranges

for the different properties (as pointed out in [163], bulk moduli vary between -27,000 and 20,500 GPa, which are obviously inaccessible values for zeolites). Essentially, it seems very difficult to find a specific mechanical or structural property for which the known zeolitic structures differentiate themselves from the rest of the database.

2.2.1 Mechanical properties

Bulk modulus and Linear compressibility

As depicted in Figure 2.2, the bulk modulus for known zeolitic structures included in the database has an average value of 54 GPa, a median value of 50 GPa with a standard deviation of 33 GPa. These values for the whole database are 46, 44 and 18 GPa respectively. Thus, the "real" structures seem to be, in average, marginally stiffer than other hypothetical structures. Of course, even if I restrict the analysis to a range from 0 to 200 GPa (which accounts for more than 99.7% of the database), the hypothetical structures with very low bulk modulus (less than 1 GPa, down to almost 0 GPa for some cases), much likely unstable, contribute to this difference. Indeed, for known structures, the minimum bulk modulus according to BKS-based calculations is attained for the BOF structure at 9 GPa. Having this threshold of stability in mind, the hypothetical structures seem quite similar in terms of global stiffness to the already known structures.

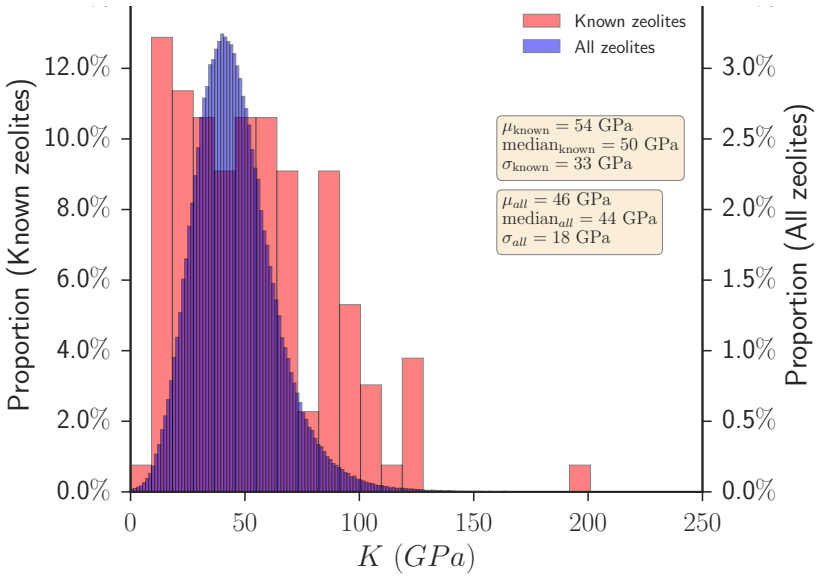

Figure 2.2: Bulk modulus distributions. In blue, the distribution of bulk moduli for the whole database is shown (right vertical scale) and in red, only the 134 known structures included in it are kept (left vertical scale). μ and σ are the mean and the standard deviation respectively.

I also compared, for stable structures for which it can be computed, the minimum and

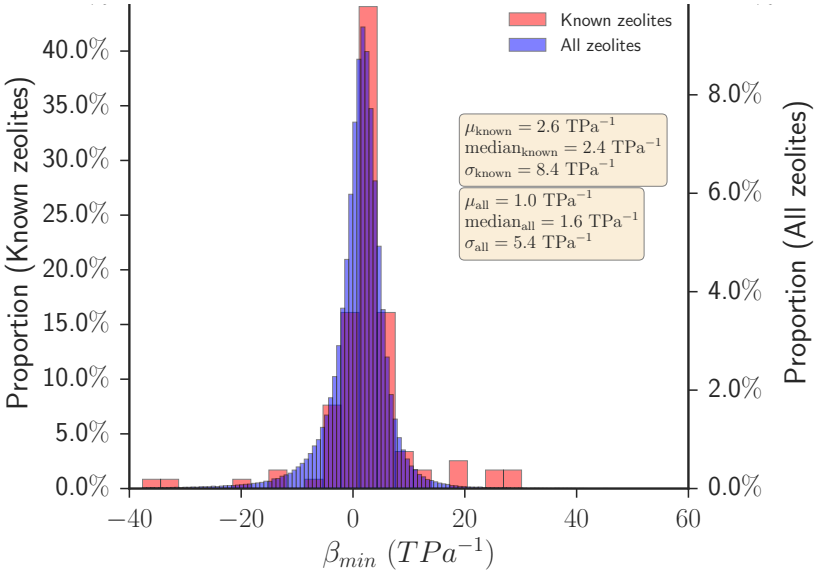

Figure 2.3: Minimum linear compressibility distributions. In blue, the distribution for the whole database is shown (right vertical scale) and in red, only the 134 known structures included in it are kept (left vertical scale).

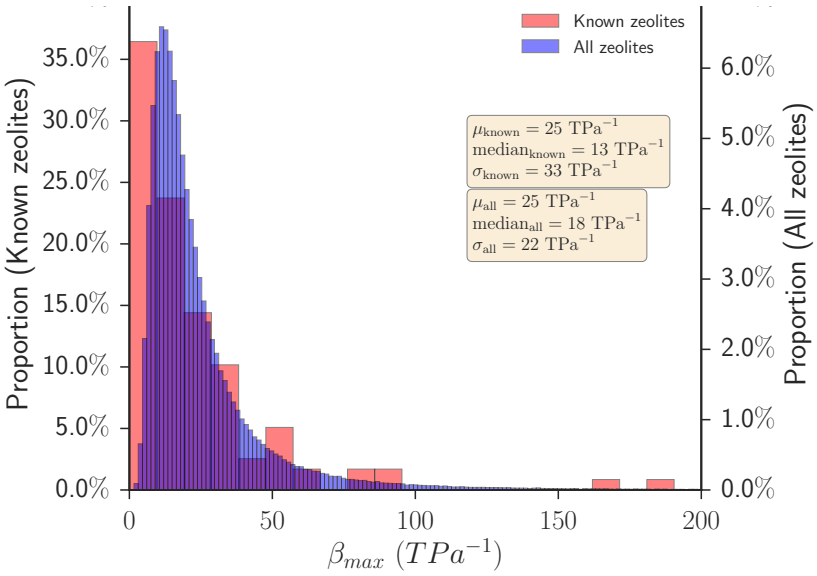

Figure 2.4: Maximum linear compressibility distributions. In blue, the distribution for the whole database is shown (right vertical scale) and in red, only the 134 known structures included in it are kept (left vertical scale).

maximum linear compressibilities of all the structures as compared with the known ones. Figure 2.3 and Figure 2.4 show these distributions. Similarly as what happens for the bulk modulus, the average, the median and the standard deviation values are not very different between the known structures and the whole database. Furthermore, the omnipresent me-

chanical anisotropy in zeolites is evidenced by these extreme values of linear compressibility. In fact, the average of the linear compressibility corresponds to the inverse of the bulk modulus. Hence with an average value of 2.6 TPa^{-1} for the minimum linear compressibility of the known structures, the equivalent stiffness is 385 GPa, meaning that there must be a compensation with larger values of linear compressibility in other directions, to lead to an average value for the bulk modulus of 54 GPa.

Young's and shear moduli

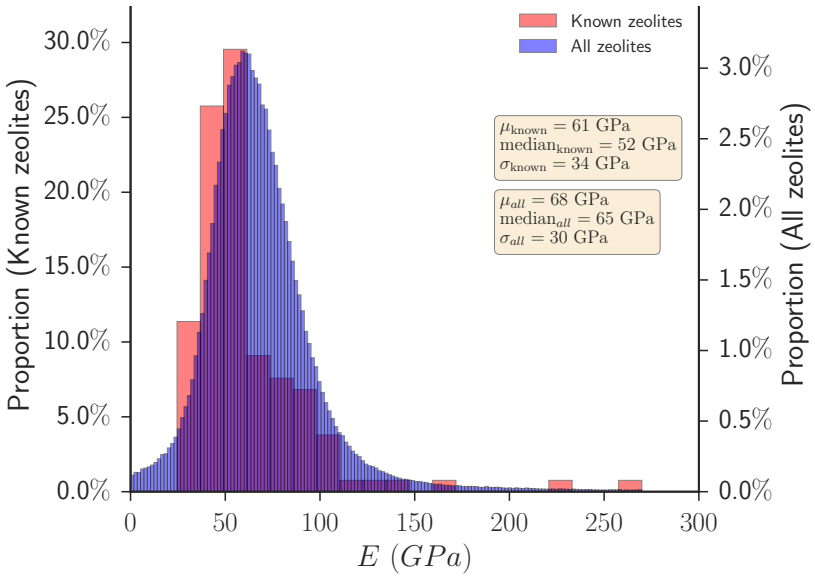

Figure 2.5: Young's modulus distributions. In blue, the distribution for the whole database is shown (right vertical scale) and in red, only the 134 known structures included in it are kept (left vertical scale).

Looking at the Young's modulus distributions confirms the similarity between the hypothetical structures and the known structures. Figures 2.5, 2.6 and 2.7 show the Young's modulus, minimum Young's modulus and maximum Young's modulus distributions respectively. Contrary to what could have been inferred by looking only at the bulk modulus, the longitudinal stiffness characterized by the Young's modulus is higher, in average, for the hypothetical structures compared to the existing ones (Figure 2.5). This stiffer behaviour is driven by the maximum values of the Young's modulus. As can be seen in Figure 2.7, the median maximum Young's modulus is 30 GPa higher for all the zeolites than for the known zeolites. The considerations developed for the Young's modulus can be similarly employed to describe the shear modulus distributions (see Figure 2.8, Figure 2.9 and Figure 2.10): G is higher in average for the whole database and it seems to be mainly due to $G_{\max}$. We will actually see later that Young's and shear moduli are statistically related.

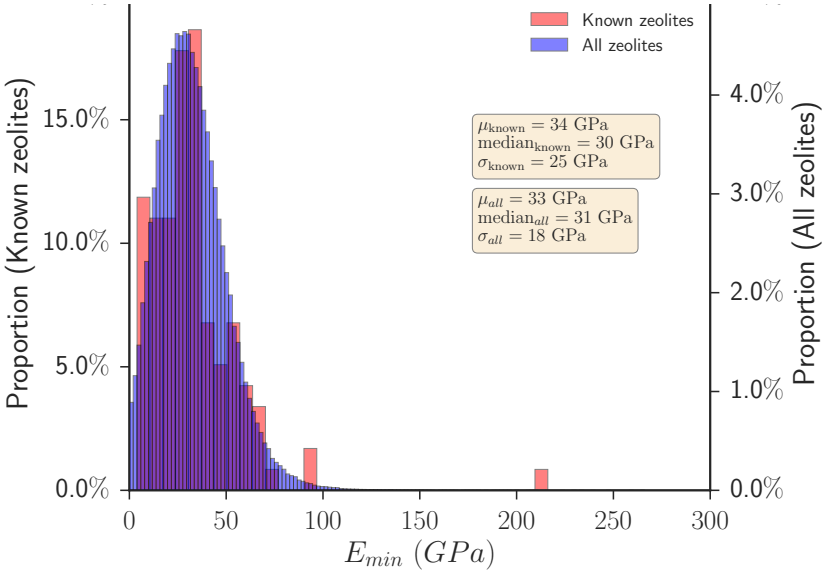

Figure 2.6: Minimum Young's modulus distributions. In blue, the distribution for the whole database is shown (right vertical scale) and in red, only the 134 known structures included in it are kept (left vertical scale).

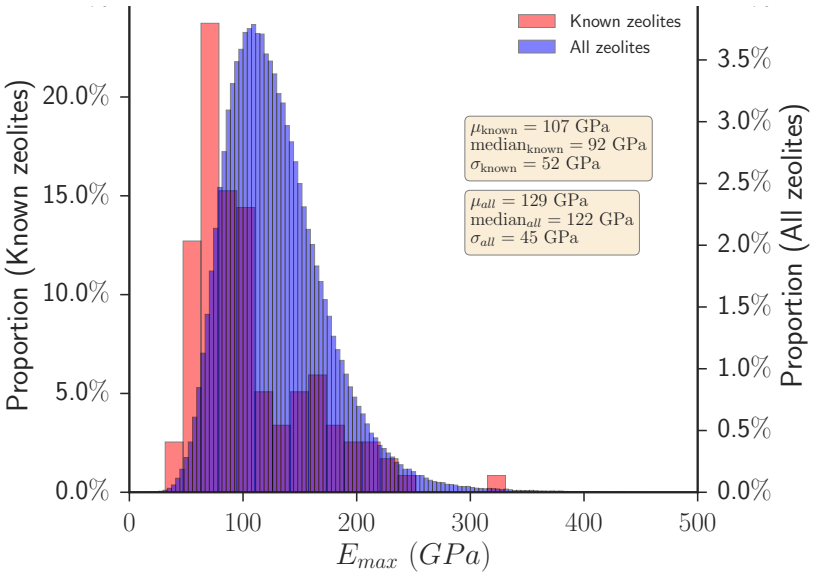

Figure 2.7: Maximum Young's modulus distributions. In blue, the distribution for the whole database is shown (right vertical scale) and in red, only the 134 known structures included in it are kept (left vertical scale).

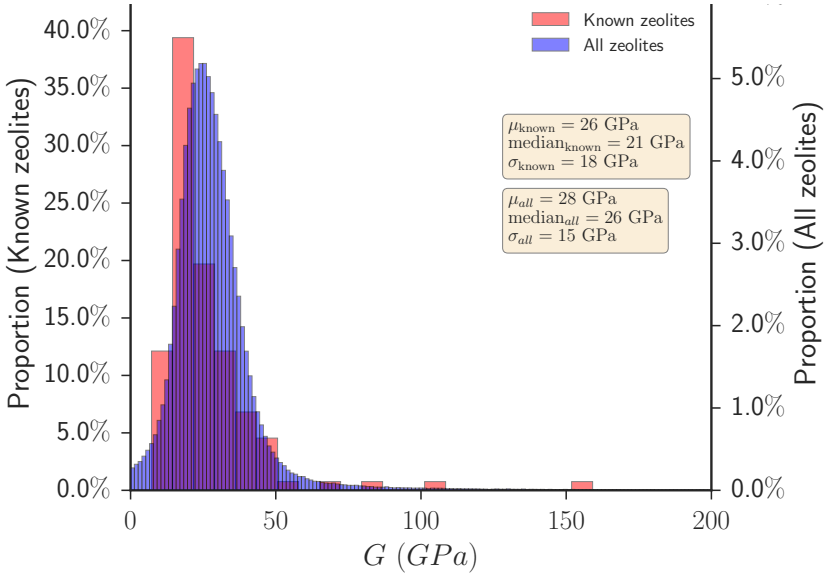

Figure 2.8: Shear modulus distributions. In blue, the distribution for the whole database is shown (right vertical scale) and in red, only the 134 known structures included in it are kept (left vertical scale).

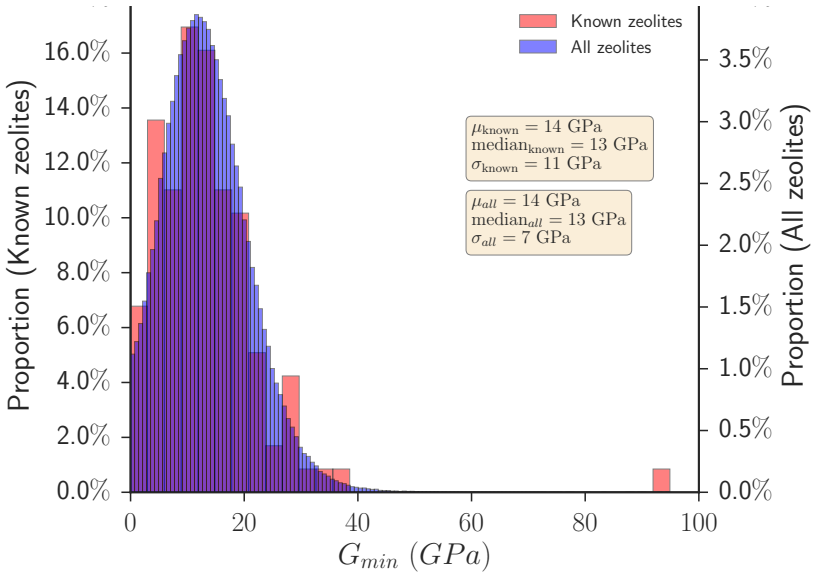

Figure 2.9: Minimum shear modulus distributions. In blue, the distribution for the whole database is shown (right vertical scale) and in red, only the 134 known structures included in it are kept (left vertical scale).

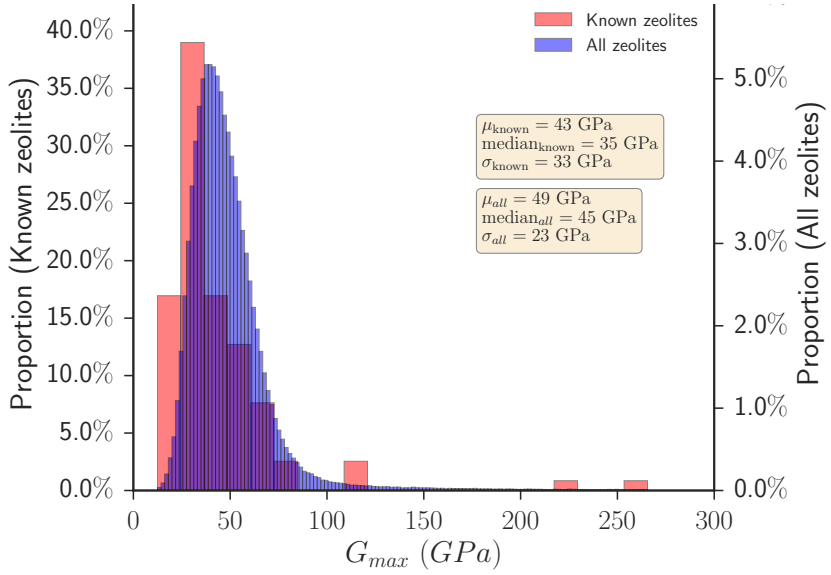

Figure 2.10: Maximum shear modulus distributions. In blue, the distribution for the whole database is shown (right vertical scale) and in red, only the 134 known structures included in it are kept (left vertical scale).

Poisson's ratio

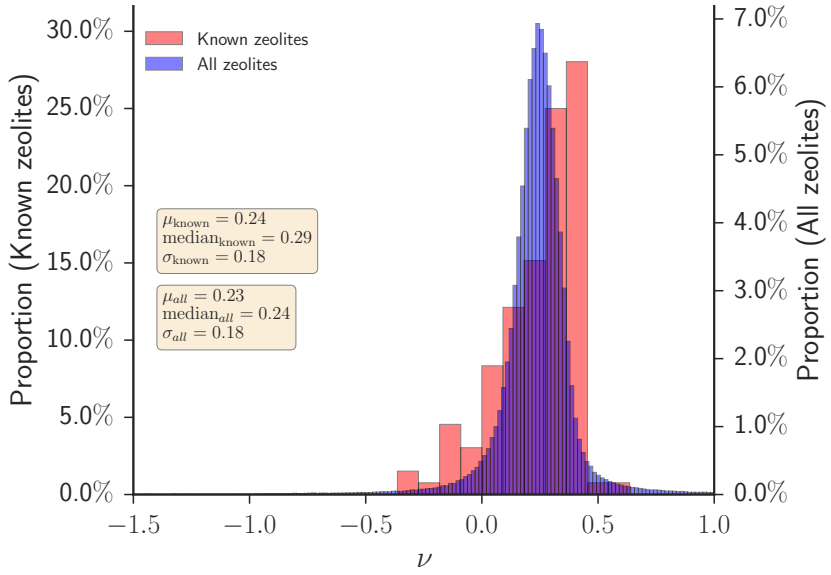

Figure 2.11: Poisson's ratio distributions. In blue, the distribution for the whole database is shown (right vertical scale) and in red, only the 134 known structures included in it are kept (left vertical scale).

As I will show in chapter 3, the Poisson's ratio is an extremely sensitive mechanical property which cannot be well captured by a force-field approach. However, as a first estimate,

I plotted the distributions of its average, its minimum and maximum, for both the known zeolites and the whole database (Figure 2.11, Figure 2.12 and Figure 2.13). Once again, the known structures seem well dispersed in the database, whether I look at the mean or the standard deviation.

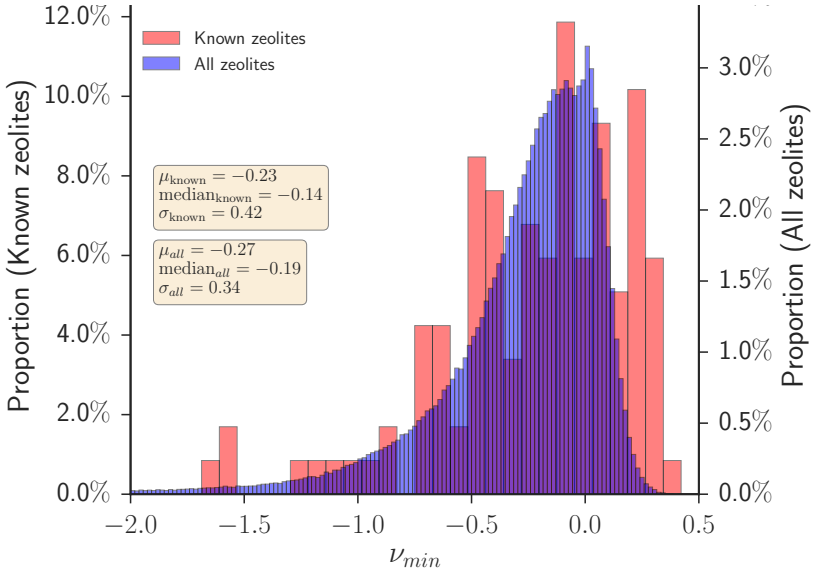

Figure 2.12: Minimum Poisson's ratio distributions. In blue, the distribution for the whole database is shown (right vertical scale) and in red, only the 134 known structures included in it are kept (left vertical scale).

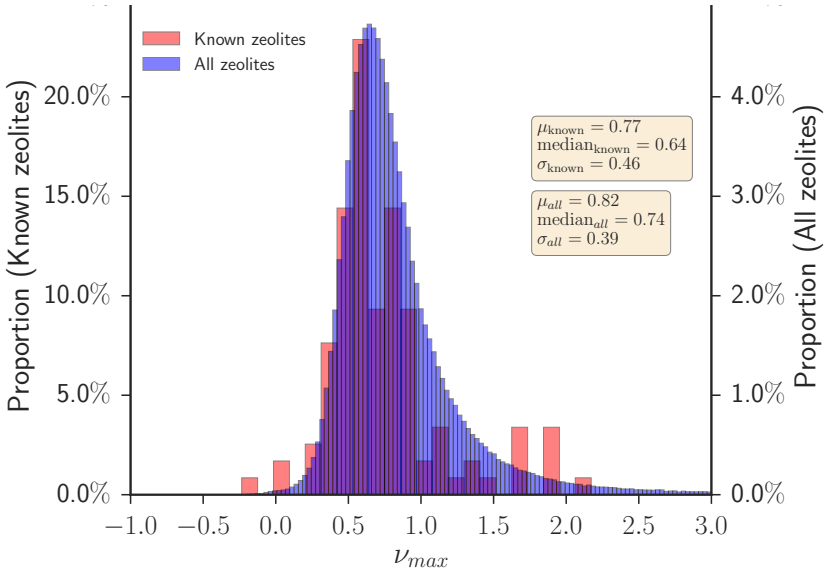

Figure 2.13: Maximum Poisson's ratio distributions. In blue, the distribution for the whole database is shown (right vertical scale) and in red, only the 134 known structures included in it are kept (left vertical scale).

2.2.2 Structural properties and energy

A fundamental property for describing zeolites is the energy per Si atom relative to the most stable polymorph of all-silica zeolites, which is α-quartz, as it is related to the enthalpy of formation. Figure 2.14 shows the distributions of energies for the known structures and the hypothetical ones. Although, the average is higher for the hypothetical zeolites, I note that there does not seem to be a threshold for known zeolites in terms of energy. Indeed, it is easy to see that more than 15% of the known structures exhibit energies above 60 kJ/mol relative to α-quartz.

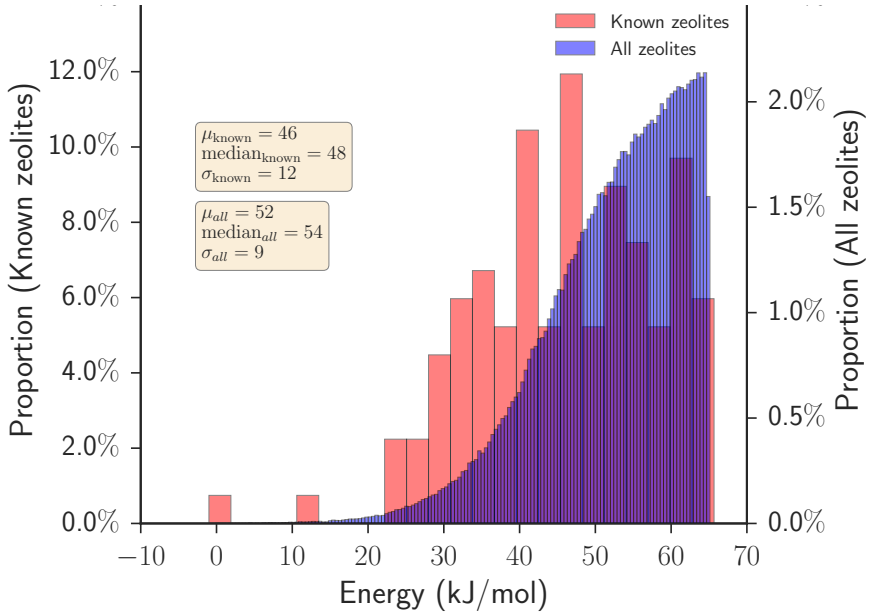

Figure 2.14: Energies per Si relative to α-quartz distributions. In blue, the distribution for the whole database is shown (right vertical scale) and in red, only the 134 known structures included in it are kept (left vertical scale).

I now move to looking at purely geometrical features of the structures. Table 2.1 presents the average and standard deviation values for properties linked to the porous network. The difference between the known structure and the whole database is striking: the database contains, in average, structures that are less porous than the known structures. In fact, the average pore sizes are 40 to 50% larger for known zeolites according to the largest free sphere (LFS), largest included sphere (LIS) and largest included free sphere (LIFS) diameters (see Figure 2.15). The largest free sphere is the size of the largest sphere that can geometrically diffuse through the framework by at least one lattice translation, the largest included sphere is the maximum distance between two nodes of the Voronoi geometrical decomposition of space and the largest included free sphere is the size of the cavity that can be accessed by the free sphere. In terms of accessible surface area, it is 2.5 times larger for known zeolites and the relative accessible porous volume is 3.6 times larger. Even when I take the total porous volume (accessible and non-accessible), it is 30% higher for the known zeolites.

	LIS (Å)	LFS (Å)	LIFS (Å)	ASA (Å^2)	NASA (Å^2)	AV/V	NAV/V
μ(all)	3.9	2.4	3.8	126	46	2.3%	4.5%
μ(known)	5.5	3.6	5.4	310	46	8.3%	0.7%
σ(all)	1.8	1.8	1.8	222	102	4.3%	1.1%
σ(known)	2.7	2.2	2.7	409	135	8.0%	2.0%

Table 2.1: Porosity properties. LIS stands for the diameter of the largest included sphere, LFS for largest free sphere, LIFS for the largest included free sphere (see Figure 2.15). ASA stands for accessible surface area, NASA for non-accessible surface area. AV/V is the relative accessible porous volume and NAV/V is the relative non-accessible porous volume. The values for areas and volumes have been computed thanks to Zeo++ [164, 165] with a probe radius of 1.2 Å. μ and $sigma$ stand for the mean and the standard deviation respectively.

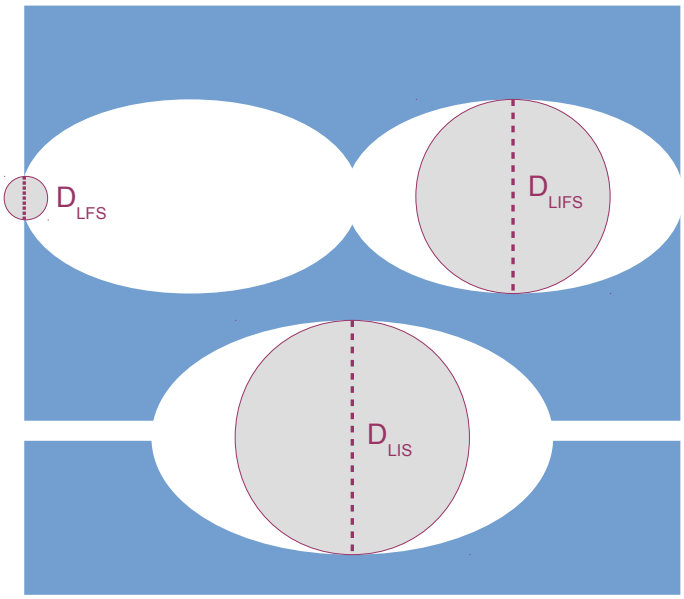

Figure 2.15: Description of the three diameters used to characterize a porous network.

Finally, another kind of properties frequently used to characterize zeolites are the numbers of N-member rings formed by silicon atoms per unit cell, with N varying from 3 to 20, as exemplified in Figure 2.16. Figure 2.17 shows the distribution of ring sizes for known zeolites and the whole database. Although the energetic and mechanical properties are pretty similar, the distributions are quite different, as for the porosity properties. In fact, in known zeolites there are essentially rings of size 6, 8, 12, 5, 10, 4 and 14 in order of importance while the most represented sizes for the whole database are 8, 6, 7, 5, 10, 12, 4 and 9. The most striking differences are probably the high proportion of 7 and 9-member rings and the

low proportion of 12-member rings in the whole database compared to known structures. Nonetheless, the very large values of standard deviation given in Figure 2.17 are a good indication that the distribution of the number of a specific N-member rings are far from being gaussian distributions. For instance, for 11-member rings, about 90% of the structures in the database have zero of them, but some structures have more than 10 of them per unit cell, hence an almost 0.5 average value with a 2.5 standard deviation value.

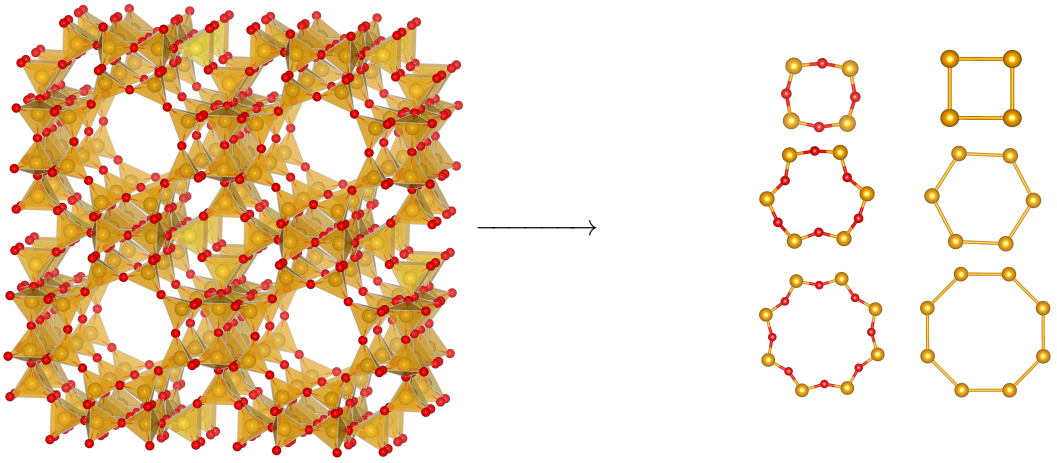

Figure 2.16: Example of silicon rings in a zeolite (LTA structure). This structure contains 3 4-member rings, 5 6-member rings and 1 8-member ring per unit cell

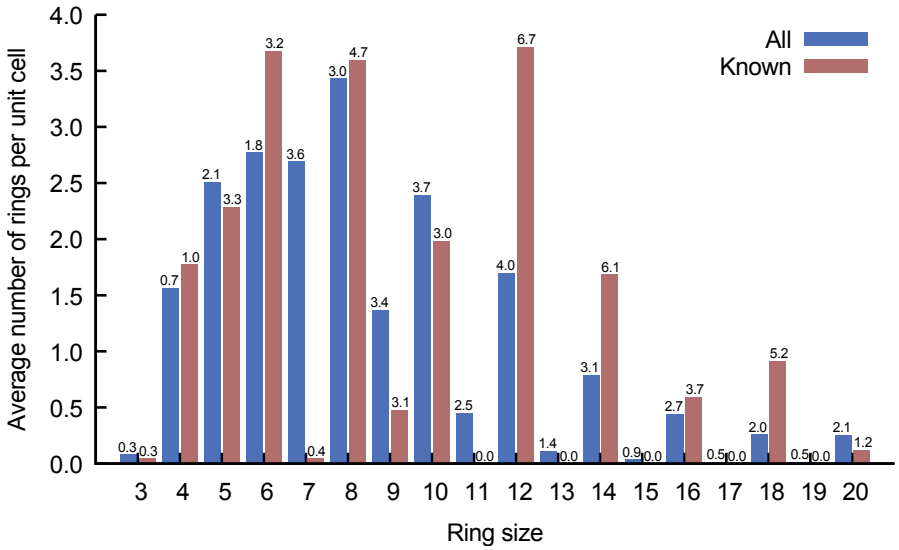

Figure 2.17: Distributions of ring sizes. In blue, the distribution for the whole database is shown and in red, only the 134 known structures included in it are kept. The numbers above each bar are the associated standard deviation values.

In conclusion, this very large structural database of Pophale *et al.* [145] seems to tackle the exploration of conformational space of zeolitic structures quite accurately. Indeed, at the force-field level, it seems that the whole database has mechanical and energetic properties

statistically quite similar to the ones of known structures. At the same time, the statistical analysis of structural properties, whether it is about porous space or the topological arrangement of atoms, shows that the structures produced are really different from the ones we already know. In the next section I explore the existing and non-existing correlations between mechanical properties, structural properties and energies, and how these are affected when looking at hypothetical structures compared to the known ones.

2.3 Noticeable correlations

Figure 2.18 shows a heatmap of all the structures of the database on a density/energy graph. On top of it, the known structures are highlighted in red, and a linear fit taking into account only these structures is shown. There is a clear negative correlation between energy and density, meaning that the structures get more and more thermodynamically stable as density increases. These calculations at force-field level are in line with what was already shown by DFT calculations on a set of 121 known structures presented by Coudert in 2013. [142] Furthermore, the hypothetical structures seem to follow a similar, although not as clear, trend. As I showed before, the known zeolites are more porous, so seeing them located mostly in the lower density part of the heatmap is logical.

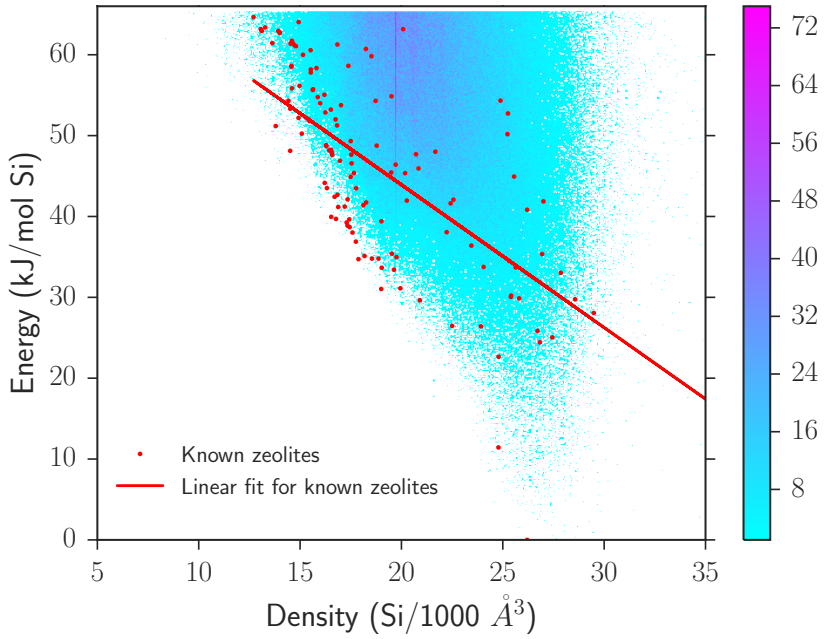

Figure 2.18: Correlation heatmap between the relative energy to α-quartz (in kJ/mol) and the density (in number of Si/1,000 Å^3).

Although the force-field level calculations are able to capture the correlation between energy and density, they fail to reproduce the correlation between low elastic anisotropy (defined in Equation 1 and low energy as presented in Figure 1 (40, extracted from [142]). In

fact, Figure 2.19 shows the correlation heatmap between elastic anisotropy and energy, with a majority of structures under 5 for the elastic anisotropy, but energy values mostly above 20 kJ/mol, whereas DFT calculations showed that an elastic anisotropy under 4 meant a very high probability of having an energy under 20 kJ/mol. The preference for lower anisotropy is thus well reproduced, but the energies for known structures are overestimated. It is to be noted that low elastic anisotropy also appears to be favorable for hypothetical zeolites. Moreover most structures with energies below 30 kJ/mol have an elastic anisotropy below 5. The link is not as clear as in the case of DFT calculations for known zeolites, but at least it means that having a high elastic anisotropy means being thermodynamically barely stable.

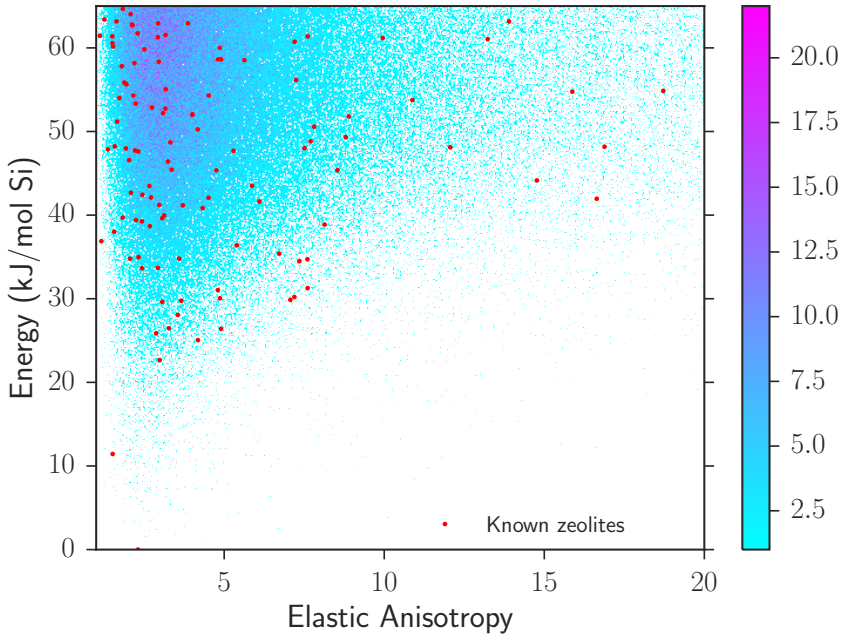

Figure 2.19: Correlation heatmap between the elastic anisotropy (unitless) and the relative energy to α-quartz (in kJ/mol).

Another correlation pointed out in [142] is the positive correlation between minimum shear modulus and minimum Young's modulus for known zeolites. The right panel of Figure 2.20 shows that the force-field calculations capture this correlation quite well as known structures all lie along a straight line in this G_{min}-E_{min} diagram. This behaviour also seems to be a generic property of any zeolitic structure as the global heatmap follows the trends for known zeolites with similar deviations. Furthermore, the left panel of Figure 2.20 shows that this correlation is even clearer when looking at the average values of shear and Young's moduli. It means that the basic SiO_4 tetrahedral unit creates a strong coupling between the response to longitudinal or shear stress, no matter the way it is assembled to form a crystal structure. This reinforces the conclusions drawn earlier (ref. 142) on a much larger database of zeolitic structures.

Finally, before going further into the exploration of auxeticity, we turn to the correlation between extreme values of the Poisson's ratio and elastic anisotropy. It was shown

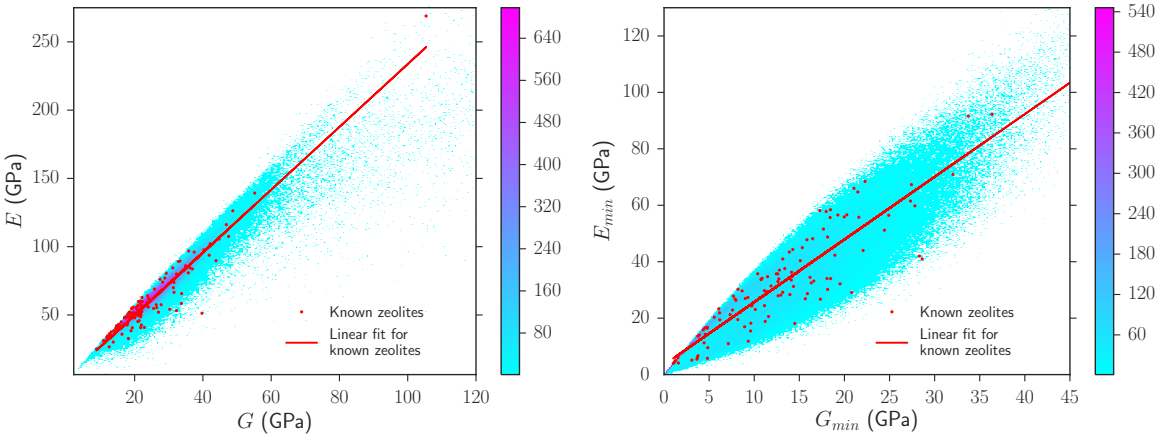

Figure 2.20: Correlation heatmap between the average shear modulus G (GPa) and the average Young's modulus E (GPa) (left). Correlation heatmap between the minimum shear modulus G_{min} (GPa) and the minimum Young's modulus E_{min} (GPa) (right).

that known zeolites (according to DFT calculations) behave similarly to dense silica crystals in terms of minimum and maximum Poisson's ratios following two separate families of curves when plotted agains Ledbetter anisotropy. [144] Ledbetter anistropy is defined as the square of the maximum shear-sound-wave velocity divided by the square of the minimum shear-sound-wave velocity and characterizes mechanical anisotropy, as well as the elastic anisotropy. In Figure 2.21, I plotted the minimum and maximum Poisson's ratios for all the zeolites, highlighting the known structures. The behaviour seen before is well reproduced for known zeolites and it can apparently be generalized for hypothetical structures as the known structures are widely dispersed among all the structures.

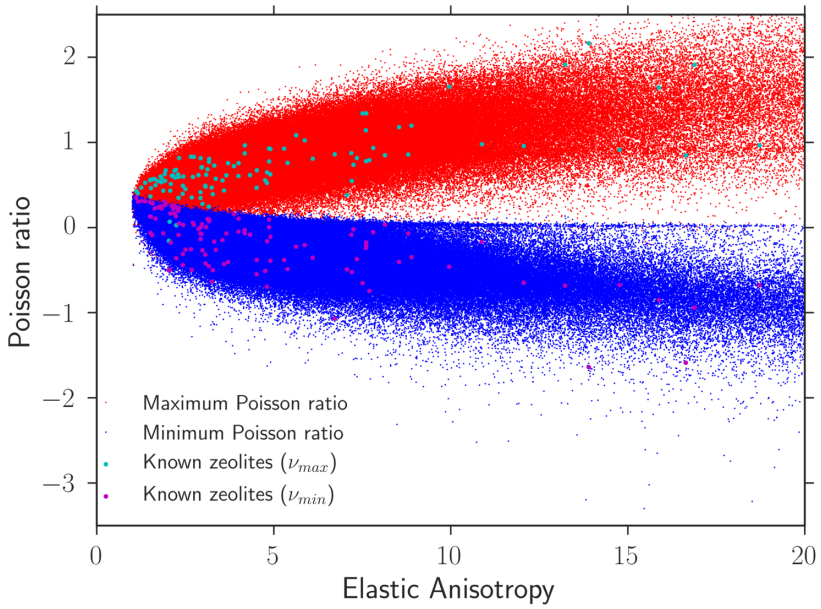

Figure 2.21: Correlation between the elastic anisotropy and the minimum and maximum Poisson's ratios (both are unitless).

Chapter 3

Exploration of completely auxetic zeolitic structures by DFT calculations

In this chapter, I present the DFT study I carried out on a specific subset of the database presented before. I chose to focus on complete auxetic (3C class of auxeticity) materials, and as such I selected hypothetical zeolitic structures for which the force-field calculations showed a negative maximum Poisson's ratio. I first present the characteristics of the subset according to force-field level calculations. Then I detail the method used to compute the mechanical properties by DFT with the CRYSTAL14 software. [166] I present the results in two parts. I first compare the results obtained by DFT to the initial force-field data, thus assessing the performance of the force-field on such "unusual" structures. In a second time, thanks to other DFT calculations on randomly chosen structures in the database, I show how I am able to better predict auxeticity in these materials by the use of machine learning techniques.

3.1 Characteristics of the selected subset

As pointed out in subsection 2.1.2 (page 56), the subset I consider here is composed of the 578 hypothetical structures which present total auxeticity (i.e. always negative Poisson's ratio) according to the force-field. Table 3.1 presents the average mechanical and energetic properties for these particular structures compared to all the structures of the database. I let aside the Poisson's ratio comparison as it is obviously negative, by construction, for the selected subset. These materials appear to be much softer than the other hypothetical structures of the database as the average value for the bulk modulus over this subset is five times lower than than the one over the whole database. Similarly, the Young's modulus is about twice lower. However, the shear modulus is almost the same for the subset and the

whole database (even a little bit higher for the subset), which is strange as they are usually related.

	Bulk modulus	Young's modulus	Shear modulus	Poisson's ratio	Energy
μ(all)	46 GPa	68 GPa	28 GPa	0.23	52 kJ/mol
μ(3C)	9 GPa	39 GPa	30 GPa	-0.27	49 kJ/mol

Table 3.1: Average values of the bulk modulus, the Young's modulus, the shear modulus, the Poisson's ratio and the relative energy to α-quartz for the whole database and the completely auxetic subset.

In Figure 3.1 I show a zoom of Figure 2.20 with the structures from the auxetic subset highlighted. The positive correlation between shear and Young's moduli seems clear for this subset too, but with lower Young's moduli overall. Another interesting feature of this subset is its average relative energy, which is very close to the one for all the zeolites, only 3 kJ/mol higher than the average for known structures. These first characteristics tend to suggest that the structures in this subset should be, for some at least, experimentally feasible.

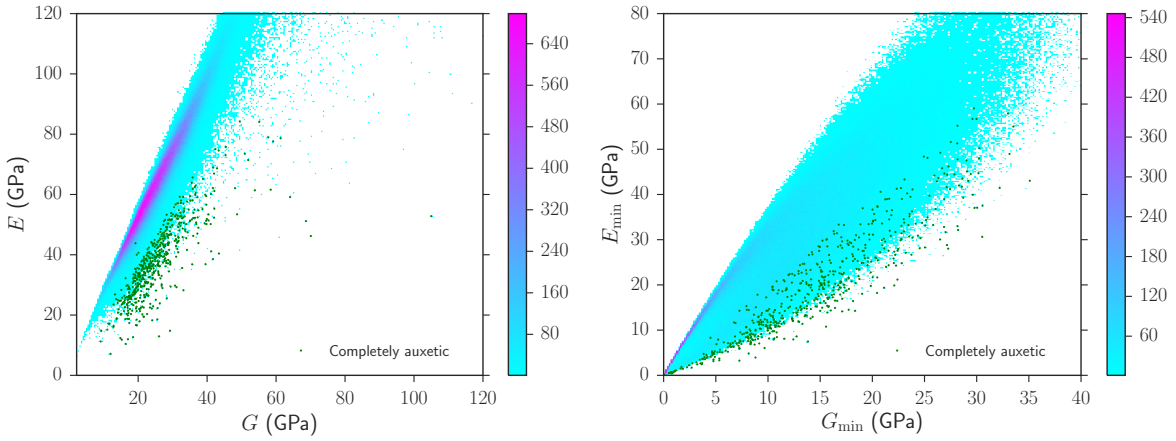

Figure 3.1: Correlation heatmap between the average shear modulus G (GPa) and the average Young's modulus E (GPa) (left) and their minima (right). The completely auxetic structures follow a trend which is parallel to the one followed by all the structures, but with lower Young's moduli.

The structural properties linked to porosity for the structures of the subset are presented in Table 3.2, with the values for the whole database for reference. Although the cages and channels are of similar sizes for the subset as compared to the whole database, as the LIS, LFS and LIFS diameters indicate, these structures appear to be much less porous. Indeed, the total porous volume – accessible and non-accessible – represents only 1.9% of the total volume in average, compared to 6.8% for the whole database and 9% for the known structures. This smaller porosity must be explained by even smaller pockets (than the probe radius of 1.2 Å) as the average density for the subset is 2.12 g/cm^{-3} (21.2 Si/1000 Å^3) while it is 2.14 g/cm^{-3} (21.4 Si/1000 Å^3) for the whole database.

To complete the characterization of these structures, I present the distribution of the dif-

	LIS (Å)	LFS (Å)	LIFS (Å)	ASA (Å^2)	NASA (Å^2)	AV/V	NAV/V
μ(all)	3.9	2.4	3.8	126	46	2.3%	4.5%
μ(3C)	3.8	2.3	3.7	88	52	1.4%	0.5%
σ(all)	1.8	1.8	1.8	222	102	4.3%	1.1%
σ(3C)	1.6	1.6	1.6	205	98	3.5%	1.1%

Table 3.2: Porosity properties. The different acronyms are defined exactly as in Table 2.1.

ferent ring sizes in Figure 3.2. They appear to have rings of similar sizes as all the hypothetical structures, and the differences observed are very small against the standard deviations. For instance, the largest differences observed are for rings of size 7, 9 and 12, with less than 0.5 ring per unit cell and standard deviations above 3.0 for the whole database and above 2.5 for the subset.

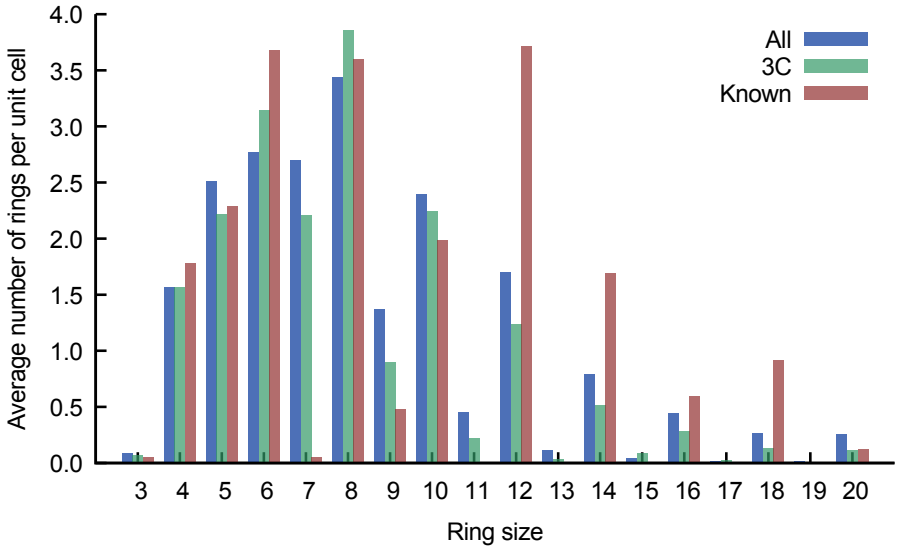

Figure 3.2: Distributions of ring sizes. In blue, the distribution for the whole database is shown, in green the 3C subset and in red the 134 known structures. Standard deviations are omitted for clarity (the ones for the 3C subset are very similar to the ones for the whole database given in Figure 2.17).

3.2 Numerical methods: mechanical properties with Crystal14

3.2.1 Parameters and details of Crystal14

For this study I used the CRYSTAL14 software as it is unique in treating periodic systems with a crystalline local orbital method. For every structure, I followed the same procedure which

is I optimized its geometry, including cell parameters and atomic positions and computed its second elastic tensor using DFT. I started from the structures given in the database, optimized with the BKS force-field.

Geometry optimizations (CRYSTAL14 keyword `PREOPTGEOM`) consist of iteratively updating the structure and subsequently computing energies and forces. This iterative procedure is repeated until convergence criteria are met, i.e. until atomic displacements and forces, and their respective gradients, are smaller than a chosen threshold. To determine the direction and amplitude of each step (in the $\mathbf{R}^{3N}$ space of atomic coordinates, with N the number of atoms per cell), I used a numerical quasi-Newton method, the Broyden-Fletcher-Goldfarb-Shanno algorithm. The convergence criteria used in CRYSTAL14 have to be tight enough to ensure high accuracy, as it is necessary to compute properties linked to derivatives of the energy such as mechanical properties, as presented in the input file for α-quartz shown in Figure 3.3.

When computing mechanical properties (CRYSTAL14 keyword `ELASTCON`), the main output is the 6×6 tensor of second-order elastic constants C_{ij} in Voigt notation. These are computed by performing small deformations along each of the 6 deformation modes, or a subset of those in high symmetry systems (2 modes are enough for cubic space groups for instance). These calculations are generally more costly than geometry optimizations, with the computation time depending not only on the system size but also on a number of other factors: the number of deformation modes to be performed, from 2 in cubic systems to 6 in triclinic systems; the point group symmetries remaining after individual deformations (for an orthorhombic system shearing modes take much more time than compression modes, which do not break any symmetry); and the number of steps needed to reach convergence, after each cell deformation, which can be decreased by decreasing the deformation amplitude. For example, the average time needed to complete a full calculation on one structure of the subset is 5 days on 16 cores ($\sim$ 2000 CPUh), but more than 10% of the calculations took more than 14 days.

	K	E	G	ν
r	0.11	0.59	0.81	0.30
RMSE	15 GPa	14 GPa	4.1 GPa	0.18
RMSE/$\lvert\text{mean}_{\text{disp}}\rvert$	84%	31%	18%	134%

Table 3.3: Preliminary results on the importance of dispersion corrections. The Pearson's correlation coefficient (r), the absolute root mean square error (RMSE) and the root mean square error relative to the average absolute value with dispersion corrections (RMSE/$\lvert\text{mean}_{\text{disp}}\rvert$) are given for the bulk modulus (K), the Young's modulus (E), the shear modulus (G) and the Poisson's ratio (ν).

More specifically, I used triple-zeta valence polarized (TZVP) basis sets and the PBE exchange-correlation functional adapted for solids (PBESOL). As DFT is known to drastically underestimate long-range dispersion interactions, I carried out preliminary calculations on 25 structures of the subset with and without dispersion corrections to determine their

```
quartz
CRYSTAL
0 0 0
154
4.95304267 5.45063836 120.0
2
14 0.468244242584 -5.551115e-17 -0.333333333333
8 0.411357593826 0.270377816093 -0.217333686507
ELASTCON
MAXCYCLE
1000
PREOPTGEOM
END
BASISSET
POB-TZVP
DFT
PBESOLXC
ENDDFT
FMIXING
40
LEVSHIFT
5 0
GRIMME
0.75 20. 25.
2
14 9.23 1.716
8 0.70 1.342
SHRINK
5 5
END
```

Figure 3.3: Representative input file for calculations with the CRYSTAL14 software package (here for quartz). Input data are given in the following order: geometrical information (space group number, cell parameters, fractional coordinates of non-equivalent atoms), keywords defining the calculation type (here computation of elastic properties, preceded by a geometry optimization), basis set information, exchange-correlation functional, technical parameters to facilitate convergence, and, here, inclusion of dispersion corrections), and finally shrink parameter, which depends on system size (set so that the minimum lattice parameter multiplied by it gives a value above 20).

importance. It turns out that these corrections make a large difference, especially on the mechanical properties. In Table 3.3, I show the deviations observed for mechanical proper-

ties computed with and without dispersion. It appears that dispersion corrections are quite important as these deviations are quite large, especially for the bulk modulus and Poisson's ratio, with 84% and 134% of relative root mean square error respectively. This is in line with previous results presented in [167] in 2014, where the importance of long-range Van der Waals interactions on the relative stability of full silica zeolites is described. We thus used them in all calculations below.

3.2.2 Systems studied: a supplementary random subset

Using the method described previously, I thus conducted 578 DFT calculations on all the structures of this specific subset. However, in order to have other points of comparison, to try to generalize, especially through machine learning, the links found between structural properties and auxeticity, I also carried out 742 DFT calculations on randomly chosen structures in the database not including the 3C subset. More precisely, I randomly selected more than 2300 structures and, given the computational time available, I could obtain 742 second-order elastic tensors. The others were too CPU-intensive to converge in reasonable times. From now on, I will call this set of 742 structures the random set. Table 3.4 shows that these 742 resulting structures are very well dispersed in the database at the same time in terms of structural properties and mechanical properties. Whether I look at the average or median values of any mechanical property, the differences are insignificant compared to the values of the standard deviations which are also almost equal with each other. The only difference lies in the structure as I note that the structures of the random set are slightly less porous than the ones of the whole database, with differences on average which are still half the standard deviation though.

	LIS (Å)	PV	En (kJ/mol)	K (GPa)	E (GPa)	G (GPa)	ν
μ(all)	3.9	2.8%	52	46	68	28	0.23
μ(random)	3.2	1.6%	51	48	75	31	0.23
median(all)	3.5	0.014%	54	44	65	26	0.24
median(random)	3.0	0.011%	53	45	71	29	0.24
σ(all)	1.8	5.5%	9	18	30	15	0.18
σ(random)	1.2	3.9%	10	19	29	13	0.14

Table 3.4: Comparison between the random set and the whole database. The average (μ), median and standard deviation (σ) are given for the diameter of the largest included sphere (LIS), the total porous volume, the relative energy to α-quartz (En), the bulk modulus (K), the Young's modulus (E), the shear modulus (G) and the Poisson's ratio (ν).

Finally, to confirm the uniformity of the random set in the whole database, I look the distribution of ring sizes in Figure 3.4. Once again, the differences observed on the average values are negligible against the standard deviations. For example, the largest absolute

difference is attained for the 7-member rings with 0.57 against standard deviations of 3.6 and 3.9 for the whole database and the random set respectively.

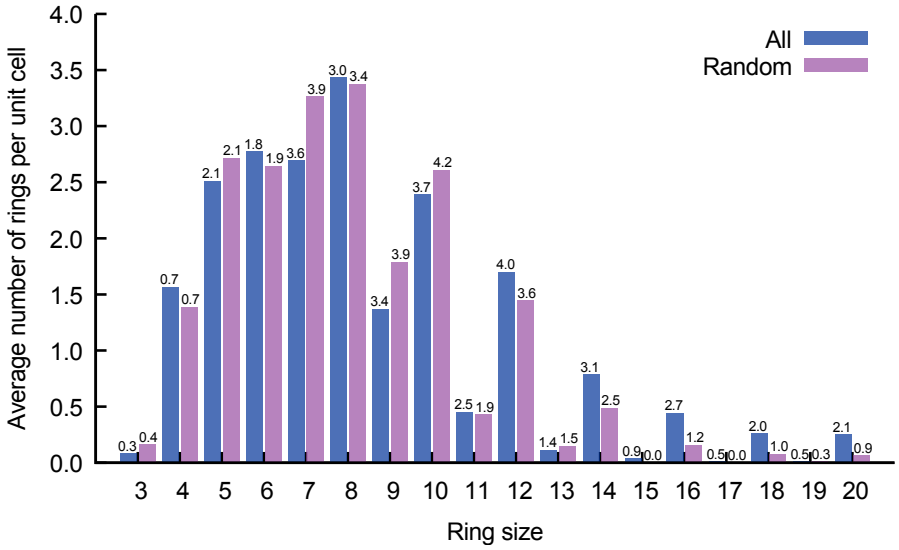

Figure 3.4: Distributions of ring sizes. In blue, the distribution for the whole database is shown, in purple the distribution for the random set containing 742 structures. The label above each bar corresponds to the standard deviation associated with the particular ring size.

In the next section, I present the results of this study. I assess the performance of the force-field on structural parameters as well as on mechanical properties, especially focusing on the Poisson's ratio. Then, I set out to find a better way to predict auxeticity, and more generally the value of the Poisson's ratio, in all-silica zeolites.

3.3 Results

I present here the results obtained by DFT calculations on the subsets described above. More precisely, I will focus exclusively on the structures for which I obtained a second-order elastic tensor corresponding to a mechanically stable structure. For the completely auxetic subset, I obtained 500 second-order elastic tensors ($\sim 87\%$ of the subset) which led to 392 mechanically stable structures. For the random subset, the 742 second-order elastic tensors led to 599 mechanically stable structures. I also carried out a simulation of α-quartz with the exact same parameters to have a reference for the computation of relative energies.

3.3.1 Force-field versus DFT on structural and mechanical properties

Structural properties

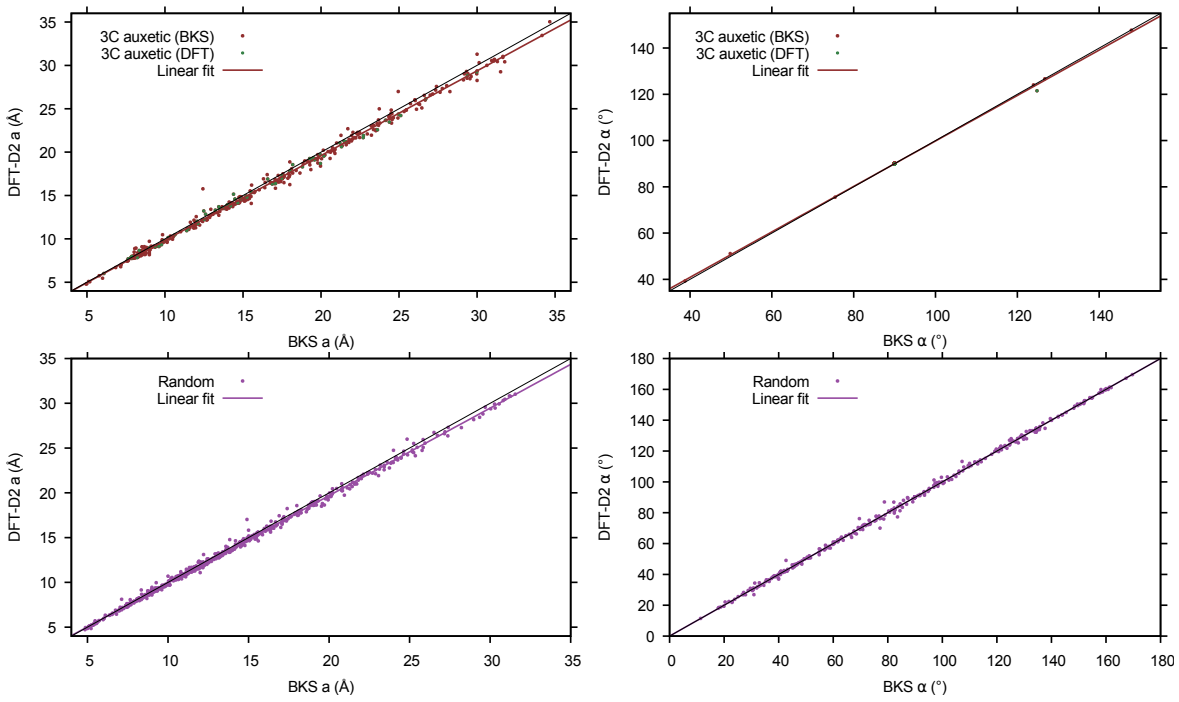

Figure 3.5: Top panel: 3C subset, left: first cell parameter (a) given by the DFT-D2 calculations as a function of the values given by the BKS force-field. The points highlighted in green are the structures which are completely auxetic according to DFT-D2 calculations. Top panel, right: the angle between the second and third unit cell vectors (α) given by the DFT-D2 calculations as a function of the values given by the BKS force-field. Bottom: same as top, but for the random subset. The solid black line in all graphs is the identity function.

As exemplified in Figure 3.5 with the first cell parameter (a) and the angle between the second and third unit cell vectors (α), the cell parameters computed at the force-field level

are statistically in agreement with the ones computed by DFT-D2, although there are some outliers, such as zeolite number 9316681 (numbered in the database from Pophale *et al.* [145]) for which BKS predicted $a = 12.4\,\text{Å}$ and DFT gives $a = 15.8\,\text{Å}$, i.e. an increase of 27%. The volumes are also almost unchanged between DFT and force-field calculations. Furthermore these first observations are independent from the subset considered, the force-field seems to perform as well on the 3C subset or the random subset.

Although the variations for the individual cell parameters are contained, the density is more affected. As Figure 3.6, the agreement is still very good in average. However, on individual structures, the maximum deviation is 12% for the random subset, but goes up to 35% for one structure of the auxetic subset (zeolite number 9420191).

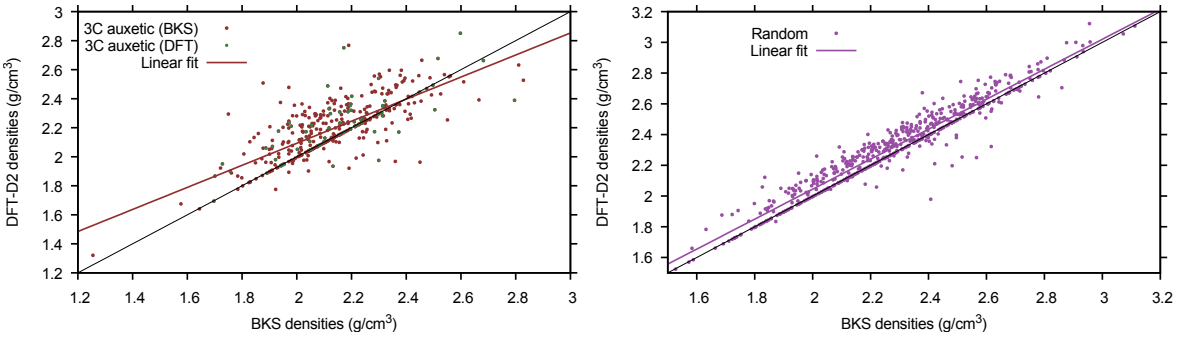

Figure 3.6: Left: density given by the DFT-D2 calculations as a function of the values given by the BKS force-field for the 3C subset. The points highlighted in green are the structures which are completely auxetic according to DFT-D2 calculations. Right: same as left, but for the random subset. The solid black line in all graphs is the identity function.

These results on these two sets with several hundreds of structures show that force-field based calculations of structural properties are suitable for high-throughput screening of new zeolitic structures. In the following subsection, I show that, on the contrary, the energy and the mechanical properties, especially the Poisson's ratio, are much more difficult to tackle via calculations with this specific force-field.

Energy and mechanical properties

Figure 3.7 shows the energies given by the DFT calculations along with the ones given by the force-field level calculations. Whether it is for the auxetic subset or for the random subset, the results provided at the force-field level are completely off the DFT values. Beyond the graphical representation, the root mean square error and the mean absolute error are both above 26 kJ/mol for both subsets. Even worse is the fact that there is rather weak correlation between the relative energies given by BKS and the ones obtained by DFT (r=0.46 for the auxetic subset and r=0.38 for the random subset).

Logically, as the second-elastic tensor coefficients depend on the variations of the energy

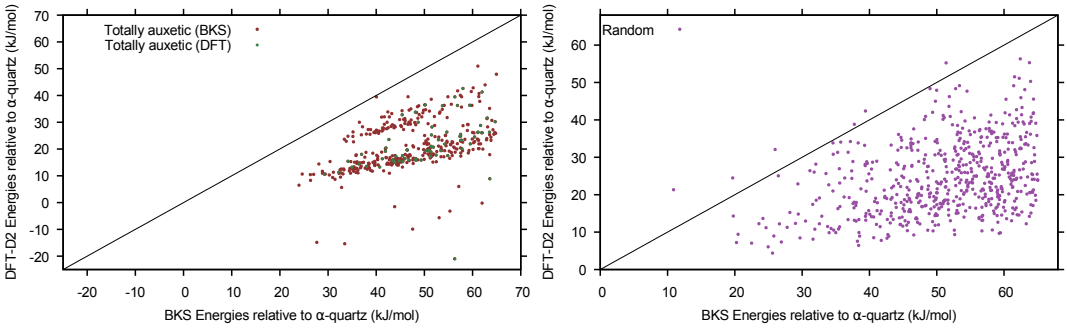

Figure 3.7: Left: energy given by the DFT-D2 calculations as a function of the values given by the BKS force-field for the 3C subset. The points highlighted in green are the structures which are completely auxetic according to DFT-D2 calculations. Right: same as left, but for the random subset. The solid black line in all graphs is the identity function.

as the material is deformed, the performance of the force-field is also quite weak on the mechanical properties. Table 3.5 shows three estimators of the deviations between DFT values and force-field values. Even taking a quite lenient measure, the relative root mean square error, which is the root mean square error divided by the range of the property in the subset considered, the lowest value is attained for the bulk modulus around 20%. However, even in this case, the mean absolute error for the auxetic subset is 7.9 GPa which represents almost half of the average value of the DFT bulk modulus for the auxetic subset (16 GPa) and more than the standard deviation over this subset of 392 structures (6.5 GPa).

	En (kJ/mol)	K (GPa)	E (GPa)	G (GPa)	ν
rRMSE(3C)	39%	22%	19%	174%	47%
rRMSE(random)	55%	21%	85%	78%	46%
MAE(3C)	26	7.9	11	10	0.29
MAE(random)	27	10	19	7.6	0.07
r(3C)	0.46	0.29	0.43	-0.01	0.002
r(random)	0.38	0.60	0.25	0.22	0.21

Table 3.5: I give here, for both subsets, the relative root mean square error (rRMSE, RMSE divided by the range of the property considered), the mean absolute error (MAE) and the Pearson's correlation coefficient (r) for the energy (En), the bulk modulus (K), the Young's modulus (E), the shear modulus (G) and the Poisson's ratio (ν).

Finally, if the aim is to determine whether a material has some degree of auxeticity, the extreme values of the Poisson's ratio ν_{min} and ν_{max} are crucial. The table below (Table 3.6) shows how unreliable the force-field data are in that regard. In fact, the correlation between the force-field and the DFT values is nonexistent and the very large values for the RMSE show that outliers are very badly described. The large values of the mean absolute error also shows that the force-field is unable to be accurate even for "average" materials.

	$\nu_{\min}$	$\nu_{\max}$
RMSE(3C)	1.93	1.5
RMSE(random)	1.35	13
MAE(3C)	0.71	0.53
MAE(random)	0.45	3.4
r(3C)	0.07	0.04
r(random)	0.03	0.09

Table 3.6: I give here, for both subsets, the root mean square error, the mean absolute error (MAE) and the Pearson's correlation coefficient (r) for the minimum and maximum of the Poisson's ratio ($\nu_{\min}$ and $\nu_{\max}$).

After making these observations, inspired by earlier work in the group [163] I used some machine learning techniques, with the DFT data I generated as training and test sets, to improve the prediction of auxeticity in these zeolitic structures. I present the results obtained in the next subsection.

3.3.2 Predicting auxeticity

Generic principles

The principle of machine learning is to create a predictor (P) by training an algorithm on two sets of variables (possibly multidimensional) X, called the descriptors, and Y, the desired output. P is trained to output Y as it is given the set of descriptors X. Then, given an other set of variable X', P is tested by comparing the output P(X') to the real output, say Y'. In the case of zeolites, as I have shown before, computing mechanical properties, and in particular the Poisson's ratio is either costly (DFT) or faster but unreliable (force-field). Hence the need for more reliable and/or less costly prediction methods.

The idea here was to train machine learning algorithms, already implemented in the `scikit-learn` python library [168] , to create four predictors of two types: three, based on regression methods, able to predict the minimum, the average and the maximum of the Poisson's ratio and another one, based on classification methods, to predict the belonging to a particular class of auxeticity, only from structural properties as input, obtainable at a almost zero computational cost. I used almost the same descriptors as Evans and Coudert in [163], summarized in Figure 3.8. The descriptors are classified into three categories: local, concerning bond length, angle and dihedrals, global, like density or ring sizes distribution and porosity-related, like accessible surface area, largest included sphere diameter or accessible volume. All the descriptors I started with are detailed in Table 3.7.

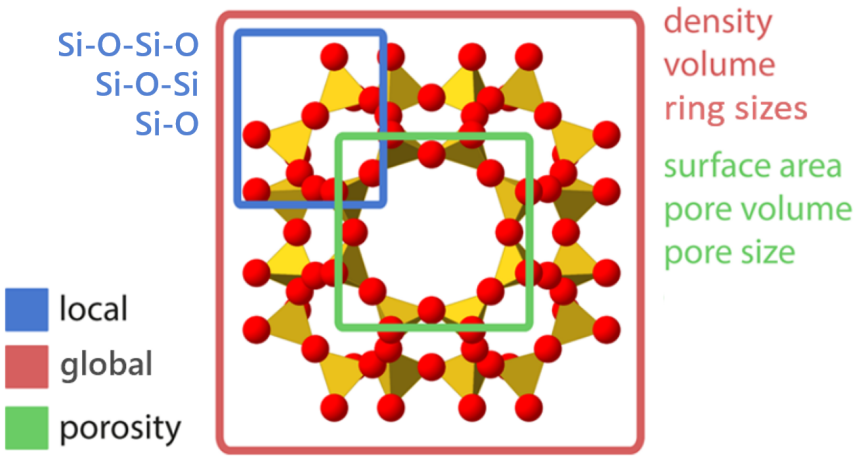

Figure 3.8: Summary of the descriptors used as entries in the machine learning process classified in local properties (Si-O bond length, Si-O-Si angle), global properties (density, volume and proportion of ring sizes) and porosity-related properties (pore and channel sizes, porous volumes, surface areas). This figure has been taken and modified from [163].

Predicting the Poisson's ratio

The first thing I did was to try and create a predictor that would be able to predict the value of the average Poisson's ratio for any zeolitic structure. To build such a model, I used a gradient boosting regressor (GBR) [169, 170] as implemented in Python `scikit-learn` package. [168] This method trains regression trees as an additive model in stepwise approach by optimizing arbitrary loss functions. At each stage, a regression tree is fit on the negative gradient of the loss function. GBR is both an accurate and effective method that has been used in many areas, such as web search ranking. [171] In particular, this method was chosen over other methods such as support vector machines, [172] as GBR models are considered robust, interpretable, and applicable for the relatively small data set I study here. [173] The implementation of GBR I used employs well-established selection criteria with 3-fold cross-validation, which was repeated 100 times to give a representation of the model accuracy.

I used a well-established scheme with 3-fold cross validation, repeated 100 times to give a good representation of the model accuracy. The hyperparameters were chosen so as to provide good prediction accuracy and minimize overfitting. In particular, as in [163], I used 1000 estimators, a learning rate of 0.01, a minimum samples split of 2, a minimum samples per leaf of 3, a maximum depth of 3, a maximum number of features equal to the square root of the number of total features and a subsample parameter of 0.4.

The results are graphically represented in Figure 3.9. Globally, the results given by the GBR predictor are much better than the ones given by force-field calculations. If I take the RMSE as a measure of the accuracy, it is 0.29 in the case of BKS, while it goes down to 0.12

	descriptor
local	SiO average/median/standard deviation (Å) SiOSi average/median/standard deviation (°) SiOSiO average/median/standard deviation (°) SiO geometric mean (Å) SiOSi geometric mean (°) SiO harmonic mean (Å) SiOSi harmonic mean (°) SiO skewness SiOSi skewness SiOSiO skewness SiO maximum (Å) SiOSi maximum (°) SiOSiO maximum (°) SiO minimum (Å) SiOSi minimum (°) SiOSiO minimum (°)
global	density numbers of N-member rings (N=3-20)
porosity	Largest included sphere (Å) Largest free sphere (Å) Largest included free sphere (Å) Accessible surface area (probe radius 1.2Å, $Å^2/Å^3$) Non-accessible surface area (probe radius 1.2Å, $Å^2/Å^3$) Accessible volume (%) Non-accessible volume (%)

Table 3.7: All the descriptors used in this study.

for the GBR predictor. It is also interesting to look at the performance of the two methods on each set, the auxetic, the random and the known subsets. Table 3.8 gives the detail of the errors for the two models. The force-field is almost as good as the GBR predictor for the known structures. However, for hypothetical structures, and especially for the auxetic subset, the GBR predictor is at least twice as good as the force-field.

One of the nice feature of the GBR model is that, although it looks like a black box model, it gives the relative importance of the different descriptors after training the algorithm. It allows to build another model with less descriptors needed. In my case, I chose to keep only the descriptors with a relative importance above 40% (compared to the most important one). Figure 3.10 presents the relative importance of the descriptors kept for the production runs. It is interesting to see that local descriptors, and especially the amplitudes of their variations are most represented with 8 descriptors over 16. In terms of porosity-related descriptors, the linear sizes and the relative surface areas matter more than the actual porous volumes. In

Subset (method)	RMSE	MAE
all(GBR)	0.12	0.096
all(BKS)	0.29	0.15
auxetic(GBR)	0.15	0.12
auxetic(BKS)	0.34	0.29
random(GBR)	0.10	0.079
random(BKS)	0.26	0.070
known(GBR)	0.15	0.13
known(BKS)	0.18	0.12

Table 3.8: Root mean square error and mean absolute error for the 3 subsets and their assembly for the prediction of the Poisson's ratio.

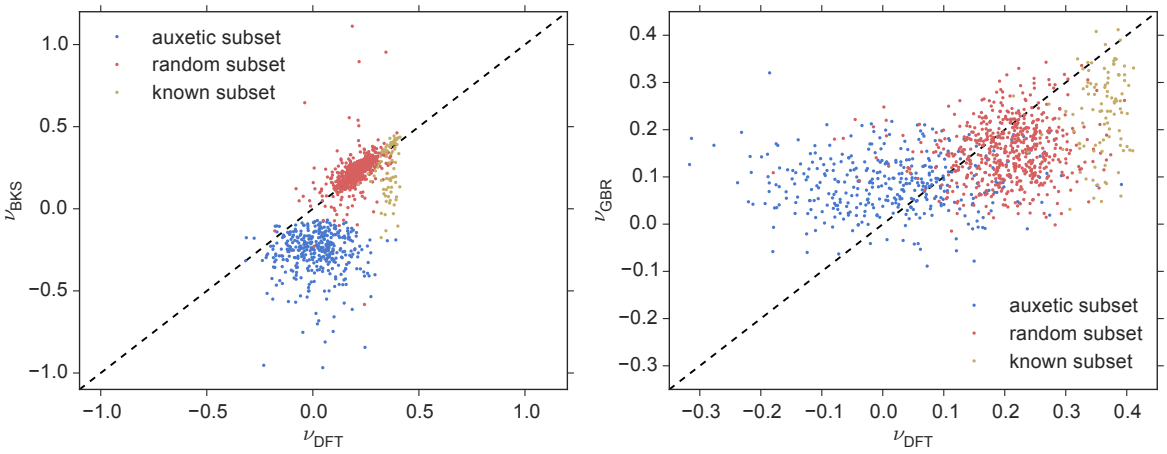

Figure 3.9: Left: Poisson's ratio values given by BKS against values given by DFT calculations. Right: Poisson's ratio values given by GBR predictor against values given by DFT calculations. Structures from the auxetic subset are highlighted in blue, from the random subset in red and from the known subset in green.

the global descriptors, the topology seem to play a big role with very specific ring sizes which have similar importances, namely the proportion of 4, 5, 6 and 8-member rings.

As the extreme values of the Poisson's ratio were particularly badly predicted (Table 3.6) by the force-field, I conducted the exact same process for the maximum and minimum Poisson's ratio, to see if the GBR algorithm was able to create a better predictor. It turns out to be the case. Although the errors are still important, as depicted in Table 3.9, they are lower than the ones obtained with the BKS force-field. In particular, looking at the errors for all the structures, the GBR model provides errors below 0.5, even for the RMSE which emphasizes the extreme cases. Looking at the errors given by the force-field, we see, again, that it cannot be used to determine auxeticity. Although my models are not perfect they give a promising way of having low-cost models to predict auxeticity in zeolites.

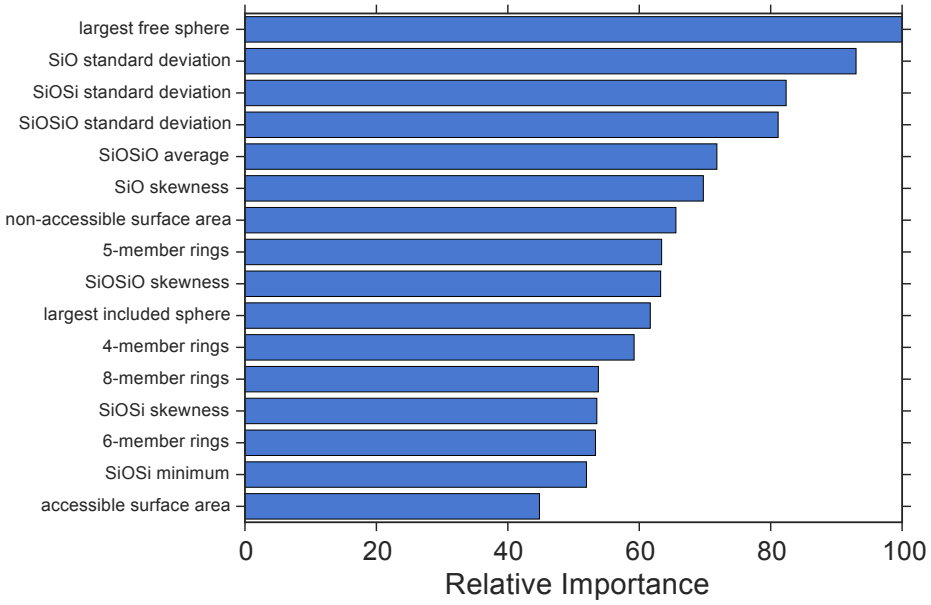

Figure 3.10: Relative importance of the different descriptors actually used for production.

Subset (method)	RMSE($\nu_{\min}$)	MAE($\nu_{\min}$)	RMSE($\nu_{\max}$)	MAE($\nu_{\max}$)
all(GBR)	0.39	0.26	0.46	0.32
all(BKS)	1.4	0.51	9.8	2.1
auxetic(GBR)	0.38	0.25	0.46	0.34
auxetic(BKS)	1. 5	0.66	0.62	0.47
random(GBR)	0.40	0.25	0.48	0.31
random(BKS)	1.4	0.45	13	3.4
known(GBR)	0.43	0.35	0.34	0.27
known(BKS)	0.50	0.35	0.47	0.32

Table 3.9: Root mean square error and mean absolute error for the 3 subsets and their assembly for the prediction of the Poisson's ratio.

Ongoing work: predicting auxeticity classes

Using similar machine learning techniques, I am now trying to build a predictive model that would be able to classify a zeolitic structure in 4 different categories: non-auxetic (0), partially auxetic ($\nu_{\min} < 0$, 1A class), auxetic in average (2B) and completely auxetic (3C). The principle is the same as in regression methods, except that the desired output is not a continuous variable, like the Poisson's ratio or its minimum or maximum, but a discrete category number. One of the difficulty of this approach is to find appropriate categories that would be easier to separate from an algorithmic point of view.

3.4 Conclusion

Using quantum chemistry calculations at the DFT level on two large sets extracted from a structural database of about 600,000 hypothetical zeolitic structures, I was able to show that the BKS force-field can be used to reliably predict structural properties of hypothetical all-silica zeolites. However, concerning mechanical properties, especially the Poisson's ratio, and even more precisely its extreme values, this force-field is unusable for screening potentially auxetic materials.

I have shown that machine learning techniques offer a way to build fast and more reliable predictive models, as I did for the Poisson's ratio and its extreme values. The only issue with these types of methods is their "black-box" behaviour. Nonetheless, most of them are still able to attribute relative importance to the descriptors they are given. Finally, my study focuses on all-silica zeolites, but it could absolutely be applied to all sorts of porous materials, given a large enough reliable database based on experiments or quantum calculations.

Part III

Melting Metal-Organic Frameworks to create new materials

Since the beginning of the MOF field, most studies on these materials have been carried out on crystalline phases. However, as reminded in chapter 1 of Part I, amorphous phases of these materials are more and more considered as objects of interest, especially to go beyond the traditional applications of MOFs relying on their large specific surface areas. In all the following, I refer to amorphization as the process of going from a crystalline to an amorphous structure without altering the chemical composition of the framework.

In this part, I present the work I carried out during my PhD on improving the understanding on the melting and quenching of Metal-Organic Frameworks by ab initio molecular dynamics simulation. The first chapter presents the different amorphization strategies for MOFs and makes a focus on the rather uncommon case of melting. The second chapter deals with the study of the melting of 4 different Zeolitic Imidazolate Frameworks, with a detailed explanation on ZIF-4 confronted to experimental data followed by a comparison with the three other frameworks. The third chapter presents the work I did on understanding the quenching process and the nature of the resulting glass from the liquid phases obtained before. Finally, the fourth chapter presents a more exploratory study on the filling of ZIF-4 with carbon dioxide before melting it, seeing the amorphization as a way to trap the gas inside the amorphized framework and considering the influence of an adsorbate on the melting process.

Chapter 1

Background on the amorphization of Metal-Organic Frameworks

Although there are some recent work on the direct synthesis of amorphous MOFs [49] I will focus here exclusively on the amorphization process that takes a crystalline MOF as a start to get an amorphous structure after alteration. In a first section I present the different ways that have been used to amorphize MOFs before focusing on the very specific case of melting and quenching.

1.1 Amorphization strategies

There are three main ways of amorphizing a MOF structure: submit it to pressures in the MPa to GPa range in a diamond anvil cell (pressure-induced amorphization), [174] induce shear stress by grinding it with a shaker mill in a steel vessel containing steel balls (ball-milling) [175] or by heating it in a furnace to temperatures between 300 and 700 °C (temperature-induced amorphization).

1.1.1 Pressure-induced amorphization

The first report of pressure-induced amorphization of a MOF was published in 2009 by Chapman *et al.* [174]. They report the irreversible amorphization of ZIF-8 at a pressure of 0.34 GPa and the subsequent decrease of sorption capacity. This amorphization phenomenon was later explained by Ortiz *et al.* in 2013 by *shear-mode softening*, meaning that the condition of stability under shear deformation ($C_{44} \geq P$ in a cubic crystal) breaks down at the amorphization pressure. [78]

In 2010, Hu *et al.* reported the irreversible amorphization of the prototypical MOF-5 at

pressure as low as 3.5 MPa. [176] They find that the amorphization is due to the destroying of part of the carboxylate groups of the ligands. They suggest that this kind of low-pressure amorphization could be employed on many other MOFs as so many other structures are also based on carboxylate-type ligands. While Chapman *et al.* showed that ZIF-8 kept a specific surface area corresponding to 84% of the one in the crystal at 0.6 GPa, MOF-5 loses almost the entirety of its internal surface area (Figure 1.1).

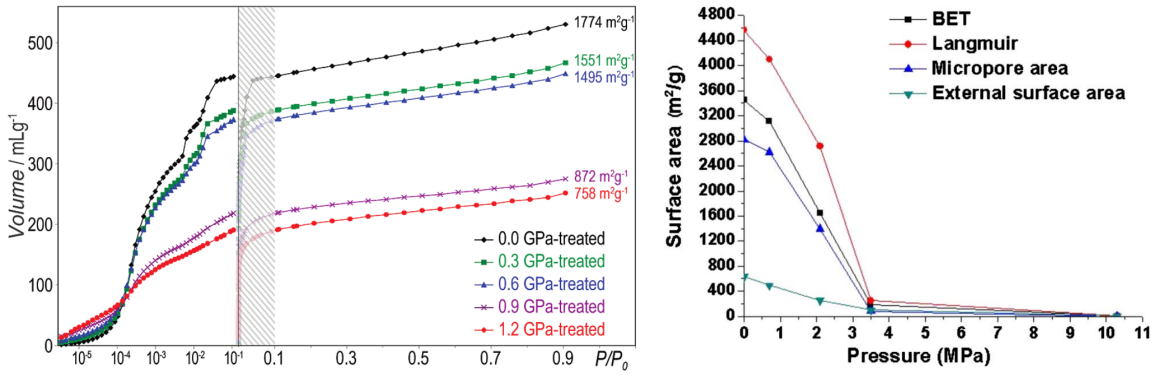

Figure 1.1: Left: N_2 sorption isotherms for pressure-treated ZIF-8 (taken from [174]). Right: Surface areas of MOF-5 subjected to compressing treatments at room temperature with various pressures from 0.0 to 10.3 MPa (taken from [176]).

It is to be noted that some MOFs do not amorphize in the 0 to 10 GPa range. For example in 2013, Gagnon *et al.* published a study on the reversible compression of a MOF called ZAG-4. [177] Thanks to the alkyl chains acting as springs (see Figure 1.2) the compression with a unit cell decrease of 27% was not accompanied by any loss in crystallinity. Furthermore, the cell parameters went back to their initial value after removal of the pressure.

Another interesting example is the one published by Bennett *et al.* in 2011. [178] They report the reversible amorphization of ZIF-4 with or without solvent molecules present in the pores. They observed a crystal-to-crystal transition when the DMF solvent was present inside the pores to a new structure called ZIF-4-I at pressure ranging from 0.12 GPa with a small molecule pressure transimitting fluid (PTF) to 0.32 GPa with a large molecule PTF. The subsequent amorphization was observed between 0.35 GPa for the already evacuated ZIF-4 with a large molecule PTF to 2.61 GPa for ZIF-4 with solvent in the pores and a large molecule PTF. The reversibility was checked by showing that the cell volume had decreased by only 0.07% after removal of the pressure compared to the initial crystalline structure.

In 2011, Chapman *et al.* presented an application to the pressure-induced amorphization of ZIF-8. [179] They used the amorphization process after adsorption of molecular I_2 to kinetically trap iodine inside the amorphous ZIF-8. This could be extremely useful as diiodine is a hazardous byproduct of nuclear energy production.

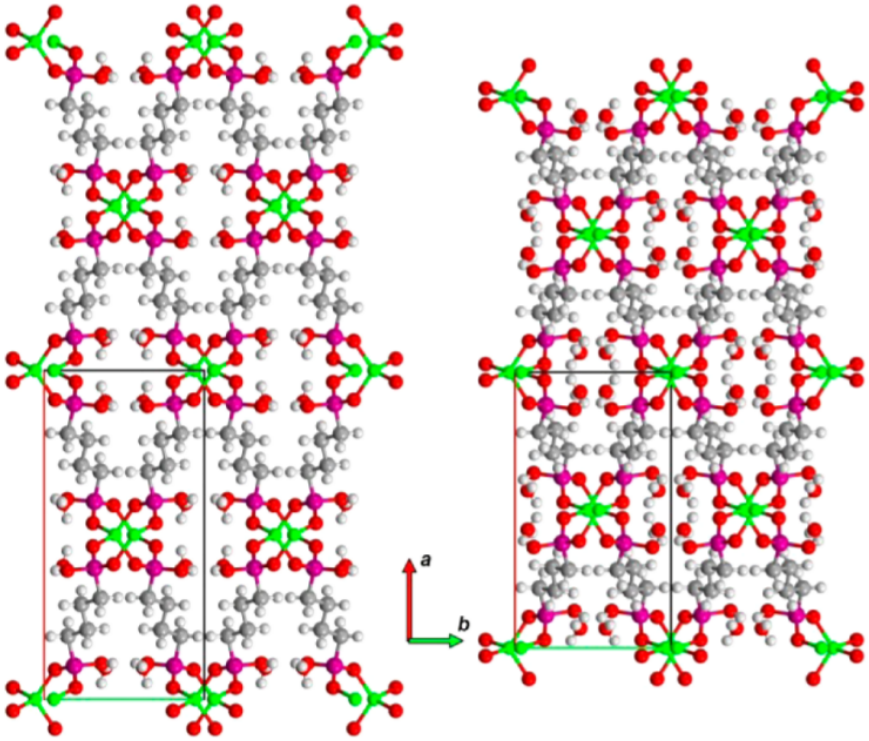

Figure 1.2: ZAG-4 as viewed down the c-axis for the ambient (left) and 7.32 GPa (right) structures.

1.1.2 Amorphization by ball-milling

Ball-milling, which is the process of milling a material inside a shaker mill with steel balls, has gained a lot of traction for the synthesis of MOFs (mechanochemistry), [58, 180] but is still not much used to create amorphous structures from crystalline counterparts. Cao, Bennett *et al.* reported the ball-milling-induced amorphization of ZIF-8 in 2012 creating a structure with a continuous random network topology. [181] In 2013, Bennett *et al.* reported the amorphization by ball-milling of ZIF-4, ZIF-8, ZIF-69 and ZIF-mnIm (see Figure 1.3). [51] They find that amorphization, for ZIF-8 and ZIF-mnIm, elevates by 200°C the temperature up to which molecular I_2 is retained, showing that ball-milled amorphous MOFs could serve as permanent storage media for harmful substances.

The amorphization of ZIF-8 was used by Kertik *et al.* in 2017 to produce a mixed matrix membrane for CO_2/CH_4 separation. [182] They amorphize ZIF-8 surrounded by a polymer in situ and find that it improves the filler-polymer adhesion. The amorphization of Zr-based MOFs, like UiO-66, by ball-milling was also reported by Orellana-Tavra *et al.* for the construction of drug delivery systems. [57, 183]. Bennett *et al.* also reported the ball-milling of MIL-140B and MIL-140C along with a computational study including UiO-66. They conclude that the amorphization of UiO-66 happens by the breakage of some Zr-carboxylate coordination bonds in UiO-66 while the inorganic backbone is also heavily

damaged in MIL-140B and MIL-140C.

Recently, Baxter *et al.* compared the amorphization behaviour under ball-milling of Zeolitic Imidazolate Frameworks, with aluminosilicate zeolites. [184] They find that the ZIFs are much less robust than their inorganic equivalent structure and that the collapse time of ZIFs is dependent on the framework density (number of tetrahedral atom per unit of volume) with higher mechanical instability for more porous structures.

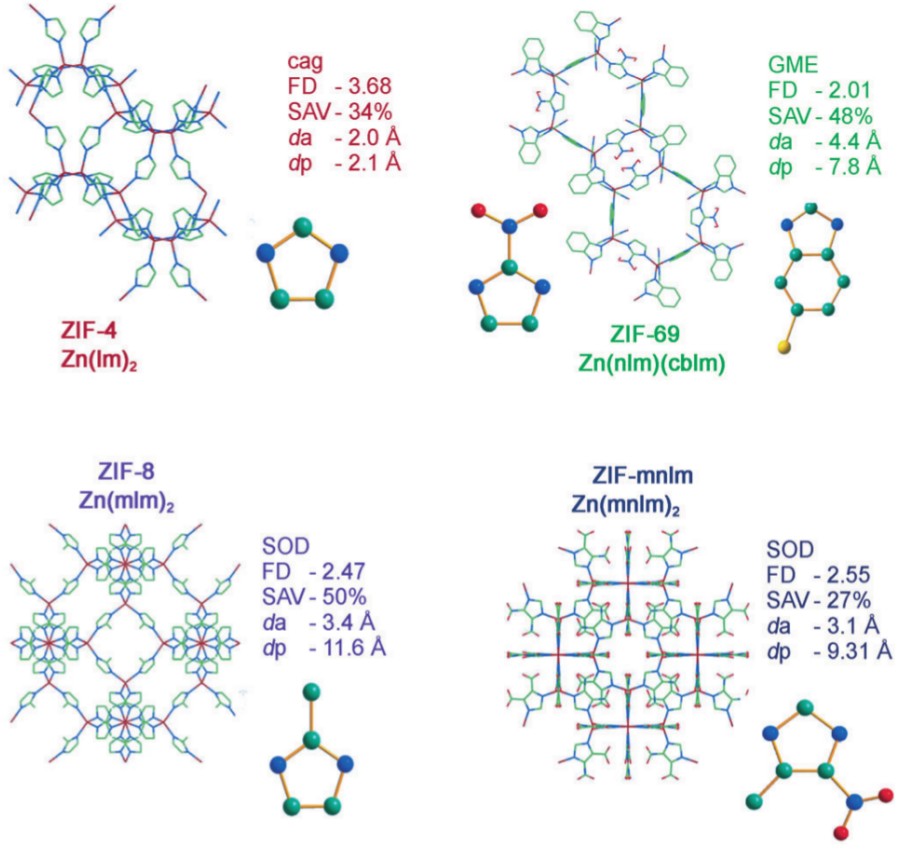

Figure 1.3: Structures of ZIF-4, ZIF-69, ZIF-8 and ZIF-mnIm with associated densities, network topologies and solvent-accessible volumes (SAV). The sodalite topology of ZIF-mnIm is not apparent owing to the number of substituents on the imidazolate ring. The largest aperture and pore diameters (d_a and d_p) are also included. C: green, N: blue, Zn: red; H and Cl are omitted for clarity. FD is framework density in tetrahedral atoms per 1000 nm^3. Figure taken from [51].

1.1.3 Temperature-induced amorphization

It has been known for 15 years that inorganic zeolites can undergo temperature-induced amorphization. [185–187] Zeolitic Imidazolate Frameworks, formed by assembly of tetrahedra based on a metal ion and four imidazolate ligands (possibly substituted), have naturally been studied with regard to their amorphization behaviour under elevation of temperature. In

2010 was published the first report of an amorphous zeolitic imidazolate framework formed by heating Zn-based framework ZIF-4. [188] Then Zn-based ZIF-1, ZIF-3 and Co-based ZIF-4 (Figure 1.4) were shown to amorphize upon temperature increase, while ZIF-8, ZIF-9, ZIF-11, ZIF-14 and ZIF-βqtz would decompose without undergoing a phase transition. [55] The only common point to the latter are their substituted ligands compared to the former which are composed of non-substituted imidazolate cycles. In Ref. 50 Bennett *et al.* detail the differences of behaviour between ZIF-8 and ZIF-4 thanks to in situ calorimetric and X-ray measurements.

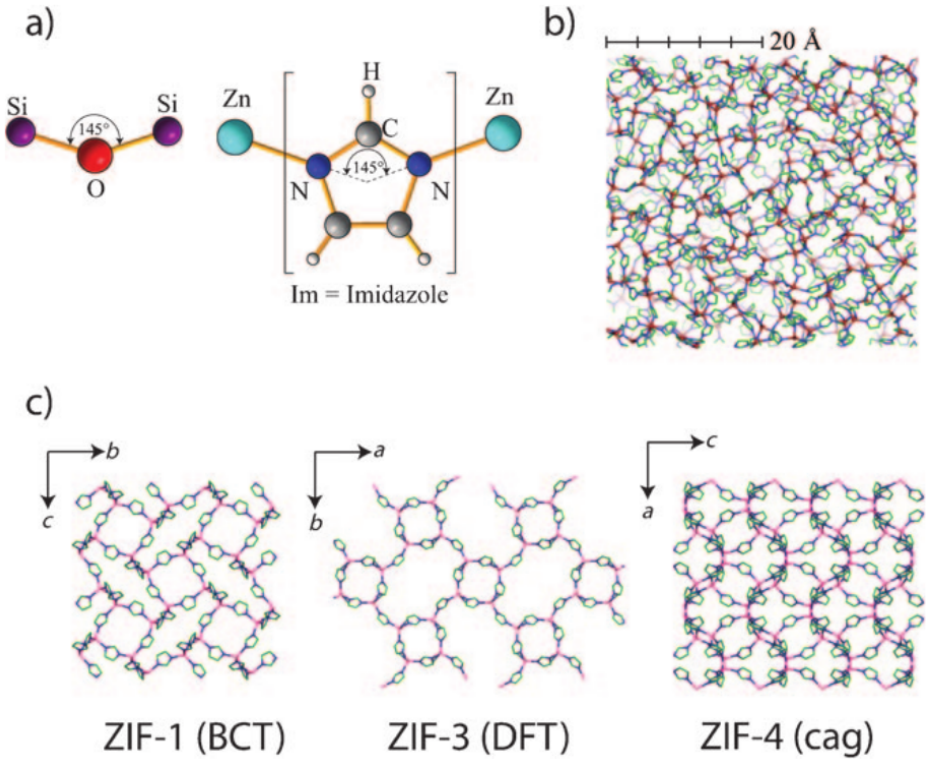

Figure 1.4: a) The similar Si-O-Si and Zn-Im-Zn linkages in zeolites and ZIFs, respectively. b) A snapshot of the continuous random network (CRN) topology of the a-ZIF gained from reverse Monte-Carlo (RMC) modeling. c) Representative views of the expanded unit cells of ZIF-1 (left), ZIF-3 (center), and ZIF-4 (right). Figure taken from [55].

More precisely, ZIF-4, ZIF-1 and ZIF-3, with formula $Zn(im)_2$ (im=$C_3N_2H_3$), amorphize around 300°C. The resulting structure is called a-ZIF and is structurally similar to silica glasses. If heated further, above 400°C, they crystallize in a phase similar to zni, the most stable polymorph of the ZIF family with non-substituted imidazolate ligands. [189] In 2015, Bennett *et al.* published a study showing that, if heated further, ZIF-4 eventually goes to a liquid phase and can be quenched to form a hybrid glass, contrary to ZIF-8 which thermally decompose before any amorphization or melting is observed. This possibility of melting ZIFs and quenching the liquid obtained offer a new way to make functional hybrid glasses. The trapping of lanthanide ions prior to amorphization is also a promising way to synthesize

glasses with optical and luminescent properties. However, this behaviour has still been rarely observed.

In the next section, I propose a brief overview of melting in materials which are cousins of ZIFs, the zeolites and the coordination polymers, and the state of the art in terms of the melting of MOFs themselves.

1.2 The rare case of melting in Metal-Organic Frameworks

1.2.1 Overview of melting in zeolites and coordination polymers

There are only a few studies on the melting of zeolites. [190,191] In [191], Song *et al.* perform a molecular dynamics study of the melting phenomena in zeolite type A. They follow the diffusion of T atoms, oxygen atoms and cations with the increase of temperature as well as the radial distribution functions and the T-O-T angle distribution. This allows them to predict a melting temperature of 2,100 K for this framework. It appears that the geometry of the original zeolite is completely broken down in the liquid phase. In [192], Yamahara *et al.* compare the melting behaviour of silica glass and cristobalite (α and β) and predicted a melting temperature for cristobalite of 4,900 K, much higher than the real one at 1,996 K. [193] Importantly they report a sudden drop in the O-Si-O angle at the melting point, indicating the drastic geometric changes. Although the molecular geometry of zeolites is strongly affected by melting, the immediate inorganic environment found in the subsequent glasses are similar to the ones found in the crystals. [194]

Figure 1.5: Photographs of **1**, the crystal, **1'**, the melt and **1"** the glass. Figure taken from [195].

Hybrid structures with lower dimensionality than MOFs have also been observed to melt. For example, in [195] a one dimensional coordination polymer, consisting of chains of four-

fold coordinated Zn^{2+} centers linked by phosphate ligands, along with charge-compensating protonated imidazole species, shows a reversible solid-to-liquid transition. The liquid phase can then be quenched to obtain a glass-like material (see Figure 1.5). Analyses such as ^{31}P nuclear magnetic resonance spectroscopy, pair distribution function (PDF) and X-ray absorption spectroscopy studies (XAS) on the crystalline and glass solids confirmed the loss of coordination bonds in the liquid state and their presence in the glass phase. The glass was found to have a one-dimensional structure similar to the crystal. However, another example published by Umeyama *et al.* [196] shows a very different behaviour. Indeed this two dimensional coordination polymer exhibits a 2D-to-0D transition upon melting and quenching. It means that the resulting glass has a discrete disorganized structure with extremely little topological relation with its parent coordination polymer.

1.2.2 Liquid Metal-Organic Frameworks: state of the art

Only a few MOFs have been observed to be able to melt upon elevation of temperature without oxidizing or decomposing. In 2016, starting from ZIF-4, Bennett *et al.* examined related frameworks: $Zn(Im_2)$(GIS) with the same composition as ZIF-4, TIF-4, with the same cag topology but a quarter of imidazolate cycles turned into methylbenzimidazolate cycles and ZIF-62 with the same topology but one eighth of the imidazolate cycles replaced by benzimidazolate cycles (see Figure 1.6). [54] $Zn(Im_2)$(GIS) has a very similar melting temperature as ZIF-4 (857 K against 863 K), but does not undergo crystallization to the zni phase before melting. TIF-4 and ZIF-62 are interesting as they allow to see the influence of the chemical change of the ligand on the melting temperature. Both, TIF-4 and ZIF-62, have shown lower melting temperatures than ZIF-4. The authors observed that larger ligands tend to decrease the melting point. The fragility m, defined in Equation 1.1, which characterizes the activation energy of the viscosity at the glass transition T_g is found to decrease with the introduction of larger ligands.

$$m = \left[\frac{d(\log \eta)}{d\left(\frac{T_g}{T}\right)} \right]_{T=T_g} \tag{1.1}$$

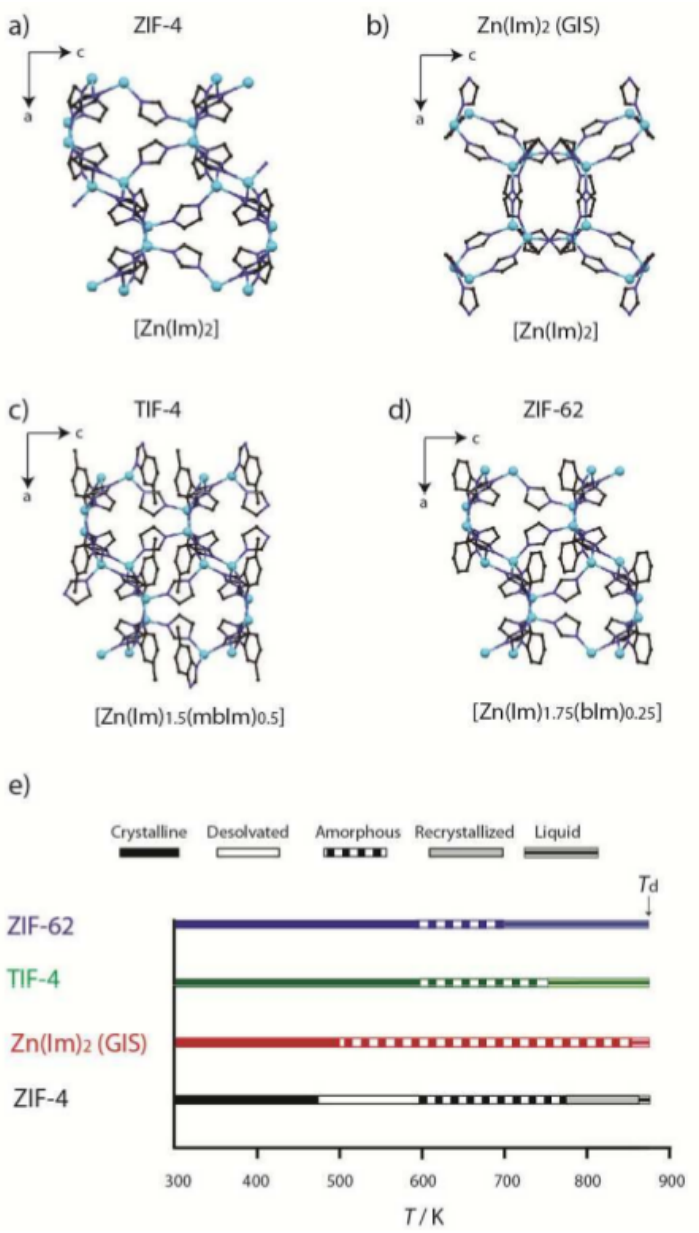

Figure 1.6: Unit cells viewed along the b axis of (a) ZIF-4, (b) $Zn(Im)_2$(GIS), (c) TIF-4 and (d) ZIF-62. N: dark blue, Zn: light blue, C: black, H: omitted. (e) Schematic of the thermal events on heating. Differences in behavior are evident, with $Zn(Im)_2$(GIS), TIF-4 and ZIF-62 undergoing amorphization upon desolvation, and a large temperature range between melting and framework decomposition for ZIF-62. Figure taken from [54].

Chapter 2

Melting different Zeolitic Imidazolate Frameworks

2.1 Systems and methods

2.1.1 The Zeolitic Imidazolate Frameworks studied

During my PhD, I focused on the melting behaviour of four zeolitic imidazolate frameworks: ZIF-8, ZIF-4, ZIF-zni and SALEM-2. Hereafter, I present the characteristics of each of these frameworks.

ZIF-8 and SALEM-2: very open and porous frameworks

ZIF-8 is composed of $Zn(mIm)_2$ (mIm = methyldimidazolate = $C_4N_2H_5$) tetrahedra linked by Zn–N coordination bonds and has the same topology as the zeolite sodalite (SOD). [97] This structure crystallizes in the space group $I-43m$. The unit cell I considered for this framework is its cubic primitive unit cell, which contains 276 atoms, with cell parameters $a = b = c = 16.993\,\text{Å}$, and $\alpha = \beta = \gamma = 90°$. The left panel of Figure 2.1 presents a 2x2x2 supercell of this unit cell. In my simulations, in order to be computationally efficient, I replaced the hydrogen atoms of all the structures by deuterium atoms (basically changing the mass attributed to H atoms to be around 2 g/mol). This allowed me to take a time step of 0.5 fs without risking a bad integration of hydrogen vibrational motions. The resulting density of ZIF-8 after deuteration is $0.965\,\text{g/cm}^3$.

SALEM-2 has the same topology as ZIF-8, but is composed of $Zn(Im)_2$ (Im = imidazolate= $C_3N_2H_3$). Its cubic unit cell (space group $I-43m$) contains 204 atoms and its cell length ($a = b = c$) is 17.014 Å. The right panel of Figure 2.1 presents a 2x2x2 supercell of this

unit cell. This framework, deuterated, has a density of 0.831 g/cm^3. This system is an idealized version of its real equivalent, meaning that in reality only 85% of the methylimidazolate cycles are exchanged for imidazolate cycles. [43]

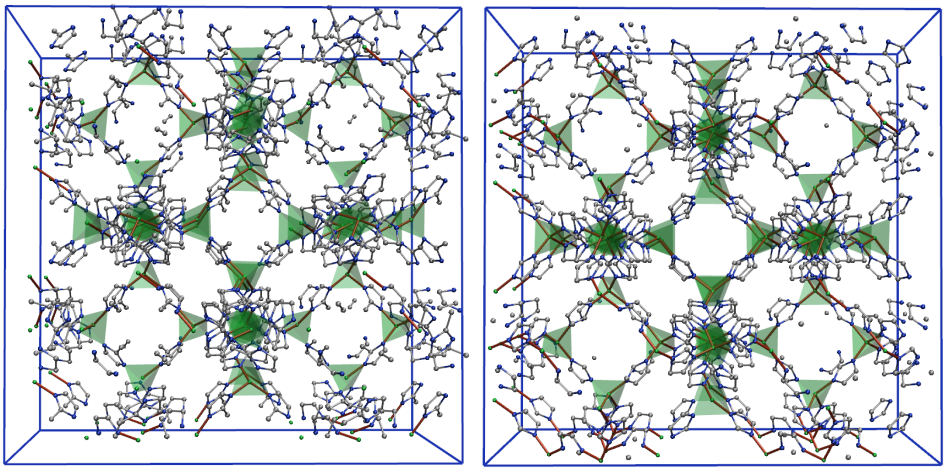

Figure 2.1: Left: 2x2x2 supercell of the unit cell studied for ZIF-8. Right: 2x2x2 supercell of the unit cell studied for SALEM-2. Zn: green, N: blue, C: gray, H: omitted. Coordination bonds between zinc atoms and nitrogen atoms are shown in red and the coordination tetrahedra are shown in green around each zinc atom.

ZIF-4

ZIF-4 is chemically very similar to ZIF-8, except for $Zn(Im)_2$ tetrahedra instead of $Zn(mIm)_2$. It is porous, less than ZIF-8 though (no BET surface for instance), and shares its cag network topology with the mineral variscite ($CaGa_2O_4$). [197] The orthorhombic unit cell (space group *Pbca*) contains 272 atoms with cell parameters $a = 15.423$ Å, $b = 15.404$ Å and $c = 18.438$ Å and $\alpha = \beta = \gamma = 90°$. The density of this deuterated framework is 1.247 g/cm^3. Figure 2.2 shows a 2x2x2 supercell of the considered unit cell.

ZIF-zni

ZIF-zni is chemically identical to ZIF-4. It is a dense non-porous framework and shares its zni network topology with the aluminosilicate banalsite ($BaSi_2Al_2O_8$). [189] The unit cell I considered for this framework is its primitive unit cell (space group $P1$) containing 272 atoms with cell parameters $a = 17.570$ Å, $b = c = 17.613$ Å and $\alpha = 138.433°$, $\beta = 97.256°$and $\gamma = 97.257°$. The density of this deuterated framework is 1.616 g/cm^3. Figure 2.3 shows a 2x2x2 supercell of the unit cell simulated here.

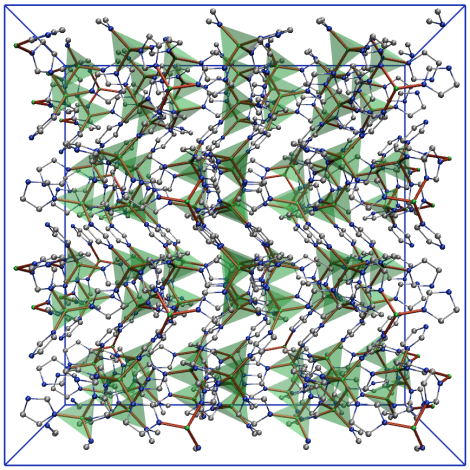

Figure 2.2: 2x2x2 supercell of the unit cell studied for ZIF-4. Zn: green, N: blue, C: gray, H: omitted. Coordination bonds between zinc atoms and nitrogen atoms are shown in red and the coordination tetrahedra are shown in green around each zinc atom.

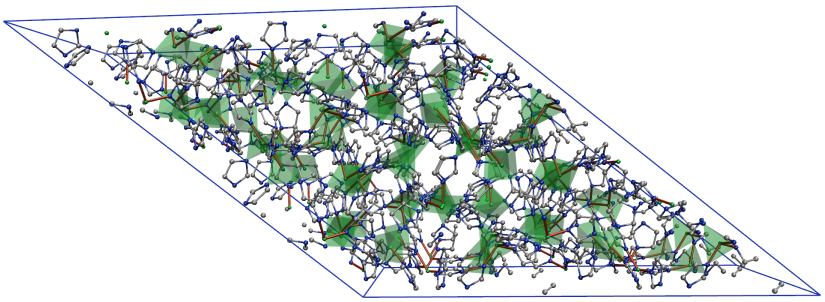

Figure 2.3: 2x2x2 supercell of the unit cell studied for ZIF-zni. Zn: green, N: blue, C: gray, H: omitted. Coordination bonds between zinc atoms and nitrogen atoms are shown in red and the coordination tetrahedra are shown in green around each zinc atom.

2.1.2 Ab initio molecular dynamics at different temperatures

To study the melting of these different frameworks, I used constant volume ab initio molecular dynamics simulations as explained in subsection 2.1.3 of Part I. Here I give the details about these specific simulations.

The unit cell parameters presented above were the result of a full geometry optimization (atomic and unit cell parameters) of the different crystals at 0 K. In order to test the validity of the constant-volume approach (dictated by reasons of computation cost), I also ran shorter constant-pressure (N, P, T) simulations at 300 K and 1,500 K on the ZIF-4 framework. These simulations both yielded an average density of 1.22 g.cm^{-3} (with instantaneous fluctuations of $\pm$0.09 g.cm^{-3}), showing that the variations of density upon heating and melting are minimal, at least in the time scales reachable by these types of methods (i.e. up to $\sim$200 ps).

The behaviour of zeolitic imidazolate frameworks as a function of temperature was studied by means of density functional theory (DFT)-based molecular dynamics (MD) simulations, using the Quickstep module [94] of the CP2K software package. [198] I used the hybrid Gaussian and plane wave method GPW as implemented in CP2K. As written above, the simulations were performed in the constant-volume (N, V, T) ensemble with fixed size and shape of the unit cell. A timestep of 0.5 fs was used in the MD runs and the temperature was controlled by canonical sampling through velocity rescaling. [199] MD simulations consisted of an equilibration period of 5 ps and a production period between 60 ps and 220 ps, depending on the temperature, to study the dynamics of the liquid. For ZIF-4, I ran simulations at 10 different temperatures: 300 K, 600 K, 800 K, 900 K, 1,000 K, 1,200 K, 1,500 K, 1,750 K, 2,000 K and 2,250 K. For ZIF-8 and ZIF-zni I screened over 9 temperatures: 300 K, 600 K, 800 K, 1,000 K, 1,200 K, 1,500 K, 1,750 K, 2,000 K and 2,250 K. Finally, I studied the melting of SALEM-2 essentially to study its quenching so I ran "only" 7 simulations at 300 K, 600 K, 1,000 K, 1,200 K, 1,500 K, 1,750 K and 2,000 K. As it is a "fictive" system, I will compare it separately from the other frameworks.

The exchange-correlation energy was evaluated in the PBE approximation, [200] and the dispersion interactions were treated at the DFT-D3 level. [201] The Quickstep module uses a multi-grid system to map the basis functions onto. I kept the default number of 4 different grids but chose a relatively high plane-wave cutoff for the electronic density to be 600 Ry, as already used in Ref. 202, and a relative cutoff (keyword REL_CUTOFF in CP2K) of 40 Ry for high accuracy. Valence electrons were described by double-zeta valence polarized basis sets and norm-conserving Goedecker–Teter–Hutter [203] pseudopotentials all adapted for PBE (DZVP-GTH-PBE) for H, C and N or optimized for solids (DZVP-MOLOPT-SR-GTH) in the case of Zn.

In the next section, I detail the study of the melting of ZIF-4, which has been compared to experimental data. I give insights on the thermodynamics of the transition, the microscopic mechanism behind the melting and the properties of the liquid phase. All the experimental data I present hereafter are due to the work realized by Kevin A. Beyer, Karena W. Chapman, David A. Keen and Thomas D. Bennett. [60]

2.2 Understanding the melting of ZIF-4

2.2.1 Structural and thermodynamical properties upon heating and melting

We first studied the evolution in structure of ZIF-4, which is composed of $Zn(Im)_4$ tetrahedra linked by Zn–N coordinative bonds assembled in a cag topology as reminded in Figure 2.4a and b. It forms a three dimensional, crystalline network containing a maximum cavity diameter of 4.9 Å (Figure 2.4c). Its experimental melting point has been determined to be *ca.* 865 K. [50]

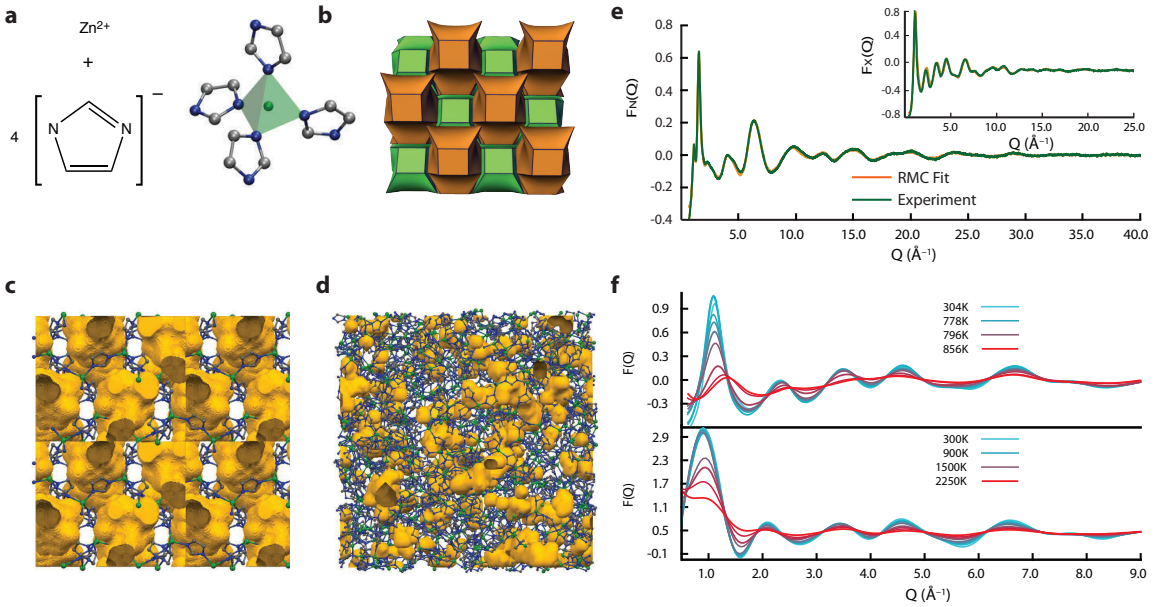

Figure 2.4: Structure of the ZIF-4 crystal, glass, and structural evolution upon heating.**a**) The construction from metal ion and linker of $Zn(Im)_4$ tetrahedra, the basic building unit of ZIF-4 (Im = imidazolate; Zn: green, N: blue, C: grey). (**b**) Representation of the cag topology adopted by ZIF-4, where each polyhedra corner corresponds to one $Zn(Im)_4$ tetrahedron. (**c**) Crystalline structure of ZIF-4, with free volume represented in orange. (**d**) Atomic configuration of the melt quenched glass, gained from modelling synchrotron and neutron total scattering data (Reverse Monte-Carlo modeling by David A. Keen). (**e**) Experimental neutron structure factor $F(Q)$ data and the fit from the configuration shown in (**d**). Inset: X-ray data and fit. (**f**) Experimental glass (top) and computational ZIF-4 (bottom) X-ray structure factors upon heating. Reproduced from [60].

Experimentally, synchrotron X-ray diffraction data was used to evaluate structural changes in the glass formed by melt-quenching ZIF-4 upon heating. Figure 2.4f shows the structure factor $F(Q)$ recorded from the glass at temperatures of 304, 778, 796 and 856 K on heating. The experimental structure factor for the glass at room temperature is largely similar to that previously reported, [50] with no visible Bragg peaks. The corresponding PDF (left panel of Figure 2.5) contains the expected peaks at *ca.* 1.3 Å, 2 Å, 3 Å, 4 Å, and 6 Å, which correspond to C–C/C–N, Zn–N, Zn–C, Zn–N and Zn–Zn pair correlations respectively.

Upon heating from 304 to 778 K, both the intensity and position of the first sharp diffraction peak (FSDP), centered at 1.1 $Å^{-1}$, remained approximately constant, as was the case with other visible features in the $F(Q)$. However, further heating to 856 K resulted in a more pronounced intensity reduction and shift in the position of the FSDP to 1.3 $Å^{-1}$, along with a near-total disappearance of any features at higher Q values. This is in stark contrast to the case of liquid silica, where negligible changes in the FSDP upon melting are indicative of significant intermediate range order. [204] The changes in the $F(Q)$ result in a significantly

decreased Zn–Zn correlation peak in the corresponding high temperature PDFs, centered on 6 Å (left panel of Figure 2.5).

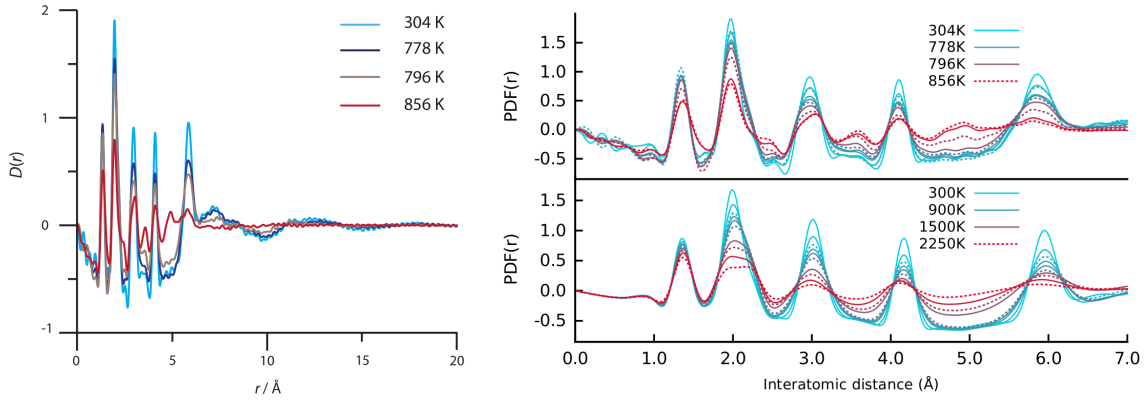

Figure 2.5: Left: Experimental X-ray total pair distribution functions at different temperatures. Right: Low-r region of the X-ray total pair distribution functions at different temperatures in experiments (top) and ab initio simulations (bottom). Figures extracted from the supplementary information of [60].

To probe the evolution of the ZIF structure upon heating and liquid formation from a microsopic point of view, I performed first principles molecular dynamics simulation (FPMD) by running constant-temperature MD simulations at temperatures between 300 K and 2,250 K (specified in subsection 2.1.2). It is worth noting here that although the higher temperatures would not be physically relevant for the experimental system, they are made necessary by the relatively short times explored due to the high computational cost of FPMD, in order to gather statistics on relatively rare events and high thermodynamic barriers. Because of the computational cost of FPMD, these simulations cannot be performed directly on the glass model — the unit cell of which is prohibitively large. Instead, I used the aforedescribed ZIF-4 crystalline phase as starting point, with the change in structure factor upon heating in good agreement with the trends observed experimentally (Figure 2.4f). Similarly close agreement is also witnessed in the variable temperature total pair distribution functions (see the right panel of Figure 2.5).

Moreover, in addition to the total PDFs, I calculated from the MD trajectories the PDFs for specific atom-atom correlations, which provide greater understanding of the salient real-space structural movements. I present in Figure 2.6 the partial radial distribution functions $g_{ij}(r)$ for Zn–N, Zn–Im (where Im is the center of mass of the imidazolate group), and Zn–Zn pairs. In addition to the overall thermal broadening of the peaks, there is a clear loss of long-range order at high temperature. At intermediate temperatures (around 1,000 K), the system has liquid-like disorder, with $g_{ij}(r)$ that do not go to zero after the first peak, though it retains some order at distances larger than 10 Å.

To characterize further this state, I show in Figure 2.6d the generalized Lindemann ratio Δ, [205] computed from the width of the first peak in the Zn–N and Zn–Zn partial radial distribution functions. Δ is a measure of the fluctuation of atomic positions and interparticular

distances defined as:

$$\Delta = \frac{\mathrm{FWHM}}{d_0} \ , \tag{2.1}$$

where FWHM is the full width at half maximum of the first partial radial distribution function peak (estimated by a Gaussian fit) and d_0 corresponds to the mean interatomic distance (calculated as the maximum of the first peak), i.e. $d_0 = 5.95\,\text{Å}$ for Zn–Zn and $d_0 = 2.0\,\text{Å}$ for Zn–N.

The usual criterion used to determine melting from the Lindemann ratio is between 10 and 15%, which indicates in this case a melting temperature between 1,000 and 1,500 K — and I note that the Zn–Zn ratio shows a clear disruption in slope at 1,200 K.

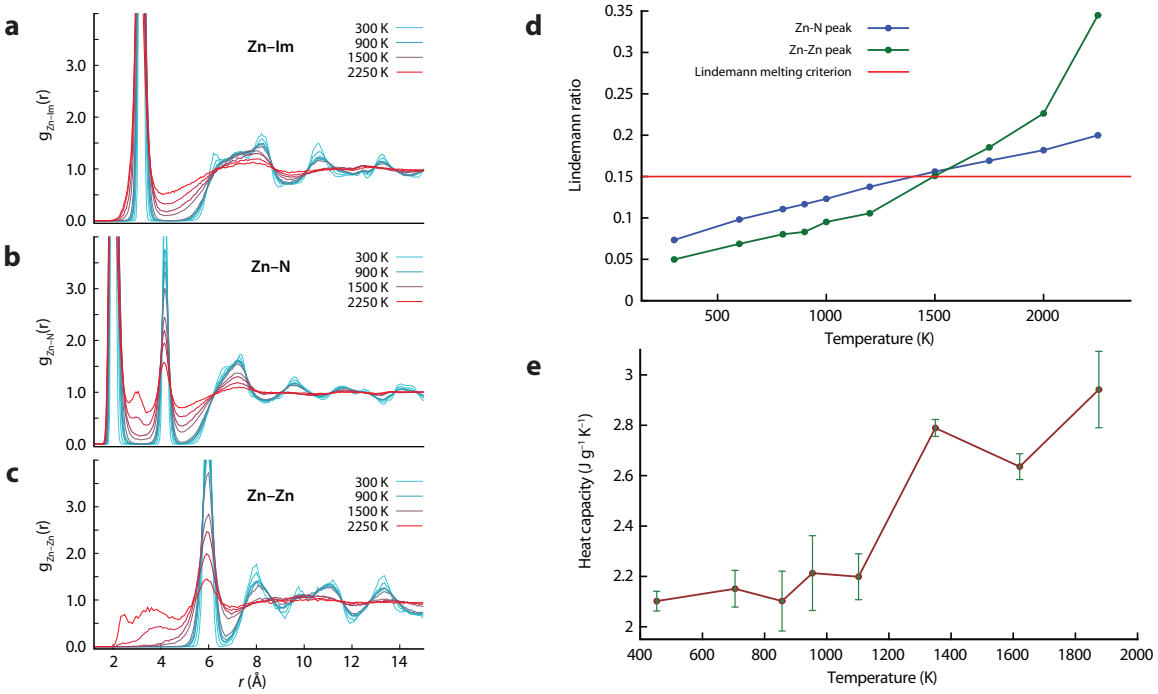

Figure 2.6: Computational data from ZIF-4 melting: structure and thermodynamics.(**a**–**c**) Evolution of the partial radial distribution function $g_{ij}(r)$ for (**a**) Zn–Im distances (where Im is the center of mass of the imidazolate group), (**b**) Zn–N distances, (**c**) Zn–Zn distances, at temperatures going from 300 K (light blue) to 2,250 K (red). (**d**) Generalized Lindemann ratio Δ, quantifying the liquid nature of the system, as a function of temperature, calculated for Zn–Zn (green) and Zn–N (blue) interatomic distances. The red horizontal line represents the "critical ratio" indicated in the literature at 10% or 15% (the value chosen here). (**e**) Evolution of the heat capacity with temperature, with uncertainties calculated by block averaging over 5 different blocks of the trajectories.

Approaching the phenomenon from a thermodynamic standpoint, I plot in Figure 2.6e the evolution of heat capacity C_V as a function of temperature. There is a clear jump in

the heat capacity, indicative of a solid–liquid phase transition, from the value of the crystal phase ($C_V \approx 2.2$ J.g^{-1}.K^{-1}) to a higher value for the ZIF liquid ($C_V \approx 2.8$ J.g^{-1}.K^{-1}). Integration yields an estimate for the enthalpy of fusion of the ZIF of $\Delta H_{\text{fus}} = 173$ J.g^{-1}, which is in line with values for materials such as quartz ($\Delta H_{\text{fus}} = 146$ J.g^{-1}) and cristobalite ($\Delta H_{\text{fus}} = 237$ J.g^{-1}). [206]

The computation of the heat capacity is made by finite differences as follows:

$$C_v\left(\frac{T_1+T_2}{2}\right) = \frac{U(T_2)-U(T_1)}{T_2-T_1} \ , \tag{2.2}$$

where T_1 and T_2 are two successive temperatures in our series of simulations and $U(T)$, the internal energy, is the average of the total energy of the system over the specific trajectory. Uncertainties were calculated by block averaging over 5 different blocks of the trajectories. Furthermore, the estimate of the enthalpy of fusion (ΔH_{fus}) is computed as:

$$\Delta U = C_V(T_1) \times (T_2 - T_1) + \Delta H_{\text{fus}} \ , \tag{2.3}$$

which consists in writing the energy difference for heating the system from $T_1 = 1,000$ K to $T_2 = 1,500$ K, as the system is considered solid at 1,000 K and liquid at 1,500 K.

Since the melting of this supramolecular network is dependent upon partial dissociation and reassociation of Zn–N coordination bonds, I used this distance as a reaction coordinate. From the Zn–N partial radial distribution function, $g_{\text{Zn–N}}(r)$, I calculated the potential of mean force (PMF) between the two atoms at all temperatures, through the relation $F(r) = -k_{\text{B}}T \ln g(r)$. From the resultant free energy profiles (left panel of Figure 2.7), I was then able to extract the temperature dependence of the activation free energy ($\Delta F^{\ddagger}$) needed to break the Zn–N bond. It can be seen in the right panel of Figure 2.7 that $\Delta F^{\ddagger}$ follows a van 't Hoff law, $\Delta F^{\ddagger}(T) = \Delta H^{\ddagger} - T\Delta S^{\ddagger}$, with $\Delta H^{\ddagger} \approx 127$ kJ.mol^{-1} and $\Delta S^{\ddagger} \approx 37$ J.mol^{-1}.K^{-1} in this temperature range.

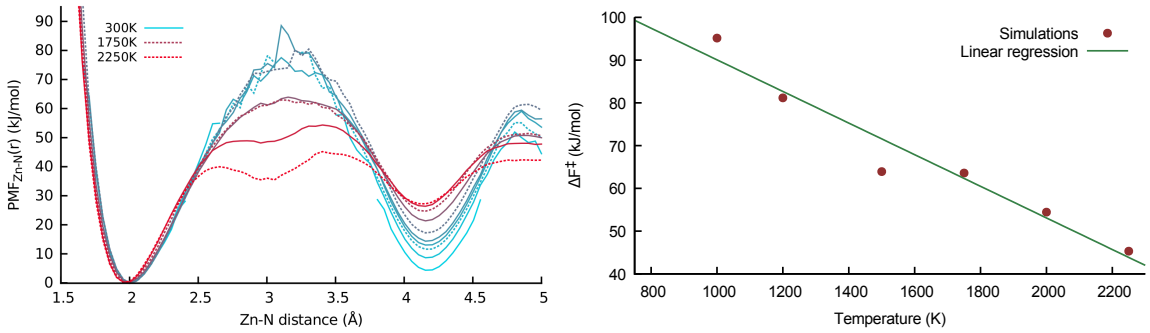

Figure 2.7: Left: Potentials of mean force along the Zn–N coordinate at different temperatures, interpreted as free energy profiles. Right: van 't Hoff plot of the free energy extracted from the potentials of mean force.

The main contribution to the free energy barrier is thus energetic in nature, accompanied by a minor entropic stabilisation. Moreover, the free energy barrier is still relatively high at the melting temperature, with $\Delta F^{\ddagger}(T = 1,000\,\text{K}) = 90$ kJ.mol^{-1} $= 10.8\,k_{\text{B}}T$.

	$\Delta U^{\ddagger}$(kJ.mol^{-1})	$\Delta S^{\ddagger}$(J.mol^{-1}.K^{-1})	$\Delta F^{\ddagger}(865K)$(kJ.mol^{-1})
Zn–N	127	37	95 ($\simeq 13kT$)
Zn–Im	128	40	93 ($\simeq 13kT$)

Table 2.1: Thermodynamic properties values. The first column shows the activation enthalpy associated with a bond cleavage, the second column shows the activation entropy and the third column shows the extrapolated activation free energy at the experimental melting temperature of 865 K.

Hence, as in conventional solids, melting occurs as a rare barrier-crossing event. [207] Finally, comparison of the potential of mean force for the Zn–Im coordinate with the PMF for Zn–N shows that breaking of the Zn–N bond is indeed an entirely suitable choice of reaction coordination for this activated process: as shown in Table 2.1, the thermodynamic parameters are almost identical in both cases.

2.2.2 Microscopic mechanism

Turning to a molecular level visualization of the melting process, I depict in Figure 2.8a and b the distribution of Zn cation coordination numbers as a function of temperature.

The ideal four-fold coordination is maintained at low temperatures up to 1,200 K, where more than 94% of the Zn ions are coordinated by four imidazolate groups. In this regime, the under-coordination of Zn^{2+} can be seen as a defect in the solid, and its concentration is found (as expected, see top panel of Figure 2.9) to be proportional to $n_{\mathrm{d}} \propto \exp(-\varepsilon/k_{\mathrm{B}}T)$, where $\varepsilon \approx 56$ kJ.mol^{-1} is the energy required for defect formation. These "undercoordinated" zinc ions can act as nucleation sites for melting. Going to higher temperature, the proportion of undercoordinated Zn^{2+} increases dramatically, e.g. at 1,500 K with 59% 4-fold coordinated, 39% in 3-fold coordination, and 2% in 2-fold coordination. In contrast, I note that pentacoordination is almost nonexistent in our simulations.

Focusing on typical individual linker exchange events of zinc cations provides the mechanistic picture shown in Figure 2.8d (snapshots from a FPMD simulation at 1,500 K); the melting process takes place over a few picoseconds through a sequence of well-defined steps. From an initial four-fold coordinated zinc, one imidazolate linker moves away and is then replaced by a neighboring Im group with a dangling nitrogen lone pair. Inspired by Laage *et al.*'s statistical treatment of the molecular mechanism of reorientation in liquid water, [208, 209] I averaged over all events during a molecular dynamics trajectory to plot the average distance of the outgoing and incoming N atoms during an exchange — taking the reference time $t = 0$ when both nitrogren atoms are at equal distance from the zinc ion. This plot (Figure 2.8c) shows that the event is concerted and that the exchange itself is rather fast, lasting less than 2 ps. This is very similar to what is seen for a switch between hydrogen bond partners in

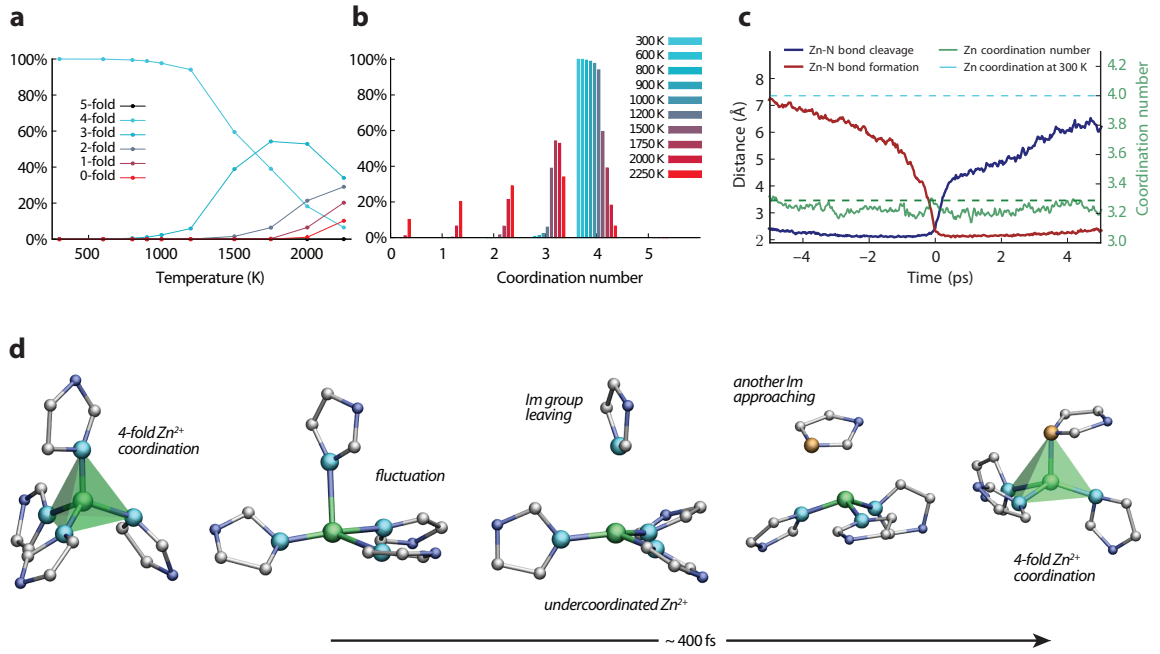

Figure 2.8: (**a**) Distribution of zinc coordination numbers as a function of temperature, from 0-fold coordinated (red) to 4-fold (light blue) (5-fold, in black, is close to zero). (**b**) Temperature evolution for each degree of coordination of zinc cations from 300 K (light blue) to 2,250 K (red). (**c**) Behaviour during an exchange of a nitrogen atom by another nitrogen atom, in the first coordination sphere of a zinc cation, averaged over all such events (all exchanges on all zinc cations). The distances between the incoming and outgoing nitrogen atoms and the zinc are plotted in red and blue respectively. In green, the average coordination number of the zinc cation involved in the exchange is shown. The flat dashed lines are the average coordination number over the whole simulation at 300 K (light blue) and 2,000 K (green). (**d**) Visualization of a representative imidazolate exchange event. Zn: green, N (initially coordinated): light blue, N: blue, N (coordinated after exchange): orange, C: grey.

liquid water: both are strongly associated liquids forming a dynamic network with preferred tetrahedral association.

To have a more complete view of the microscopic mechanism of ZIF melting, I calculated the frequencies at which the Zn–N bonds or Zn–Im linkages break. Plotting the log of these frequencies against inverse temperature (see bottom left and right panels of Figure 2.9) demonstrates the Arrhenian behaviour of the system, reinforcing the idea that melting is driven by rare events disturbing the network. I also note that the two activation energies for Zn–N and Zn–Im are very close. Extrapolating to the melting temperature — where in the limited time window of our simulations I cannot directly observe enough of these rare events to gather good statistics — shows that the timescale at which bond breaking occurs becomes sub-nanosecond near the melting temperature.

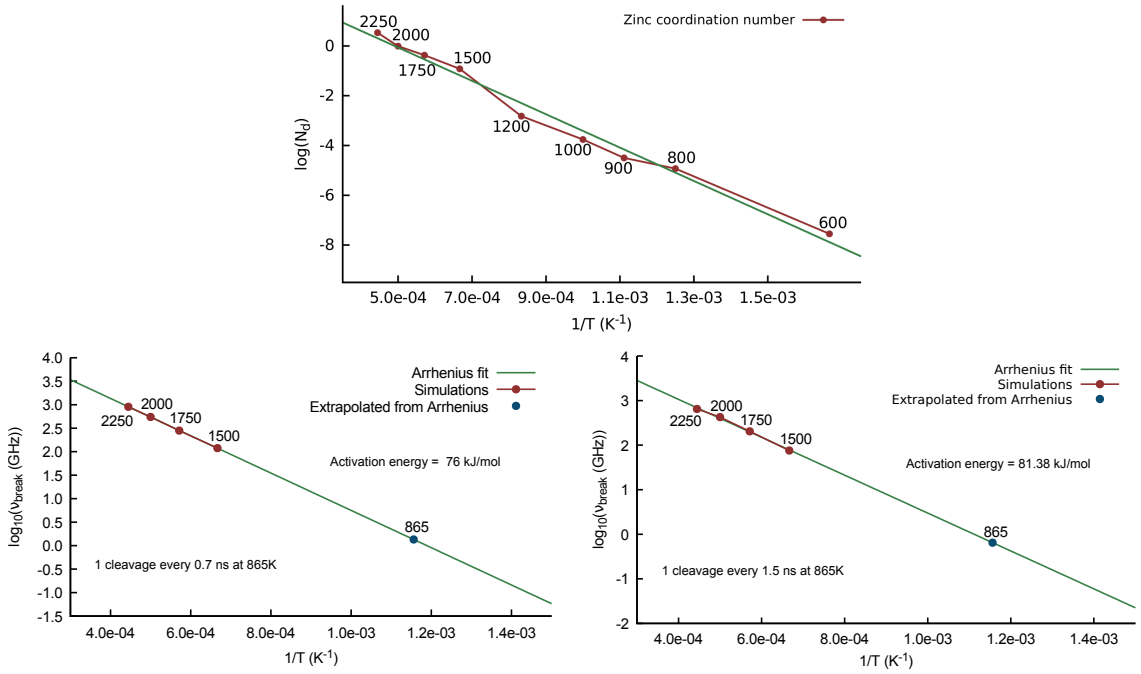

Figure 2.9: Top: van 't Hoff plot of the number of defects ($n_{\mathrm{d}} = 4 - C_{\mathrm{Zn}}$ where C_{Zn} is the zinc coordination number): the formation of defects follows an Arrhenius law associated with an activation energy of 56 kJ/mol. Bottom left: Frequency of Zn–N bond breaking. Bottom right: Frequency of Zn–Im bond breaking.

As Table 2.2 shows, for any given zinc cation, I expect one coordinative bond breaking every 143 ms at 300 K, every 58 ns at 600 K, and every 0.7 ns at 865 K. Moreover, looking at these events in detail, I see that at low temperature, the majority of bond-breaking events leads to a simple flip of the imidazolate linker, and do not result in exchange between two linkers (Table 2.3). As temperature increases, this "local" motion of lower energy becomes dominated by events which lead to linker exchange, and thus allows the ZIF to melt. Finally, I see that the duration of the coordinative bond breaking and reformation is independent of temperature, and is only guided by the timescale for approach of another imidazolate partner and local dynamics.

2.2.3 Properties of the resulting liquid

To characterize the dynamics of the ZIF in the liquid phase, I calculated from the translational diffusion of both zinc cations and imidazolate anions. The plots of mean square displacement over time, shown in Figure 2.10a and b, clearly show diffusive behaviour at temperatures above 1,200 K, i.e. in the liquid phase. The translational diffusion of zinc and imidazolate are clearly linked strongly, as the coefficients are very similar (see Table 2.4) and both follow an Arrhenius law (see left and right panels of Figure 2.11): for example, at 1,500 K we have $D_{\mathrm{Im}} = 7.7\ 10^{-10}\ \mathrm{m}^2.\mathrm{s}^{-1}$ and $D_{\mathrm{Zn}} = 6.5\ 10^{-10}\ \mathrm{m}^2.\mathrm{s}^{-1}$. This similarity in anion and cation

T (K)	1 Zn–N cleavage/Zn every	1 Zn–Im cleavage/Zn every	%(Im flip) in Zn–N cleavages
300	143 ms	2.8 s	95%
600	58 ns	228 ns	75%
865	0.7 ns	1.5 ns	68%

Table 2.2: Characteristics of coordinative bond breaking. Columns 2 and 3 give average times for one Zn–N (respectively Zn–Im) cleavage per Zn atom.

T (K)	$\Delta t^{\text{cleav}}_{\text{Zn-N}}$(fs)	$\Delta t^{\text{form}}_{\text{Zn-N}}$(fs)	$\Delta t^{\text{cleav}}_{\text{Zn-Im}}$(fs)	$\Delta t^{\text{form}}_{\text{Zn-Im}}$(fs)	%(Im flip) in Zn–N cleavages
1,500	336	330	866	894	33%
1,750	303	322	732	768	27%
2,000	393	374	713	720	22%
2,250	418	426	669	675	17%

Table 2.3: Coordinative bond breaking dynamics. The duration of the actual cleavages and reforming of bonds are rather constant and independent of temperature. I also show the observed percentage of Zn–N bond cleavages that correspond to a flip of the Im linker (rather than Zn–Im bond cleavage).

diffusion is a rather common feature for ionic liquids. From these diffusion coefficients, we estimate the viscosity using the Stokes-Einstein relation ($\eta = kT/6\pi rD$): with a Zn^{2+} ionic radius of 88 pm, the viscosity at 1,500 K is 19 mPa.s, and can be extrapolated by the Arrhenius law to 2915 mPa.s at 865 K, the experimental melting temperature.

Temperature (K)	D_{Im} ($\text{m}^2.\text{s}^{-1}$)	D_{Zn} ($\text{m}^2.\text{s}^{-1}$)
1,500	$7.7\ 10^{-10}$	$6.5\ 10^{-10}$
1,750	$3.0\ 10^{-9}$	$2.1\ 10^{-9}$
2,000	$6.5\ 10^{-9}$	$5.3\ 10^{-9}$
2,250	$1.2\ 10^{-8}$	$1.1\ 10^{-8}$

Table 2.4: Diffusion coefficients extracted from the MD simulations.

In addition to the characterization of translation diffusive behaviour, I found that the translational diffusion coefficients over temperature follow an Arrhenius law (see Figure 2.11), compatible with a jump-like diffusion of "partner exchange" events. [209] The activation energies for Zn and Im respectively are found to be 105 kJ.mol^{-1} and 102 kJ.mol^{-1} respectively. The rotational diffusion of imidazolate cycles can also be measured, where I chose to follow rotation around the N–N axis and the associated angle θ. Orientational diffusion happens at lower temperatures than translational diffusion, starting around 800 K, and can be associated with an activation energy three times lower ($\approx$ 40 kJ.mol^{-1}). At intermediate temperatures,

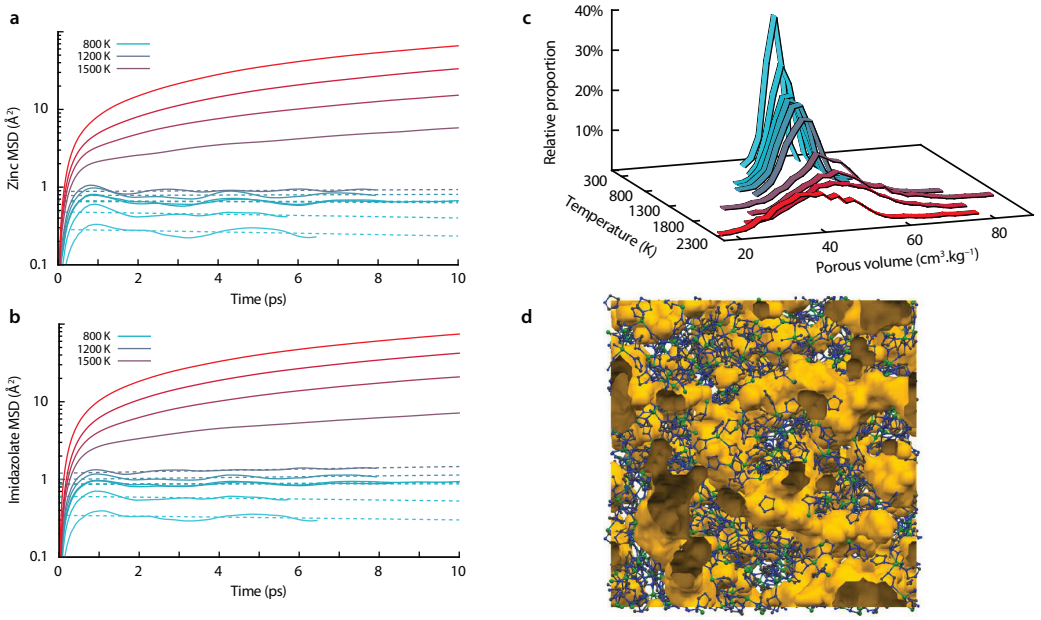

Figure 2.10: Structure and dynamics in the ZIF liquid. (**a**-**b**) Mean square displacement (MSD) as a function of time for (**a**) zinc cations and (**b**) the center of mass of the imidazolate linkers, plotted in logarithmic scale, for temperatures ranging from 300 K (light blue) to 2,250 K (red). Dashed curves represent fits of the MSD (excluding short times) for lower temperatures, showing the absence of diffusive behaviour. (**c**) Temperature evolution of the distribution of the total pore volume, determined for a standard probe of radius 1.2 Å. The average pore volume takes the following values: 52 $cm^3.kg^{-1}$ at 300 K, 49 $cm^3.kg^{-1}$ at 2,000 K, and 41 $cm^3.kg^{-1}$ at 2,250 K. (**d**) Atomic configuration of the ZIF melt, gained from Reverse Monte Carlo modelling of the total scattering data collected at 856 K (work by David A. Keen). Free volume is represented in orange, Zn atoms in green, N in blue, and C in grey. Figure reproduced from [60].

before melting, there thus exists a regime of free rotation of the imidazolate linkers.

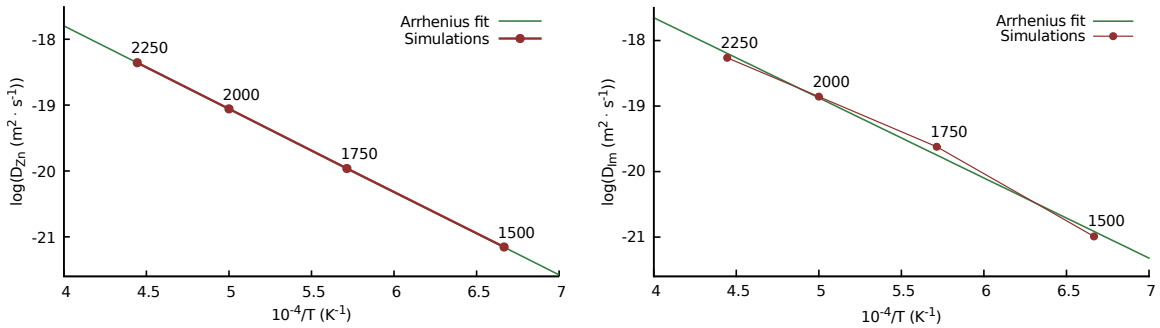

Figure 2.11: Left: van 't Hoff plot of Zinc diffusion coefficient. Right: van 't Hoff plot of Imidazolate diffusion coefficient.

Given the focus on porosity in MOFs, I also investigated the nature of the liquid ZIF from

a structural point of view. I performed statistical analysis of the instantaneous porosity along FPMD trajectories at all temperatures using a geometric criterion for the determination of porosity and a probe diameter of 2.4 Å, corresponding to the kinetic diameter of helium. This computation of the total porous volumes was done with the freely available software Zeo++. [164, 165, 210] It uses a geometric decomposition of space to compute the accessible and non-accessible volume to a sphere of a given radius. I thus computed the distribution of instantaneous total pore space (sum of the accessible and the non-accessible volume) along the MD trajectories at each temperature as seen by a helium molecule. I also studied the evolution of pore volume distribution as a function of probe radius at 1,500 K, as plotted in the left panel of Figure 2.12.

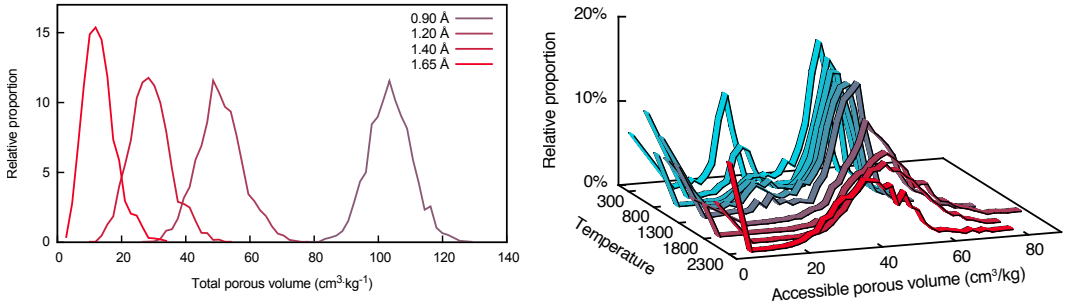

Figure 2.12: Left: Distribution of instantaneous pore volume at 1,500 K, for probes of radius 0.90 Å, 1.20 Å, 1.40 Å, and 1.65 Å. Right: Temperature evolution of the distribution of the accessible pore volume, determined for a standard probe of radius 1.2 Å.

The evolution of the pore volume distribution is depicted in Figure 2.10c, from 300 K to higher temperatures. As expected for the solid phase ($T < 1,200$ K), a slight broadening of the distribution is observed, which corresponds to increased thermal motion. However, at higher temperatures and particularly in the liquid phase, I see that the porosity is maintained overall, with only a slight deviation in average to lower pore volumes. This result, obtained in constant-volume simulations performed at density of 1.25 g.cm^{-3} inferred from the experimentally available data, were confirmed by shorter constant-pressure simulations.

Moreover, analysis of the accessible pore volume (*i.e.* excluding nonconnected void pockets) shows in the right panel of Figure 2.12 that a large fraction of the void space in the ZIF liquid is accessible porosity (going from 74% in crystalline ZIF-4 at 300 K to 95% in the liquid at 1,500 K). I thus conclude that, even at very high temperatures, the ZIF forms a hybrid "porous liquid", quite different in nature from the organic systems recently reported, [211] which are formed from cage molecules providing a well-defined pore space in solvents whose molecules are too bulky to enter the pores. [212, 213] This finding is in agreement with the available experimental data on the free volume of ZIF glasses. [214] This porosity is found to be larger than that typical of imidazolium ionic liquids (whose ions are roughly of the same size as the imidazolate anion): those systems feature void space whose size distribution is typically negligible above 1 Å in radius. [215, 216]

To link the predicted liquid structure to experimental information, David A. Keen performed Reverse Monte Carlo (RMC) modelling on the X-ray total scattering data collected at 856 K (Figure 2.4f). The atomistic configuration derived for the glass in Figure 2.4d was used as a starting model, with a reduced density to reflect the changes upon melting. The final configuration is shown in Figure 2.10d. Whereas the internal surface of the glass at ambient temperature was calculated on the RMC model to be 4.8%, again using standard probe diameter of 2.4 Å, that of the liquid at 856 K increased to 16.2%. Whilst transient in nature, linked voids appear irregularly distributed throughout the configuration.

2.2.4 Conclusion

In this work, we introduced, with all my coauthors of [60], the general term "MOF liquid", for a liquid formed from the melting of a MOF, due to the retention of chemical configuration and coordinative bonding modes between the solid and liquid phases. Importantly, we show the retention of porosity in the liquid state, with a pore volume larger than in the glass state, making liquid ZIF-4 a rare example of an intrinsically porous liquid, enabling a compromise between the selectivity of crystalline MOFs and diffusivity of amorphous membranes. [217] The demonstration and rationalization of melting in ZIF-4 provides a prototypical example in this new area, and a foundation on which further studies can be based, thus opening the way to the design or identification of other MOFs with accessible liquid or glass phases. The generality of the phenomenon depends upon a complex balance of melting temperature T_{m} and ligand decomposition temperature T_{d}. The latter is dependent on a multitude of factors including atmosphere, heating rate and particle size, with faster heating rates of larger particles in inert atmospheres observed to prolong degradation temperatures from *ca.* 473 K to 773 K for ZIF-8. [218,219] It is also however dependent upon chemistry, with species such as nitroimidazole undergoing early thermal decomposition due to C–NO_2 bond cleavage. This is consistent with the experimental observation that ZIFs containing NO_2-functionalized ligands decompose at *ca.* 573 K, compared with 773 K for ZIF-4 and ZIF-8. [51]

In the next section I describe the investigation I carried out on the high-temperature behaviour of ZIF-8, which experimentally does not melt, ZIF-zni, which does melt, and SALEM-2 for which no experimental result on melting has been published yet. I show how the retention of chemical configuration, the changes in the coordination network, and the variation of the porous volume in the liquid phase are influenced by the parent crystalline framework.

2.3 Influence of the topology and chemistry on the melting behaviour

In this section, I first compare ZIF-4, ZIF-8 and ZIF-zni with each other on the structural, thermodynamic and mechanistic points of view during the melting as well as the obtained liquids. Then I present the results obtained for the idealized SALEM-2 framework.

2.3.1 Differences in the structural changes upon heating and melting

In order to compare the structural evolution and onset of disorder of the frameworks associated with an increase of temperature, I first look at the Zn–N radial distribution functions (RDF) for each system upon heating (left panel of Figure 2.13). In all cases, the overall trend observed is the same: the peaks around 2 Å and 4 Å widen, but remain present, while the other peaks flatten and ultimately disappear at very high temperature. Another common feature of interest is the fact that, above 800 K, the RDF does not go to zero between the first two peaks, indicating the presence of nitrogen exchanges between the first and the second coordination spheres of the zinc cations. Beyond this, I also observe differences between the different frameworks, at low and intermediate temperatures. There, ZIF-8 appears more structured than ZIF-zni, with better defined and narrower peaks; and ZIF-zni itself shows more structuration than ZIF-4. Moreover, the liquid obtained from ZIF-4 has features that are closer to its crystalline precursor than the two other frameworks. These trends observed on the partial Zn–N radial distribution functions are confirmed when I look at the total RDF (right panel of Figure 2.13), containing all pair of atoms, showing the crucial role of the zinc–nitrogen coordination bond in monitoring and understanding the process of melting in ZIFs.

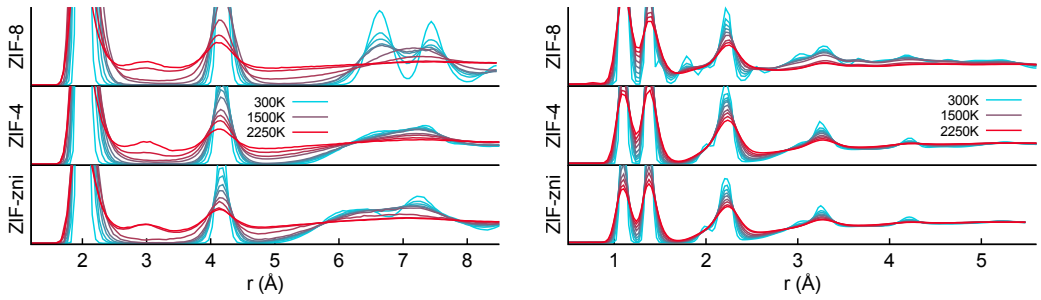

Figure 2.13: Left: Radial distribution functions for the pair of zinc and nitrogen atoms in the three ZIFs as a function of temperature. Right: Total radial distribution functions for the three ZIFs. The low temperature curves show the different orderings due to the different topologies, while the high temperature curves converge to a much more similar behaviour.

To quantify this analysis, I computed the Lindemann ratio for the three ZIFs as a function of temperature (left panel of Figure 2.14). As written in the previous section, a jump in the

Lindemann ratio, which is rather linear at low temperature, and the crossing of the threshold value of 15%, are typically understood to evidence the melting of a solid. This occurs in the temperature range of 1,200 K to 1,500 K for ZIF-4, in the range of 1,500 K to 1,750 K for ZIF-zni, and above that value for ZIF-8. I can thus assign an "order" to the melting temperatures of the three frameworks, with T_m(ZIF-4) < T_m(ZIF-zni) < T_m(ZIF-8). This may explain why ZIF-8 is experimentally observed not to melt, because its melting temperature is too high compared to its decomposition temperature.

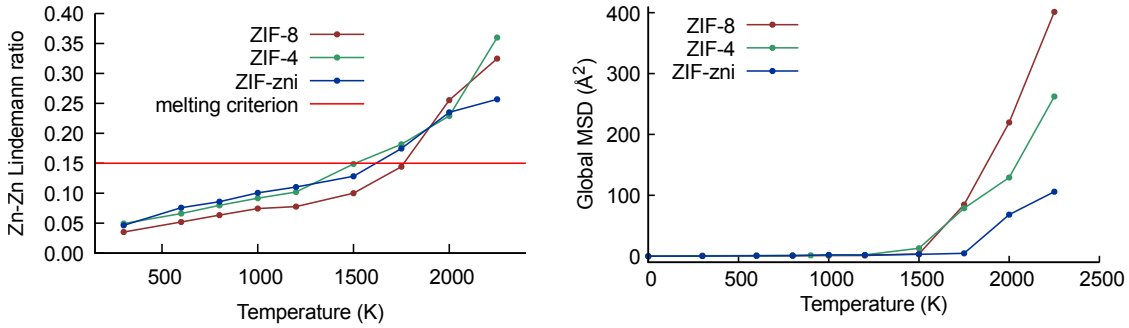

Figure 2.14: Left: Comparison of the evolution of the Lindemann ratios for the 3 ZIFs showing melting is happening at different temperatures. Right: Global mean square displacements Mean square displacements per atom of all the atoms of the framework as a function of temperature for ZIF-8 (red), ZIF-4 (green) and ZIF-zni (blue).

Finally, I computed the average mean square displacement per atom (summed over all atoms of a framework), over a reference length of time (τ = 75 ps). I observe in the right panel of Figure 2.14 that diffusion really starts between 1,250 K and 1,500 K for ZIF-4 and only above 1,500 K for ZIF-8. Diffusion in ZIF-zni seems to be hindered by its very dense structure, qualitatively different from the porous structures of ZIF-4 and ZIF-8. As a result, diffusion only appears above 1,750 K in this framework, whereas its Lindemann ratio at this temperature is higher than the one for ZIF-8. The comparison between the three frameworks indicates again that ZIF-8 ordering is more affected when melting.

Although the "theoretical" melting temperatures I report are well above experimental melting temperatures (around 865 K for ZIF-4 [50]), I believe my modelling still provides insights on the underlying mechanism happening at the "real" melting temperatures. Ab initio methods do not allow long time scales and very large systems, but by going to higher temperatures and checking the Arrhenian behaviour of the rare events observed, such as bond cleavages, I am able to compare the real melting behaviour of these three frameworks.

2.3.2 Thermodynamics of melting

As done for ZIF-4 I proceeded to use the Zn–N distance as a reaction coordinate, following the breaking and reformation of zinc–imidazolate coordination. From the partial radial distribution function between Zn and N, $g_{\text{Zn–N}}(r)$, I computed the potential of mean force

(PMF), $F(r) = -k_B T \ln g(r)$, at all temperatures for the three frameworks. The resulting free energy profiles are shown in Figure 2.15, and present similar features: the barrier at 300 K is too high to be measured (since no dissociation event is observed during the time of our simulations), and lower with increasing temperature. The barrier height, when it can be measured, is the activation free energy $\Delta F^\ddagger$ associated with the breaking of the Zn–N coordination bond. Its temperature dependence is displayed as a van 't Hoff plot in Figure 2.16, and a linear approximation (van 't Hoff law, $\Delta F^\ddagger(T) = \Delta U^\ddagger - T\Delta S^\ddagger$) is used in each case — with a reasonable fit — to obtain values for the activation energy and entropy, $\Delta U^\ddagger$ and $\Delta S^\ddagger$ respectively. The values obtained are given in Table 2.5.

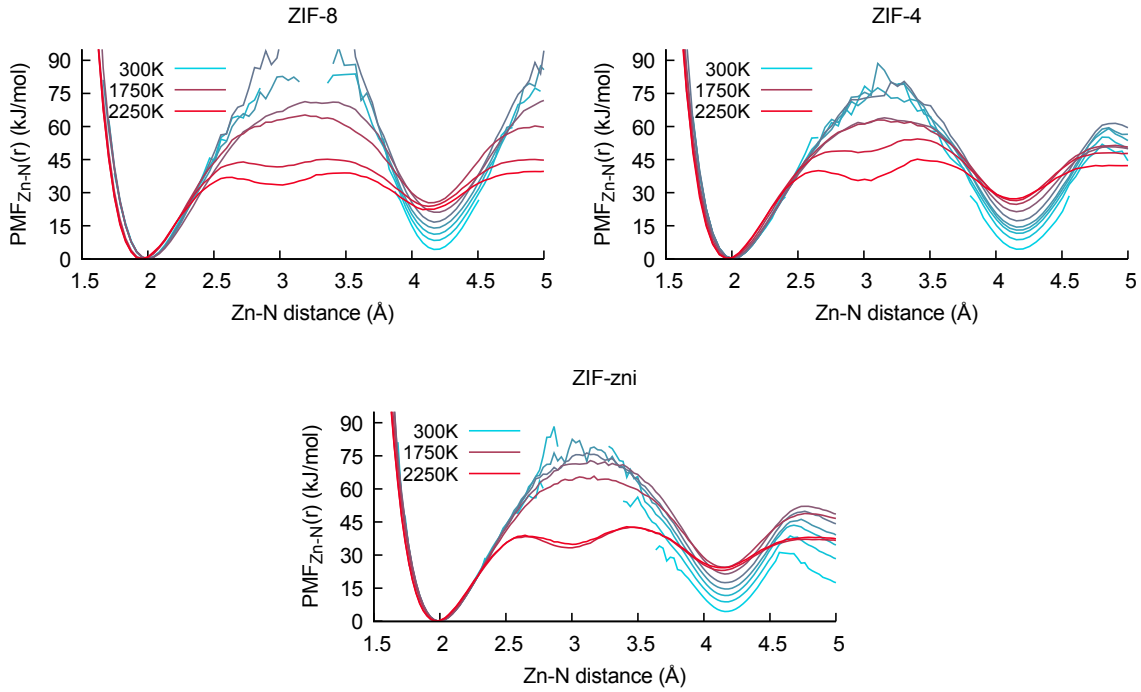

Figure 2.15: Potentials of mean force along the nitrogen-zinc reaction coordinate as functions of temperature for the three ZIFs.

In all cases the free energy barrier is dominated by the energetic term, while the activation entropy brings a small stabilization at high temperature. I observe that the free energy barriers encountered at the estimated melting temperatures are of $6\,k_B T$ for ZIF-8 (at 1,500 K), and $8\,k_B T$ for ZIF-4 and ZIF-zni (at 1,200 K), significantly higher than thermal fluctuations.

Thus, I confirm for ZIF-8 and ZIF-zni what I earlier found for ZIF-4, namely that melting occurs through an activation process leading to rare events of bond breaking. [207] That is, melting occurs not at the limit of stability of the solid phase, but at a point where it is still metastable.

Comparing the potential of mean force for the Zn–Im coordinate allows us to distinguish better between the behaviour of the different frameworks. In fact, as shown in Table 2.5, the thermodynamic parameters obtained from Zn–N to Zn–Im potential of mean forces are

	$\Delta U^{\ddagger}$(kJ.mol^{-1})	$\Delta S^{\ddagger}$(J.mol^{-1}.K^{-1})	$\Delta F^{\ddagger}(865K)$(kJ.mol^{-1})
ZIF-8 (Zn–N)	145	48	103 ($\simeq 14kT$)
ZIF-8 (Zn–Im)	207	77	140 ($\simeq 20kT$)
ZIF-4 (Zn–N)	127	37	95 ($\simeq 13kT$)
ZIF-4 (Zn–Im)	123	36	92 ($\simeq 13kT$)
ZIF-zni (Zn–N)	126	38	93 ($\simeq 13kT$)
ZIF-zni (Zn–Im)	128	39	94 ($\simeq 13kT$)

Table 2.5: The first column shows the activation enthalpy associated with a bond cleavage, the second column shows the activation entropy and the third column shows the extrapolated activation free energy at the experimental melting temperature for ZIF-4 of 865 K.

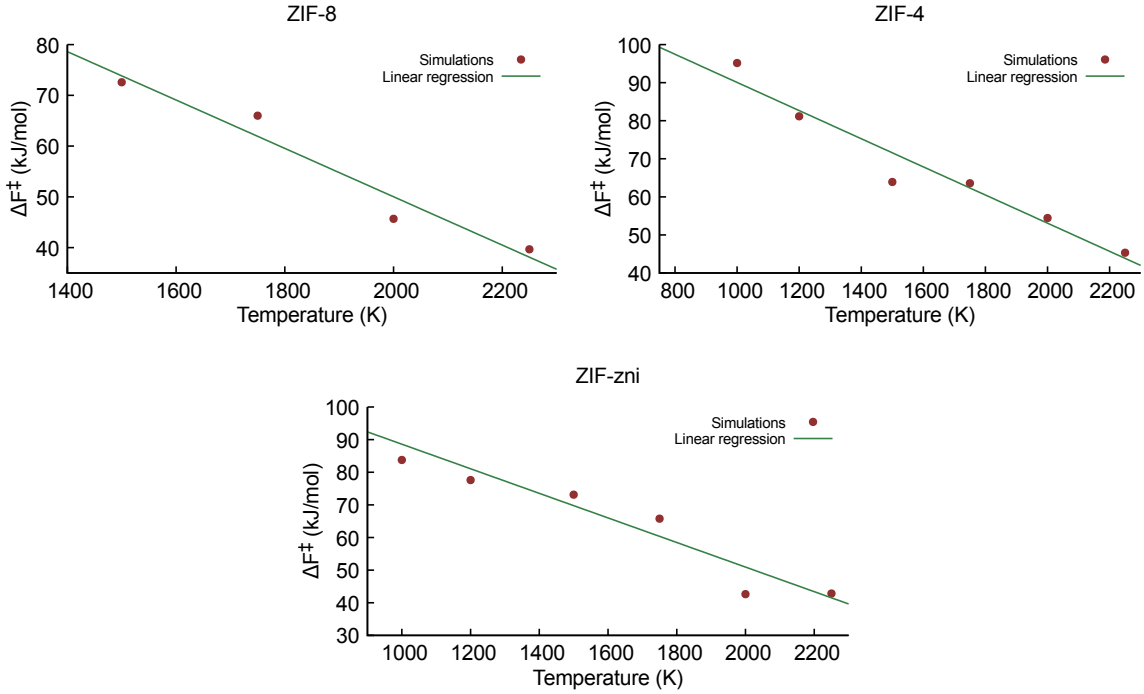

Figure 2.16: Activation free energies needed to break the Zn–N bond for the three ZIFs.

not the same for the three frameworks. For ZIF-4, there is almost no variation with less than 3% difference for the enthalpic and entropic terms. ZIF-zni shows a similar behaviour with less than 3% difference for both terms too. Although these two frameworks show that Zn–N bond breaking can almost be identified to Zn–Im bond breaking in terms of temperature dependence, the story for ZIF-8 is pretty different. In fact, the increase in enthalpy is 43% and even 60% for the entropic term. It explains why ZIF-8 seems to melt at a higher temperature than ZIF-4 as the resulting activation free energy with this reaction coordinate is still equivalent 11.5 $k_{\mathrm{B}}T$ at 1,200 K and only goes down to 7 $k_{\mathrm{B}}T$ at 1,500 K. Moreover, we

observe that there is a large difference between the $\Delta U^{\ddagger}$ of the Zn–N coordinate and that of the Zn–Im coordinate in ZIF-8. This shows that the difference in behaviour between ZIF-8 and the two other frameworks does not find its root only in the intrinsic strength of the Zn–N bond itself (as they are almost chemically equivalent), but rather in the influence of the environment of the framework.

2.3.3 A similar microscopic mechanism

As I have shown, melting appears through creation of defects in the coordination structure, where the Zn–N coordination bonds are broken and later re-formed. In my molecular dynamics simulations, I can track directly the formation of such defects by computing the Zn coordination number as a function of framework and temperature. These averaged coordination numbers are shown in an Arrhenius plot on the left panel of Figure 2.17. This leads to energies ε associated with defect formation, which are 71 kJ.mol^{-1} for ZIF-8, 56 kJ.mol^{-1} for ZIF-4, 67 kJ.mol^{-1} for ZIF-zni. These values are in the same range of magnitude, but we note here again that ZIF-4 exhibits the smallest defect formation energy, in line with thermodynamic and structural properties.

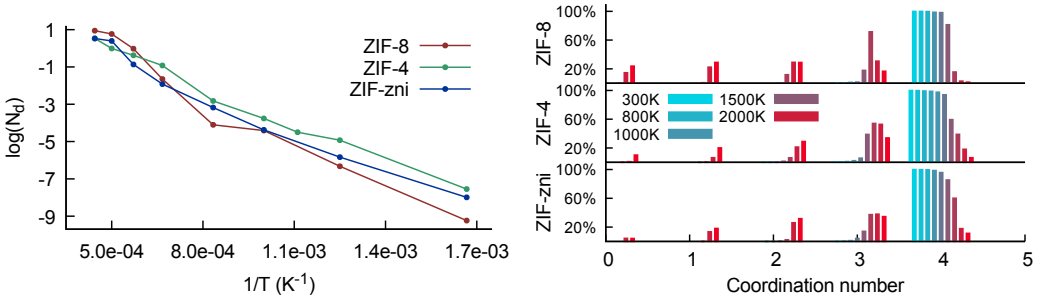

Figure 2.17: Left: van 't Hoff plot of the number of defects. The formation of defects follows an Arrhenius law with respective activation energies of 59, 52 and 50 kJ.mol^{-1} for ZIF-8, ZIF-4 and ZIF-zni. Right: Distribution of discrete zinc-nitrogen coordination numbers as a function of temperature for ZIF-8, ZIF-4 and ZIF-zni.

Right panel of Figure 2.17 shows the proportion of n-fold zinc atoms (n = 0 to 5) for the three ZIFs studied, as functions of temperature. For all structures, I see that increase in temperature leads to undercoordination of the zinc atoms through breaking of the Zn–N bonds. The trend I see on the four-fold coordination matches the structural quantities studied before, as the under-coordination comes at lower temperatures for ZIF-4 (35% drop between 1,200 K and 1,500 K) but is then much larger for ZIF-8 (66% drop between 1,500 K and 1,750 K), consistently with a greater disorganization due to diffusion. ZIF-zni four-fold coordination really jumps at higher temperatures, with a 45% drop between 1,750 K and 2,000 K. The microscopic mechanism, which I first unveiled in ZIF-4, is broadly similar in ZIF-8 and ZIF-zni. The transition into the liquid state involves rapid, activated events of imidazolate linker switching from a zinc cation. From an initial fourfold coordinated zinc,

one imidazolate linker moves away and is then replaced by a neighbouring Im group with a dangling nitrogen lone pair.

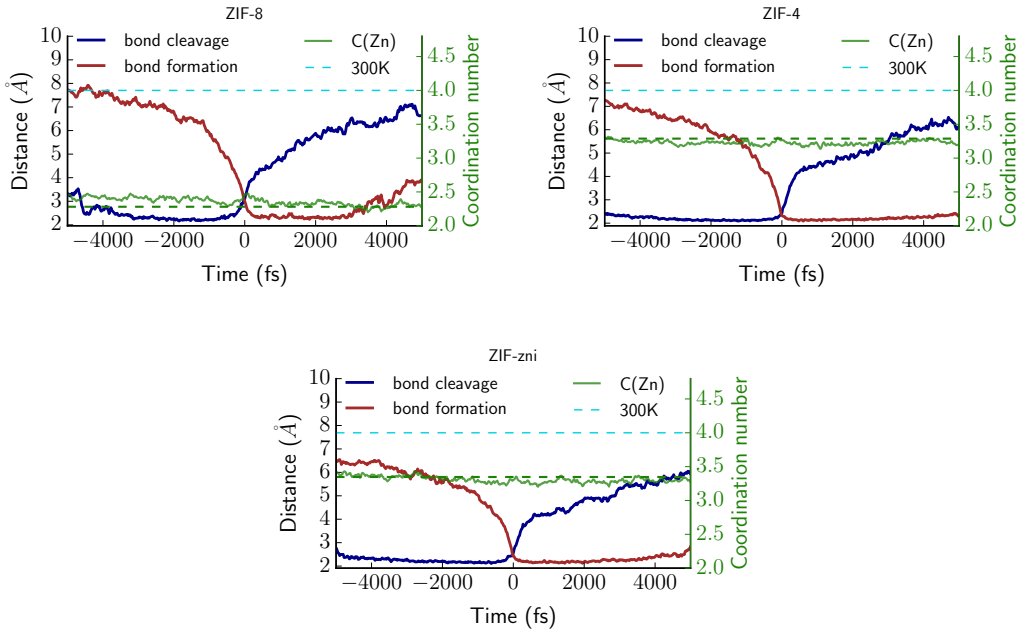

Figure 2.18: Behaviour during an exchange of a nitrogen atom by another nitrogen atom, in the first coordination sphere of a zinc cation, averaged over all such events (all exchanges on all zinc cations) in the three ZIFs. The distance between the incoming nitrogen and the zinc is plotted in red, and that between the outgoing nitrogen and the zinc in blue. The green curve corresponds to the average coordination number of the zinc cation involved in the exchange. The flat dashed lines are the average coordination number over the whole simulation at 300 K (light blue) and 2,000 K (green).

Exactly as in the case of ZIF-4 I analyzed these "linker exchange" events, which are depicted in Figure 2.18. The resulting average dynamics show that the bond cleavage mechanism is similar for the three frameworks. The only small difference is the coordination state during the exchange for ZIF-8. Although for ZIF-zni, as for ZIF-4, the exchange happens under slight undercoordination ($\simeq -2\%$), in the case of ZIF-8 it actually happens under a small overcoordination ($\simeq 3\%$). However, this can be explained by the fact that the average coordination number in ZIF-8 liquid is indeed much lower ($\simeq 2.3$) than it is in ZIF-4 and ZIF-zni ($\simeq 3.3$).

Presented in Table 2.6 are the activation energies associated with the Zn–N and Zn–imidazolate cleavage frequencies. ZIF-zni shows the highest value (137 kJ.mol^{-1}) in terms of activation energy for Zn–N bond breaking which confirms the difficulty to initiate the melting in this framework. In ZIF-4 the two processes were clearly related as the difference in activation energy was only 6.5% more for Zn–Im than for Zn–N. However for ZIF-8 this difference rises to 58%. This can be understood by looking at Table 2.7. Indeed the proportion of Zn–N cleavage corresponding to a Zn–Im/mIm cleavage is slowly growing in ZIF-4 while it goes

System	$E_a^{Zn–N}$ (kJ.mol^{-1})	$E_a^{Zn–Im/mIm}$ (kJ.mol^{-1})
ZIF-8	112	177
ZIF-4	76	81
ZIF-zni	137	160

Table 2.6: This table presents the activation energies needed to break a Zn–N bonds (first column) and Zn–Im/mIm bonds (second column) in the three ZIFs.

from 18% to 94% between 1,500 K and 2,000 K in ZIF-8. ZIF-zni does show a 28% increase between the two activation energies, which can be ascribed to the imidazolate diffusion being hindered due to its denser structure.

T (K)	ZIF-8	ZIF-4	ZIF-zni
1,500	18%	67%	31%
1,750	62%	73%	58%
2,000	94%	78%	74%
2,250	94%	83%	72%

Table 2.7: I show here the observed percentage of Zn–N bond cleavages that correspond to real Zn–Im cleavages in the three ZIFs at different temperatures.

2.3.4 Characterization of the liquid ZIFs

I have characterized the liquids obtained at temperatures above the melting point by computing the translational diffusion coefficients of zinc cations and imidazolate groups (see Table 2.8). The behaviour observed is qualitatively similar to what I saw with the global RMSD presented in the right panel of Figure 2.14: diffusion in ZIF-8 starts to be significant at higher temperature than in ZIF-4. For instance at 1,500 K, $D_{Im}^{ZIF\text{-}4}$ is equal to 7.7 10^{-10} ($m^2.s^{-1}$) which is more than ten times the diffusion coefficient of methylimidazolate in ZIF-8 (4.7 10^{-11}) at the same temperature, but this ratio is inverted at 2,000 K where $D_{Im}^{ZIF\text{-}4}$ is about one third of $D_{mIm}^{ZIF\text{-}8}$. ZIF-zni shows smaller diffusion coefficients all the way as expected. Nonetheless, the three ZIFs exhibit the same symmetry between the transport of zinc and imidazolate groups, as their diffusion coefficients are always very close, a behaviour commonly encountered in classical ionic liquids with strong association.

From the diffusion coefficients at various temperatures, I fitted Arrhenius laws — although I note that there are clearly uncertainties and fluctuations in the values of diffusion coefficients, due to the relatively short trajectories allowed on these large systems by first-principles methods. Characteristic activation energies for all frameworks are presented in Table 2.8. For example, in the case of Zn I have the following values: 302 kJ.mol^{-1} for ZIF-8, 105 kJ.mol^{-1}

Temperature (K)	$D_{\mathrm{mIm}}^{\text{ZIF-8}}$	$D_{\mathrm{Zn}}^{\text{ZIF-8}}$	$D_{\mathrm{Im}}^{\text{ZIF-4}}$	$D_{\mathrm{Zn}}^{\text{ZIF-4}}$	$D_{\mathrm{Im}}^{\text{ZIF-zni}}$	$D_{\mathrm{Zn}}^{\text{ZIF-zni}}$
1,500	$2.1\ 10^{-11}$	$1.5\ 10^{-11}$	$7.7\ 10^{-10}$	$6.5\ 10^{-10}$	$3.8\ 10^{-12}$	$3.5\ 10^{-12}$
1,750	$4.3\ 10^{-9}$	$3.2\ 10^{-9}$	$3.0\ 10^{-9}$	$2.1\ 10^{-9}$	$1.1\ 10^{-10}$	$3.5\ 10^{-11}$
2,000	$1.5\ 10^{-8}$	$1.8\ 10^{-8}$	$6.5\ 10^{-9}$	$5.3\ 10^{-9}$	$4.2\ 10^{-9}$	$4.0\ 10^{-9}$
2,250	$2.1\ 10^{-8}$	$2.5\ 10^{-8}$	$1.2\ 10^{-8}$	$1.1\ 10^{-8}$	$3.8\ 10^{-9}$	$5.6\ 10^{-9}$
E_a (kJ.mol^{-1})	258	302	102	105	304	284

Table 2.8: The diffusion coefficients (in $m^2.s^{-1}$) for the zinc atoms and the center of mass of the imidazolate cycles were extracted from the MD simulations. The last line contains the associated activation energies extracted from Arrhenius fits.

for ZIF-4 and 284 kJ.mol^{-1} for ZIF-zni. The ordering of activation energies associated with diffusion match the one associated with breaking the Zn–imidazolate/methylimidazolate, thus confirming a diffusive mechanism. Contrary to fully dissociated ionic liquid though, zinc atoms and imidazolate ligands stay strongly associated in average as the aforementioned coordination numbers show.

Finally, I examined the porosity as a function of temperature for all the frameworks (Figure 2.19). I let aside ZIF-zni as it is almost non-porous, though I note that this very little porosity is not affected by melting. The ZIF-4 liquid, as already demonstrated in previous work, retains most of the modest porosity of its parent crystalline phase, with instantaneous "pockets" or voids in the liquid, even at high temperatures. In stark contrast, ZIF-8 — well known for high porosity of its crystal structure — sees its pore space suffer a lot from the melting process. More than half of its porosity is lost, and the distribution of instantaneous porous volume is rather broad. I note that it is, however, still larger than that of the ZIF-4 liquid.

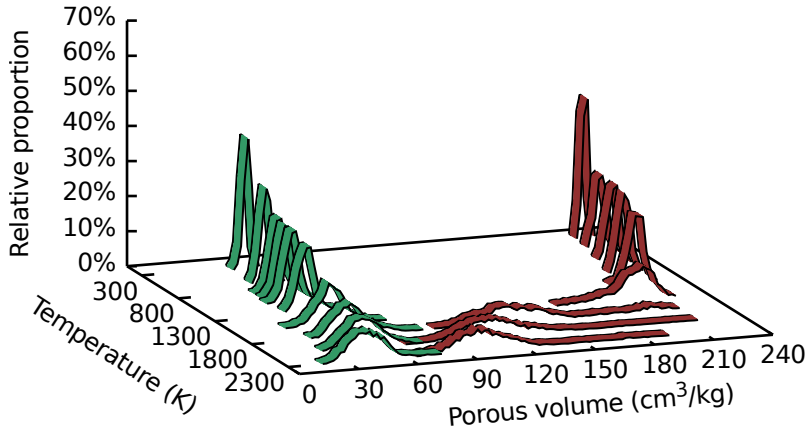

Figure 2.19: Comparison of temperature-dependent porosity between ZIF-4 (green) and ZIF-8 (red). The relative stability of the porous volume in ZIF-4 is striking compared to the collapse of the one in ZIF-8.

2.3.5 Conclusion

Here, I have used first-principles molecular simulations in order to investigate the question of transferability of the melting phenomenon among three different ZIF frameworks, and the influence of the nature of the parent crystalline ZIF on the physico-chemical properties of the resulting liquid. I conclude that the phenomenon is general, and also that the mechanism by which melting occurs is similar in all three frameworks. I also show that there is a clear impact of the characteristics of the ZIF crystals on both the melting, with ZIF-8 melting above its experimental temperature of decomposition, and thus not a candidate. I link this to the high free energy barrier for the detachement of imidazolate linkers from the metal cations. I hypothesize that this may be due to the high porosity of ZIF-8: while for denser ZIFs, like ZIF-4 and ZIF-zni, the movement of the ligand allows it to keep good contact with other ligands and be stabilized by dispersive interactions, in highly porous ZIF-8 the detachement of the imidazolate group implies that it be very isolated in the intermediate state, and thus a high energetic barrier.

Thus, framework topology plays an important role in the determination of melting, as well as in the properties and retention of the porosity in the liquid phase. In the next subsection I present the study I did on SALEM-2. As it has the same chemical composition as ZIF-4 but the topology of ZIF-8, I will see which one of these two factors influence the most the melting behaviour of ZIFs.

2.3.6 SALEM-2

The left panel of Figure 2.20 shows the van 't Hoff plot of the number of zinc-nitrogen coordination defects in SALEM-2 as a function of temperature. The associated activation energy has a value of 56 kJ/mol which is larger than the one for ZIF-4 (52 kJ/mol) but slighly less than the one for ZIF-8 (59 kJ/mol). I note that these differences are small, and should be taken with caution. However, the right panel of Figure 2.20 seems to confirm the behaviour of SALEM-2 as being in between the one of ZIF-4 and ZIF-8. Indeed the Zn–N coordination number distribution for SALEM-2, compared to the ones for ZIF-4 and ZIF-8 shown in Figure 2.20, indicates that at 1500 K SALEM-2 has 74% of four-fold coordination zinc atoms while ZIF-4 has 60% and ZIF-8 has 81%. Then, at 1,750 K the framework of ZIF-8 has collapsed to keep only 16% of four-fold coordinated zinc atoms while SALEM-2 still has 50% and ZIF-4 39%. These observations confirm that the metastability of the sodalite topology is high and even higher if associated with non-substituted imidazolate ligands.

As expected because of the same nature of the Zn–N bond in the two frameworks, the activation free energies needed to break this bond in SALEM-2 is similar as the ones in ZIF-4. As can be seen in Figure 2.21, where the potential of mean force along this coordinate (left panel) and the van 't Hoff plot of the resulting activation free energies (right panel) are displayed, the values of $\Delta U^{\ddagger}$ and $\Delta S^{\ddagger}$ are very similar to the ones reported for ZIF-4. Indeed

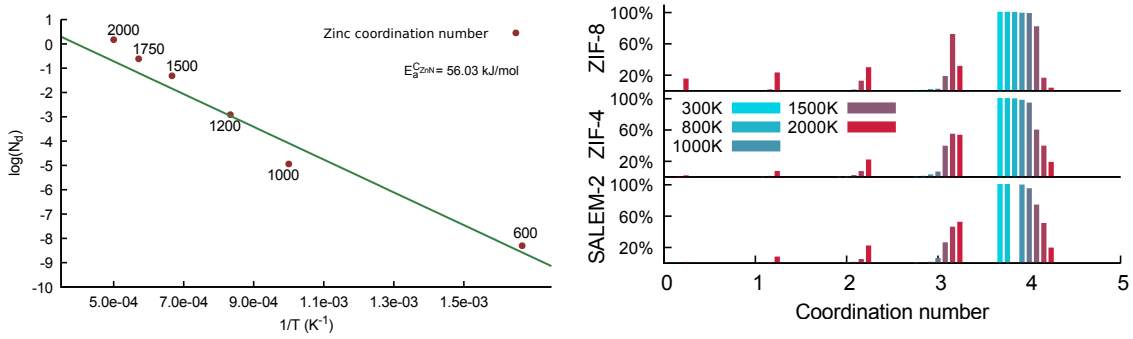

Figure 2.20: Left: van 't Hoff plot of the number of defects for SALEM-2, following an Arrhenius law with activation energy of 56 kJ.mol^{-1}. Right: Distribution of discrete zinc-nitrogen coordination numbers as a function of temperature for ZIF-8, ZIF-4 and SALEM-2.

the difference on the activation enthalpy with ZIF-4 is of 1 kJ/mol and of 4 J mol^{-1} K^{-1} for the activation entropy. This could suggest that melting is similarly easy in SALEM-2 as in ZIF-4. However, as I have shown before with ZIF-8, the most important reaction coordinate to correctly consider the disorganization of the framework leading to melting is the Zn–Im (or mIm in the case of ZIF-8) coordinate.

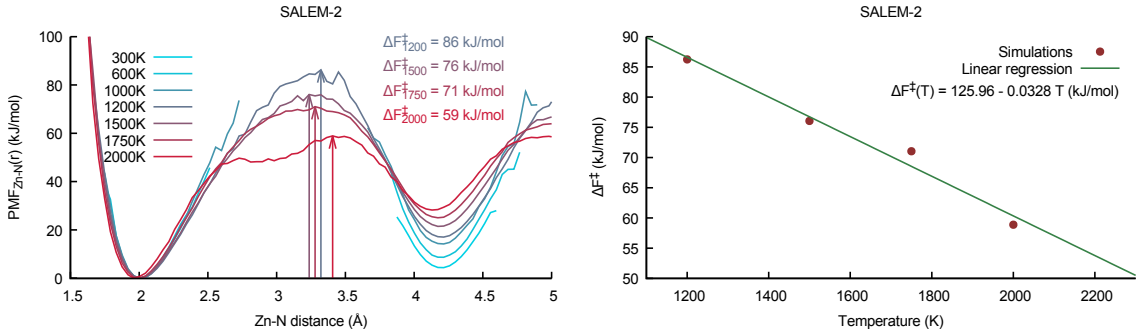

Figure 2.21: Left: Potentials of mean force along the Zn–N coordinate at different temperatures for SALEM-2. Right: van 't Hoff plot of the activation free energies associated with the breaking of Zn–N bonds in SALEM-2.

In this case, when looking at the activation free energies associated with the zinc-imidazolate coordinate (left panel of Figure 2.22), SALEM-2 seems to behave much more like ZIF-8. Indeed the increases compared to Zn–N are similar as the activation enthalpy goes up by 40% (43% for ZIF-8) and the activation entropy by 81% (60% for ZIF-8). So, although the chemistry of SALEM-2 is exactly the same as ZIF-4 or ZIF-zni, its very open topology generates supplementary cost for the melting. This is completely confirmed by looking at the Lindemann ratio (right panel of Figure 2.22) as SALEM-2 is the framework for which its value reaches the critical value of 15% at the highest temperature (above 1,750 K).

Finally, looking at the diffusion coefficients of the zinc atoms in the framework and the associated activation energy confirms the previous finding that it follows the same order as the

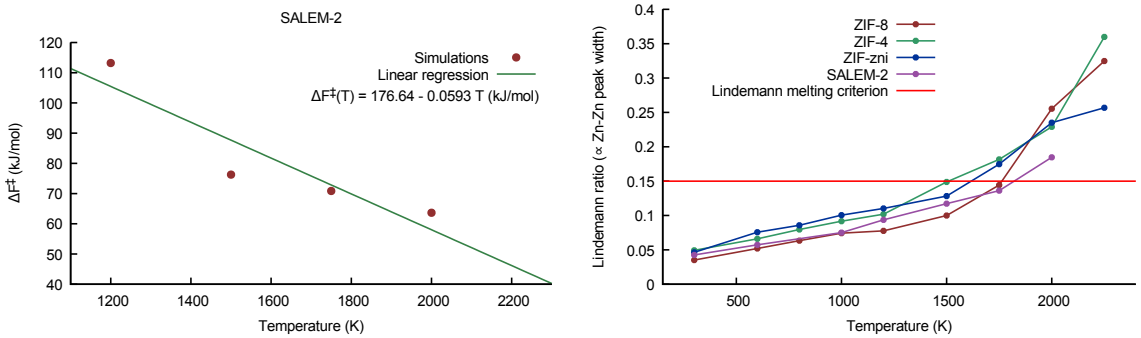

Figure 2.22: Left: van 't Hoff plot of the activation free energies associated with the breaking of Zn–Im coordination in SALEM-2. Right: Lindemann ratios as a function of temperature for the three ZIFs and SALEM-2.

activation energy needed to break the Zn–Im/mIm bond, in porous structures. Indeed it is 245 kJ/mol for SALEM-2 (with diffusion only beginning at 1,500 K) compared to 105 kJ/mol for ZIF-4 and 302 kJ/mol for ZIF-8.

All these observations go in the sense of the claim written in [50] that zeolitic imidazolate frameworks will have melting points close to their inorganic zeolites equivalent and thus the topology plays the main role in the capability of a framework to melt or not. Indeed, as soon as the melting point of the inorganic equivalent is far above the temperature of thermal decomposition of the organic ligands, like sodalite for ZIF-8 and SALEM-2 with a melting point of 1,557 K, melting is probably not expected to happen.

2.4 Conclusion on the melting of ZIFs

In this chapter, I presented the study of four different zeolitic imidazolate frameworks. It is obviously not enough to have a final conclusion on the influence of the chemistry or the topology on the melting behaviour of a ZIF. However, the comparison of three frameworks with the same chemistry (ZIF-4, ZIF-zni and SALEM-2) and another one with a slight chemical difference but the same topology (ZIF-8) led me to conclude about the great importance of the topology over chemistry for the capability of a framework to melt. I also unraveled the microscopic mechanism underlying this phenomenon: melting happens by rare activated events of ligand exchanges between the metallic cations.

There is still a great need to study the melting of other ZIF materials, combining experimental and theoretical forces, in order to confirm this hypothesis and establish general criteria for low melting temperatures in ZIFs. This will require the study of ZIFs with different organic ligands, different topologies, but also different metal cations (such as cadmium) [184] that can influence the strength of the zinc–imidazolate interaction — something that has not been studied much to date. The goal would be to provide porous MOF liquids with tunable chemical and physical properties, as is done for crystalline MOF architectures that can be

designed and tailored for specific applications. Such materials would be of interest for liquid phase separations, homogeneous catalysis and ion transport. They could also be used as intermediaries to obtain mechanically and thermally stable porous MOF glasses.

Chapter 3

Quenching Zeolitic Imidazolate Frameworks

In this chapter, I present the results obtained from ab initio molecular dynamics simulation of the quenching of three different Zeolitic Imidazolate Framework liquids: ZIF-8, ZIF-4 and SALEM-2. I first detail the starting point I chose for these simulations and the thermal process I applied. Then, I try to explain how the topology and the chemistry of each framework influence the links between the crystalline phase and the glass obtained.

3.1 Simulation methods for quenching

3.1.1 Systems considered

Following the simulations I carried out to study the melting of ZIF-4, ZIF-8 and SALEM-2, I used the trajectories at 1,500 K as initial liquid phases. More precisely, I chose the lowest temperature at which all the three frameworks exhibited liquid-like behaviour, either by looking at free diffusion or cleavage frequencies of Zn–N bonds.

More precisely, for ZIF-4 I took ten configurations of the liquid phase at 1,500 K corresponding to snapshots of the equilibrated trajectory after 6 ps (11 ps after the beginning with 5 ps of equilibration) and every 15 ps after that up to 141 ps. I took the exact same snapshot for ZIF-8 on the trajectory at 1,500 K. For SALEM-2, the first configuration is the snapshot after 55 ps of the equilibrated trajectory and the last one is the one after 190 ps. Figure 3.1 shows a 2x2x2 supercell of a snapshot of ZIF-4 at 1,500 K.

The reason why I took ten different configurations of the liquid before conducting quenching simulations is the small size of the unit cell I can simulate with AIMD. Hence the need to have several simulations of the quenching to get a representative view of what might be

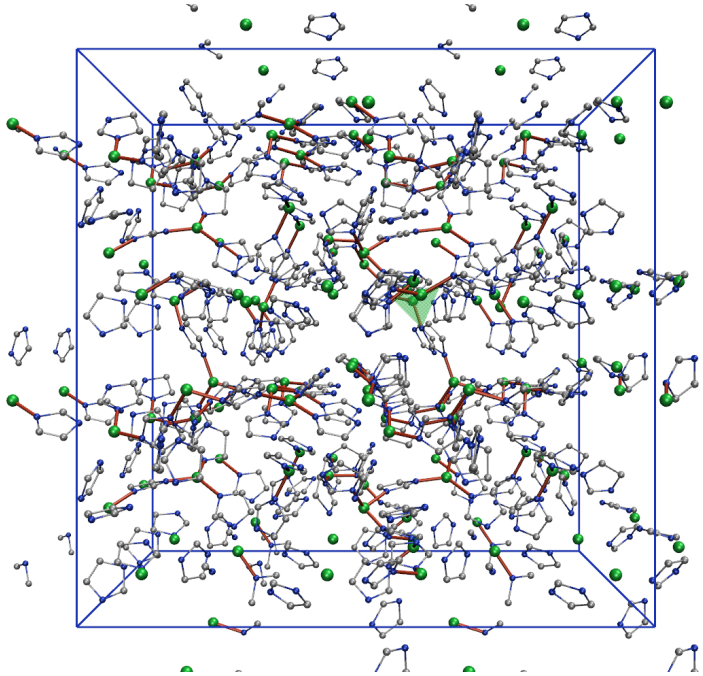

Figure 3.1: Supercell of a snapshot of the trajectory of ZIF-4 at 1,500 K. Zinc: green, Nitrogen: blue, Carbon: gray, Hydrogen: omitted. I show the Zn–N coordination bonds in red.

the real glass configuration, disordered in nature, by averaging the properties over the ten different trajectories. Indeed this statistical approach was needed to study static disordered phases because of the rather small sizes of our systems (∼15 Å linear expansion, about 270 atoms for ZIF-4 and ZIF-8, 204 atoms for SALEM-2). I thus took snapshots as far as possible in the liquid phase trajectory in order to better sample the configurational space.

As ZIF-8 does not melt experimentally, the quenching simulations I made on this structure were used to compare the effect of changing the chemistry with SALEM-2, while SALEM-2 compared to ZIF-4 provides a good point of comparison for a change of the topology only.

During my PhD, I also conducted quenching simulations by starting from snapshots at 2,000 K for ZIF-4 and ZIF-8. I will not present in detail the results of this study as the trajectories at 1,500 K were considered closer to what could happen in reality, with regard to the undercoordination. However, I will sometimes use them as a point of comparison.

3.1.2 Thermal process

For each initial configuration of each framework, I launched consecutive 4 ps constant temperature simulations at 1,300 K, 1,100 K, 900 K, 700 K, 500 K and 300 K. The instantaneous temperature followed a well-defined ramp as the time constant I chose for the thermostat is of 1 ps. Figure 3.2 shows an example per framework of the look of the instantaneous

temperature as a function of time. It is clear that this quenching rate is much faster than anything physically possible in the lab. However, due to the small size and time scales accessed by ab initio molecular dynamics the resulting glass configurations can be analyzed as physically sound phases. This procedure has been performed before on silica glass with good results. [220]

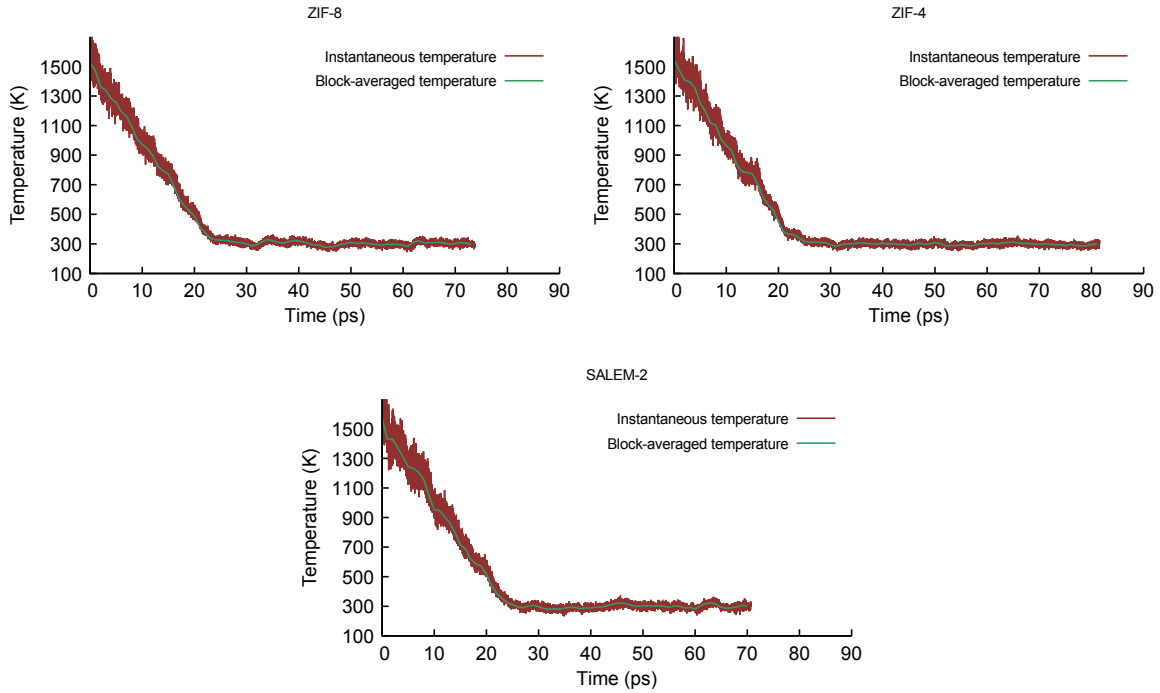

Figure 3.2: Examples of the instantaneous temperatures resulting from the imposed decrease of temperature. The instantaneous temperature is shown in red and its block-averaged value (per block of 1 ps) is shown in green.

In the next section I present the results from the analyses done on the 30 glasses configurations (10 for each framework). In order to be sure not to analyze any of the trajectory *during* the quenching, all the results have been averaged on the part of the trajectory after 25 ps of dynamics.

3.2 Different glasses from different crystals

For each framework, I obtained ten trajectories to analyze to output properties of interest. In order to have a representative view of the real structure of the glass phase, I averaged these properties over the different configurations. For every property investigated, whether it is structural, thermodynamical or porosity-related, I compared the three frameworks to conclude on the influence of the initial crystalline topology and chemistry on the properties of the glass. In all the following I will note a_gZIF-4, a_gZIF-8 and a_gSALEM-2 the "average" glass obtained for ZIF-4, ZIF-8 and SALEM-2 respectively.

3.2.1 Structural characterization

Radial distribution functions

The first property I look at to characterize the structure of the glasses is the total radial distribution function (RDF, see Figure 3.3). I see that, in average, the glass phase looks a lot like the crystalline phase. However, the variations between the ten different configurations are large, as I show by plotting the average behaviour plus or minus the standard deviation (in light-grey on Figure 3.3). Thus, as expected when looking at all the atoms, the short range order globally comes back to a similar state than in the crystal. I note that the differences between the three framework in this regard are quite small, even though ZIF-8 seems to exhibit a greater difference compared to its crystalline form than the two others.

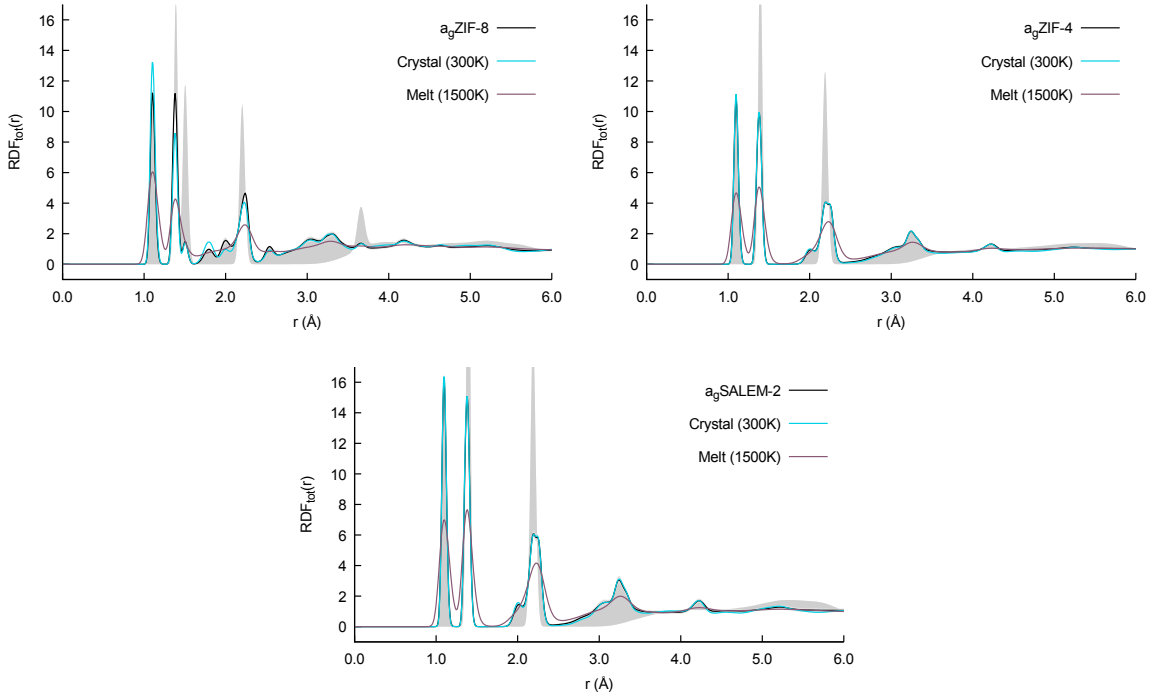

Figure 3.3: Total radial distribution functions (RDF) for the three structures. In light blue I remind the crystalline RDF obtained from my previous simulations, in purple I plot the average RDF for the melt at 1,500 K and in black the average RDF over all the glass configurations. To give an idea of the variance exhibited by the ten different trajectories, I filled curves in light gray correspond to the black curve plus or minus the standard deviation associated with the ten samples.

To be more precise about the structuration of the networks which are based on the zinc cations, I show the RDF associated with the pair of zinc atoms for the three systems in Figure 3.4. The thermal widening of the first peak during melting vanishes as the structures are cooled down, which is expected and with little difference between the frameworks. However, ZIF-8 has a peculiar behaviour: although the widening was symmetric, the final peak (for the

glass) is shifted to higher r values compared to the crystal, as evidenced by the cumulative curve accounting for the average number of neighbors at a given distance. Looking at the numbers I see that the first sphere of neighbors for the zinc atoms remains much more affected for ZIF-8 than the other two frameworks. More precisely, Table 3.1 details the average distances to the first and second neighboring zinc atoms from a zinc atom, in the crystalline phase, at 1,500 K and in the averaged glass phase. The distance to the three first neighbors are little affected by the events of melting and quenching, with a very small enlargement at high temperature that disappears after quenching. Nonetheless, the distance to the fourth neighbor is much more affected, especially in ZIF-8. In fact, for ZIF-4, even at 1,500 K, this distance only goes up by 1.5% and goes down by 6% after quenching. For both ZIF-8 and SALEM-2 this distance goes up by more than 15% in the liquid phase, but whereas in SALEM-2 it almost goes back to its value of in the crystal, quenching ZIF-8 has the opposite effect, where the fourth neighbor actually goes to 8 Å in average, i.e. 23% further than in the crystal. This leads me to conclude that the roles of the topology and the chemistry with regard to the melting and quenching seem to have inverted importances. It seems like the disorganization during the melting is more influenced by the topology, but that the precise chemical interactions play a larger role in the partial reconstruction of the framework during quenching.

	ZIF-8 (3^{rd}-4^{th})	ZIF-4 (3^{rd}-4^{th})	SALEM-2 (3^{rd}-4^{th})
Crystal (300 K)	6.1-6.5 Å	6.1-6.5 Å	6.1-6.5 Å
Melt (1500 K)	6.3-7.6 Å	6.2-6.6 Å	6.3-7.5 Å
Glass (300 K)	6.1-8.0 Å	6.1-6.2 Å	6.1-6.4 Å

Table 3.1: Average distances to the third and fourth neighboring zinc atoms from a zinc for the three frameworks at different temperatures and in the glass phase.

The tetrahedral angle: a measure of the local order

As a measure of the very local order around the zinc atoms, I present here the result of the analysis of the N–Zn–N angle, usually called the tetrahedral angle in coordination chemistry. [221] Figure 3.5 presents the distributions of this angle for the three frameworks at 300 K in the crystalline phase, at 1,500 K in the melt and at 300 K in the glass phase. The distributions are all pseudo-gaussians, the thermal widening in the melt is visible and is partially conserved in the glass phase. With the undercoordination of the zinc atoms happening during the melting, this angle can only go up in average. And it seems indeed to be linked to the percentage of four-fold coordination present in the system.

I give in Table 3.2 the average values and the associated standard deviations corresponding to these distributions. At 1,500 K there are 60% of four-fold coordinated zincs accompanying an increase of 4.5% of the tetrahedral angle, whereas the 74% of four-fold coordination in SALEM-2 gives an increase of 3.9% and the 81% in ZIF-8 an increase of 3.5%. Despite these differences during melting, the average values obtained in the glass phase present surprisingly

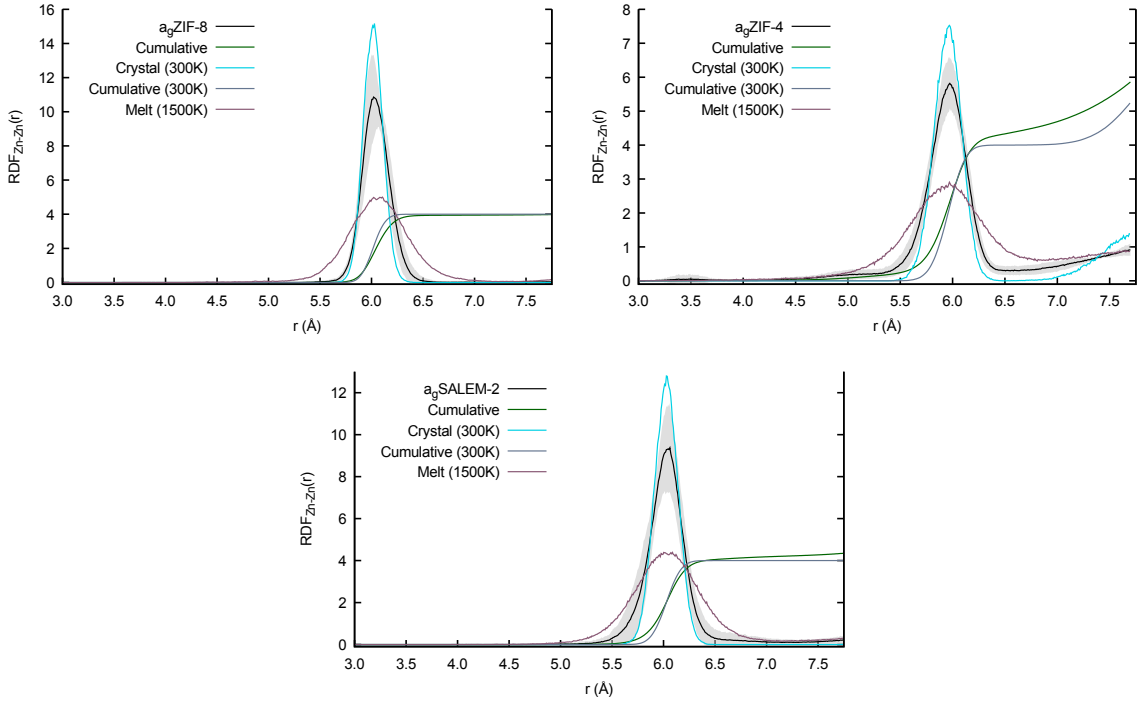

Figure 3.4: Radial distribution functions (RDF) for the Zn–Zn pair for the three structures. In light blue I remind the crystalline RDF obtained from my previous simulations, in purple I plot the average RDF for the melt at 1,500 K and in black the average RDF over all the glass configurations. As previously described the light gray areas correspond to the standard deviation between the ten trajectories. Cumulative functions corresponding to the number of neighbors are shown (in green for the glass, in blue for the crystal).

	ZIF-8	ZIF-4	SALEM-2
Crystal (300 K)	$111.3(\pm 1.4)°$	$112.2(\pm 1.6)°$	$111.6(\pm 1.6)°$
Melt (1500 K)	$115.2(\pm 4.0)°$	$117.3(\pm 3.7)°$	$116.0(\pm 4.1)°$
Glass (300 K)	$112.5(\pm 2.4/0.3)°/1.0°$	$113.3(\pm 2.2/0.2)°/0.8°$	$112.7(\pm 2.4/0.5)°/1.0°$

Table 3.2: Average value of the tetrahedral angle and its standard deviation for the three frameworks in the crystal, the melt and the glass. For the glass phase, the standard deviation indicated after $\pm$ is the average of the standard deviations observed for the ten initial configurations. The first value after (after a /) is the statistical standard deviation on this first value over the ten initial configurations. Finally, the last number is the statistical standard deviation associated with the average of the ten mean values.

similar deviations from the crystal value. Actually, ZIF-4 has, by a small amount, the smallest positive deviation of 0.98% (0.99% and 1.1% for SALEM-2 and ZIF-8 respectively) indicating a greater reconstruction of the coordination network. Another hint is given by the value of the standard deviation: it is 71% higher in a_gZIF-8 than in ZIF-8, 50% higher in SALEM-2 and only 38% higher in ZIF-4, indicating a smaller structural disorder for ZIF-4.

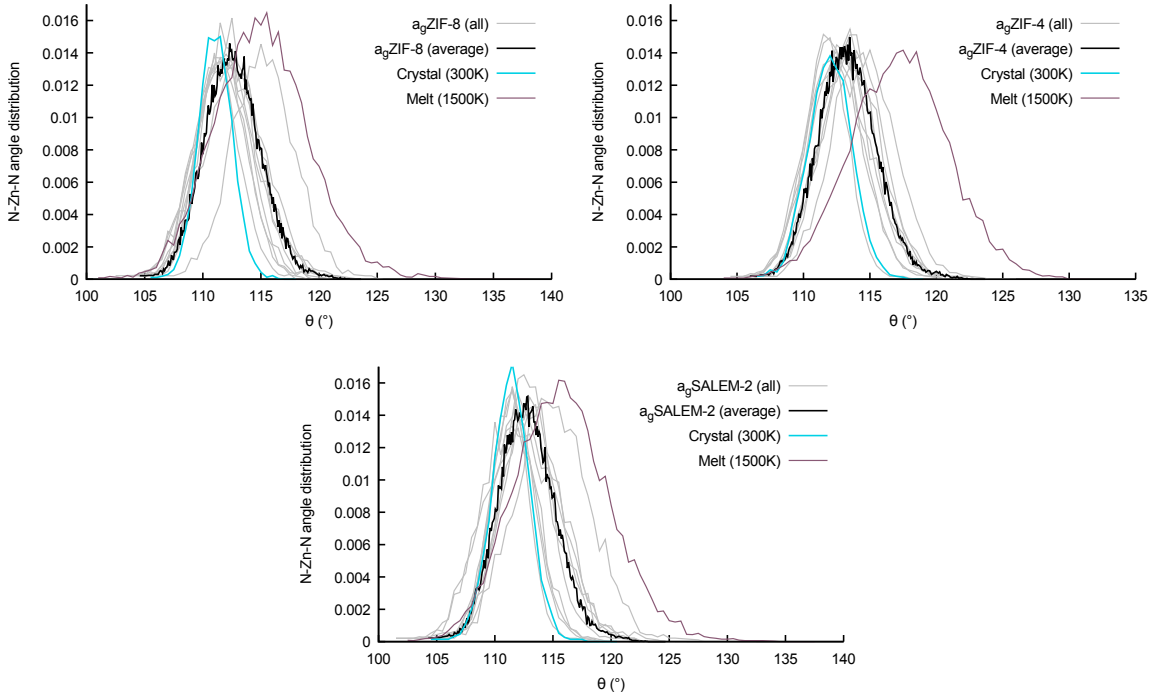

Figure 3.5: Distributions of the N–Zn–N angle for the three frameworks in the three phases (crystalline (light blue), molten (purple) and glass (black)). The light gray curves correspond to the ten different initial configurations for each framework.

Zinc-nitrogen coordination

Figure 3.6 shows the distributions of discrete coordination numbers for zinc atoms coordinated to nitrogen atoms. This is a firm confirmation of the reconstruction mechanism happening in ZIF-4, as already suggested in [50]. The proportion of four-fold coordinated zincs in ZIF-4 goes from 60% to 93% through quenching, regaining an average coordination number of 3.93 (compared to the crystalline value of 4). This increase of 33% is lower in SALEM-2, with 22%, or in ZIF-8, where it is of 17% with the same thermal process. Actually, the similar simulations I conducted starting from snapshots of the trajectories at 2000 K for ZIF-4 and ZIF-8 confirms that the reconstruction happens much more easily in ZIF-4: from 28% of four-fold coordinated zincs at 2,000 K, ZIF-4 recovers to 65%, whereas ZIF-8, starting from 3%, recovers "only" to 18% of four-fold coordination.

Zinc-imidazolate rings

Figure 3.7 shows the distributions of ring sizes for the three frameworks at different temperatures and in the melt-quenched glass. Here by ring size, I mean the size of the topological rings formed by following alternate zinc-imidazolate bonds (ABAB type rings with A=Zn and B=Im). For this reason, all the ring sizes I report are even. I note that the small size of

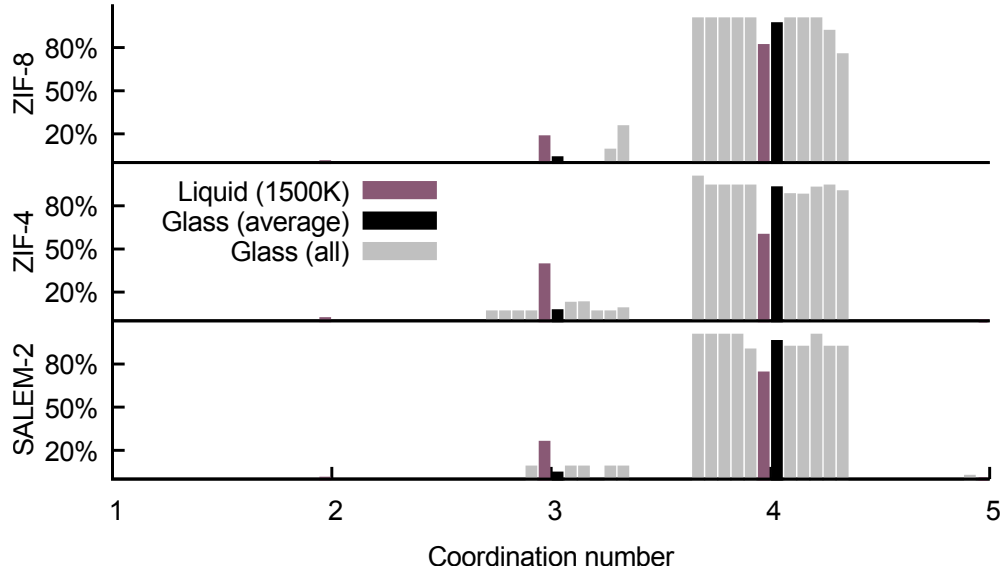

Figure 3.6: Distribution of the zinc-nitrogen discrete coordination number. The threshold of 2.5 Å used for the study of the melting is still employed.

the systems I studied prevent me from seeing the formation of very large rings. However, this constitutes a topological characterization useful to characterize the difference between ZIF-4 and the two other frameworks. If one wishes to compare the sizes I present with zeolites, the values have to be divided by 2, as usually only the metals are taken into account.

On Figure 3.7, the relative stabilization of ZIF-4 during melting and quenching compared to ZIF-8 or SALEM-2 appears clearly. Indeed the increase in temperature in ZIF-4 leads to the formation of other ring structures with size 6 and 8 respectively, while the number of 8-member rings decreases by a quarter at 1,500 K. On the contrary, in ZIF-8, and also in SALEM-2, the destroying of the 8-member rings do not lead to the formation of any other structures (a little in SALEM-2). The reconstruction mechanism in ZIF-4 is even visible as the number of 8-member rings grows again during the quenching, while it dramatically decreases for ZIF-8 and SALEM-2. I note here that the larger 6-zinc windows in SALEM-2 and ZIF-8 are not considered as it would correspond to 12-member rings. Therefore, this analysis confirms that the local topology is at the same time less affected in ZIF-4 during melting and better recovered during quenching compared to ZIF-8 and SALEM-2.

These structural observations seem to put the focus on the topology rather than the chemistry of the frameworks to explain the quenching behaviour as SALEM-2 resembles ZIF-8 much more than ZIF-4. Indeed, except in the case of the zinc-zinc distance, where the size of the methylimidazolate compared to the imidazolate seems to be the major factor, all the properties linked to metal-ligand coordination point to the crucial character of the topology.

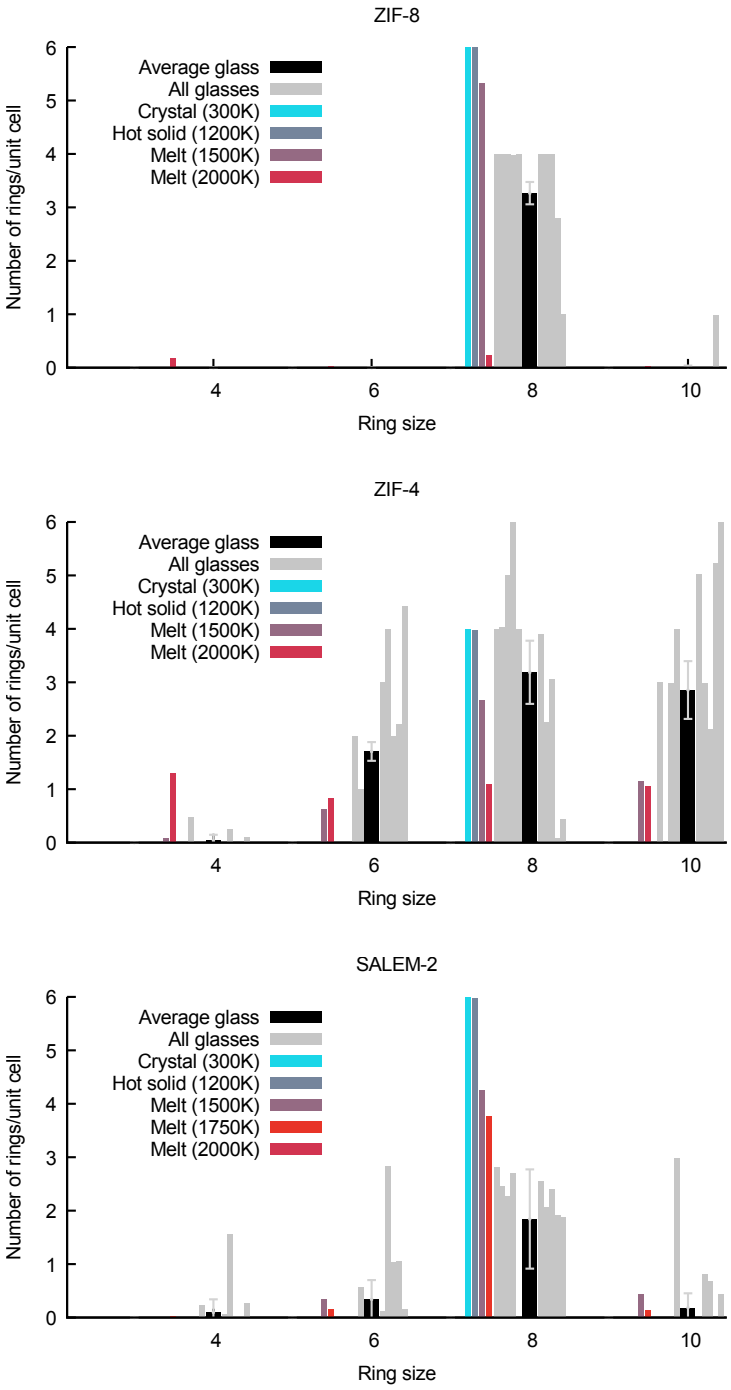

Figure 3.7: Distributions of the sizes of zinc-imidazolate alternate rings for the three frameworks in the three phases (crystalline (light blue), liquid (purple, red and dark red) and glass (black)). The light gray curves correspond to the ten different initial configurations for each framework. At 2000 K SALEM-2 shows no rings at all, hence the absence of dark red bar in the bottom panel.

3.2.2 Thermodynamics

Figure 3.8 presents the potentials of mean force along the zinc-nitrogen coordinates in unit of kT, where k is the Boltzmann constant. This allows to see that, even though the barrier obtained in the glass is small in absolute value, if it were at high temperatures, for ZIF-4 and SALEM-2 with 22 and 27 kJ/mol respectively, at 300 K this barrier of about 10 kT will be only rarely overcome. I note here that I see absolutely no bond cleavage happening in the trajectory of the glasses at 300 K. Here the force of the chemical interaction between the ligand and the zinc seems to play a large role. Indeed, while ZIF-4 and SALEM-2 conserve configurations where an imidazolate cycle is perpendicular to a zinc (in the sense that the normal vector to the plan of the imidazolate goes towards the zinc) and thus exhibit Zn–N distances between 2.7 and 3.7, ZIF-8 seems to rearrange enough to avoid this behaviour.

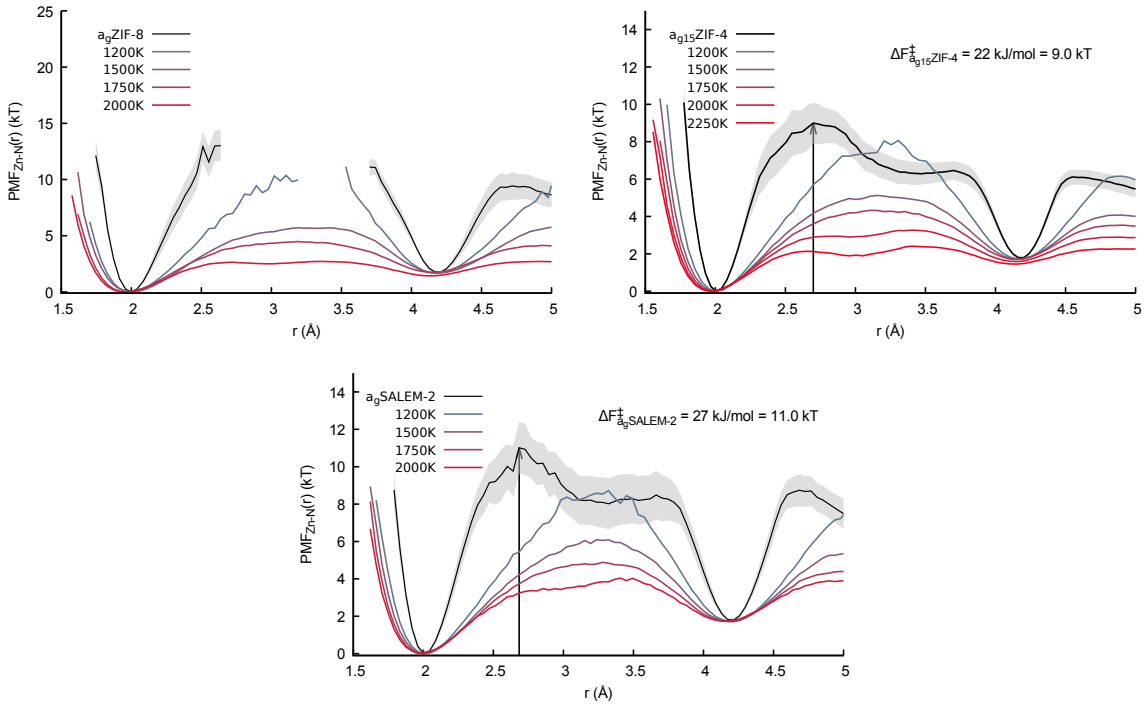

Figure 3.8: Potentials of mean force (PMF) along the Zn–N coordinate for the three structures in unit of kT. In red colors the evolution with the elevation of temperature are reminded and in black the average PMF over all the glass configurations. As previously described the light gray areas correspond to the standard deviation between the ten trajectories.

3.2.3 Porosity

Finally, as in the case of the melting, I studied the total porosity left in the frameworks after quenching. Figure 3.9 presents the distributions of total porous volumes for the three frameworks in the crystalline phase, in the melt and in the glass phase. These graphs reinforce

even more the idea that the topology governs the disorganization and the reconstruction of the frameworks. Indeed, although the average porous volumes of ZIF-8 and SALEM-2 in the glass are 249 and 377 cm^3/g respectively compared to 67 cm^3/g for the ZIF-4 glass, the comparison with the crystal is largely in favour of ZIF-4.

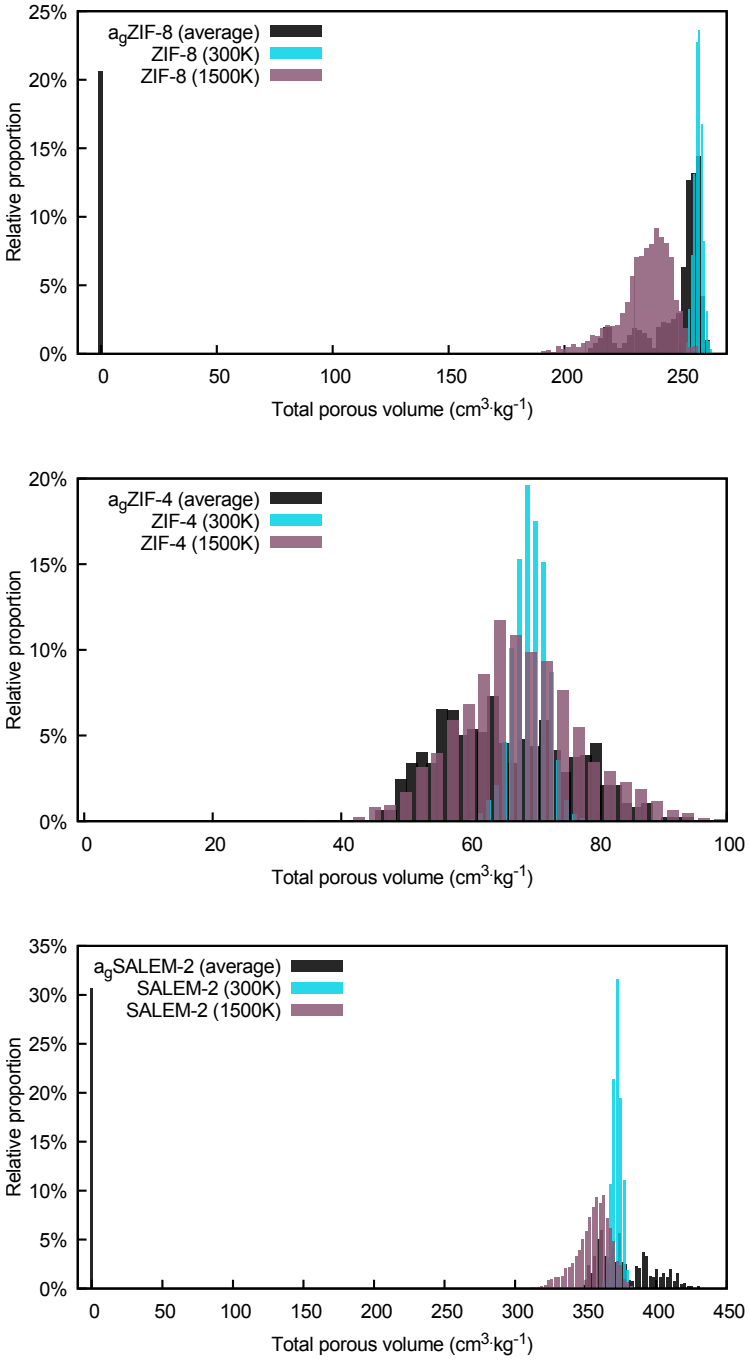

Figure 3.9: Total porous volumes for the three frameworks in all phases: crystalline (light blue), melt (purple) and glass (black). The light gray curves correspond to the ten different initial configurations.

The first remarkable difference is that this average porous volume is 29% higher for ZIF-4 than it was in the crystalline phase, whereas for ZIF-8 it is 3.5% lower and almost unchanged (1% higher) in SALEM-2. Moreover, the values observed in ZIF-8 and SALEM-2, although close to their crystalline equivalent, are tempered by the large proportion of configurations with no porosity at all, accounting for about 20% in ZIF-8 and 30% in SALEM-2. When looking at the average accessible volumes, the difference is even more pronounced between ZIF-4 and the other two frameworks (Table 3.3). For ZIF-8 and SALEM-2, the accessible volume and the total porous volume coincide for a helium probe, so the decrease in ZIF-8 and the small increase in SALEM-2 are unchanged. However, for ZIF-4, the melting process seems to open larger channels than in the crystal, leading to an increase in accessible volume of 64%. Actually, in the crystal the average accessible volume was only 74% of the total porous volume, while it represents 96% in the glass. This result is in line with the experimental findings on the porosity of the ZIF-4 glass analyzed by positron annihilation lifetime spectroscopy (PALS). [214] I note that the large magnitude of the increase I see here is probably exacerbated by the fact that I do not take into account the densification as ZIF-4 is melted and quenched. Nonetheless, the opening of larger voids is confirmed by the PALS analyses which provides another validation of the methods I used.

	ZIF-8	ZIF-4	SALEM-2
Crystal	258	39	372
Glass	249	64	377

Table 3.3: Average accessible volumes (in cm^3/kg) for the three frameworks in the crystalline and the glass phase.

3.3 Conclusion on the quenching of ZIFs

In this chapter, I presented the study of the quenching of ZIF-4, ZIF-8 and SALEM-2 liquids. These quenching simulations were realized by taking snapshots of the trajectories at 1,500 K and cooling them down to 300 K in about 25 ps. The unrealistic quenching rate employed here made the analysis of the process itself impossible, and will not be accessible by this type of methods. However, I could characterize the resulting glass configurations. The comparison between the frameworks indicates that the substitution of the imidazolate cycle and the topology of the frameworks both have roles in the quenching behaviour. However, the topology of ZIF-4, allowing rearrangement of the ring structures during melting and partial recovery during quenching, seems to play a large role in the stabilization of this framework with regard to melting and quenching. In fact, SALEM-2, though it has the same non-substituted imidazolate ligand, sees a collapse of its topology which, far from being countered by quenching, seems to be reinforced by it. However, when looking only at the average distance between the nodes of the framework, the zinc cations, SALEM-2 behaves more like ZIF-4 than ZIF-8 in the sense that the quenching makes it look more like the crystal. Similarly, the proportion of four-fold coordinated zincs increases more in SALEM-2

than in ZIF-8.

This leaves a lot of open questions about the influence of the initial properties of the frameworks on their melting and quenching behaviour, or even if it is possible to melt them. These will have to be addressed experimentally and theoretically. A possible theoretical development would be to directly simulate with classical molecular mechanics methods the glass structures obtained by reverse Monte-Carlo modelling. This would allow to get informations on the structure and dynamics of the glass at larger scale in order to have a better view of the statistical disorder and the thermodynamics of these new exciting materials. Another idea would be to try to simulate the melting and quenching processes with classical methods relying on reactive force-fields, where coordination bonds can be broken, although it probably requires further force-field development before.

Chapter 4

Filling ZIF-4 with CO_2 before melting it

In this chapter, I present the work I did on the melting of ZIF-4 loaded with CO_2. The idea was to simulate the forced filling of ZIF-4 with carbon dioxide and melting it in a confined environment such that CO_2 cannot escape. This is an exploratory study on both the influence of such conditions on the melting of ZIF-4 and on the way CO_2 could be trapped afterwards in the amorphous phase. This study is in the same vein as the one published by Corradini *et al.* in 2016 on the solvation and the transport mechanism of carbon dioxide in molten carbonates investigated by ab initio molecular dynamics methods. [90] It is also consistent with the previous use of amorphous MOFs to trap species. [179]

I briefly present the numerical methods I used and then I show how the carbon dioxide gets along with the ZIF-4 framework, by coordinating itself to the zinc cations and thus influencing the melting.

4.1 Numerical methods

4.1.1 Grand Canonical Monte Carlo simulations

In order to know from which configuration to start to simulate a ZIF-4 unit cell filled with CO_2 molecules, I used Grand Canonical Monte Carlo (GCMC) adsorption simulations as described in chapter 2 of Part I. For that matter, I used the Gibbs software, [222] which is the result of a joint development of the IFP Energies Nouvelles, the CNRS, and Université Paris Sud. [223]

Starting from the aforementioned optimized configuration of ZIF-4 at 0 K, I thus conducted GCMC simulations at increasing partial pressures of carbon dioxide to find the maxi-

mum number of CO_2 molecules I could fill per cell. I considered the ZIF-4 framework as rigid and used the parameters given in [224] for the fixed charges of the framework and the charges and radii of the atoms of CO_2. In Figure 4.1 I present the average number of molecules per cell as a function of the CO_2 partial pressure, as it converges with the number of Monte Carlo steps.

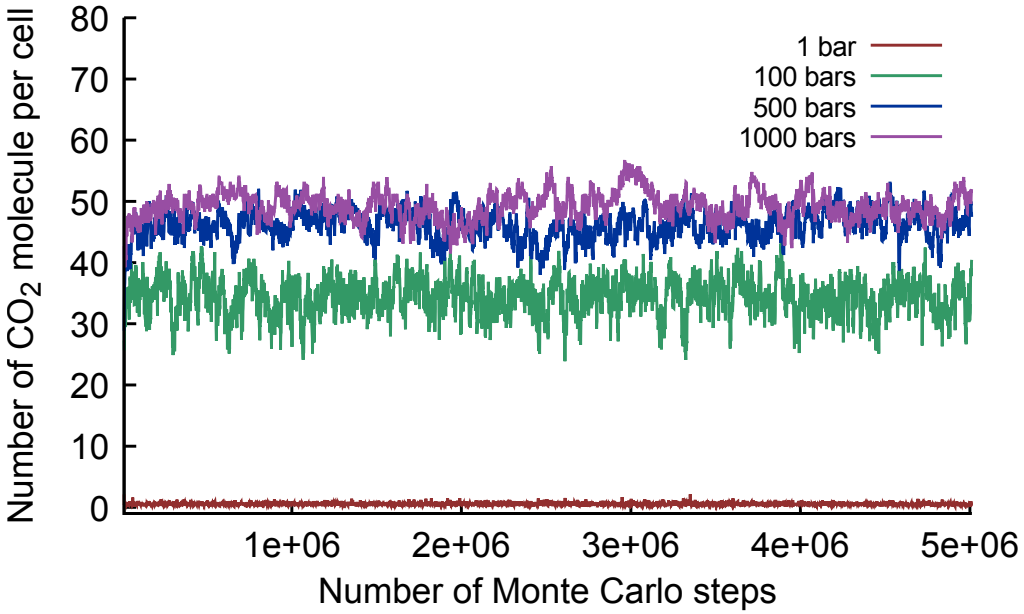

Figure 4.1: Average number of molecules per cell at different pressures. At 1 bar, it converges to about 0.5 molecule/unit cell, 34 molecules/cell at 100 bars, 46 molecules/cell at 500 bars and 49 molecules/cell at 1,000 bars.

I considered the already very high pressure of 1000 bars of carbon dioxide to provide a configuration of ZIF-4 loaded with a maximum number of molecules. Finally, the configuration I took has 52 molecules per unit cell.

4.1.2 Ab initio molecular dynamics simulations for melting

I then optimized the geometry of this initial configuration with CP2K at 0 K with the same parameters as the ones used for the optimization before melting the empty frameworks. This yielded the structure shown in Figure 4.2.

Starting from this structure I then carried out 8 simulations at different temperatures with the same methods employed for the empty frameworks. The temperatures considered are: 300 K, 600 K, 900 K, 1,000 K, 1,200 K, 1,350 K, 1,500 K and 1,750 K.

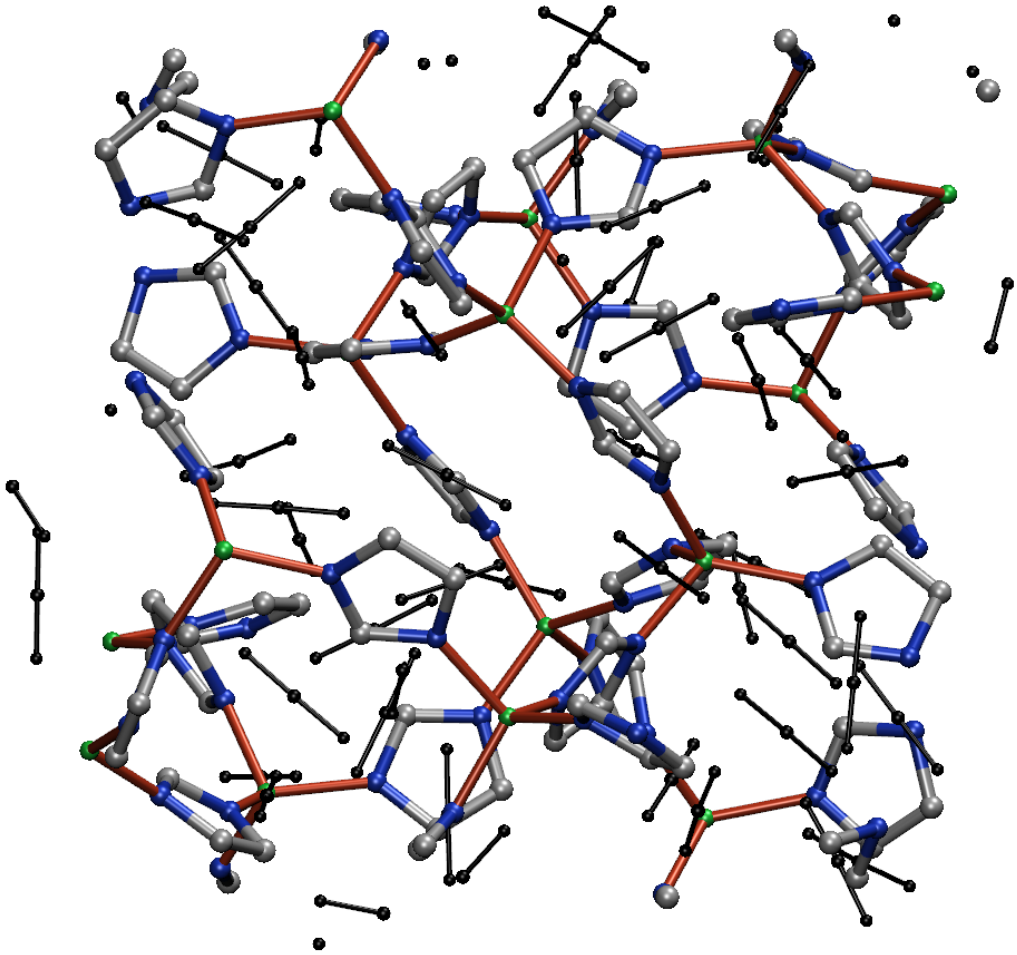

Figure 4.2: Configuration of the loaded ZIF-4 after DFT optimization. CO_2 molecules are shown in black, zinc atoms in green, nitrogen atoms in blue, carbon atoms from the framework in gray and zinc-nitrogen coordination bonds in red.

4.2 Influence of the carbon dioxide in melting

4.2.1 Zinc-nitrogen and zinc-oxygen coordinations

The left panel of Figure 4.3 shows a complete view of the zinc coordination during melting. In green only the Zn–N coordination is taken into account, in red I added the coordination with oxygen atoms from the carbon dioxide molecules. It means that a four-fold coordination for the red histogram can correspond to 3 nitrogens and 1 oxygen coordinated to a zinc. In blue, I remind the situation with no CO_2.

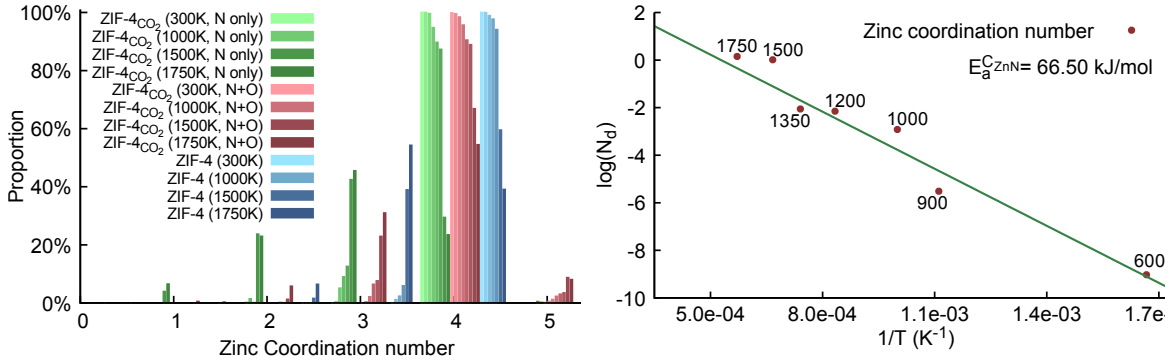

Figure 4.3: Left: green: Zn–N coordination only, red: coordination with oxygen atoms is added (four-fold coordination for the red histogram can correspond to 3 nitrogens and 1 oxygen coordinated to a zinc), blue: situation without CO_2. Right: van 't Hoff plot of the formation of Zn–N coordination defects ($E_a^{C_{ZnN}}$ is the associated activation energy). The linear fit, taking into account the temperatures where four-fold coordination is still the most represented (to talk about defects) is in green.

Before melting and up to 1,350 K, oxygen coordination is extremely weak with about 0.09 oxygen per zinc at 1,350 K (and 3.9 nitrogens). However, in the liquid phase at 1,500 K, this number goes to about 0.85 oxygen per zinc while there is almost 1 nitrogen less per zinc in average (3.0 against 3.9). As a result, carbon dioxide seems to form quite strong interactions with the exposed cations during melting. On the other hand, the activation energy associated with the Zn–N coordination defects goes up compared to the empty ZIF-4. Indeed, from 52 kJ/mol, it increases to 66.5 kJ/mol, representing a 28% increase, which can be interpreted as a higher difficulty to create defects at low temperature. I note that this does not mean that during melting less Zn–N coordination defects are created, but rather that the transition from the defects regime to a majority of non four-fold coordination is happening at lower temperature (between 1,350 K and 1,500 K with CO_2 and above 1,500 K without).

4.2.2 Deformation of carbon dioxide

As melting happens, some carbon dioxide molecules get coordinated to the zinc cations which results in the bending of the O–C–O angle as presented in Figure 4.4. At low temperatures,

the angle is close to 180°. Then it progressively shifts to lower values in average with the thermal widening. Finally, at 1,000 K there is already a trace of the deformation linked to the small oxygen-zinc coordination, which becomes important at 1,500 K and higher. Whether this is physically realistic remains to be confirmed by experimental evidence.

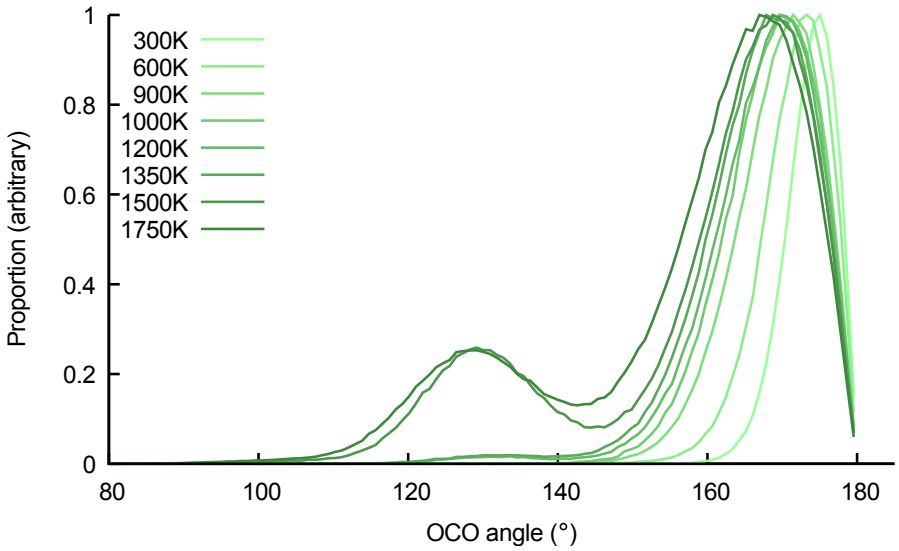

Figure 4.4: Distribution of the O–C–O angle in the carbon dioxide molecules as a function of temperature.

4.2.3 Thermodynamics

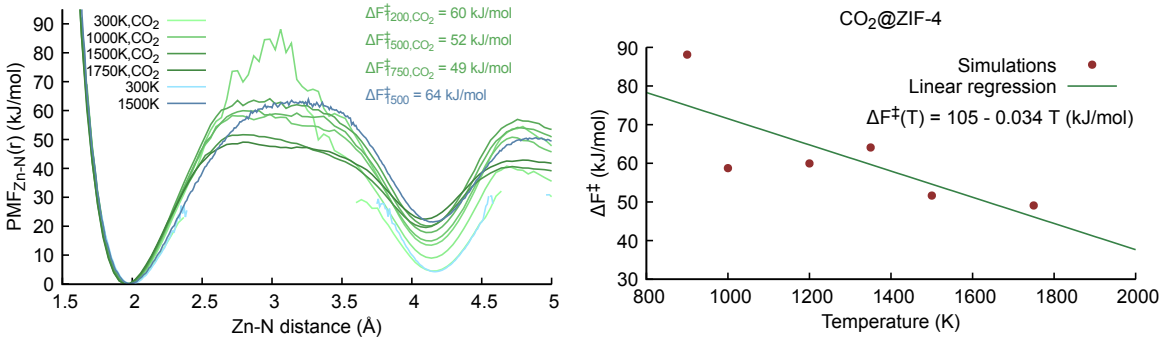

Figure 4.5: Left: Potential of mean force along the zinc-nitrogen coordinate at different temperatures (green) with the ones for the empty framework at 300 K and 1,500 K (blue). Right: van 't Hoff plot of the activation free energy necessary to break a Zn–N coordination bond.

Looking at the free energy profiles along the Zn–N coordinate, I see an interesting behaviour (see Figure 4.5). The associated activation free enthalpy of 105 kJ/mol is significantly lower than the one observed with the melting of the empty ZIF-4 (127 kJ/mol). This seems to point to a facilitating role of the carbon dioxide in the melting process, as I have shown

before that it depends very much on this value of activation enthalpy.

4.2.4 Dynamics of the liquid phase

To characterize the dynamics of the liquid phase, I looked at the diffusion coefficients of the oxygen atoms and the zinc atoms (see Figure 4.6). As expected, carbon dioxide diffusion is present in my simulations at temperature as low as 900 K, despite the small time scales achieved (about 50 ps). The associated activation energy is relatively small, although not negligible compared to kT with 24 kJ/mol corresponding to about $10k$T at room temperature.

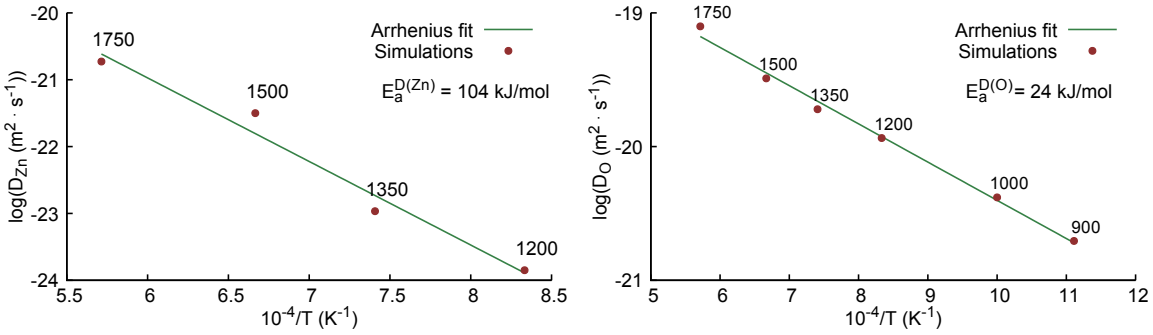

Figure 4.6: Left: van 't Hoff plot of the diffusion coefficient for the zinc atoms. Right: van 't Hoff plot of the diffusion coefficient for the oxygen atoms.

On the other hand, the zinc diffusion starts also at relatively low temperatures. In the empty framework, free diffusion was starting only at 1,500 K, whereas here it starts at 1,200 K. Again, this goes in the sense that carbon dioxide has a facilitating role in the disorganization of the framework leading to melting.

4.3 Perspectives

This last chapter is a report on a work that is still ongoing. A lot of analyses can still be carried on these already ran simulations to investigate further the mechanism by which carbon dioxide coordinates to zinc cations in ZIF-4 during melting. I showed here that it appears to have a role in the reduction of the melting temperature by enhancing the diffusion of the zinc atoms and the breakage of the Zn–N coordination bond. The topological analysis of the modification of the framework would be interesting to see the change in the melting behaviour.

This study being purely theoretical, it calls for associated experiments to be performed. I note here that the values used for the pressure are unreachable in practice but were used in the simulations to observe rare activated events, namely CO_2–Zn coordination, in short time scales.

Main conclusion

Using quantum level calculations I was able to show that the mechanical properties of hypothetical zeolite structures are very sensitive properties, which have to be taken with caution when computed by force-field level calculations. I have shown that machine learning techniques can offer a way to build fast and more reliable predictive models, as I did for the Poisson's ratio and its extreme values.

The study of the melting and quenching of ZIFs shed light on the crucial importance of the topology over chemistry for the capability of a ZIF framework to melt. During this study, I also uncovered the microscopic mechanism behind the melting of ZIFs. Combining theoretical and experimental studies will be essential to further confirm my hypotheses by comparing frameworks with different ligands, different cations and different topologies. The goal would be to have a way to tune porous MOF liquids and glasses, as is done for crystalline MOFs. The liquids would be of interest for liquid phase separations, homogeneous catalysis and ion transport and could also be used as intermediaries to obtain mechanically and thermally stable porous MOF glasses. The glasses could serve as new materials to trap harmful or polluting substances and as optically or electronically active glasses through the incorporation of such functionalities in the crystalline MOF structure.

Overall, the questions opened by this thesis relate to how structures and properties are connected in microporous materials. A lot of perspectives are now open, whether it is about zeolites or MOFs, and amorphous MOFs in particular.

The main question for the study of mechanical properties of zeolites and their link to structural descriptors is the interaction of this link with the changes in chemistry. Indeed, by studying zeolitic structures with different chemical elements, not only limited to aluminium, but also gallium or germanium, and different extra-framework cations, one could uncover what is inherent to the topology of the framework and what lies in the details of the chemical interactions for the determination of the mechanical properties of zeolites. I focused a lot on auxeticity, but other anomalous properties can also be investigated such as negative linear compressibility, or a mixed thermal-mechanical property like negative thermal expansion.

Beyond the screening of interesting zeolitic structures with regard to a particular property, the question of their feasibility remains. The zeolite conundrum has resisted many theoretical

and experimental studies, though there have been recent experimental advances, with the creation of the ADOR process to synthesize "unfeasible" zeolites. [225, 226] Some of these new structures have even been investigated in a theoretical study. [227] A way that still has to be explored and could give more theoretical insights on the feasibility of these frameworks would be to model the synthesis process itself to understand the driving forces and be able to really design zeolites for specific applications, that would have been predicted earlier.

In the realm of amorphous MOFs, as written before, a lot remains to be understood. One of the perspective of my work is to determine criteria for the capability of a framework to melt based on the nature of the metal, the composition of the ligand and the topology. In order to tackle this interrogation, an idea would be to train reactive force-fields on ab initio molecular dynamics simulations of the melting of different MOFs to be able to simulate and understand the capability of melting for these materials in a less computationally expensive way. Even beyond standard conditions, the study of the influence of physical parameters on the melting, such as increase of pressure, could widen the possibilities, for example by making melting possible in a framework for which it was unreachable at ambient pressure. In a second time, simpler physical models could be proposed to reduce further the dimensionality of the problem and identify the key factors leading to a particular melting behaviour. For instance as we have seen that the topology plays a role, a question that could be addressed would be: which particular topological properties (symmetry, connectivity, topology of the metal-ligand coordination) matter the most? With such criteria and a better knowledge of the experimental feasibility of the frameworks considered a real rational design of new porous liquids and glasses could be achieved.

List of publications

Publications linked to my PhD work:

- Romain Gaillac, Pluton Pullumbi and François-Xavier Coudert, "ELATE: an open-source online application for analysis and visualization of elastic tensors", *Journal of Physics: Condensed Matter* 28(27), 275201 July 2016.
- Jack D. Evans, Guillaume Fraux, Romain Gaillac, Daniela Kohen, Fabien Trousselet, Jean-Mathieu Vanson and François-Xavier Coudert, "Computational Chemistry Methods for Nanoporous Materials", *Chemistry of Materials* September 2016.
- Romain Gaillac, Pluton Pullumbi, Kevin A. Beyer, Karena W. Chapman, David A. Keen, Thomas D. Bennett and François-Xavier Coudert, "Liquid metal–organic frameworks", *Nature Materials* October 2017.
- Romain Gaillac, Pluton Pullumbi and François-Xavier Coudert, "Melting of Zeolitic Imidazolate Frameworks with Different Topologies: Insight from First-Principles Molecular Dynamics", *The Journal of Physical Chemistry C* 122(12), 6730–6736 March 2018.

Publications from a previous work:

- Romain Gaillac, Morgane Vacher, Alfred Maquet, Richard Taïeb and Jérémie Caillat, "Attosecond photoemission dynamics encoded in real-valued continuum wave functions", *Physical Review A* 93(1) January 2016.
- Morgane Vacher, Romain Gaillac, Alfred Maquet, Richard Taïeb and Jérémie Caillat, "Transition dynamics in two-photon ionisation", *Journal of Optics* 19(11), 114011 November 2017.

References

References

[1] M. E. Davis, "Ordered porous materials for emerging applications", *Nature* 417(6891), 813 (2002).

[2] K. D. Mondale, R. M. Carland and F. F. Aplan, "The comparative ion exchange capacities of natural sedimentary and synthetic zeolites", *Miner. Eng.* 8(4-5), 535–548 (1995).

[3] M. Suzuki, "Activated carbon fiber: fundamentals and applications", *Carbon* 32(4), 577–586 (1994).

[4] S. Kitagawa, "Future Porous Materials", *Acc. Chem. Res.* 50(3), 514–516 (2017).

[5] N. Eroglu, M. Emekci and C. G. Athanassiou, "Applications of natural zeolites on agriculture and food production", *J. Sci. Food Agric* 97(11), 3487–3499 (2017).

[6] B. Yilmaz, N. Trukhan and U. MüLler, "Industrial Outlook on Zeolites and Metal Organic Frameworks", *Chin. J. Catal.* 33(1), 3–10 (2012).

[7] P. Silva, S. M. F. Vilela, J. P. C. Tomé and F. A. Almeida Paz, "Multifunctional metal–organic frameworks: from academia to industrial applications", *Chem. Soc. Rev.* 44(19), 6774–6803 (2015).

[8] RnR Market Research, "World Activated Carbon Market to Reach 1.733 Million Tons by 2017, Says a New Research Report at RnRMarketResearch.com". https://www.prnewswire.com/news-releases/world-activated-carbon-market-to-reach-1733-million-tons-by-2017-says-a-new-research-report-at-rnrmarketresearchcom-499576251.html.

[9] R. Geyer, J. R. Jambeck and K. L. Law, "Production, use, and fate of all plastics ever made", *Sci. Adv.* 3(7), e1700782 (2017).

[10] D. Das, D. P. Samal and M. BC, "Preparation of Activated Carbon from Green Coconut Shell and its Characterization", *Journal of Chemical Engineering & Process Technology* 06(05), 1000248 (2015).

[11] K. Momma and F. Izumi, "VESTA 3 for three-dimensional visualization of crystal, volumetric and morphology data", *J. Appl. Cryst.* 44(6), 1272–1276 (2011).

[12] R. J.-M. Pellenq, B. Rousseau and P. E. Levitz, "A Grand Canonical Monte Carlo study of argon adsorption/condensation in mesoporous silica glasses", *Phys. Chem. Chem. Phys.* 3(7), 1207–1212 (2001).

[13] H. M. Rietveld, "A profile refinement method for nuclear and magnetic structures", *J. Appl. Crystallogr.* 2(2), 65–71 (1969).

[14] F. Mouhat and F.-X. Coudert, "Necessary and sufficient elastic stability conditions in various crystal systems", *Phys. Rev. B* 90(22), 224104 (2014).

[15] H. J. Monkhorst and J. D. Pack, "Special points for Brillouin-zone integrations", *Phys. Rev. B* 13(12), 5188 (1976).

[16] T. D. Bennett and A. K. Cheetham, "Amorphous Metal–Organic Frameworks", *Acc. Chem. Res.* 47(5), 1555–1562 (2014).

[17] C. Colella and A. F. Gualtieri, "Cronstedt's zeolite", *Micropor. Mesopor. Mat.* 105(3), 213–221 (2007).

[18] M. D. Foster and M. M. J. Treacy, "A Database of Hypothetical Zeolite Structures". http://www.hypotheticalzeolites.net.

[19] B. F. Hoskins and R. Robson, "Infinite polymeric frameworks consisting of three dimensionally linked rod-like segments", *J. Am. Chem. Soc.* 111(15), 5962–5964 (1989).

[20] H. Li, M. Eddaoudi, M. O'Keeffe and O. M. Yaghi, "Design and synthesis of an exceptionally stable and highly porous metal-organic framework", *Nature* 402(6759), 276–279 (1999).

[21] H. Furukawa, K. E. Cordova, M. O'Keeffe and O. M. Yaghi, "The Chemistry and Applications of Metal-Organic Frameworks", *Science* 341(6149), 1230444 (2013).

[22] J. C. Tan and A. K. Cheetham, "Mechanical properties of hybrid inorganic–organic framework materials: establishing fundamental structure–property relationships", *Chem. Soc. Rev.* 40(2), 1059 (2011).

[23] J. Urquhart, "World's first commercial MOF keeps fruit"(2016). https://www.chemistryworld.com/news/worlds-first-commercial-mof-keeps-fruit-fresh/1017469.article.

[24] F.-X. Coudert, "Responsive Metal–Organic Frameworks and Framework Materials: Under Pressure, Taking the Heat, in the Spotlight, with Friends", *Chem. Mater.* 27(6), 1905–1916 (2015).

[25] T. D. Bennett, A. K. Cheetham, A. H. Fuchs and F.-X. Coudert, "Interplay between defects, disorder and flexibility in metal-organic frameworks", *Nat. Chem.* 9(1), 11–16 (2017).

[26] F.-X. Coudert and A. H. Fuchs, "Computational characterization and prediction of metal–organic framework properties", *Coord. Chem. Rev.* 307(2), 211–236 (2015).

[27] G. Fraux and F.-X. Coudert, "Recent advances in the computational chemistry of soft porous crystals", *ChemComm* 53, 7211–7221 (2017).

[28] T. Tian, Z. Zeng, D. Vulpe, M. E. Casco, G. Divitini, P. A. Midgley, J. Silvestre-Albero, J.-C. Tan, P. Z. Moghadam and D. Fairen-Jimenez, "A sol–gel monolithic metal–organic framework with enhanced methane uptake", *Nat. Mater.* 17(2), 174–179 (2017).

[29] H. Oh, S. Maurer, R. Balderas-Xicohtencatl, L. Arnold, O. V. Magdysyuk, G. Schütz, U. Müller and M. Hirscher, "Efficient synthesis for large-scale production and characterization for hydrogen storage of ligand exchanged MOF-74/174/184-M (M = Mg^{2+}, Ni^{2+})", *Int. J. Hydrog. Energy* 42(2), 1027–1035 (2017).

[30] M. Witman, S. Ling, A. Gladysiak, K. C. Stylianou, B. Smit, B. Slater and M. Haranczyk, "Rational Design of a Low-Cost, High-Performance Metal–Organic Framework for Hydrogen Storage and Carbon Capture", *J. Phys. Chem. C* 121(2), 1171–1181 (2017).

[31] T. J. Strathmann and S. C. B. Myneni, "Speciation of aqueous Ni(II)-carboxylate and Ni(II)-fulvic acid solutions: Combined ATR-FTIR and XAFS analysis", *Geochim. Cosmochim. Acta* 68(17), 3441–3458 (2004).

[32] M. Eddaoudi, J. Kim, N. Rosi, D. Vodak, J. Wachter, M. O'Keeffe and O. M. Yaghi, "Systematic Design of Pore Size and Functionality in Isoreticular MOFs and Their Application in Methane Storage", *Science* 295, 469–472 (2002).

[33] O. M. Yaghi, M. O'keeffe, N. W. Ockwig, H. K. Chae, M. Eddaoudi and J. Kim, "Reticular synthesis and the design of new materials", *Nature* 423(6941), 705 (2003).

[34] D. J. Tranchemontagne, J. L. Mendoza-Cortés, M. O'Keeffe and O. M. Yaghi, "Secondary building units, nets and bonding in the chemistry of metal–organic frameworks", *Chem. Soc. Rev.* 38(5), 1257 (2009).

[35] M. Jahan, Q. Bao and K. P. Loh, "Electrocatalytically Active Graphene–Porphyrin MOF Composite for Oxygen Reduction Reaction", *J. Am. Chem. Soc.* 134(15), 6707–6713 (2012).

[36] Honghan Fei and Seth M. Cohen, "A robust, catalytic metal–organic framework with open 2,2'-bipyridine sites", *Chem. Commun.* 50(37), 4810–4812 (2014).

[37] K. S. Park, Z. Ni, A. P. Côté, J. Y. Choi, R. Huang, F. J. Uribe-Romo, H. K. Chae, M. O'Keeffe and O. M. Yaghi, "Exceptional chemical and thermal stability of zeolitic imidazolate frameworks", *Proc. Natl. Acad. Sci. U.S.A.* 103(27), 10186–10191 (2006).

[38] Z. Ni and R. I. Masel, "Rapid Production of Metal-Organic Frameworks via Microwave-Assisted Solvothermal Synthesis", *J. Am. Chem. Soc.* 128(38), 12394–12395 (2006).

[39] N. Stock and S. Biswas, "Synthesis of Metal-Organic Frameworks (MOFs): Routes to Various MOF Topologies, Morphologies, and Composites", *Chem. Rev.* 112(2), 933–969 (2012).

[40] U. Müller, H. Pütter, M. Hesse, H. Wessel, M. Schubert, J. Huff and M. Guzmann. "Method for Electrochemical Production of a Crystalline Porous Metal Organic Skeleton Material", number WO/2005/049892(2005).

[41] Seth M. Cohen, "The Postsynthetic Renaissance in Porous Solids", *J. Am. Chem. Soc.* 139(8), 2855–2863 (2017).

[42] K. M. L. Taylor-Pashow, J. Della Rocca, Z. Xie, S. Tran and W. Lin, "Postsynthetic Modifications of Iron-Carboxylate Nanoscale Metal-Organic Frameworks for Imaging and Drug Delivery", *J. Am. Chem. Soc.* 131(40), 14261–14263 (2009).

[43] O. Karagiaridi, M. B. Lalonde, W. Bury, A. A. Sarjeant, O. K. Farha and J. T. Hupp, "Opening ZIF-8: A Catalytically Active Zeolitic Imidazolate Framework of Sodalite Topology with Unsubstituted Linkers", *J. Am. Chem. Soc.* 134(45), 18790–18796 (2012).

[44] B Panella, M. Hirscher, H. Pütter and U. Müller, "Hydrogen Adsorption in Metal–Organic Frameworks: Cu-MOFs and Zn-MOFs Compared", *Adv. Funct. Mater.* 16(4), 520–524 (2006).

[45] O. I. Lebedev, F. Millange, C. Serre, G. Van Tendeloo and G. Férey, "First Direct Imaging of Giant Pores of the Metal-Organic Framework MIL-101", *Chem. Mater.* 17(26), 6525–6527 (2005).

[46] J. Moellmer, E.B. Celer, R. Luebke, A.J. Cairns, R. Staudt, M. Eddaoudi and M. Thommes, "Insights on Adsorption Characterization of Metal-Organic Frameworks: A Benchmark Study on the Novel soc-MOF", *Micropor. Mesopor. Mat.* 129(3), 345–353 (2010).

[47] N. L. Rosi, J. Eckert, M. Eddaoudi, D. T. Vodak, J. Kim, M. O'Keeffe and O. M. Yaghi, "Hydrogen Storage in Microporous Metal-Organic Frameworks", *Science* 300(5622), 1127–1129 (2003).

[48] H. K. Chae, D. Y. Siberio-Pérez, J. Kim, Y. Go, M. Eddaoudi, A. J. Matzger, M. O'Keeffe and O. M. Yaghi, "A route to high surface area, porosity and inclusion of large molecules in crystals", *Nature* 427(6974), 523–527 (2004).

[49] Y. Zhao, S.-Y. Lee, N. Becknell, O. M. Yaghi and C. A. Angell, "Nanoporous Transparent MOF Glasses with Accessible Internal Surface", *J. Am. Chem. Soc.* 138(34), 10818–10821 (2016).

[50] T. D. Bennett, J.-C. Tan, Y. Yue, E. Baxter, C. Ducati, N. J. Terrill, H. H. M. Yeung, Z. Zhou, W. Chen, S. Henke, A. K. Cheetham and G. N. Greaves, "Hybrid glasses from strong and fragile metal-organic framework liquids", *Nat. Commun.* 6, 8079 (2015).

[51] T. D. Bennett, P. J. Saines, D. A. Keen, J.-C. Tan and A. K. Cheetham, "Ball-Milling-Induced Amorphization of Zeolitic Imidazolate Frameworks (ZIFs) for the Irreversible Trapping of Iodine", *Chem. Eur. J.* 19(22), 7049–7055 (2013).

[52] D. Xu, Y. Liu, Y. Tian and L.-M. Wang, "Communication: Enthalpy relaxation in a metal-organic zeolite imidazole framework (ZIF-4) glass-former", *J. Chem. Phys.* 146(12), 121101 (2017).

[53] M. R. Ryder, T. D. Bennett, C. S. Kelley, M. D. Frogley, G. Cinque and J.-C. Tan, "Tracking thermal-induced amorphization of a zeolitic imidazolate framework via synchrotron in situ far-infrared spectroscopy", *ChemComm* 53(52), 7041–7044 (2017).

[54] T. D. Bennett, Y. Yue, P. Li, A. Qiao, H. Tao, N. G. Greaves, T. Richards, G. I. Lampronti, S. A. T. Redfern, F. Blanc, O. K. Farha, J. T. Hupp, A. K. Cheetham and D. A. Keen, "Melt-Quenched Glasses of Metal-Organic Frameworks", *J. Am. Chem. Soc.* 138(10), 3484–3492 (2016).

[55] T. D. Bennett, D. A. Keen, J.-C. Tan, E. R. Barney, A. L. Goodwin and A. K. Cheetham, "Thermal amorphization of zeolitic imidazolate frameworks", *Angew. Chem.* 123(13), 3123–3127 (2011).

[56] T. D. Bennett, T. Todorova, E. Baxter, D. G. Reid, C. Gervais, B. Bueken, B. Van De Voorde, D. E. De Vos, D. A. Keen and C. Mellot-Draznieks, "Connecting Defects and Amorphization in UiO-66 and MIL-140 Metal-organic Frameworks: A Combined Experimental and Computational Study", *Phys. Chem. Chem. Phys.* 18, 2192–2201 (2015).

[57] C Orellana-Tavra, E. F. Baxter, T. Tian, T. D. Bennett, N. K. H. Slater, A. K. Cheetham and D. Fairen-Jimenez, "Amorphous metal–organic frameworks for drug delivery", *ChemComm* 51(73), 13878–13881 (2015).

[58] T. D. Bennett, S. Cao, J. C. Tan, D. A. Keen, E. G. Bithell, P. J. Beldon, T. Friscic and A. K. Cheetham, "Facile Mechanosynthesis of Amorphous Zeolitic Imidazolate Frameworks", *J. Am. Chem. Soc.* 133(37), 14546–14549 (2011).

[59] S. Tominaka, H. Hamoudi, T. Suga, T. D. Bennett, A. B. Cairns and A. K. Cheetham, "Topochemical conversion of a dense metal–organic framework from a crystalline insulator to an amorphous semiconductor", *Chem. Sci.* 6(2), 1465–1473 (2015).

[60] R. Gaillac, P. Pullumbi, K. A. Beyer, K. W. Chapman, D. A. Keen, T. D. Bennett and F.-X. Coudert, "Liquid metal–organic frameworks", *Nat. Mater.* 16, 1149–1154 (2017).

[61] N. Metropolis, A. W. Rosenbluth, M. N. Rosenbluth, A. H. Teller and E. Teller, "Equation of State Calculations by Fast Computing Machines", *J. Chem. Phys.* 21(6), 1087–1092 (1953).

[62] I. E. Fermi, P. Pasta, S. Ulam and M. Tsingou. "Studies of the nonlinear problems". Technical report, Los Alamos Scientific Lab., N. Mex., (1955).

[63] B. J. Alder and T. E. Wainwright, "Phase Transition for a Hard Sphere System", *J. Chem. Phys.* 27(5), 1208–1209 (1957).

[64] F. Sterpone and S. Melchionna, "Thermophilic proteins: insight and perspective from in silico experiments", *Chem. Soc. Rev.* 41(5), 1665–1676 (2012).

[65] J. L. Jenkins, A. Bender and J. W. Davies, "In silico target fishing: Predicting biological targets from chemical structure", *Drug. Discov. Today. Technol.* 3(4), 413–421 (2006).

[66] A. Boutin and R. Vuilleumier, "De Boltzmann aux expériences " in silico"", *L'actualité chimique* (353-354), 61–65 (2011).

[67] M. Chebbi, S. Chibani, J.-F. Paul, L. Cantrel and M. Badawi, "Evaluation of volatile iodine trapping in presence of contaminants: A periodic DFT study on cation exchanged-faujasite", *Micropor. Mesopor. Mat.* 239, 111–122 (2017).

[68] G. G. N. Angilella and A. La Magna, editors, *Correlations in Condensed Matter under Extreme Conditions*, Springer International Publishing (2017).

[69] D. S. Sholl and J. A. Steckel, *Density functional theory: a practical introduction*, Wiley (2009).

[70] P. Hohenberg and W. Kohn, "Inhomogeneous electron gas", *Phys. Rev.* 136(3B), B864 (1964).

[71] W. Kohn and L. J. Sham, "Self-Consistent Equations Including Exchange and Correlation Effects", *Phys. Rev.* 140(4A), A1133 (1965).

[72] R. G. Parr, "Aspects of density functional theory", *Philos. Mag. B* 69(5), 737–743 (1994).

[73] K. Lejaeghere, G. Bihlmayer, T. Bjorkman, P. Blaha, S. Blugel, V. Blum, D. Caliste, I. E. Castelli, S. J. Clark, A. Dal Corso, S. de Gironcoli, T. Deutsch, J. K. Dewhurst, I. Di Marco, C. Draxl, M. Du ak, O. Eriksson, J. A. Flores-Livas, K. F. Garrity, L. Genovese, P. Giannozzi, M. Giantomassi, S. Goedecker, X. Gonze, O. Granas, E. K. U. Gross, A. Gulans, F. Gygi, D. R. Hamann, P. J. Hasnip, N. A. W. Holzwarth, D. Iu an, D. B. Jochym, F. Jollet, D. Jones, G. Kresse, K. Koepernik, E. Kucukbenli, Y. O. Kvashnin, I. L. M. Locht, S. Lubeck, M. Marsman, N. Marzari, U. Nitzsche, L. Nordstrom, T. Ozaki, L. Paulatto, C. J. Pickard, W. Poelmans, M. I. J. Probert, K. Refson, M. Richter, G.-M. Rignanese, S. Saha, M. Scheffler, M. Schlipf, K. Schwarz, S. Sharma, F. Tavazza, P. Thunstrom, A. Tkatchenko, M. Torrent, D. Vanderbilt, M. J. van Setten, V. Van Speybroeck, J. M. Wills, J. R. Yates, G.-X. Zhang and S. Cottenier, "Reproducibility in density functional theory calculations of solids", *Science* 351(6280), aad3000 (2016).

[74] J. P. Perdew, "Jacob's ladder of density functional approximations for the exchange-correlation energy", *AIP Conf. Proc.* 577(1), 1–20 (2001).

[75] J. P. Perdew, A. Ruzsinszky, G. I. Csonka, O. A. Vydrov, G. E. Scuseria, L. A. Constantin, X. Zhou and K. Burke, "Restoring the Density-Gradient Expansion for Exchange in Solids and Surfaces", *Phys. Rev. Lett.* 100(13), 136406 (2008).

[76] A. W. Thornton, R. Babarao, A. Jain, F. Trousselet and F.-X. Coudert, "Defects in metal–organic frameworks: a compromise between adsorption and stability?", *Dalton Trans.* 45(10), 4352–4359 (2016).

[77] S. J. Lee, C. Doussot, A. Baux, L. Liu, G. B. Jameson, C. Richardson, J. J. Pak, F. Trousselet, F.-X. Coudert and S. G Telfer, "Multicomponent Metal–Organic Frameworks as Defect-Tolerant Materials", *Chem. Mater.* 28(1), 368–375 (2016).

[78] A. U. Ortiz, A. Boutin, A. H. Fuchs and F.-X. Coudert, "Metal–organic frameworks with wine-rack motif: What determines their flexibility and elastic properties?", *J. Chem. Phys.* 138(17), 174703 (2013).

[79] J. Heyd and G. E. Scuseria, "Efficient hybrid density functional calculations in solids: Assessment of the Heyd–Scuseria–Ernzerhof screened Coulomb hybrid functional", *J. Chem. Phys.* 121(3), 1187–1192 (2004).

[80] S. Grimme, "Semiempirical GGA-type density functional constructed with a long-range dispersion correction", *J. Comput. Chem.* 27(15), 1787–1799 (2006).

[81] S. Grimme, A. Hansen, J. G. Brandenburg and C. Bannwarth, "Dispersion-Corrected Mean-Field Electronic Structure Methods", *Chem. Rev.* 116(9), 5105–5154 (2016).

[82] J. Moellmann and S. Grimme, "DFT-D3 Study of Some Molecular Crystals", *J. Phys. Chem. C* 118(14), 7615–7621 (2014).

[83] A. Tkatchenko, R. A. DiStasio, R. Car and M. Scheffler, "Accurate and Efficient Method for Many-Body van der Waals Interactions", *Phys. Rev. Lett.* 108(23), 236402 (2012).

[84] D. E. P. Vanpoucke, K. Lejaeghere, V. Van Speybroeck, M. Waroquier and A. Ghysels, "Mechanical Properties from Periodic Plane Wave Quantum Mechanical Codes: The Challenge of the Flexible Nanoporous MIL-47(V) Framework", *J. Phys. Chem. C* 119(41), 23752–23766 (2015).

[85] K. Barthelet, J. Marrot, D. Riou and G. Férey, "A Breathing Hybrid Organic–Inorganic Solid with Very Large Pores and High Magnetic Characteristics", *Angew. Chem. Int. Ed.* 41(2), 281–284 (2002).

[86] C. G. Broyden, "A class of methods for solving nonlinear simultaneous equations", *Math. Comput.* 19(92), 577–593 (1965).

[87] D. D. Johnson, "Modified Broyden's method for accelerating convergence in self-consistent calculations", *Phys. Rev. B* 38(18), 12807 (1988).

[88] A. E. Reed, R. B. Weinstock and F. Weinhold, "Natural population analysis", *J. Chem. Phys.* 83(2), 735–746 (1985).

[89] T. A. Manz and D. S. Sholl, "Chemically Meaningful Atomic Charges That Reproduce the Electrostatic Potential in Periodic and Nonperiodic Materials", *J. Chem. Theory Comput.* 6(8), 2455–2468 (2010).

[90] D. Corradini, F.-X. Coudert and R. Vuilleumier, "Carbon dioxide transport in molten calcium carbonate occurs through an oxo-Grotthuss mechanism via a pyrocarbonate anion", *Nat. Chem.* 8(5), 454–460 (2016).

[91] E. Deumens, A. Diz, R. Longo and Y. Öhrn, "Time-dependent theoretical treatments of the dynamics of electrons and nuclei in molecular systems", *Rev. Mod. Phys.* 66(3), 917–983 (1994).

[92] R. Car and M. Parrinello, "Unified Approach for Molecular Dynamics and Density-Functional Theory", *Phys. Rev. Lett.* 55(22), 2471–2474 (1985).

[93] G. Lippert, J. Hutter and M. Parrinello, "The Gaussian and augmented-plane-wave density functional method for ab initio molecular dynamics simulations", *Theor. Chem. Acc.* 103(2), 124–140 (1999).

[94] J. VandeVondele, M. Krack, F. Mohamed, M. Parrinello, T. Chassaing and J. Hutter, "Quickstep: Fast and accurate density functional calculations using a mixed Gaussian and plane waves approach", *Comput. Phys. Commun.* 167(2), 103–128 (2005).

[95] J. VandeVondele and J. Hutter, "Gaussian basis sets for accurate calculations on molecular systems in gas and condensed phases", *J. Chem. Phys.* 127(11), 114105 (2007).

[96] F. Mouhat, S. Sorella, R. Vuilleumier, A. M. Saitta and M. Casula, "Fully Quantum Description of the Zundel Ion: Combining Variational Quantum Monte Carlo with Path Integral Langevin Dynamics", *J. Chem. Theory Comput.* 13(6), 2400–2417 (2017).

[97] F.-X. Coudert and D. Kohen, "Molecular Insight into CO_2 "Trapdoor" Adsorption in Zeolite Na-RHO", *Chem. Mater.* 29(7), 2724–2730 (2017).

[98] K. De Wispelaere, B. Ensing, A. Ghysels, E. J. Meijer and V. Van Speybroeck, "Complex Reaction Environments and Competing Reaction Mechanisms in Zeolite Catalysis: Insights from Advanced Molecular Dynamics", *Chem. Eur. J.* 21(26), 9385–9396 (2015).

[99] V. Haigis, F.-X. Coudert, R. Vuilleumier, A. Boutin and A. H. Fuchs, "Hydrothermal Breakdown of Flexible Metal–Organic Frameworks: A Study by First-Principles Molecular Dynamics", *J. Phys. Chem. Lett.* 6(21), 4365–4370 (2015).

[100] M. Martinez, M.-P. Gaigeot, D. Borgis and R. Vuilleumier, "Extracting effective normal modes from equilibrium dynamics at finite temperature", *J. Chem. Phys.* 125(14), 144106 (2006).

[101] E. A. Carter, G. Ciccotti, J. T. Hynes and R. Kapral, "Constrained reaction coordinate dynamics for the simulation of rare events", *Chem. Phys. Lett.* 156(5), 472–477 (1989).

[102] M. Sprik and G. Ciccotti, "Free energy from constrained molecular dynamics", *J. Chem. Phys.* 109(18), 7737–7744 (1998).

[103] V. Haigis, Y. Belkhodja, F.-X. Coudert, R. Vuilleumier and A. Boutin, "Challenges in first-principles NPT molecular dynamics of soft porous crystals: A case study on MIL-53(Ga)", *J. Chem. Phys.* 141(6), 064703 (2014).

[104] J. D. Evans, D. M. Huang, M. R. Hill, C. J. Sumby, D. S. Sholl, A. W. Thornton and C. J. Doonan, "Molecular Design of Amorphous Porous Organic Cages for Enhanced Gas Storage", *J. Phys. Chem. C* 119(14), 7746–7754 (2015).

[105] J. D. Evans and F.-X. Coudert, "Microscopic Mechanism of Chiral Induction in a Metal–Organic Framework", *J. Am. Chem. Soc.* 138(19), 6131–6134 (2016).

[106] J. D. Evans, D. M. Huang, M. R. Hill, C. J. Sumby, A. W. Thornton and C. J. Doonan, "Feasibility of Mixed Matrix Membrane Gas Separations Employing Porous Organic Cages", *J. Phys. Chem. C* 118(3), 1523–1529 (2014).

[107] F. Trousselet, A. Boutin and F.-X. Coudert, "Novel Porous Polymorphs of Zinc Cyanide with Rich Thermal and Mechanical Behavior", *Chem. Mater.* 27(12), 4422–4430 (2015).

[108] J. D. Evans, G. Fraux, R. Gaillac, D. Kohen, F. Trousselet, J.-M. Vanson and F.-X. Coudert, "Computational Chemistry Methods for Nanoporous Materials", *Chem. Mater.* 29(1), 199–212 (2017).

[109] N. L. Allinger, K. Chen and J. Lii, "An improved force field (MM4) for saturated hydrocarbons", *J. Comput. Chem.* 17(5-6), 642–668 (1996).

[110] A. K. Rappé, C. J. Casewit, K. S. Colwell, W. A. Goddard Iii and W. M. Skiff, "UFF, a full periodic table force field for molecular mechanics and molecular dynamics simulations", *J. Am. Chem. Soc.* 114(25), 10024–10035 (1992).

[111] W. D. Cornell, P. Cieplak, C. I. Bayly, I. R. Gould, K. M. Merz, D. M. Ferguson, D. C. Spellmeyer, T. Fox, J. W. Caldwell and P. A. Kollman, "A second generation force field for the simulation of proteins, nucleic acids, and organic molecules", *J. Am. Chem. Soc.* 117(19), 5179–5197 (1995).

[112] H. Sun, "COMPASS: an ab initio force-field optimized for condensed-phase applications overview with details on alkane and benzene compounds", *J. Phys. Chem. B* 102(38), 7338–7364 (1998).

[113] R. B. Getman, Y.-S. Bae, C. E. Wilmer and R. Q. Snurr, "Review and Analysis of Molecular Simulations of Methane, Hydrogen, and Acetylene Storage in Metal–Organic Frameworks", *Chem. Rev.* 112(2), 703–723 (2012).

[114] L. Vanduyfhuys, S. Vandenbrande, T. Verstraelen, R. Schmid, M. Waroquier and V. Van Speybroeck, "QuickFF: A program for a quick and easy derivation of force fields for metal-organic frameworks from ab initio input", *J. Comput. Chem.* 36(13), 1015–1027 (2015).

[115] J. Wieme, L. Vanduyfhuys, S. M. J. Rogge, M. Waroquier and V. Van Speybroeck, "Exploring the Flexibility of MIL-47(V)-Type Materials Using Force Field Molecular Dynamics Simulations", *J. Phys. Chem. C* 120(27), 14934–14947 (2016).

[116] M. A. Addicoat, N. Vankova, I. F. Akter and T. Heine, "Extension of the Universal Force Field to Metal–Organic Frameworks", *J. Chem. Theory Comput.* 10(2), 880–891 (2014).

[117] A. C. Fogarty, F.-X. Coudert, A. Boutin and D. Laage, "Reorientational Dynamics of Water Confined in Zeolites", *ChemPhysChem* 15(3), 521–529 (2014).

[118] D. Fincham, "Choice of timestep in molecular dynamics simulation", *Comput. Phys. Commun.* 40(2-3), 263–269 (1986).

[119] P. H. Hünenberger. "Thermostat Algorithms for Molecular Dynamics Simulations". In C. Holm and K. Kremer, editors, *Thermostat Algorithms for Molecular Dynamics Simulations*", pages 105–149. Springer Berlin Heidelberg, Berlin, Heidelberg, (2005).

[120] S. M. J. Rogge, L. Vanduyfhuys, A. Ghysels, M. Waroquier, T. Verstraelen, G. Maurin and V. Van Speybroeck, "A Comparison of Barostats for the Mechanical Characterization of Metal–Organic Frameworks", *J. Chem. Theory Comput.* 11(12), 5583–5597 (2015).

[121] S. Nosé, "A unified formulation of the constant temperature molecular dynamics methods", *J. Chem. Phys.* 81(1), 511–519 (1984).

[122] W. G. Hoover, "Canonical dynamics: equilibrium phase-space distributions", *Phys. Rev. A* 31(3), 1695 (1985).

[123] G. J. Martyna, D. J. Tobias and M. L. Klein, "Constant pressure molecular dynamics algorithms", *J. Chem. Phys.* 101(5), 4177–4189 (1994).

[124] D. Dubbeldam, A. Torres-Knoop and K. S. Walton, "On the inner workings of Monte Carlo codes", *Mol. Simul.* 39(14-15), 1253–1292 (2013).

[125] W. K. Hastings, "Monte Carlo sampling methods using Markov chains and their applications", *Biometrika* 57(1), 97–109 (1970).

[126] A. Kundu, K. Sillar and J. Sauer, "Ab Initio Prediction of Adsorption Isotherms for Gas Mixtures by Grand Canonical Monte Carlo Simulations on a Lattice of Sites", *J. Phys. Chem. Lett.* 8(12), 2713–2718 (2017).

[127] S. De Gironcoli, P. Giannozzi and S. Baroni, "Structure and thermodynamics of Si x Ge 1- x alloys from ab initio Monte Carlo simulations", *Phys. Rev. Lett.* 66(16), 2116 (1991).

[128] W. M. C. Foulkes, L. Mitas, R. J. Needs and G. Rajagopal, "Quantum Monte Carlo simulations of solids", *Rev. Mod. Phys.* 73(1), 33 (2001).

[129] A. Zen, J. G. Brandenburg, J. Klime**s**, A. Tkatchenko, D. Alfè and A. Michaelides, "Fast and accurate quantum Monte Carlo for molecular crystals", *Proc. Natl. Acad. Sci. U.S.A.* 115(8), 1724–1729 (2018).

[130] M.M.J. Treacy, K.H. Randall, S. Rao, J.A. Perry and D.J. Chadi, "Enumeration of periodic tetrahedral frameworks", *Z. Kristall.* 212(11), 768–791 (1997). cited By 135.

[131] S. M. Woodley and R. Catlow, "Crystal structure prediction from first principles", *Nat. Mater.* 7(12), 937–946 (2008).

[132] O. D. Friedrichs, Andreas W. M. Dress, Daniel H. Huson, J. Klinowski and A. L. Mackay, "Systematic enumeration of crystalline networks", *Nature* 400(6745), 644–647 (1999).

[133] M.M.J. Treacy, I. Rivin, E. Balkovsky, K.H. Randall and M.D. Foster, "Enumeration of periodic tetrahedral frameworks. II. Polynodal graphs", *Micropor. Mesopor. Mat.* 74(1-3), 121–132 (2004).

[134] E. G. Derouane and J. G. Fripiat, "Quantum mechanical calculations on molecular sieves. 1. Properties of the Si-OT (T= Si, Al, B) bridge in zeolites", *J. Phys. Chem.* 91(1), 145–148 (1987).

[135] C. Kosanović, J. Bronić, A. **Ciz**mek, B. Subotić, I. **S**mit, M. Stubi**c**ar and A. Tonejc, "Mechanochemistry of zeolites: Part 2. Change in particulate properties of zeolites during ball milling", *Zeolites* 15(3), 247–252 (1995).

[136] J. O'Brien-Abraham, M. Kanezashi and Y. S. Lin, "A comparative study on permeation and mechanical properties of random and oriented MFI-type zeolite membranes", *Micropor. Mesopor. Mat.* 105(1-2), 140–148 (2007).

[137] R. Astala, S. M. Auerbach and P. A. Monson, "Density Functional Theory Study of Silica Zeolite Structures: Stabilities and Mechanical Properties of SOD, LTA, CHA, MOR, and MFI", *J. Phys. Chem. B* 108(26), 9208–9215 (2004).

[138] Z. Li, M. C. Johnson, M. Sun, E. T. Ryan, D. J. Earl, W. Maichen, J. I. Martin, S. Li, C. M. Lew, J. Wang, M. W. Deem, M. E. Davis and Y. Yan, "Mechanical and Dielectric Properties of Pure-Silica-Zeolite Low-k Materials", *Angew. Chem. Int. Ed.* 45(38), 6329–6332 (2006).

[139] B. Coasne, J. Haines, C. Levelut, O. Cambon, M. Santoro, F. Gorelli and G. Garbarino, "Enhanced mechanical strength of zeolites by adsorption of guest molecules", *Phys. Chem. Chem. Phys.* 13(45), 20096 (2011).

[140] I. A. Bryukhanov, A. A. Rybakov, V. L. Kovalev, A. V. Larin and G. M. Zhidomirov, "Chemical reduction of the elastic properties of zeolites: a comparison of the formation of carbonate species versus dealumination", *Dalton Trans.* 44(6), 2703–2711 (2015).

[141] I. A. Bryukhanov, A. A. Rybakov, A. V. Larin, D. N. Trubnikov and D. P. Vercauteren, "The role of water in the elastic properties of aluminosilicate zeolites: DFT investigation", *J. Mol. Model.* 23(3) (2017).

[142] F.-X. Coudert, "Systematic investigation of the mechanical properties of pure silica zeolites: stiffness, anisotropy, and negative linear compressibility", *Phys. Chem. Chem. Phys.* 15(38), 16012 (2013).

[143] A. B. Cairns and A. L. Goodwin, "Negative linear compressibility", *Phys. Chem. Chem. Phys.* 17(32), 20449–20465 (2015).

[144] M. Siddorn, F.-X. Coudert, K. E. Evans and A. Marmier, "A systematic typology for negative Poisson's ratio materials and the prediction of complete auxeticity in pure silica zeolite JST", *Phys. Chem. Chem. Phys.* 17(27), 17927–17933 (2015).

[145] R. Pophale, P. A. Cheeseman and M. W. Deem, "A database of new zeolite-like materials", *Phys. Chem. Chem. Phys.* 13(27), 12407 (2011).

[146] A. Marmier, Z. A. D. Lethbridge, R. I. Walton, C. W. Smith, S. C. Parker and K. E. Evans, "ElAM: A computer program for the analysis and representation of anisotropic elastic properties", *Comput. Phys. Commun.* 181(12), 2102–2115 (2010).

[147] W Voigt, *Handbook of Crystal Physics*, Teubner, Leipzig (1928).

[148] A. Reuss, "Berechnung der Fließgrenze von Mischkristallen auf Grund der Plastizitätsbedingung für Einkristalle .", *Z. Angew. Math. Mech.* 9(1), 49–58 (1929).

[149] R Hill, "The Elastic Behaviour of a Crystalline Aggregate", *Proc. Phys. Soc., Sec. A* 65(5), 349–354 (1952).

[150] A. L. Goodwin, D. A. Keen and M. G. Tucker, "Large negative linear compressibility of Ag3 [Co (CN) 6]", *Proc. Natl. Acad. Sci.* 105(48), 18708–18713 (2008).

[151] L. Wang, C. Wang, H. Luo and Y. Sun, "Correlation between Uniaxial Negative Thermal Expansion and Negative Linear Compressibility in Ag $_3$ [Co(CN) $_6$]", *J. Phys. Chem. C* 121(1), 333–341 (2017).

[152] Q. Zeng, K. Wang, Y. Qiao, X. Li and B. Zou, "Negative Linear Compressibility Due to Layer Sliding in a Layered Metal–Organic Framework", *J. Phys. Chem. Lett.* 8(7), 1436–1441 (2017).

[153] J. Dagdelen, J. Montoya, M. de Jong and K. Persson, "Computational prediction of new auxetic materials", *Nat. Commun.* 8, 323 (2017).

[154] O. H. Nielsen and R. M. Martin, "First-Principles Calculation of Stress", *Phys. Rev. Lett.* 50(9), 697–700 (1983).

[155] O. H. Nielsen and R. M. Martin, "Quantum-mechanical theory of stress and force", *Phys. Rev. B* 32(6), 3780–3791 (1985).

[156] J. R. Ray, "Fluctuations and thermodynamic properties of anisotropic solids", *J. Appl. Phys.* 53(9), 6441–6443 (1982).

[157] M. Parrinello and A. Rahman, "Strain fluctuations and elastic constants", *J. Chem. Phys.* 76(5), 2662–2666 (1982).

[158] A. U. Ortiz, A. Boutin, A. H. Fuchs and F.-X. Coudert, "Investigating the Pressure-Induced Amorphization of Zeolitic Imidazolate Framework ZIF-8: Mechanical Instability Due to Shear Mode Softening", *J. Phys. Chem. Lett.* 4(11), 1861–1865 (2013).

[159] R. Gaillac, P. Pullumbi and F-X. Coudert, "ELATE: an open-source online application for analysis and visualization of elastic tensors", *J. Phys.: Condens. Matter* 28(27), 275201 (2016).

[160] K-P. Schriider, J. Sauer, M. Leslie, C. R. A. Catlow and J. M. Thomas, "Bridging hydroxyl groups in zeolitic catalysts: a computer simulation of their structure, vibrational properties and acidity in protonated faujasites (H-Y zeolites)", *Chem. Phys. Lett.* 188(3), 6 (1992).

[161] B. W. H. van Beest, G. J. Kramer and R. A. van Santen, "Force fields for silicas and aluminophosphates based on *ab initio* calculations", *Phys. Rev. Lett.* 64(16), 1955–1958 (1990).

[162] Julian D. Gale and Andrew L. Rohl, "The General Utility Lattice Program (GULP)", *Mol. Simul.* 29(5), 291–341 (2003).

[163] J. D. Evans and F.-X. Coudert, "Predicting the Mechanical Properties of Zeolite Frameworks by Machine Learning", *Chem. Mater.* 29, 7833–7839 (2017).

[164] T. F. Willems, C. H. Rycroft, M. Kazi, J. C. Meza and M. Haranczyk, "Algorithms and tools for high-throughput geometry-based analysis of crystalline porous materials", *Micropor. Mesopor. Mat.* 149(1), 134–141 (2012).

[165] R. L. Martin, B. Smit and M. Haranczyk, "Addressing Challenges of Identifying Geometrically Diverse Sets of Crystalline Porous Materials", *J. Chem. Inf. Model.* 52(2), 308–318 (2012).

[166] R. Dovesi, R. Orlando, A. Erba, C. M. Zicovich-Wilson, B. Civalleri, S. Casassa, L. Maschio, M. Ferrabone, M. De La Pierre, P. D'Arco, Y. Noël, M. Causà, M. Rérat and B. Kirtman, "CRYSTAL14: A program for the ab initio investigation of crystalline solids", *Int. J. Quantum Chem.* 114(19), 1287–1317 (2014).

[167] E. I. Román-Román and C. M. Zicovich-Wilson, "The role of long-range van der Waals forces in the relative stability of SiO2-zeolites", *Chem. Phys. Lett.* 619, 109–114 (2015).

[168] F. Pedregosa, G. Varoquaux, A. Gramfort, V. Michel, B. Thirion, O Grisel, M. Blondel, P. Prettenhofer, R. Weiss, V. Dubourg, J. Vanderplas, A. Passos, D. Cournapeau, M. Brucher, M. Perrot and E. Duchesnay, "Scikit-learn: Machine Learning in Python", *J. Mach. Learn. Res.* (12), 2825–2830 (2011).

[169] J. H. Friedman, "Greedy Function Approximation: A Gradient Boosting Machine", *Ann. Stat.* 29(5), 1189–1232 (2001).

[170] Jerome Friedman, Trevor Hastie and Robert Tibshirani, *The elements of statistical learning*, volume 1, Springer series in statistics New York (2001).

[171] A. Mohan, Z. Chen and K. Weinberger, "Web-Search Ranking with Initialized Gradient Boosted Regression Trees", *Proceedings of the Learning to Rank Challenge* 14, 77–89 (2011).

[172] H. Li, Y. Liang and Q. Xu, "Support vector machines and its applications in chemistry", *Chemom. Intell. Lab. Syst.* 95(2), 188–198 (2009).

[173] R. Caruana and A. Niculescu-Mizil, "An empirical comparison of supervised learning algorithms", *Proceedings of the 23rd International Conference on Machine Learning* pages 161–168 (2006).

[174] K. W. Chapman, G. J. Halder and P. J. Chupas, "Pressure-Induced Amorphization and Porosity Modification in a Metal-Organic Framework", *J. Am. Chem. Soc.* 131(48), 17546–17547 (2009).

[175] W. Yuan, J. O'Connor and S. L. James, "Mechanochemical synthesis of homo- and hetero-rare-earth(iii) metal–organic frameworks by ball milling", *CrystEngComm* 12(11), 3515 (2010).

[176] Y. H. Hu and L. Zhang, "Amorphization of metal-organic framework MOF-5 at unusually low applied pressure", *Phys. Rev. B* 81(17), 174103 (2010).

[177] K. J. Gagnon, C. M. Beavers and A. Clearfield, "MOFs Under Pressure: The Reversible Compression of a Single Crystal", *J. Am. Chem. Soc.* 135(4), 1252–1255 (2013).

[178] T. D. Bennett, P. Simoncic, S. A. Moggach, F. Gozzo, P. Macchi, D. A. Keen, J.-C. Tan and A. K. Cheetham, "Reversible pressure-induced amorphization of a zeolitic imidazolate framework (ZIF-4)", *ChemComm* 47(28), 7983 (2011).

[179] K. W. Chapman, D. F. Sava, G. J. Halder, P. J. Chupas and T. M. Nenoff, "Trapping Guests within a Nanoporous Metal–Organic Framework through Pressure-Induced Amorphization", *J. Am. Chem. Soc.* 133(46), 18583–18585 (2011).

[180] F. Yang, W. Li and B. Tang, "Facile synthesis of amorphous UiO-66 (Zr-MOF) for supercapacitor application", *J. Alloys Compd.* 733, 8–14 (2018).

[181] S. Cao, T. D. Bennett, David A. Keen, Andrew L. Goodwin and Anthony K. Cheetham, "Amorphization of the prototypical zeolitic imidazolate framework ZIF-8 by ball-milling", *ChemComm* 48(63), 7805 (2012).

[182] A. Kertik, L. H. Wee, M. Pfannmöller, S. Bals, J. A. Martens and I. F. J Vankelecom, "Highly selective gas separation membrane using in situ amorphised metal–organic frameworks", *Energy Environ. Sci.* 10(11), 2342–2351 (2017).

[183] C. Orellana-Tavra, R. J. Marshall, E. F. Baxter, I. A. Lázaro, A. Tao, A. K. Cheetham, R. S. Forgan and D. Fairen-Jimenez, "Drug delivery and controlled release from biocompatible metal–organic frameworks using mechanical amorphization", *J. Mater. Chem. B* 4(47), 7697–7707 (2016).

[184] E. F. Baxter, T. D. Bennett, A. B. Cairns, N. J. Brownbill, A. L. Goodwin, D. A. Keen, P. A. Chater, F. Blanc and A. K. Cheetham, "A comparison of the amorphization of zeolitic imidazolate frameworks (ZIFs) and aluminosilicate zeolites by ball-milling", *Dalton Trans.* 45(10), 4258–4268 (2016).

[185] G. N. Greaves, F. Meneau, A. Sapelkin, L. M. Colyer, I. ap Gwynn, S. Wade and G. Sankar, "The rheology of collapsing zeolites amorphized by temperature and pressure", *Nat. Mater.* 2(9), 622–629 (2003).

[186] M. Colligan, P. M. Forster, A. K. Cheetham, Y. Lee, T. Vogt and J. A. Hriljac, "Synchrotron X-ray Powder Diffraction and Computational Investigation of Purely Siliceous Zeolite Y under Pressure", *J. Am. Chem. Soc.* 126(38), 12015–12022 (2004).

[187] J. Haines, C. Levelut, A. Isambert, P. Hébert, S. Kohara, D. A. Keen, T. Hammouda and D. Andrault, "Topologically Ordered Amorphous Silica Obtained from the Collapsed Siliceous Zeolite, Silicalite-1-F: A Step toward "Perfect" Glasses", *J. Am. Chem. Soc.* 131(34), 12333–12338 (2009).

[188] T. D. Bennett, A. L. Goodwin, M. T. Dove, D. A. Keen, M. G. Tucker, E. R. Barney, A. K. Soper, E. G. Bithell, J.-C. Tan and A. K. Cheetham, "Structure and Properties of an Amorphous Metal-Organic Framework", *Phys. Rev. Lett.* 104(11), 115503 (2010).

[189] D. W. Lewis, A. R. Ruiz-Salvador, A. Gómez, L. M. Rodriguez-Albelo, F.-X. Coudert, B. Slater, A. K. Cheetham and C. Mellot-Draznieks, "Zeolitic imidazole frameworks: structural and energetics trends compared with their zeolite analogues", *CrystEngComm* 11(11), 2272 (2009).

[190] S. Komarneni and R. Roy, "Anomalous microwave melting of zeolites", *Mater. Lett.* 4(2), 107–110 (1986).

[191] M. K. Song, J. M. Shin, H. Chon and M. S. Jhon, "Molecular dynamics study on the collapse of A-type zeolite framework. 1. Temperature dependence and prediction of melting phenomena", *J. Phys. Chem.* 93(17), 6463–6468 (1989).

[192] K. Yamahara, K. Okazaki and K. Kawamura, "Molecular dynamics study of the thermal behaviour of silica glass/melt and cristobalite", *J. Non-Cryst. Solids* 291(1-2), 32–42 (2001).

[193] R. A. Robie, B. S. Hemingway and J. R. Fisher. "Thermodynamic properties of minerals and related substances at 298.15 K and 1 bar (10^5 pascals) pressure and at higher temperatures". Technical report, Geological Survey, Washington, DC (USA), (1978).

[194] G. N. Greaves and S. Sen, "Inorganic glasses, glass-forming liquids and amorphizing solids", *Adv. Phys.* 56(1), 1–166 (2007).

[195] D. Umeyama, S. Horike, M. Inukai, T. Itakura and S. Kitagawa, "Reversible Solid-to-Liquid Phase Transition of Coordination Polymer Crystals", *J. Am. Chem. Soc.* 137(2), 864–870 (2015).

[196] D. Umeyama, N. P. Funnell, M. J. Cliffe, J. A. Hill, A. L. Goodwin, Y. Hijikata, T. Itakura, T. Okubo, S. Horike and S. Kitagawa, "Glass formation via structural fragmentation of a 2D coordination network", *Chem. Commun.* 51(64), 12728–12731 (2015).

[197] J. C. Tan, T. D. Bennett and A. K. Cheetham, "Chemical structure, network topology, and porosity effects on the mechanical properties of Zeolitic Imidazolate Frameworks", *Proc. Natl. Acad. Sci. U.S.A.* 107(22), 9938–9943 (2010).

[198] `http://www.cp2k.org`.

[199] G. Bussi, D. Donadio and M. Parrinello, "Canonical sampling through velocity rescaling", *J. Chem. Phys.* 126, 014101 (2007).

[200] John P. Perdew, Kieron Burke and Matthias Ernzerhof, "Generalized gradient approximation made simple", *Phys. Rev. Lett.* 77, 3865–3868 (1996).

[201] S. Grimme, J. Antony, S. Ehrlich and H. Krieg, "A consistent and accurate ab initio parametrization of density functional dispersion correction (DFT-D) for the 94 elements H-Pu", *J. Chem. Phys.* 132, 154104 (2010).

[202] V. Haigis, F.-X. Coudert, R. Vuilleumier and A. Boutin, "Investigation of structure and dynamics of the hydrated metal-organic framework MIL-53(Cr) using first-principles molecular dynamics", *Phys. Chem. Chem. Phys.* 15, 19049–19056 (2013).

[203] S. Goedecker, M. Teter and J. Hutter, "Separable dual-space Gaussian pseudopotentials", *Phys. Rev. B* 54, 1703–1710 (1996).

[204] Q. Mei, C. J. Benmore and J. K. R. Weber, "Structure of Liquid SiO 2 : A Measurement by High-Energy X-Ray Diffraction", *Phys. Rev. Lett.* 98(5), 057802 (2007).

[205] C. Chakravarty, P. G. Debenedetti and F. H. Stillinger, "Lindemann measures for the solid-liquid phase transition", *J. Chem. Phys.* 126(20), 204508 (2007).

[206] K. K. Kelly, "Heats of Fusion of Inorganic Compounds", *US Bur. Mines Bull* 393, 152 (1936).

[207] A. Samanta, M. E. Tuckerman, T.-Q. Yu and W. E, "Microscopic mechanisms of equilibrium melting of a solid", *Science* 346, 729–732 (2014).

[208] D. Laage and J. T. Hynes, "A Molecular Jump Mechanism of Water Reorientation", *Science* 311(5762), 832–835 (2006).

[209] D. Laage and J. T. Hynes, "On the Molecular Mechanism of Water Reorientation", *J. Phys. Chem. B* 112(45), 14230–14242 (2008).

[210] M. Pinheiro, R. L. Martin, C. H. Rycroft, A. Jones, E. Iglesia and M. Haranczyk, "Characterization and comparison of pore landscapes in crystalline porous materials", *J. Mol. Graph. Model.* 44, 208–219 .

[211] N. Giri, M. G. Del Pópolo, G. Melaugh, R. L. Greenaway, K. Rätzke, T. Koschine, L. Pison, M. F. Costa Gomes, A. I. Cooper and S. L. James, "Liquids with permanent porosity", *Nature* 527(7577), 216–220 (2015).

[212] N. O'Reilly, N. Giri and S. L. James, "Porous Liquids", *Chem. Eur. J.* 13, 3020–3025 (2007).

[213] T. Hasell and A. I. Cooper, "Porous organic cages: soluble, modular and molecular pores", *Nat. Rev. Mater.* 1, 16053 (2016).

[214] A. W. Thornton, K. E. Jelfs, K. Konstas, C. M. Doherty, A. J. Hill, A. K. Cheetham and T. D. Bennett, "Porosity in metal–organic framework glasses", *Chem. Commun.* 52(19), 3750–3753 (2016).

[215] N. C. Forero-Martinez, R. Cortes-Huerto and P. Ballone, "The glass transition and the distribution of voids in room-temperature ionic liquids: A molecular dynamics study", *J. Chem. Phys.* 136, 204510 (2012).

[216] J. Deschamps, M. F. Costa Gomes and A. A. H. Pádua, "Mol. Simul. Study of Interactions of Carbon Dioxide and Water with Ionic Liquids", *ChemPhysChem* 5, 1049–1052 (2004).

[217] B. D. Freeman, "Basis of Permeability/Selectivity Tradeoff Relations in Polymeric Gas Separation Membranes", *Macromolecules* 32, 375–380 (1999).

[218] B. R. Pimentel, A. Parulkar, E.-k. Zhou, N. A. Brunelli and R. P. Lively, "Zeolitic Imidazolate Frameworks: Next-Generation Materials for Energy-Efficient Gas Separations", *ChemSusChem* 7, 3202–3240 (2014).

[219] J. B. James and Y. S. Lin, "Kinetics of ZIF-8 Thermal Decomposition in Inert, Oxidizing, and Reducing Environments", *J. Phys. Chem. C* 120, 14015–14026 (2016).

[220] T. F. Soules, "A molecular dynamic calculation of the structure of sodium silicate glasses", *J. Chem. Phys.* 71(11), 4570–4578 (1979).

[221] K. Robinson, G. V. Gibbs and P. H. Ribbe, "Quadratic Elongation: A Quantitative Measure of Distortion in Coordination Polyhedra", *Science* 172(3983), 567–570 (1971).

[222] "Gibbs code User's guide". `http://www.lcp.u-psud.fr/IMG/pdf/mode_d_emploi_gibbs.pdf`.

[223] `http://www.materialsdesign.com/medea/gibbs`.

[224] L. Zhang, Z. Hu and J. Jiang, "Sorption-Induced Structural Transition of Zeolitic Imidazolate Framework-8: A Hybrid Molecular Simulation Study", *J. Am. Chem. Soc.* 135(9), 3722–3728 (2013).

[225] M. Mazur, P. S. Wheatley, M. Navarro, W. J. Roth, M. Polo**z**ij, A. Mayoral, P. Eliá**s**ová, P. Nachtigall, J. **C**ejka and R. E. Morris, "Synthesis of 'unfeasible' zeolites", *Nat. Chem.* 8(1), 58–62 (2016).

[226] P. Eliá**s**ová, M. Opanasenko, P. S. Wheatley, M. Shamzhy, M. Mazur, P. Nachtigall, W. J. Roth, R. E. Morris and J. **C**ejka, "The ADOR mechanism for the synthesis of new zeolites", *Chem. Soc. Rev.* 44(20), 7177–7206 (2015).

[227] M. Trachta, P. Nachtigall and O. Bludský, "The ADOR synthesis of new zeolites: In silico investigation", *Catalysis Today* 243, 32–38 (2015).

Résumé

Pendant ma thèse, j'ai mené des études basées sur les méthodes de simulation moléculaire pour des matériaux de deux familles différentes : les zéolithes d'une part, utilisées industriellement et dans de nombreux usages quotidiens et les *Metal-Organic Frameworks* (ou MOFs), qui présentent un potentiel applicatif important avec des développements commerciaux en cours de développement.

Les zéolithes sont des aluminosilicates poreux à la fois naturels et artificiels, connus depuis 1756 et synthétisés depuis les années 1940. Elles ont été étudiées en profondeur pour leurs propriétés liées à l'adsorption et à la catalyse depuis plus de 50 ans. Cependant, leur comportement mécanique n'a commencé à être vraiment considéré, en particulier sur le plan théorique, il y a seulement une quinzaine d'années. Pourtant, grâce à leurs structures complexes, certains de ces aluminosilicates poreux présentent des propriétés mécaniques fascinantes, appelés propriétés anomales, comme la compressibilité linéaire négative ou l'auxéticité (i.e. le ratio de Poisson négatif). En utilisant une grande base de données structurales de zéolithes hypothétiques et à l'aide de calculs quantiques, je me suis intéressé aux liens entre les caractéristiques structurales et les propriétés mécaniques des zéolithes totalement silicées. Grâce aux données générées par ces calculs quantiques, j'ai utilisé des techniques d'apprentissage statistique (ou *machine learning*) pour développer une méthodologie à même de prédire l'auxéticité dans ce type de matériaux et capable de calculer précisément et pour un coût numérique faible leur ratio de Poisson.

Les MOFs constituent une nouvelle classe de matériaux poreux très étudiée depuis 25 ans et en croissance exponentielle, notamment vis-à-vis du nombre de structures synthétisées et consignées dans la littérature. Jusqu'à très récemment, ils ont été appréhendés essentiellement en tant que matériaux cristallins. Pourtant leur amorphisation, par augmentation de température, de pression ou encore par broyage mécanique présente un grand intérêt tant sur le plan des mécanismes à l'œuvre que des applications potentielles des phases amorphes obtenues. Je me suis en particulier intéressé à la compréhension des phénomènes de fonte et de trempe de certains de ces matériaux appartenant à la famille des *zeolitic imidazolate frameworks* (ZIFs). Les ZIFs sont un sous-groupe des MOFs, topologiquement isomorphes aux zéolithes, et possèdent une stabilité thermique particulièrement bonne, ce qui en fait des bons candidats à l'amorphisation sous l'effet de l'augmentation de la température. Ainsi, à l'aide de simulations de dynamique moléculaire quantique (ou *ab initio*), j'ai pu expliqué le mécanisme moléculaire sous-jacent au phénomène de fusion et caractérisé la nature du liquide obtenu. J'ai également éclairé les liens existant entre la topologie initiale du cristal, le comportement lors de la fusion et la structure de la phase vitreuse résultant de la trempe. J'ai aussi modélisé une situation qui n'a pas encore été abordée expérimentalement : le remplissage forcé d'une de ces structures par du dioxyde de carbone avant et pendant la fusion. J'ai ainsi pu inférer l'influence qu'un tel ajout pourrait avoir sur la fusion de cette ZIF et proposé un moyen de piéger le gaz initialement adsorbé dans la phase amorphe.

Dans une première partie je vais décrire rapidement ce que sont les matériaux microporeux en général, et les zéolithes et les MOFs en particulier. J'évoquerai ensuite les méthodes numériques que j'ai utilisé. Le troisième volet sera consacré au résumé de mes travaux sur les propriétés mécaniques des zéolithes. Enfin, j'aborderai mon étude de la fusion et de la trempe des MOFs.

Matériaux et méthodes

Matériaux étudiés

Les matériaux poreux

Les matériaux poreux sont des matériaux possédant des cavités de différentes formes, tailles et régularités dans leur structure tridimensionnelle. [1] Il en existe de nombreux exemples, aussi bien naturels que synthétiques. [2] Leur nature chimique est variable, allant de matériaux purement inorganiques, comme les zéolithes, à des matériaux purement organiques, comme les polymères, en passant par des hybrides organiques-inorganiques, comme les MOFs. Leur porosité est souvent caractérisé par leur surface spécifique, c'est-à-dire la surface par unité de masse où peut se former une interface liquide-solide ou gaz-solide.

Leurs grandes surfaces spécifiques les rendent intéressants pour des applications industrielles exploitant l'adsorption ou la catalyse. Ils peuvent par exemple être utilisés comme matériaux isolants, avec un fluide, comme l'air, piégé dans leurs pores. Les matériaux poreux sont aussi très utilisés pour la séparation, la purification et le stockage de gaz, le raffinage de produits pétroliers, la catalyse hétérogène, comme substrat pour échangeurs d'ions, comme revêtement diélectrique et pour piéger des substances dangereuses ou radioactives. [3–5] Comme la taille des pores influence les propriétés de ces matériaux, ils sont classés en trois catégories par l'Union internationale de chimie pure et appliquée (UICPA ou *International Union of Pure and Applied Chemistry, IUPAC* en anglais) :

- les solides microporeux avec des pores dont les dimensions sont inférieures à 2 nm
- les solides mésoporeux avec des pores dont les dimensions se situent entre 2 nm et 50 nm
- les solides macroporeux avec des pores dont les dimensions sont supérieures à 50 nm

Les matériaux microporeux et mésoporeux sont regroupés sous l'appellation matériaux nanoporeux avec des pores dont la taille est inférieure à 50 nm. Sur la Figure 1 je montre trois exemples de matériaux nanoporeux.

Il y a beaucoup plus de matériaux poreux inorganiques que de matériaux poreux organiques. Les matériaux purement organiques sont composés de structures carbonées comme les polymères, les charbons actifs ou les *Covalent-Organic Frameworks* (COFs). Au sein des matériaux inorganiques poreux, on dénombre de nombreux oxydes (de silicium, titane, zirconium) comme les zéolithes, ou des composés binaires comme les sulfates ou les aluminophosphates (basés sur $AlPO_4$).

La régularité des structures permet aussi de classer ces matériaux. Il y a les matériaux cristallins, comme les zéolithes et les MOFs, dans lesquels les atomes forment un motif tridimensionnel répété périodiquement construisant ainsi un réseau périodique (cf. Figure 1 avec l'exemple de la maille unitaire d'une zéolithe). Par symétrie le réseau poreux d'un matériau cristallin est aussi régulier et périodique. D'autres matériaux sont réguliers mais ne sont pas

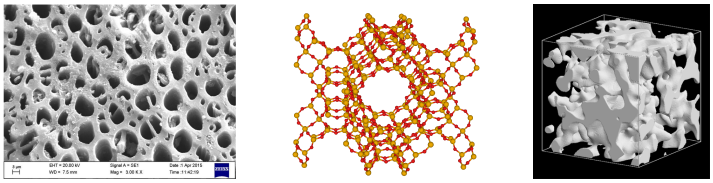

Figure 1 : Trois exemples de différents matériaux poreux. À gauche on voit une image de microscopie électronique à balayage d'un charbon actif [10] (ordonné, mais non cristallin), au milieu la structure moléculaire cristalline de la zéolithe faujasite (figure réalisée avec VESTA [11]) et à droite un verre de vycor amorphe est représenté (désordonné). [12]

cristallins, comme les argiles ou les nanotubes de carbones. Ces derniers ont des pores avec des caractéristiques très bien définies, mais il n'y a pas d'arrangement périodique tridimensionnel. Le troisième type de matériaux, qui représente la majorité des matériaux, est celui des solides amorphes. Il en existe de nombreux exemples, des charbons actifs aux verres de Vycor en passant par les aérogels ou la silice amorphe. Leurs pores ont souvent une grande polydispersité avec des formes irrégulières (cf. Figure 1 avec l'exemple d'un verre de Vycor).

Les zéolithes : des aluminosilicates poreux

Le terme zéolithe vient des mots grecs $\zeta\varepsilon\omega$, qui signifie « bouillir » et $\lambda\iota\vartheta o\sigma$, qui signifie « pierre ». Ce terme a été proposé par Axel Frederik Cronstedt en 1756 alors qu'il observait que beaucoup de vapeur d'eau (précédemment adsorbée dans le matériau) s'échappait du matériau lorsque celui-ci était échauffé. [17] Les zéolithes font partie des matériaux nanoporeux (et essentiellement microporeux) et sont composés d'oxygène, de silicium et d'aluminium, d'où leur appartenance à la famille des aluminosilicates. À l'échelle moléculaire elles sont constituées d'assemblages de tétraèdres liés par leurs sommets avec un atome central appelé atome T (T = Al ou Si) et quatre atomes d'oxygène (cf. Figure 2). Il est mathématiquement possible de créer une infinité de tels assemblages cristallins et il existe des bases de données de zéolithes hypothétiques contenant jusqu'à 2 millions de structures différentes. [18] Cependant, aujourd'hui seulement 228 structures ont été consignées dans la littérature expérimentale, parmi lesquelles 67 sont des zéolithes naturelles (selon l'association internationale pour les zéolithes ou *International Zeolite Association*). Chaque zéolithe est identifiée par un code à 3 lettres comme FAU pour la faujasite ou LTA pour Linde Type A (cf. Figure 2).

Les zéolithes ont pour formule générique $M_{x/m}Al_xSi_{1-x}O_2$. Le ratio entre le nombre d'atomes de silicium et le nombre d'atomes d'aluminium ($\frac{1-x}{x}$) appelé le ratio Si/Al est un paramètre important qui varie entre 1 (autant d'Al que de Si) et l'infini (aucun Al). La plupart des zéolithes n'existent que pour un rapport Si/Al dans une gamme bien définie. Dans le cas où il n'y a pas d'aluminium, on dit que la zéolithe est totalement silicée. Dans tous les autres cas, lorsque certains atomes de silicium sont remplacés par des atomes d'aluminium, la différence entre le degré d'oxydation (+IV pour Si, +III pour Al) crée un défaut de charge délocalisé dans la structure. Ces défauts sont compensés par des cations extra-charpentes qui n'appartiennent pas à l'arrangement cristallin, d'où le terme *extra-charpente*. Le cation le plus communément utilisé est Na^+, mais Li^+, K^+, Ba^{2+}, Ca^{2+} et d'autres sont aussi uti-

lisés. Ces cations délocalisés créent des gradients électrostatiques locaux qui améliorent les propriétés d'adsorption des zéolithes vis-à-vis des molécules avec des moments dipolaires ou quadrupolaires. Leur accessibilité par des adsorbats est aussi utile pour l'usage des zéolithes en catalyse car ils peuvent servir de sites catalytiques actifs (par exemple avec des protons pour de la catalyse acide hétérogène).

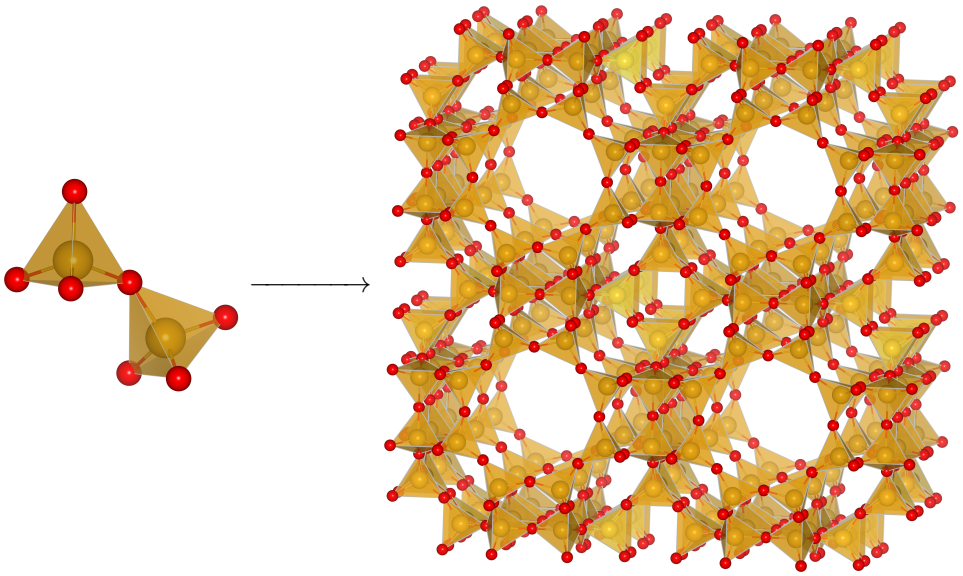

Figure 2 : À gauche, deux tétraèdres de coordination sont représentés et à droite on peut voir la structure moléculaire de la zéolithe LTA (Linde Type A) (figure réalisée avec VESTA [11]). Si, jaune ; O, rouge.

La dénomination de zéolithe est souvent étendue pour décrire les réseaux tétraédriques de structures poreuses avec d'autres éléments comme les aluminophosphates ou encore les oxydes de germanium et de gallium. Ces matériaux sont massivement utilisés dans l'industrie. Par exemple, la zéolithe A (LTA) substituée avec différents cations est utilisée pour retirer le dioxyde de carbone du gaz naturel, comme déshydratant ou pour extraire sélectivement les alcanes linéaires dans les procédés de raffinage. D'autres zéolithes sont utilisées pour la production d'oxygène médical, la capture du dioxyde de carbone lors de la production de ciment ou la décontamination de sites radioactifs. Elles sont aussi utilisées dans des applications domestiques, par exemple pour l'adoucissement de l'eau ou dans les lessives en remplacement des phosphates.

Les MOFs : une versatilité source de richesse

Le concept de MOFs est apparu il y a presque 30 ans dans la littérature [19] pour désigner une classe de matériaux composés de nœuds inorganiques liés par des ligands organiques. Dans cet article, Hoskins et Robson utilisent le terme « *Infinite Polymeric Frameworks* » et ils insistent sur les grandes cavités créées par de tels assemblages tridimensionnels prometteurs pour des applications comme « *molecular sieve* » (tamis moléculaire), pour « *ion exchange* » (l'échange ionique) ou en « *heterogeneous catalysis* » (catalyse hétérogène). Dix

ans plus tard, le premier usage du terme « MOF » est fait par l'équipe d'Omar Yaghi à UCLA pour la synthèse d'un matériau appelé MOF-5. [20] Dès lors le champ des MOFs a crû exponentiellement que ce soit en terme de publications ou de nombre de structures consignées dans la littérature. Pour donner un ordre de grandeur de cette croissance l'article de Yaghi et al. est cité plus de 5000 fois avec plus de 400 citations par an sur les 5 dernières années. La Figure 3 montre la croissance du nombre de structures rapportées dans la *Cambridge Structural Database* avec un doublement de ce nombre tous les 3,9 ans pour les MOFs tridimensionnels. Ces études académiques sont également soutenues par un intérêt industriel grandissant pour les MOFs. De fait leur grande versatilité et les surfaces spécifiques très importantes atteintes par ces matériaux en font de bons candidats pour une nouvelle génération de matériaux, suivant les zéolithes, pour les applications reposant sur la catalyse ou l'adsorption.

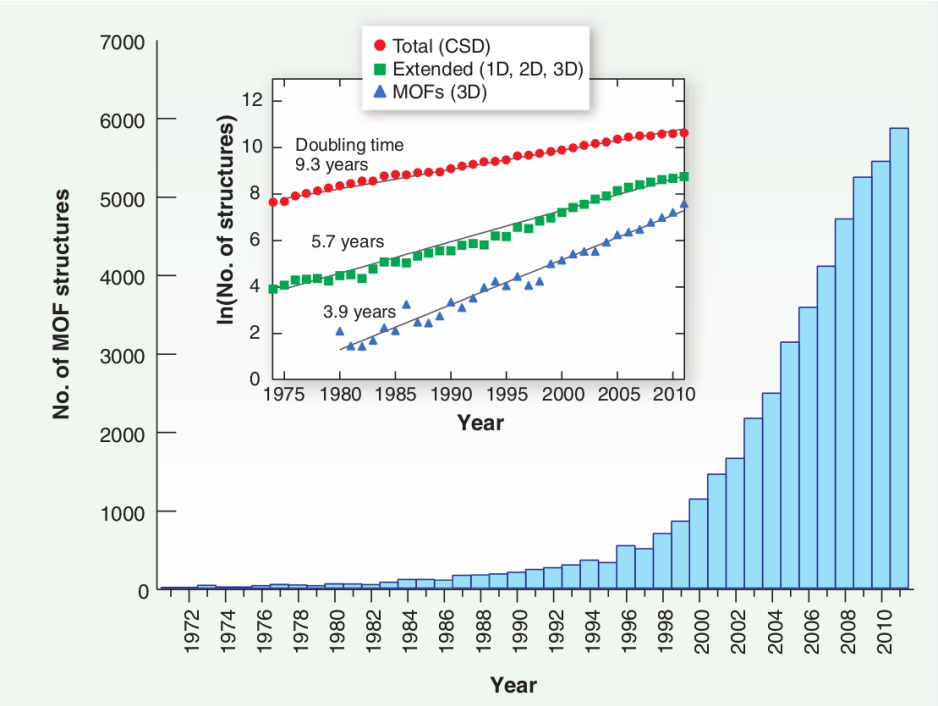

Figure 3 : Cette figure montre la croissance du nombre de structures de type MOF rapportées dans la *Cambridge Structural Datadabase* ou *CSD* (figure reproduite de [21]).

Cependant, la présence de ligands organiques et de liaisons plus faibles que la liaison covalente Si-O font que ces matériaux ne sont généralement stables thermiquement que jusqu'à des températures situées entre 300 °C et 500 °C, tandis que les zéolithes peuvent supporter des températures dépassant les 1000 °C. Les MOFs sont également difficiles à incorporer dans des procédés industriels du fait d'une robustesse mécanique inférieure à celle des zéolithes inorganiques. [22] Néanmoins des MOFs ont été produits à l'échelle de la tonne par des sociétés industrielles, essentiellement BASF et MOF Technologies. Cette dernière a présenté la première application commerciale d'un MOF en 2016, intégré dans un système dont l'usage est de garder les fruits et les légumes frais par une délivrance contrôlée de 1-methylcyclepropene, contenu initialement dans le MOF. [23]

Un des principaux avantages des MOFs par rapport aux zéolithes ou aux charbons ac-

tifs est la diversité de structures qui peuvent être construites à partir des différents unités inorganiques et des ligands organiques existants. La Figure 4 montre une partie des unités inorganiques (appelés *secondary building units* ou SBU en anglais) et des ligands organiques à disposition pour créer ces structures. Grâce à la diversité apportée par la chimie de coordination et la chimie organique, le nombre de structures n'est limité que par la stabilité thermodynamique des phases obtenues. Le défi de synthèse consiste aussi à obtenir un polymorphe poreux lorsque qu'une phase dense avec la même composition existe et a une meilleure stabilité thermodynamique.

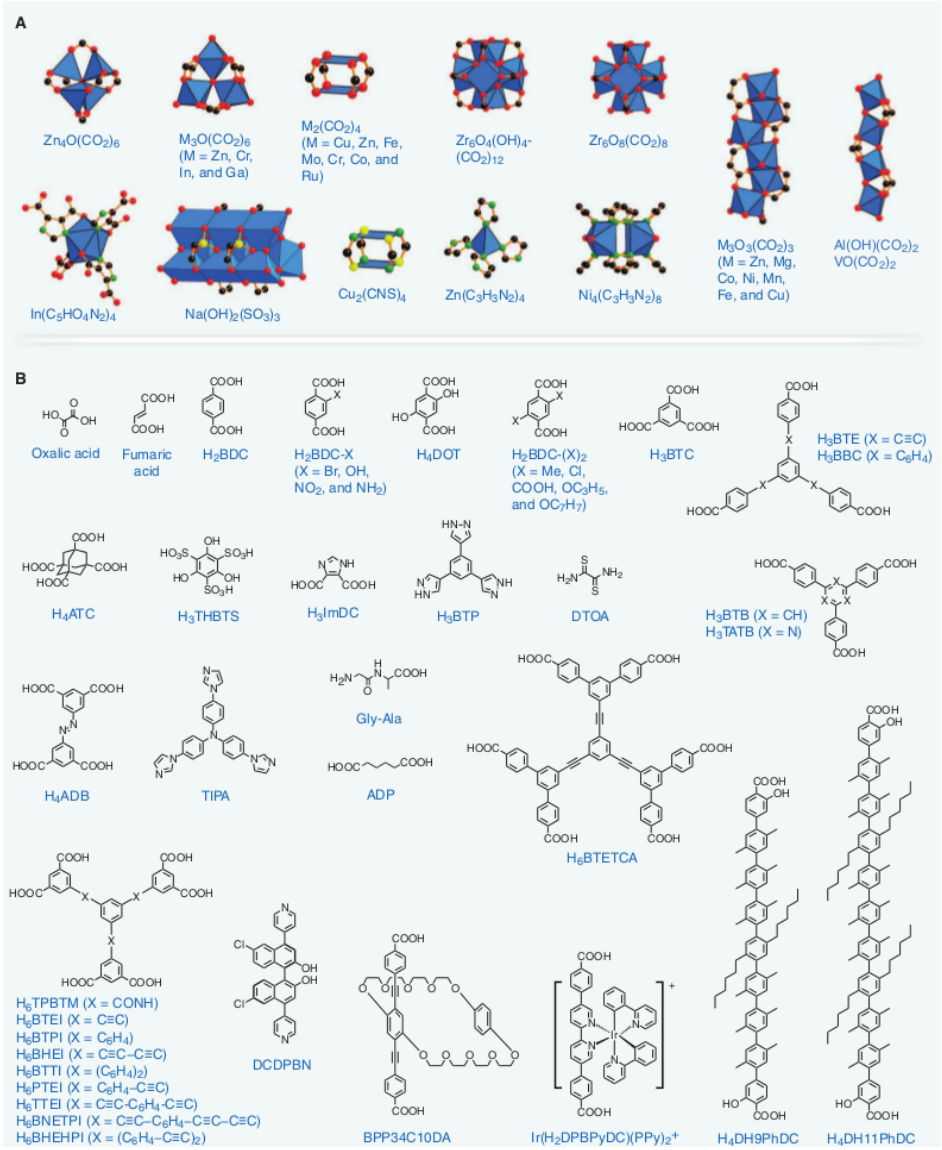

Figure 4 : Cette figure montre quelques exemples d'unités inorganiques (A) et de ligands organiques (B) (figure tirée de [21]).

Cette diversité de structures a donné naissance à une approche de type *design to applications* où le but est de trouver la meilleure structure pour une application donnée. Par exemple, le MOF ayant la plus grande capacité d'adsorption du méthane à ce jour a été rapporté [28]

tout comme celui ayant la plus grande capacité connue pour l'adsorption d'hydrogène. [29] Parfois les contraintes sont multiples, comme dans l'étude rapportée dans [30] où la capacité d'adsorption d'hydrogène, la sélectivité entre le dioxyde de carbone et l'hydrogène et le coût économique sont pris en compte.

Afin de rationaliser le procédé de design des structures, les nœuds inorganiques et les ligands organiques sont représentés par des polyèdres avec des géométries plus ou moins complexes. [33] 131 SBUs ont été identifiées, allant du simple tétraèdre à des configurations géométriques avec 66 points d'extension en passant par le cuboctaèdre, l'icosaèdre ou de simples cubes. [34]

Les ZIFs, que j'ai particulièrement étudiées pendant ma thèse, sont constituées de ligands imidazolate, fonctionnalisés ou non (cf. Figure 5). Leur ressemblance topologique avec les zéolithes vient du fait que l'angle métal–imidazolate–métal a la même valeur de 145 ° que l'angle Si–O–Si dans les zéolithes. [37] Le centre métallique est souvent un Zn(II) ou un Co(II) avec une coordination tétraédrique. Cette famille de MOFs est particulièrement étudiée pour leurs stabilités chimique et thermique meilleures que la plupart des autres MOFs.

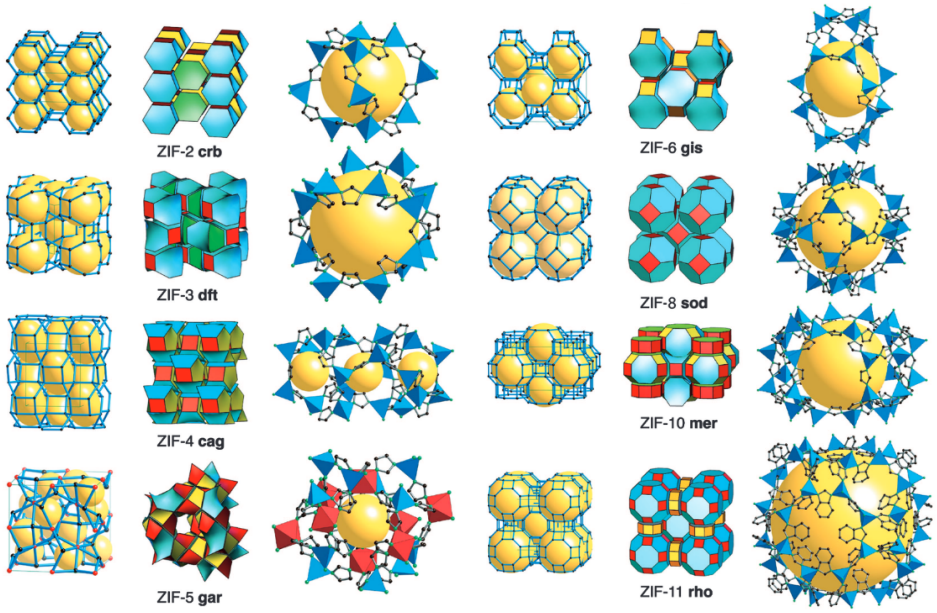

Figure 5 : Exemples de ZIFs (construite à partir de la Figure 1 de [37]).

Comme la majorité des MOFs sont cristallins, la technique de caractérisation principale utilisée pour déterminer leur cristallinité et leur structure est la diffraction aux rayons X. Elle peut être réalisée sur un monocristal si la synthèse produit des cristaux suffisamment grands ou sur poudre. La microscopie électronique à balayage est utilisée pour étudier la taille et la régularité des particules obtenues. [44] La microscopie électronique à transmission, la diffraction d'électrons et la microscopie électronique haute résolution peuvent être combinées pour imager directement des grands pores de MOFs, comme ceux de la structure MIL-101. [45] Afin de déterminer les surfaces spécifiques, l'adsorption de diazote à 77 K est une technique de routine. Les propriétés d'adsorption de gaz importants pour les applications, comme CO_2, H_2 ou CH_4, sont aussi fréquemment étudiées à basse pression. [46] Les isothermes d'adsorption

à pression plus élevées ou la caractérisation par diffusion de neutrons sont moins fréquentes du fait des moyens nécessaires. [47] Enfin, des méthodes de spectroscopie avancée comme l'EXAFS ou le XPS peuvent être utiles pour déterminer l'environnement chimique des centres métalliques, mais les spectroscopies classiques, que ce soit IR, UV ou Raman sont aussi utilisées, en partie pour appréhender les propriétés des molécules adsorbées dans les pores. [48]

Méthodes numériques

La simulation numérique, et en particulier la simulation moléculaire, a commencé dans les années 1950 après la deuxième guerre mondiale, pour une grande part dans le champ de la neutronique pour la compréhension des réactions nucléaires. La présentation de l'algorithme de Monte Carlo par Metropolis et al. en 1953 [61], a été suivie par la simulation d'un cristal anharmonique unidimensionnel par Fermi *et al.* en 1955 [62] et une simulation de dynamique moléculaire d'un système de sphères dures par Alder et Wainwright publiée en 1957. [63] Depuis ces études fondatrices, avec l'amélioration des algorithmes et l'augmentation exponentielle de la puissance de calcul, les simulations numériques utilisées pour l'étude de systèmes chimiques et physiques constituent aujourd'hui un champ de recherche à part entière. Ces simulations sont complémentaires des expériences et des théories analytiques et sont parfois appelées expériences *in silico*. [64–66] En fait, les mesures expérimentales donnent souvent une vue globale du système ou des phénomènes et ne peuvent parfois que peu éclairer les mécanismes microscopiques à l'œuvre. D'un autre côté, les théories analytiques, bien que très élégantes, représentent le système étudié avec des simplifications, pour rendre les calculs faisables, qui peuvent altérer leur capacité à prédire le comportement d'un système *réel*.

Ces expériences *in silico* permettent aussi d'étudier des conditions inaccessibles expérimentalement. Par exemple, elles sont très utiles pour étudier des systèmes dans des conditions extrêmes, comme des radionucléides en cas d'incident nucléaire majeur [67] ou des systèmes sous très hautes pression ou température ou très hauts champs électriques. [68] Elles permettent aussi d'amener des éléments de compréhension pour des phénomènes temporellement très courts ou très longs, inobservables en temps réel. Les simulations moléculaires en particulier donnent une vision microscopique du système qui nous aide à proposer des explications mécanistiques à des phénomènes macroscopiques.

Il existe deux grandes classes de simulations moléculaires que je vais brièvement décrire : celles reposant sur une description quantique de tout ou partie du système, et celles reposant sur une description classique du système.

Calculs quantiques

Parmi les nombreuses méthodes au niveau quantique, la théorie de la fonctionnelle de la densité (*density functional theory* ou DFT en anglais) est la plus utilisée et la seule qui soit numériquement tractable pour des systèmes avec plusieurs centaines d'atomes et des conditions aux limites périodiques. [69]

Dans les simulations quantiques de propriétés de l'état fondamental, le but est de trouver

la fonction d'onde (ψ) qui satisfasse l'équation de Schrödinger pour obtenir l'énergie (E) du système. L'équation 1 donne un exemple d'équation de Schrödinger pour un système d'électrons interagissant avec des noyaux fixes. Dans cette équation, m est la masse de l'électron, V est l'énergie d'interaction entre les noyaux atomiques et chaque électron et U est l'énergie d'interaction entre les électrons.

$$\left[-\frac{\hbar^2}{2m}\sum_{i=1}^{N}\nabla_i^2+\sum_{i=1}^{N}V(\boldsymbol{r}_i)+\sum_{i=1}^{N}\sum_{j<i}U(\boldsymbol{r}_i,\boldsymbol{r}_j)\right]\psi \quad = \quad E\psi \tag{1}$$

La fonction d'onde est une fonction mathématique très complexe de $3N$ variables, où N est le nombre d'électrons. Par exemple, la fonction d'onde complète de H_2O est une fonction à 30 variables. D'autre part, le terme de répulsion interélectronique de l'hamiltonien ($\sum_{i=1}^{N}\sum_{j<i}U(\boldsymbol{r}_i,\boldsymbol{r}_j)$) est crucial et requiert de considérer la corrélation entre chaque électron et tous les autres. Ainsi, sauf pour des systèmes à moins de 3 électrons, il est vain de traiter l'équation de Schrödinger analytiquement. La théorie de la fonctionnelle de la densité s'intéresse donc à chercher plutôt la densité électronique (cf. équation 2) qui peut être calculée à partir des fonctions d'ondes monoélectroniques ψ_i.

$$n(\boldsymbol{r})=2\sum_i\psi_i^*(\boldsymbol{r})\psi_i(\boldsymbol{r}) \tag{2}$$

Les méthodes de DFT reposent sur deux théorèmes démontrés par Hohenberg et Kohn qui permettent de réduire beaucoup la dimension du problème. [70] Le premier théorème est qu'il existe une unique densité électronique pour laquelle l'énergie est l'énergie de l'état fondamental. Ainsi, la connaissance de la densité électronique — un scalaire à 3 variables — suffit à déterminer une solution à l'équation de Schrödinger. Le deuxième théorème est que la densité électronique de l'état fondamental minimise l'énergie et correspond donc à la solution de l'équation de Schrödinger. Kohn et Sham ont appliqués ces théorèmes pour construire un système d'équations monoélectroniques, illustré par l'équation 3, qui permettent de trouver la densité électronique de l'état fondamental. [71] Les solutions de ces équations sont de simples fonctions d'onde monoélectroniques, qui n'ont pas de sens physique.

$$\left[-\frac{\hbar^2}{2m}\nabla^2+V(\boldsymbol{r})+V_{\mathrm{H}}(\boldsymbol{r})+V_{\mathrm{XC}}(\boldsymbol{r})\right]\psi_i(\boldsymbol{r})=\varepsilon_i\psi_i(\boldsymbol{r}) \tag{3}$$

Les équations de Kohn-Sham comportent trois potentiels V, V_{H} et V_{XC}. V décrit l'interaction entre un électron et les noyaux atomiques de façon analytique. Le deuxième, V_{H}, décrit la répulsion entre un électron et la densité électronique totale. Il s'agit du potentiel de Hartree définie par l'équation 4, où n est la densité électronique.

$$V_{\mathrm{H}}(\boldsymbol{r})=e^2\int\frac{n(\boldsymbol{r}')}{|\boldsymbol{r}-\boldsymbol{r}'|}\mathrm{d}^3r' \tag{4}$$

V_{H} contient une interaction non-physique d'un électron avec lui-même, corrigée par V_{XC}. V_{XC} caractérise les interactions d'échange et corrélations. Il s'agit d'une dérivée fonctionnelle de l'énergie d'échange-corrélation (E_{XC}) qui n'est pas connue exactement, sauf pour un gaz d'électrons libres. Néanmoins, de nombreuses approximations existent et permettent de calculer précisément des quantités physiques relatives au système.

V_{H} dépend de n, qui dépend des ψ_i, qui sont les solutions de l'équation de Kohn-Sham, dépendant donc de V_{H}. On utilise donc un procédé itératif pour obtenir une solution. [72] La méthode est une méthode de champ auto-cohérent (*self-consistent field* en anglais). Une version simplifiée de l'algorithme employé est donnée ci-dessous :

1. Définir une densité initiale, $n(\boldsymbol{r})$
2. Calculer les potentiels correspondant, V, V_H et V_{XC}, pour la densité électronique considérée.
3. Résoudre les équation de Kohn-Sham pour obtenir les ψ_i.
4. Calculer la densité électronique, n_{KS}, à partir des ψ_i obtenues à l'étape 3.
5. Comparer $n_{\mathrm{KS}}(\boldsymbol{r})$ avec $n(\boldsymbol{r})$. Si les deux densités sont identiques, alors il s'agit de la densité de l'état fondamental et elle peut être utilisée pour calculer l'énergie totale. Si les deux densités diffèrent on revient à l'étape 2 avec la nouvelle densité.

Les fonctions d'onde monoélectroniques sont représentés par une superposition de fonctions de base, rassemblées en bases de différentes tailles. La taille de la base doit être choisie pour avoir le meilleur compromis en coût numérique et précision. J'ai essentiellement utilisé des bases de type DZVP (*double-ζ valence polarized*) ou TZVP (*triple-ζ valence polarized*) lorsque la précision l'exigeait. Le choix de la fonctionnelle d'échange-corrélation (E_{XC}) est également crucial. Pendant toute ma thèse, j'ai utilisé des fonctionnelles de type GGA (*generalized gradient approximation*) qui prennent en compte l'échange non-local et la corrélation. En particulier, j'ai utilisé les fonctionnelles PBE et sa version adaptée pour les solides (PBE-SOL). L'échantillonnage de l'espace réciproque est également un facteur important, notamment pour le calcul des propriétés mécaniques. Dans le code CRYSTAL14 cet échantillonnage est contrôlé par un facteur de *shrink* pour construire une grille de points k dans l'espace réciproque. En première approximation ce paramètre doit être tel que son produit avec la valeur du plus petit vecteur de la maille cristalline soit supérieur à 20 Å.

La dynamique à température finie de systèmes peut être étudiée au niveau quantique en utilisant la dynamique moléculaire *ab initio* (*ab initio molecular dynamics* ou AIMD en anglais). La dynamique moléculaire *ab initio* est un outil essentiel pour sonder les propriétés dynamiques sub-nanosecondes. J'utilise la dynamique moléculaire *ab initio* telle qu'implémentée dans le logiciel CP2K — un logiciel open source de simulation pour la chimie quantique et la physique du solide, disponible sur `https://www.cp2k.org`. Plusieurs méthodes de dynamique moléculaire *ab initio* existent : la dynamique d'Ehrenfest, la dynamique Car-Parinello et la dynamique Born-Oppenheimer. Pendant ma thèse, j'ai utilisé uniquement la méthode de dynamique Born-Oppenheimer.

L'idée sous-jacente à la dynamique Born-Oppenheimer est de considérer la dynamique des électrons indépendamment de celle des noyaux, de par la grande différence de masse entre l'électron et le noyau. Ceci permet d'explorer la dynamique des molécules par la résolution de l'équation de Newton pour les noyaux :

$$\boldsymbol{F}_i(\boldsymbol{r}^N) = -\nabla_i U(\boldsymbol{r}^N) = m_i \frac{\mathrm{d}^2 \boldsymbol{r}_i}{\mathrm{d}t^2} \tag{5}$$

La force, $\boldsymbol{F}_i$ ressentie par un atome i de masse m_i et à la position $\boldsymbol{r}_i$ est égal à l'opposé du gradient, ∇_i, de l'énergie potentielle du système définie par la densité électronique, $U(\boldsymbol{r}^N)$. En dynamique moléculaire *ab initio*, les forces sont calculées au niveau quantique, typiquement par DFT. Le caractère quantique de ces simulations reposent uniquement sur la description des électrons, le noyaux sont considérés comme des objets massifs classiques.

L'équation de Newton pour les noyaux est ainsi intégrée numériquement avec un pas de temps fini Δt de l'ordre de la femtoseconde, correspondant à la dynamique des noyaux. À chaque pas de temps, la fonction d'onde est optimisée par DFT. Cette méthode est donc bien plus coûteuse que des calculs statiques (calcul de l'énergie ou des modes de vibration par exemple), mais elle permet d'étudier des phénomènes où les ruptures de liaisons sont essentielles ou bien des systèmes qu'aucune approximation classique (de type champ de force, voir section suivante) ne permet d'appréhender. Ces simulations peuvent être faites dans différents ensembles thermodynamiques : nombre constant de particules, volume constant et température constante (N, V, T) ou nombre constant de particules, pression constante et température constante (N, P, T).

Un certain nombre de propriétés peuvent être calculées par l'analyse des trajectoires. Tout d'abord, les fonctions de distribution de paires (PDF) qui peuvent être comparées à des données expérimentales quand tous les atomes sont pris en compte. L'examen des fonctions de distribution de paires par type d'atomes permet de comprendre quelles sont les interactions pertinentes, ce qui est compliqué à partir de PDFs expérimentales. Il est par exemple ainsi possible d'extraire des profils d'énergie libre par l'identification de potentiels de force moyenne ou par des approches plus sophistiquées comme la dynamique moléculaire sous contrainte ou l'approche de l'ensemble *Blue Moon*. [101, 102] Ces méthodes sont puissantes et ont par exemple permis d'expliquer le mécanisme par lequel le dioxyde de carbone peut rentrer dans une zéolithe où les cations bloquent les pores aux autres gaz. [97]

Calculs classiques

Pour simuler des systèmes plus grands pendant des durées plus longues les méthodes employées sont appelées méthodes classiques. Typiquement ces méthodes permettent de simuler plusieurs milliers d'atomes, et jusqu'à 100000 atomes. [104] Les temps de simulation vont de quelques nanosecondes à quelques centaines de nanosecondes. Cela permet d'étudier au niveau moléculaire des phénomènes tels que l'adsorption, la diffusion ou la dynamique du matériau. [105–107]

L'énergie potentielle $(U(\boldsymbol{r}^N))$, dans les simulations classiques, est calculée à partir de fonctions de l'énergie interatomique décrite par des paramètres qui viennent de ce qui est

appelé le champ de force. Celui-ci est un ensemble d'expressions analytiques des interactions entre atomes et des paramètres correspondant. Le choix et l'implémentation des champs de force est crucial pour l'obtention d'une bonne précision.

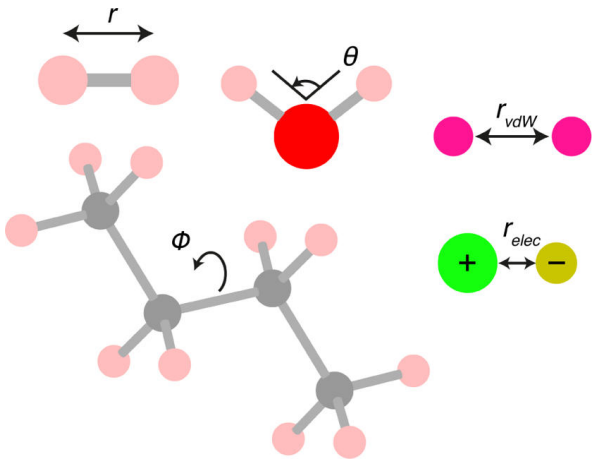

Figure 6 : Exemples de paramètres structuraux décrits explicitement dans les modèles champ de force utilisés en simulations moléculaires classiques. Cette figure est tirée de [108].

Les champs de force sont paramétrés pour reproduire la géométrie moléculaire ou des propriétés thermodynamiques expérimentales ou décrites au niveau quantique. La forme générale de l'énergie potentielle inclue des termes liants pour les liaisons covalentes (ou les liaisons métal-ligand), et des termes non-liants qui décrivent les interactions à plus longues portées comme l'électrostatique ou les forces de van der Waals (cf. Figure 6). La décomposition spécifique des termes dépend du champ de force choisi, mais une forme générique est donnée dans les équations 6, 7 et 8.

$$U_{\text{total}} = U_{\text{liés}} + U_{\text{non-liés}} \tag{6}$$

$$U_{\text{liés}} = U_{\text{liaison}} + U_{\text{angle}} + U_{\text{dièdre}} \tag{7}$$

$$U_{\text{non-liés}} = U_{\text{électrostatique}} + U_{\text{van der Waals}} \tag{8}$$

La dynamique moléculaire est simulée grâce au même procédé itératif que dans le cas quantique. Cependant, le coût plus faible des simulations classiques permet de suivre des processus à des échelles plus larges comme la dynamique de molécules d'eau confinées dans des zéolithes. [117]

Outre la dynamique moléculaire, un autre type de simulations très utilisées sont les simulations de type Monte Carlo. En particulier, cette méthode est utilisée pour simuler l'adsorption par déplacement, insertions et délétions de molécules de gaz dans la structure. [124] La différence entre la façon dont la dynamique moléculaire et le Monte Carlo en terme d'exploration de l'espace des phases est illustrée en Figure 7. Pour l'acceptation d'un pas Monte Carlo, l'algorithme souvent utilisé est celui de Metropolis. [125] L'application des étapes suivantes constitue la base de cet algorithme :

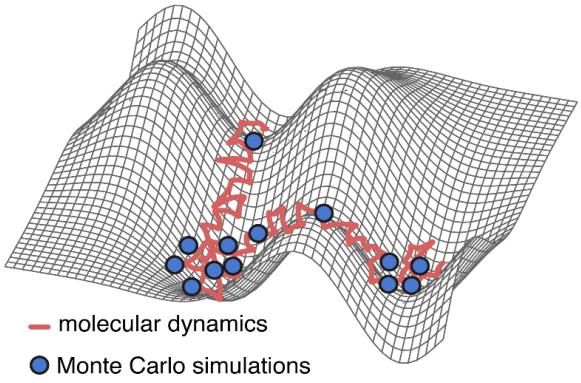

Figure 7 : Représentation de la façon dont la surface d'énergie potentielle est explorée par les simulations de dynamique moléculaire et de Monte Carlo.

1. Calculer l'énergie potentielle de l'état initial (U_i).
2. Choisir un déplacement d'une molécule aléatoire à partir d'une distribution uniforme.
3. Calculer l'énergie potentielle du nouvel état (U_f).
4. Si $U_f \leq U_i$, accepter le pas.
5. Si $U_f > U_i$, sélectionner un nombre aléatoire, w, avec $w \in [0, 1]$ à partir d'une distribution uniforme et si $\exp[-\beta(U_f - U_i)] > w$, accepter le pas.
6. Répéter les étapes 2 à 5.

Liens entre structure et propriétés mécaniques dans les zéolithes : exemple de l'auxéticité

Les propriétés mécaniques des tamis moléculaires, en particulier des zéolithes, ont beaucoup été étudiés dans un contexte d'ingénierie de procédés. [135, 136] . En 2013, F-X. Coudert a publié la première étude systématique sur les propriétés mécaniques des zéolithes connues avec des calculs quantiques. [142]

Au-delà de la confirmation de corrélations connues, comme celle existant entre l'énergie de réseau et le volume spécifique, il a suggéré un critère de faisabilité basé sur l'anisotropie élastique (cf. Figure 8) comme définie dans l'équation 9 :

$$\eta = max\left(\frac{E_{max}}{E_{min}}, \frac{G_{max}}{G_{min}}\right), \tag{9}$$

où $E_{min/max}$ sont les modules d'Young minimal et maximal et $G_{min/max}$ sont les modules de cisaillement minimal et maximal. Le critère proposé est que la faisabilité des structures correspond à un double critère : $\Delta E < 20\,\mathrm{kJ/mol}$ et $\eta < 4$, en vertu du fait que presque toutes

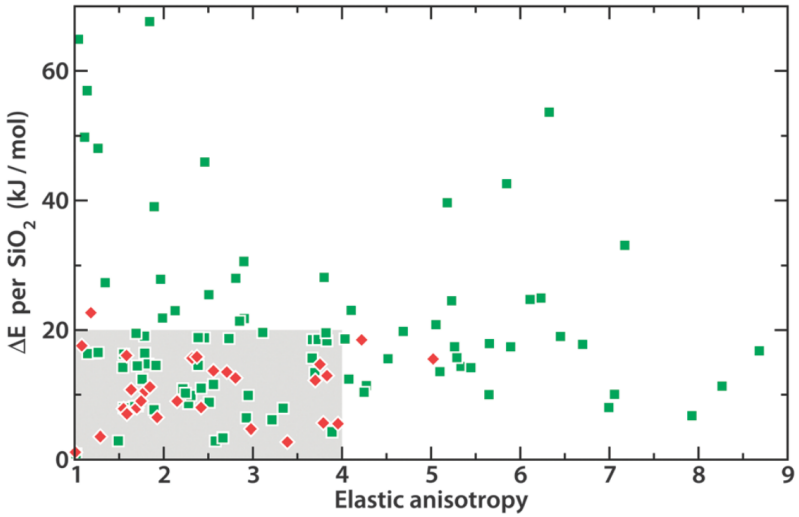

Figure 8 : L'énergie relative au α-quartz est représentée en fonction de l'anisotropie élastique ; les points rouges correspondent aux zéolithes synthétisées sous forme purement silicée. La zone grise correspond au critère de faisabilité proposé dans [142]. Cette figure est extraite de [142].

les structures déjà synthétisées respecte ces conditions. Cette étude est l'une des premières à mentionner les propriétés mécaniques anomales des zéolithes avec la compressibilité linéaire négative qui est le fait qu'un matériau s'étende linéairement dans une direction alors qu'il est soumis à une pression isotrope. [143]

Une autre étude, publiée en 2015 par Siddorn et al., s'intéresse à une autre propriété anomale dans les zéolithes silicées : l'auxéticité. [144] L'auxéticité est un phénomène, existant surtout dans des mousses isotropes, qui correspond à un allongement linéaire dans une direction alors qu'une autre direction est soumise à une élongation. Ce phénomène est caractérisé par un ratio de Poisson négatif.

Afin d'étudier les liens existant entre la structure et les propriétés mécaniques anomales des zéolithes, j'ai utilisé une base de données de zéolithes hypothétiques générée par Pophale et al. . [145] Cette base de données contient 590811 structures avec leurs propriétés mécaniques calculées par des méthodes classiques. J'ai réalisé une analyse des propriétés mécaniques des structures contenues dans cette base de données. J'ai ensuite utilisé des méthodes de chimie quantique sur un sous-ensemble de cette base de données pour tenter d'expliquer le mécanisme sous-jacent à l'auxéticité.

Calcul des propriétés mécaniques

Le but de la mécanique des matériaux est d'étudier le comportement des matériaux soumis à des contraintes mécaniques extérieures, caractérisées par le tenseur des contraintes(σ). Le matériau réagit en changeant sa forme et sa taille et ces déformations sont caractérisées par le tenseur des déformations (ε). Ces tenseurs de rang 2 sont représentés par des matrices symétriques 3×3 (équations 10 et 11).

$$\varepsilon = \begin{pmatrix} \varepsilon_{xx} & \varepsilon_{xy} & \varepsilon_{xz} \\ \varepsilon_{yx} & \varepsilon_{yy} & \varepsilon_{yz} \\ \varepsilon_{zx} & \varepsilon_{zy} & \varepsilon_{zz} \end{pmatrix} \tag{10}$$

$$\sigma = \begin{pmatrix} \sigma_{xx} & \sigma_{xy} & \sigma_{xz} \\ \sigma_{yx} & \sigma_{yy} & \sigma_{yz} \\ \sigma_{zx} & \sigma_{zy} & \sigma_{zz} \end{pmatrix} \tag{11}$$

La relation entre σ et ε peut être résumée par la Figure 9 : pour des petites déformations, la réponse est appelée élastique, réversible (et souvent linéaire), et pour des déformations plus grandes la réponse est dite plastique, irréversible et non-linéaire, jusqu'au point de fracture.

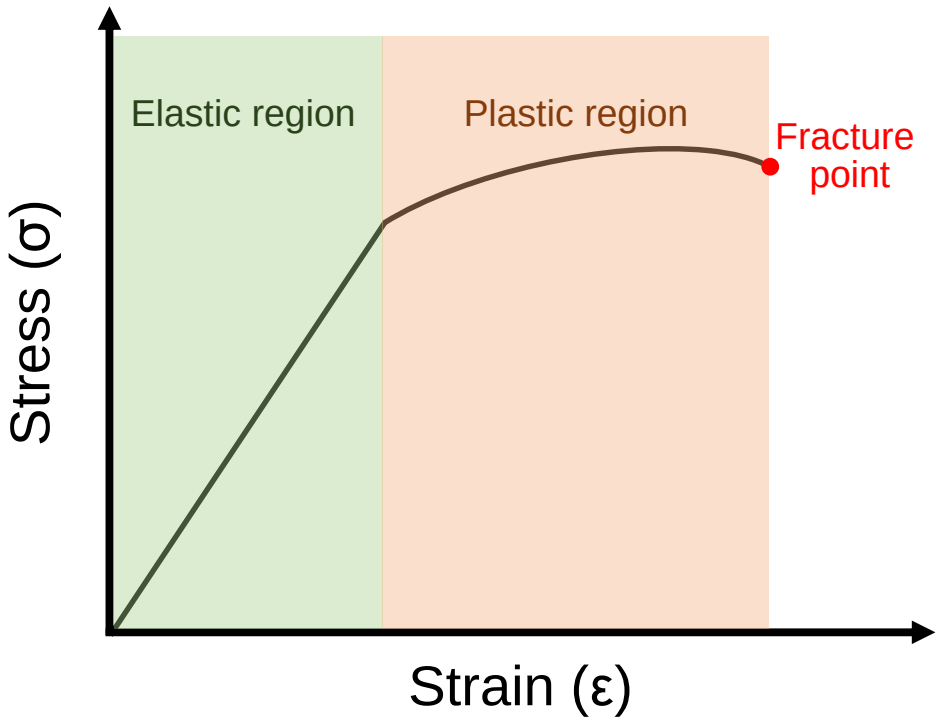

Figure 9 : Représentation schématique de la relation contrainte-déformation dans les matériaux.

Selon le matériau, cette région élastique va d'une fraction de pourcent (par exemple pour l'acier) et jusqu'à 700% pour certains élastomères. Dans la partie élastique linéaire, les contraintes et les déformations sont reliés par le tenseur élastique du second ordre, ou les constantes élastiques. Le calcul des propriétés mécaniques usuelles (module d'élasticité isostatique, module d'Young, module de cisaillement, ratio de Poisson) se fait de manière analytique à partir de ce tenseur, représenté par une matrice symétrique 6×6.

Durant ma thèse, j'ai développé une application nommée ELATE, disponible en ligne (`www.progs.coudert.name/elate`), qui permet de calculer les propriétés mécaniques usuelles

à partir du tenseur élastique et de représenter graphiquement les variations spatiales de ces propriétés, en 2D et en 3D.

Propriétés mécaniques d'une base de donnée structurale

Principes de construction et analyses initiales

En 2011, Pophale et al. ont rapporté la création d'une base de données basée sur le champ de force BKS (Beest–Kramer–van Santen). [161] La génération de la base de données a impliqué plusieurs étapes incluant du Monte Carlo, des recuits simulés et des optimisations de géométries. Sur 590811 structures uniques, 590465 tenseurs élastiques convergés ont été obtenus. Ceux-ci ont été publiés en ligne à part, mais n'ont jamais été analysés.

Les premières analyses que j'ai faites sur cette base de données ont porté sur la prévalence d'instabilités mécaniques et les propriétés mécaniques anomales. Les résultats sont les suivants pour l'entièreté de la base de données :

- 128563 structures sont mécaniquement instables (soit $\simeq 22\%$ de la base) : ces structures correspondent à des minima très locaux qui deviennent instables suite à une petite perturbation ($\simeq 1\%$ d'élongation).
- 148974 structures présentent de la compressibilité linéaire négative, soit 32% des structures stables.
- 368508 structures appartiennent à la classe d'auxéticité 1A avec $\nu_{\text{min}} < 0$ ($\simeq 80\%$ des structures stables), i.e. au moins une direction présente de l'auxéticité sur au moins un axe d'élongation.
- 30342 structures appartiennent à la classe d'auxéticité 2B avec un ratio de Poisson moyen négatif ($\simeq 6.6\%$ des structures stables).
- 578 structures sont totalement auxétiques (classe 3C) avec un ratio de Poisson maximal négatif ($\simeq 0.1\%$ des structures stables).

La proportion de structures présentant de la compressibilité linéaire négative ou de l'auxéticité semble élevée selon les données basées sur les calculs classiques. Pour voir à quel point cette base de données est proche du champ des zéolithes connus, je compare ces résultats à ceux obtenus en ne gardant que les 134 structures connus au sein de la base. Les résultats sont les suivants :

- 14 structures mécaniquement instable ($\simeq 10\%$ des structures connus).
- 24 structures présentant de la compressibilité linéaire négative, soit 20% des structures connus mécaniquement stables.
- 78 structures appartenant à la classe d'auxéticité 1A ($\simeq 65\%$ des structures connus mécaniquement stables).

- 13 structures appartiennent à la classe d'auxéticité 2B ($\simeq$ 11% des structures connus mécaniquement stables).
- 1 structure est totalement auxétiques (classe 3C) ($\simeq$ 0,8% des structures connus mécaniquement stables).

Pour référence, les données calculées au niveau quantique par Coudert [142] sur 121 structures connues donnent : 1 structure instable, 13% de structures présentant de la compressibilité linéaire négative, 26% de structures appartenant à la classe d'auxéticité 1A, 0,8% des structures appartenant à la fois à la classe 2B et 3C.

Le champ de force donne l'impression de surestimer la prévalence de propriétés mécaniques anomales. Cependant, pour des propriétés mécaniques plus simples comme le module d'élasticité isostatique ou le module de cisaillement, ses prédictions sont meilleures (voir Figure 10 tirée de [163]). La corrélation entre les données BKS et DFT est correcte, même si l'analyse quantitative révèle que la racine carrée de l'erreur quadratique moyenne est de 23 GPa et 36 GPa pour le module d'élasticité isostatique et le module de cisaillement respectivement.

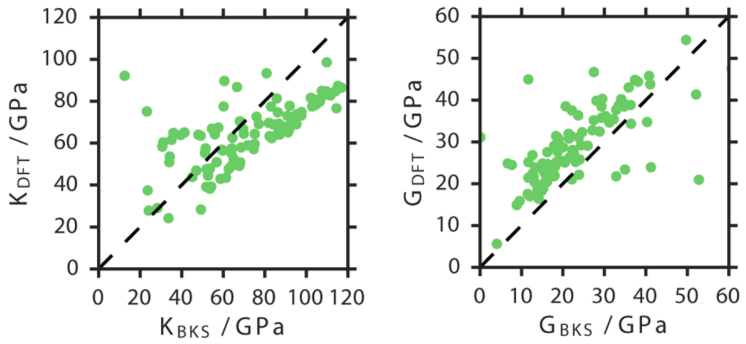

Figure 10 : À gauche : modules d'élasticité isostatique obtenus par DFT comparés à ceux obtenus grâce au champ de force BKS. À droite : modules de cisaillement obtenus par DFT comparés à ceux obtenus grâce au champ de force BKS. Figures tirées de [163].

Comparaison avec les structures connues

Je montre à présent à quel point les structures de la base de données sont statistiquement proches des structures connues, qui représentent une fraction infime de celle-ci (environ 0.02%). Globalement, les structures hypothétiques ont des propriétés similaires, en excluant les extrêmes manifestes (moins de 1% de la base) en restreignant les gammes de valeurs à des bornes raisonnables (comme noté dans [163], les modules d'élasticité isostatiques varient entre -27000 et 20500 GPa, valeurs évidemment inaccessibles pour des zéolithes). Il semble difficile de trouver une propriété structurale ou mécanique pour laquelle les zéolithes connues se différencient vraiment du reste de la base de données

Par exemple, le module d'élasticité isostatique a une valeur moyenne de 54 GPa, une médiane de 50 GPa et un écart-type de 33 GPa pour les zéolithes connues inclues dans la

base de données, tandis que ces valeurs sont de 46, 44 et 18 GPa pour la base de données entière. La seule différence est la prédiction de structures hypothétiques avec des modules très bas (<1 GPa) alors que la zéolithe connue avec le plus petit module d'élasticité isostatique est la structure BOF avec 9 GPa. Que ce soit pour les compressibilités linéaires minimale et maximale, les modules d'Young et de cisaillement et leurs extrema, le ratio de Poisson et ses extrema, les zéolithes connues présentent des caractéristiques similaires à toutes les structures de la base de données.

Une des propriétés fondamentales utilisée pour décrire les zéolithes est l'énergie par atome de silicium relative au quartz α qui est le polymorphe le plus stable des zéolithes totalement silicée car elle est reliée directement à l'enthalpie de formation. La valeur moyenne de cette énergie pour les zéolithes connues est de 46 kJ/mol tandis qu'elle est de 52 kJ/mol pour la base de données entière. Néanmoins, contrairement au cas du module d'élasticité isostatique, il ne semble pas y avoir de seuil au-delà duquel on ne trouve aucune zéolithe connue. Par exemple, plus de 15% des structures connues ont une énergie supérieure à 60 kJ/mol par rapport au quartz.

Sur le plan des propriétés purement géométriques, l'analyse du milieu poreux montre des différences significatives entre les structures connues et la base de données complète. Les structures contenues dans la base de données sont en moyenne moins poreuses que les structures connues avec des tailles de pores environ 45% plus importantes dans les structures connues. De même la surface accessible, à une sonde hélium, est 2,5 fois plus grande pour les structures connues, et le volume accessible relatif 3,6 fois plus important.

Une dernière propriété fréquemment étudiée dans les zéolithes est la distribution des tailles d'anneaux formés par les atomes de silicium au sein d'une maille élémentaire. En comparant pour chaque taille d'anneau les moyennes et les écart-types entre la base de donnée complète et les zéolithes connues, j'observe que la base de données contient des zéolithes avec des caractéristiques structurales assez différentes des zéolithes déjà connues.

En conclusion, cette très grande base de données construite par Pophale et al. [145] explore de façon relativement exhaustive l'espace conformationnel des zéolithes. En effet, les propriétés mécaniques et énergétiques calculées avec des méthodes de type champ de force montrent une probable faisabilité d'un certain nombre de structures hypothétiques, tandis que l'analyse des propriétés structurales pointent de véritables différences avec les structures connues.

Corrélations notables

L'analyse de la corrélation entre la densité et l'énergie par silicium relative au quartz confirme la corrélation négative existante démontrée sur les zéolithes connues au niveau quantique par Coudert. [142] D'autre part, le champ de force semble défavoriser thermodynamiquement les structures avec des anisotropies mécaniques élevées, également comme dans le cas des zéolithes connues au niveau quantique, bien que la corrélation soit moindre avec les données champ de force. La corrélation positive entre le module d'Young et le module de cisaillement est aussi très bien reproduite.

Étude de l'auxéticité dans les zéolithes

J'ai étudié au niveau quantique les propriétés mécaniques d'un sous-ensemble de la base de données contenant les 578 structures qui présentent une auxéticité totale (un ratio de Poisson toujours négatif). J'ai obtenu 500 tenseurs élastiques du second ordre convergés, dont 392 correspondant à des structures mécaniquement stables. Je nomme cet ensemble l'ensemble auxétique.

Pour comparaison et afin de créer un ensemble sur lequel utiliser des méthodes d'apprentissage statistique, j'ai également calculé 742 tenseurs élastiques du second ordre au niveau quantique sur des structures choisies au hasard dans la base de données, en vérifiant la représentativité de cet ensemble vis-à-vis de la base de données entière. Ce second ensemble a produit 599 structures mécaniquement stables. Je nomme cet ensemble l'ensemble aléatoire. J'ai analysé les résultats uniquement pour les structures dont les calculs quantiques prédisent une stabilité mécanique.

Comparaison entre propriétés calculées par champ de force et par DFT

Les paramètres de maille cristalline sont quasiment identiques par calcul quantique à ceux obtenus avec le champ de force, et de même pour les volumes de la maille. Néanmoins, pour ce qui est de la densité, bien que l'accord global soit bon, dans le sous-ensemble aléatoire la déviation maximale est de 12% et elle monte à 35% pour une des structures de l'ensemble auxétique. La comparaison entre les énergies données par le champ de force et celles obtenues par DFT montre que celui-ci est peu fiable pour ce qui est de la stabilité thermodynamique relative des zéolithes silicées (cf. Figure 11). Les valeurs du champ de force sont non seulement éloignées, mais également très peu corrélées avec celles données par les calculs quantiques.

Les constantes élastiques dépendant des variations de l'énergie vis-à-vis de déformations du matériau, la performance du champ de force s'avère également piètre sur le plan des propriétés mécaniques. Le tableau 1 montre trois estimateurs de l'erreur commise par le champ de force : la racine carrée de l'erreur quadratique moyenne divisée par la gamme des valeurs observées (rRMSE), l'erreur absolue moyenne et le coefficient de corrélation. Quelque soit l'estimateur choisi, on voit que le champ de force est inutilisable pour un criblage de matériaux pour des propriétés mécaniques précises.

Enfin, si le but est de s'intéresser à l'auxéticité dans ces matériaux, la prédiction des extrema du ratio de Poisson joue un grand rôle. Or, les valeurs données par le champ de force sont extrêmement peu fiables.

Par exemple, la racine carrée de l'erreur quadratique moyenne est de 1,5 pour le maximum du ratio de Poisson sur le sous-ensemble auxétique et s'envole à 13 sur le sous-ensemble aléatoire.

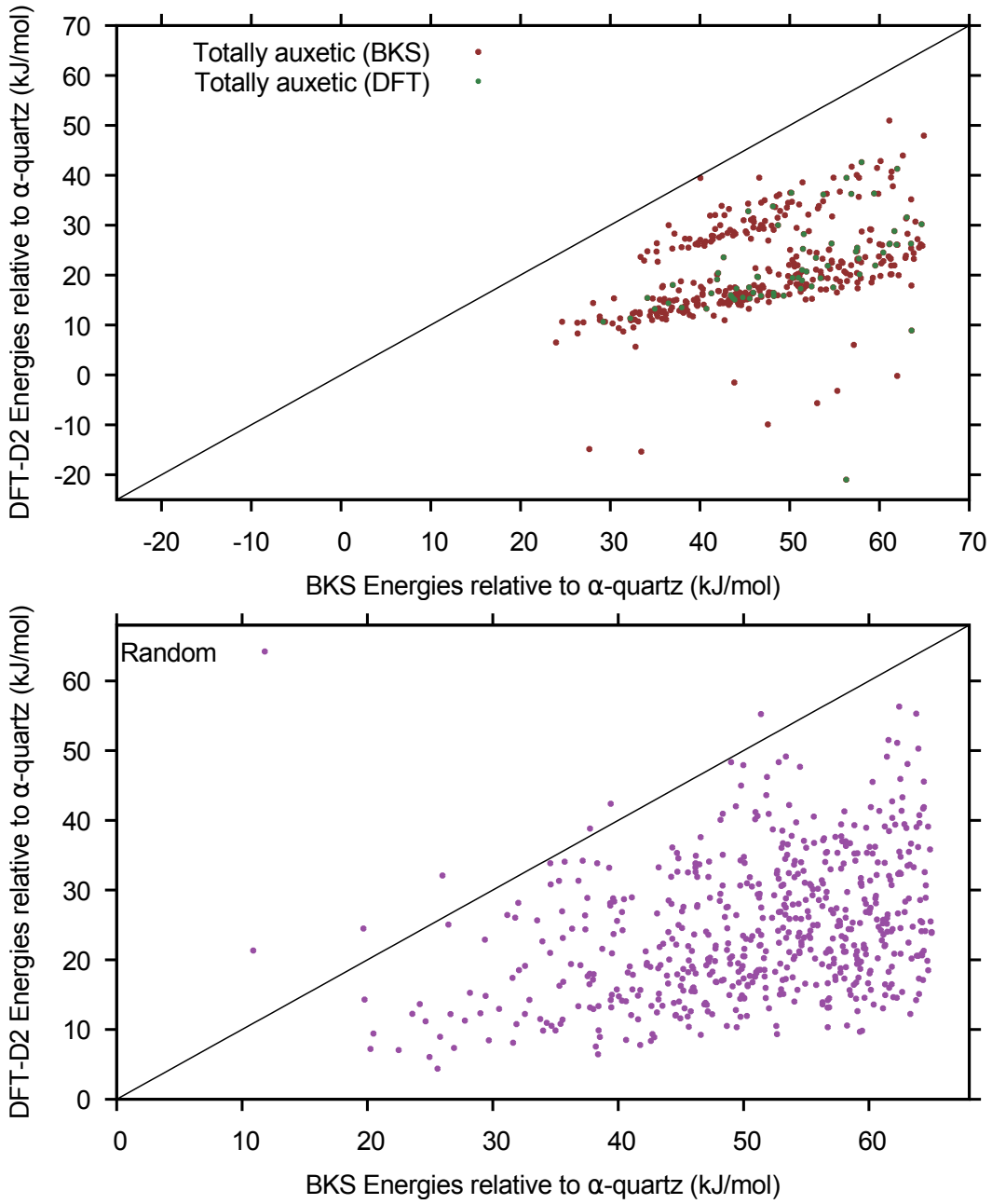

Figure 11 : En haut : énergies obtenues par les calculs quantiques en fonction des énergies obtenues par calcul avec le champ de force BKS pour les sous-ensemble auxétique. Les points verts correspondent aux structures prédites comme totalement auxétiques par les calculs quantiques. En bas : comme à gauche, mais pour le sous-ensemble aléatoire. La ligne noire correspond à l'identité.

Prédire l'auxéticité

Le principe de l'apprentissage statistique ou *machine learning* est de créer un prédicteur (P) en entraînant un algorithme sur deux ensembles de variables (multidimensionnelles a priori)

	En (kJ/mol)	K	E	G	ν
rRMSE(3C)	39%	22%	19%	174%	47%
rRMSE(random)	55%	21%	85%	78%	46%
MAE(3C)	26	7,9	11	10	0,29
MAE(random)	27	10	19	7,6	0,07
r(3C)	0,46	0,29	0,43	-0,01	0,002
r(random)	0,38	0,60	0,25	0,22	0,21

Tableau 1 : Je donne ici, pour les deux sous-ensembles, la racine carrée de l'erreur quadratique moyenne relative (rRMSE, RMSE divisée par la gamme des valeurs observées), l'erreur absolue moyenne (MAE) et le coefficient de corrélation de Pearson (r) pour l'énergie (En), le module d'élasticité isostatique (K, en GPa), le module d'Young (E, en GPa), le module de cisaillement (G, en GPa) et le ratio de Poisson (ν).

X, appelé l'ensemble des descripteurs et Y, le résultat désiré. P est alors tel que P(X)=Y. Subséquemment, à partir d'un ensemble X', P est testé en comparant P(X') à Y' le résultat réel correspondant à X'.

J'ai utilisé un algorithme d'apprentissage statistique appelé *gradient boosting regressor* (GBR) tel qu'implémenté dans la bibliothèque python `scikit-learn` pour créer trois prédicteurs : un pour la prédiction du minimum du ratio de Poisson, un pour la prédiction de son maximum et un pour la prédiction de sa valeur moyenne, uniquement à partir de descripteurs structuraux, très peu coûteux à calculer. J'ai utilisé quasiment les mêmes descripteurs que Evans et Coudert dans [163]. Ceux-ci sont classés en trois catégories : locaux, concernant les longueurs de liaisons, les angles de torsion, les angles dièdres, globaux, comme la densité ou la distribution des tailles d'anneaux de silicium et en lien avec la porosité, comme la surface accessible ou le volume poreux accessible.

Le résultat obtenu pour le ratio de Poisson est montré dans la Figure 12. Globalement, le prédicteur obtenu par apprentissage statistique est bien meilleur que le champ de force. Le champ de force a une performance similaire sur le sous-ensemble des zéolithes connues, mais ne tient pas la comparaison sur aucun des deux autres sous-ensembles (auxétique et aléatoire). Cet algorithme permet en outre de savoir quels sont les descripteurs qui comptent le plus pour expliquer le résultat : ici, les descripteurs locaux jouent un rôle important, tout comme les tailles de pores et la proportion des anneaux de taille 4, 5, 6 et 8.

De même pour les extrema du ratio de Poisson : les prédicteurs générés par apprentissage statistique sont non seulement meilleurs, mais tout simplement utilisables pour rechercher de l'auxéticité dans ces matériaux. En effet, quelque soit le sous-ensemble considéré, ou sur la totalité des zéolithes considérées, les erreurs absolues et quadratiques sont inférieures à 0.5 pour ces propriétés, tandis que le champ de force ne présente une telle performance (moins bonne que GBR) que pour le ratio de Poisson maximum des zéolithes connues.

Conclusion

En utilisant des calculs quantiques sur deux ensembles de structures extraites d'une base de données d'environ 600000 structures hypothétiques, j'ai pu montrer que le champ de force

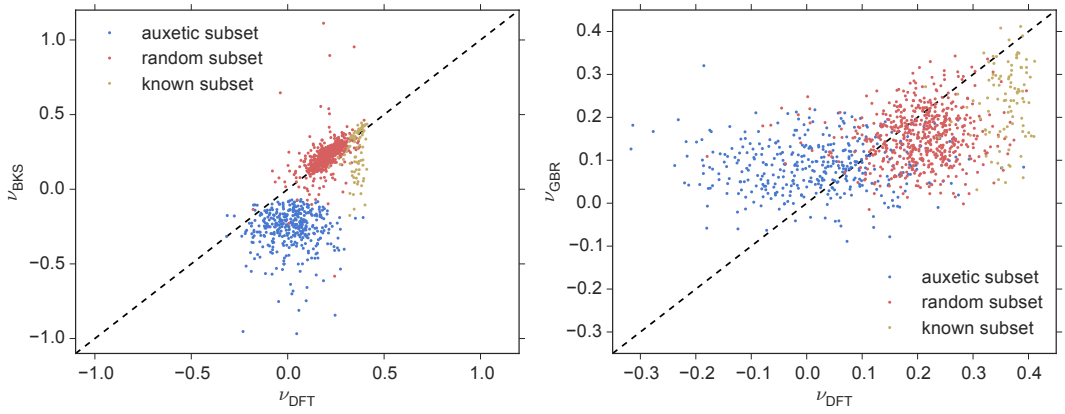

Figure 12 : À gauche : ratios de Poisson donnés par BKS en fonction des valeurs calculées en DFT. À droite : ratios de Poisson donnés par le prédicteur construit en utilisant l'algorithme GBR en fonction des valeurs calculées en DFT. Les structures du sous-ensemble auxétique sont indiquées en bleu, celles du sous-ensemble aléatoire en rouge et les structures connues, en vert.

BKS peut être utilisé pour déterminer les propriétés structurales des zéolithes. Cependant, en ce qui concerne les propriétés mécaniques, et en particulier le ratio de Poisson, et plus précisément ces extrema, ce champ de force ne peut être utilisé pour explorer les propriétés d'auxéticité des zéolithes. J'ai montré que les techniques d'apprentissage statistique offrent une manière de construire des modèles prédictifs rapides et peu coûteux, comme je l'ai fait pour le ratio de Poisson et ces extrema. L'importance des descripteurs structuraux dans la détermination d'une propriété donnée peut en outre être extraite du processus d'apprentissage. Enfin, mon étude porte uniquement sur les zéolithes totalement silicées, mais les mêmes méthodes pourraient être appliquées à d'autres matériaux poreux, étant donnée une base de données suffisamment large de données expérimentales ou provenant de calculs quantiques.

Fondre des MOFs pour créer de nouveaux matériaux

La plupart des études sur les MOFs ont été menées sur leurs phases cristallines. Cependant, leurs phases amorphes présentent un intérêt, notamment pour aller au-delà des application traditionnelles des MOFs reposant sur de très grandes surfaces spécifiques. Ces phases amorphes peuvent en effet profiter de la versatilité inhérente à ces structures pour des applications comme la délivrance contrôlée de gaz ou de médicaments, ou encore le piégeage de substances toxiques ou radioactives.

État de l'art de l'amorphisation des MOFs

Des travaux récents ont montré la possibilité de synthétiser directement des MOFs amorphes [49], mais je vais décrire ici uniquement les processus d'amorphisation partant d'une structure cristalline pour obtenir une structure amorphe après altération. Il y a trois manières d'amorphiser un MOF : le soumettre à des pressions de l'ordre de quelques mégapascals à

quelques gigapascals dans une cellule à enclume diamant (amorphisation sous pression), [174] induire des contraintes de cisaillement par broyage mécanique (*ball-milling* en anglais) [175] ou en le chauffant dans un four à des températures entre 300 et 700 °C (amorphisation sous température).

Amorphisation sous pression

La première étude rapportant l'amorphisation d'un MOF a été publié en 2009 par Chapman et al. [174]. Les auteurs observent l'amorphisation irréversible de la structure ZIF-8 à une pression de 0.34 GPa et le déclin de la capacité d'adsorption résultant. En 2010, Hu et al. ont rapporté l'amorphisation irréversible de MOF-5 à une pression très basse de 3.5 MPa. [176] L'amorphisation est due à une destruction d'une partie des groupes carboxylates des ligands. Tandis que dans le cas de ZIF-8 la surface spécifique se maintenait à 84% de celle du cristal à 0.6 GPa, MOF-5 perd quasiment toute sa surface spécifique interne (Figure 13).

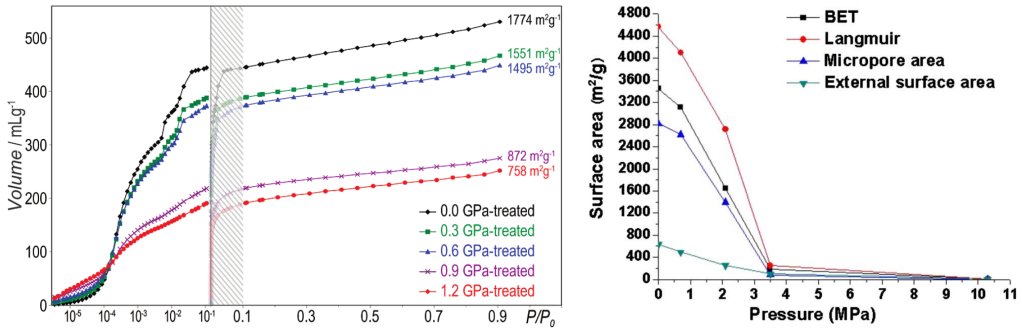

Figure 13 : À gauche : isothermes d'adsorption de N_2 pour ZIF-8 sous pression (figure prise de [174]). À droite : surfaces spécifiques de MOF-5 soumis à des compressions à température ambiante (figure prise de [176]).

D'autres comportements peuvent être observés : par exemple ZAG-4 ne s'amorphise pas avec des pressions jusqu'à 10 GPa, [177] ou encore l'exemple de l'amorphisation réversible de ZIF-4 rapportée par Bennett et al. en 2011. [178]

Dès 2011, Chapman et al. ont présenté une application à l'amorphisation sous pression de ZIF-8. [179] Ils ont utilisé ce processus d'amorphisation pour piéger cinétiquement le diiode dans la phase amorphe de ZIF-8. Or I_2 est un sous-produit dangereux de la production d'énergie nucléaire et qui peut être rejeté en grande quantité en cas d'accident nucléaire.

Amorphisation par broyage mécanique

Le broyage mécanique est de plus en plus utilisé pour la synthèse des MOFs, méthode qui est appelée mécanochimie, [58, 180] mais il est encore rarement utilisé pour l'amorphisation de structures cristallines. On peut néanmoins citer quelques exemples intéressants : en 2012, Cao, Bennett et al. ont rapporté l'amorphisation par broyage mécanique de ZIF-8 ; [181] en 2013, Bennett et al. ont publié un article détaillant l'amorphisation par broyage mécanique

de ZIF-4, ZIF-8, ZIF-69 et ZIF-mnIm. [51] Pour ZIF-8 et ZIF-mnIm, l'amorphisation permet d'augmenter la température jusqu'à laquelle I_2 est adsorbé de 200°C, montrant le potentiel de ce processus pour le piégeage de substances dangereuses.

Amorphisation sous température

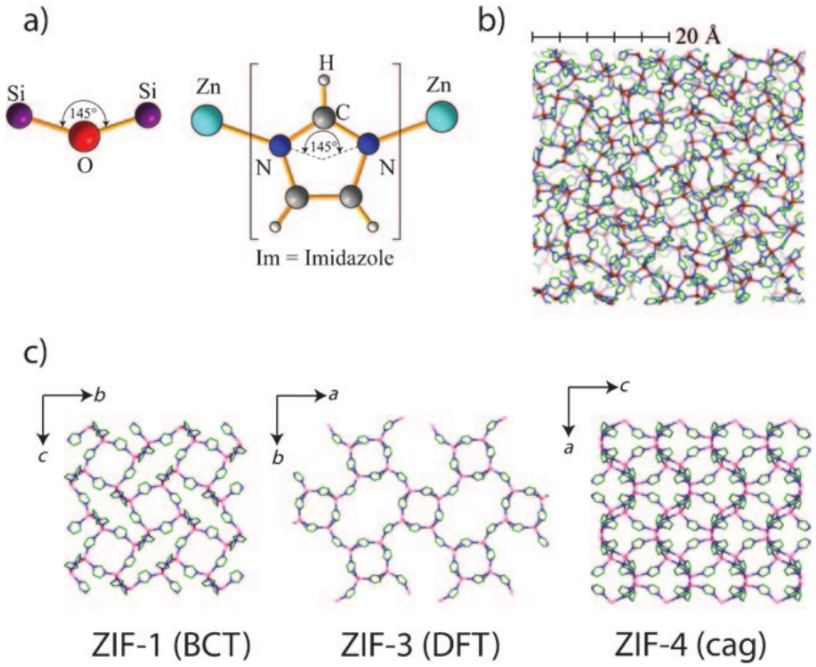

Figure 14 : a) Les liaisons similaires Si-O-Si et Zn-Im-Zn des zéolithes et des ZIFs respectivement. b) Une configuration instantanée de la topologie de type modèle continu aléatoire (*continuous random network* ou CRN en anglais) de ZIF amorphe obtenue par modélisation de type *reverse* Monte-Carlo (RMC). c) Mailles unitaires étendues de ZIF-1 (à gauche), ZIF-3 (au centre), et ZIF-4 (à droite). Cette figure est tirée de [55].

Comme rapporté depuis 15 ans, les zéolithes inorganiques peuvent s'amorphiser grâce à une élévation de la température. [185–187] Les ZIFs, formées par assemblage de tétraèdres basés sur un ion métallique et quatre ligands imidazolates (substitués ou non), ont naturellement été étudiées sur le plan de leur altération structurale suite à une élévation de température. En 2010 la première étude décrivant une structure amorphe de ZIF-4(Zn) obtenue par amorphisation sous température de la structure cristalline fut publiée. [188] Ensuite il a été montré que ZIF-1(Zn), ZIF-3(Zn) et ZIF-4(Co) (cf. Figure 14) peuvent s'amorphiser sous température, tandis que ZIF-8, ZIF-9, ZIF-11, ZIF-14 and ZIF-βqtz se décomposent avant toute transition structurale. [55] Le seul point commun entre ces dernières structures est le fait que leurs ligands sont substitués alors que les précédentes sont basées sur des imidazolates non substitués.

Plus précisément, ZIF-4, ZIF-1 and ZIF-3, qui ont pour formule $Zn(Im)_2$ ($Im=C_3N_2H_3$), s'amorphise atour de 300°C. La structure résultante est appelée a-ZIF et est structurellement similaire aux verres de silice. En élevant encore la température, au-delà de 400°C, elles re-

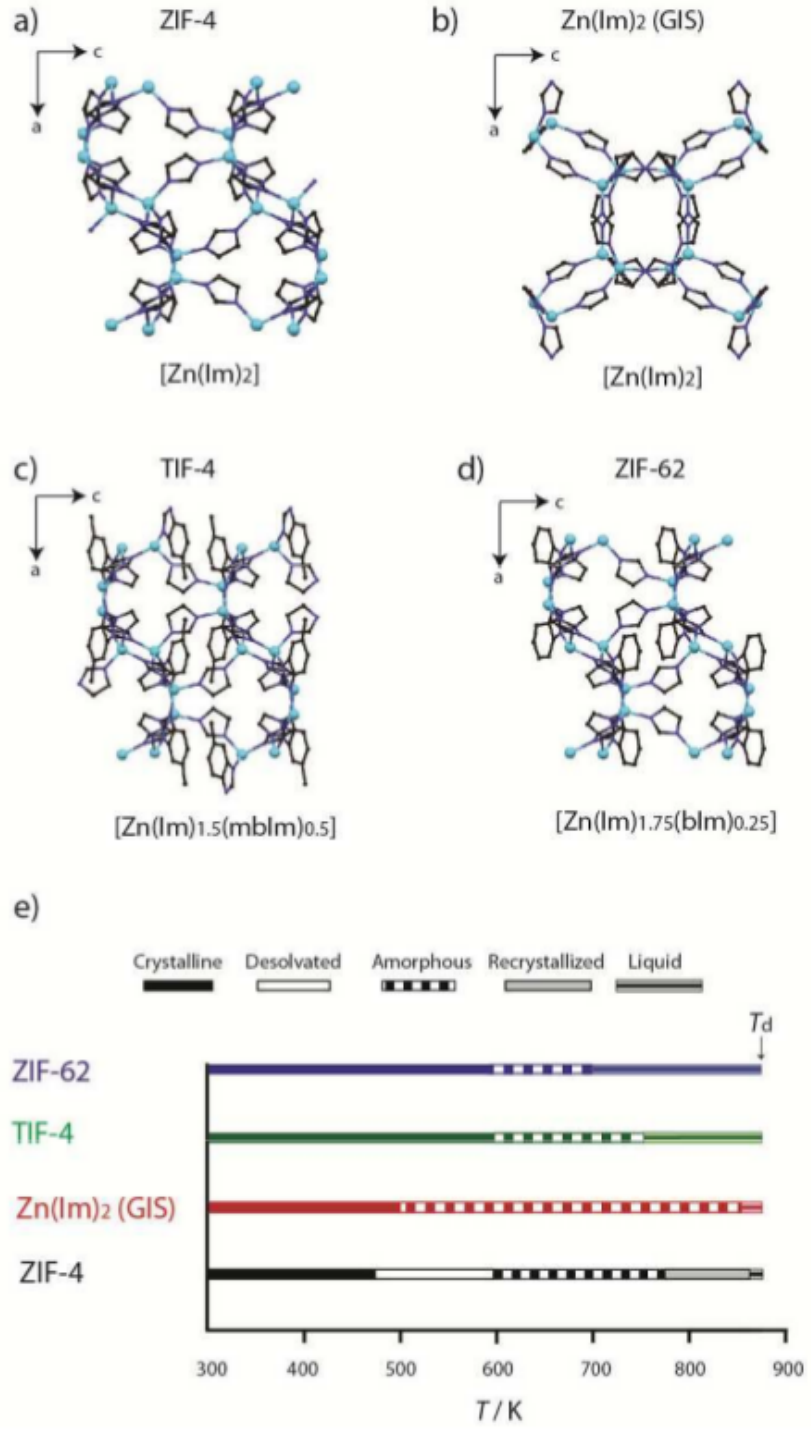

Figure 15 : Mailles unitaires selon l'axe b pour (a) ZIF-4, (b) $Zn(Im)_2$(GIS), (c) TIF-4 et (d) ZIF-62. N : bleu foncé, Zn : bleu clair, C : noir, H : non visible. (e) Vue schématique des évènements thermiques pendant le chauffage. Cette figure est prise de [54].

cristallisent dans une phase similaire à zni, le polymorphe le plus stable de la famille des ZIFs avec des ligands imidazolates non substitués. [189] En 2015, Bennett et al. ont publié une

étude montrant que ZIF-4 peut atteindre un état liquide autour de 565°C, contrairement à ZIF-8 qui se décompose. Cette possibilité de fondre des ZIFs puis de faire subir une trempe aux liquides obtenus offre une nouvelle manière de créer des verres hybrides. Par exemple, le piégeage de lanthanides avant amorphisation est une voie prometteuse pour synthétiser des verres avec des propriétés optiques et luminescentes. Cependant, cette capacité pour un MOF de fondre a pour l'instant été peu observée.

En 2016, Bennett et al. ont étudié des structures similaires à ZIF-4 : $Zn(Im_2)(GIS)$ avec la même composition, TIF-4, avec la même topologie, mais avec un quart des imidazolates transformés en méthylimidazolates et ZIF-62 avec la même topologie, mais avec un huitième des imidazolates remplacés par des benzylimidazolates (cf Figure 15). [54] $Zn(Im_2)(GIS)$ a une température de fusion similaire à celle de ZIF-4 (857 K contre 863 K), mais ne montre pas de recristallisation préalable vers une phase zni. TIF-4 et ZIF-62 permettent d'étudier l'influence du changement de ligand sur la température de fusion. Elles montrent toutes les deux des températures de fusion plus basses que celle de ZIF-4. Les auteurs concluent ainsi que l'augmentation de la taille des ligands diminuent la température de fusion.

Étude de la fusion de différentes ZIFs

Systèmes étudiés

J'ai étudié le comportement de fusion de quatre ZIFs : ZIF-8, ZIF-4, ZIF-zni et SALEM-2. ZIF-8 est composée de tétraèdres $Zn(mIm)_2$ (mIm = méthylimidazolate = $C_4N_2H_5$) et a la même topologie que la zéolithe sodalite (SOD). [97] Son groupe d'espace est le groupe $I-43m$ et sa maille unitaire, comportant 276 atomes, a un paramètre de maille unique de 16,993Å. Le panneau de gauche de la Figure 16 montre 8 mailles élémentaires. Cette structure est très ouverte et poreuse avec une densité de 0,965 g/cm^3.

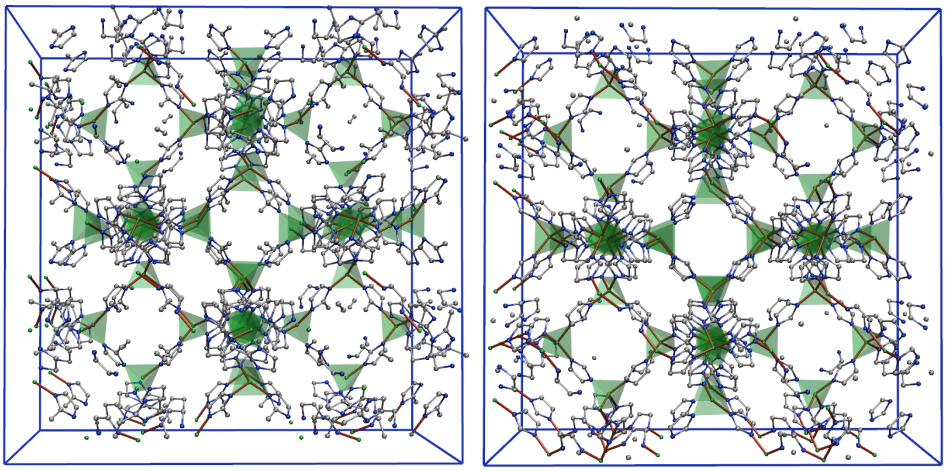

Figure 16 : À gauche : ZIF-8. À droite : SALEM-2. Zn : vert, N : bleu, C : gris, H : non visible. Les liaisons de coordination entre les atomes de zinc et les atomes d'azote sont indiqués en rouge et les tétraèdres de coordination sont représentés en vert autour de chaque zinc.

SALEM-2 a la même topologie que ZIF-8, mais les méthylimidazolates sont remplacés par des imidazolates (panneau de droite, Figure 16). La densité résultante est de 0,831 g/cm^3. En réalité, ce système est une version idéalisée de son équivalent expérimental, dans lequel seuls 85% des méthylimidazolates sont remplacés. [43]

ZIF-4 est chimiquement très similaire à ZIF-8, avec pour formule $Zn(Im)_2$ au lieu de $Zn(mIm)_2$. Cette structure est poreuse, mais moins que ZIF-8 (la surface BET est nulle par exemple), et a la même topologie cag que le minéral variscite ($CaGa_2O_4$). [197] Sa maille orthorhombique (groupe d'espace *Pbca*) contient 272 atomes avec les paramètres suivants : $a = 15,423\,\text{Å}$, $b = 15,404\,\text{Å}$ et $c = 18,438\,\text{Å}$ et $\alpha = \beta = \gamma = 90°$. Sa densité est de 1,247 g/cm^3. Enfin, ZIF-zni est chimiquement identique à ZIF-4. Il s'agit d'une structure dense non poreuse qui a la même topologie que l'aluminosilicate banalsite ($BaSi_2Al_2O_8$). [189] Sa maille primitive (groupe d'espace $P1$) contient 272 atomes et a pour paramètres : $a = 17,570\,\text{Å}$, $b = c = 17.613\,\text{Å}$ et $\alpha = 138,433°$, $\beta = 97,256°$and $\gamma = 97,257°$. Sa densité est de 1,616 g/cm^3.

J'ai utilisé des simulations de dynamique moléculaire ab initio dans l'ensemble canonique (à volume constant) à une dizaine de températures différentes pour chaque structure afin d'obtenir des informations thermodynamiques sur la fusion, son mécanisme microscopique et d'explorer la nature du liquide obtenu. Toutes les données expérimentales auxquelles je compare la fusion de ZIF-4 sont le fruit du travail réalisé par Kevin A. Beyer, Karena W. Chapman, David A. Keen et Thomas D. Bennett. [60]

La fusion de ZIF-4 : comparaison avec les données expérimentales

Expérimentalement les données de diffraction aux rayons X obtenues au synchrotron ont été utilisées pour évaluer les changements structuraux survenant pendant le chauffage du verre formé par fusion puis trempe de ZIF-4 (cf. Figure 17f). Les simulations de dynamique moléculaire ab initio ne peuvent être menées à partir du verre dont la maille unitaire est trop volumineuse pour être tractable numériquement. J'ai donc utilisé la maille unitaire de la phase cristalline de la ZIF-4 comme point de départ, observant des changements dans le facteur de structure en ligne avec les variations expérimentales (cf. Figure 17f).

Comme la fusion de ce réseau supramoléculaire dépend essentiellement de la dissociation partielle et de la reconstruction des liaisons de coordination Zn–N, j'ai utilisé cette distance comme coordonnée de réaction. Concrètement, à partir de la fonction de distribution radiale Zn–N, $g_{\text{Zn–N}}(r)$, j'ai calculé le potentiel de force moyenne (*potential of mean force* ou PMF en anglais) entre ces deux atomes à toutes les températures simulées par la relation $F(r) = -k_\text{B}T \ln g(r)$.

À partir des profils d'énergie libre (panneau de gauche de la Figure 18) j'ai pu extraire la dépendance en température de l'énergie libre d'activation ($\Delta F^\ddagger$) nécessaire pour casser une liaison Zn–N. Celle-ci suit une loi de van 't Hoff (cf. panneau de droite de la Figure 18) de la forme $\Delta F^\ddagger(T) = \Delta H^\ddagger - T\Delta S^\ddagger$, avec $\Delta H^\ddagger \approx 127$ kJ.mol^{-1} et $\Delta S^\ddagger \approx 37$ J.mol^{-1}.K^{-1} dans cette gamme de température.

Pour appréhender le phénomène de fusion à l'échelle moléculaire, je montre dans les Fi-

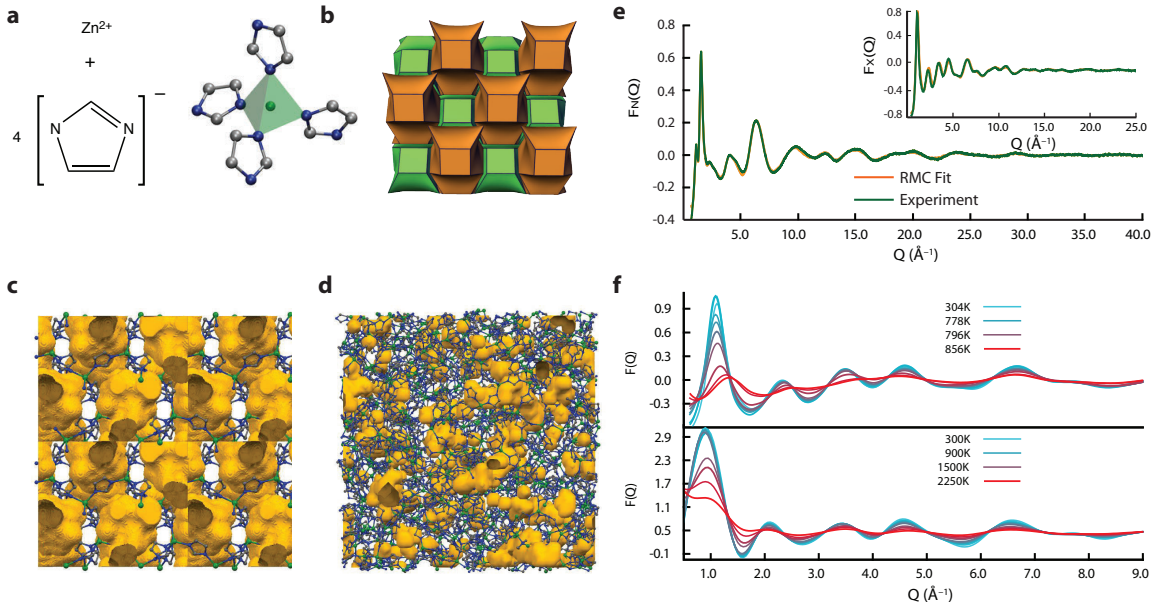

Figure 17 : Structure de la ZIF-4 sous forme cristalline, vitreuse et évolution structurelle pendant le chauffage.**a**) Tétraèdre $Zn(Im)_4$. (**b**) Topologie cag de la ZIF-4. (**c**) Structure cristalline, avec le volume libre en orange. (**d**) Configuration du verre obtenue par *reverse* Monte Carlo (par David A. Keen). (**e**) Facteur de structure expérimental $F(Q)$ et le fit venant de la configuration montrée en (**d**). (**f**) Facteurs de structures (rayons X) expérimentaux (en haut) et obtenus par simulation (en bas) en fonction de la température. Figure tirée de [60].

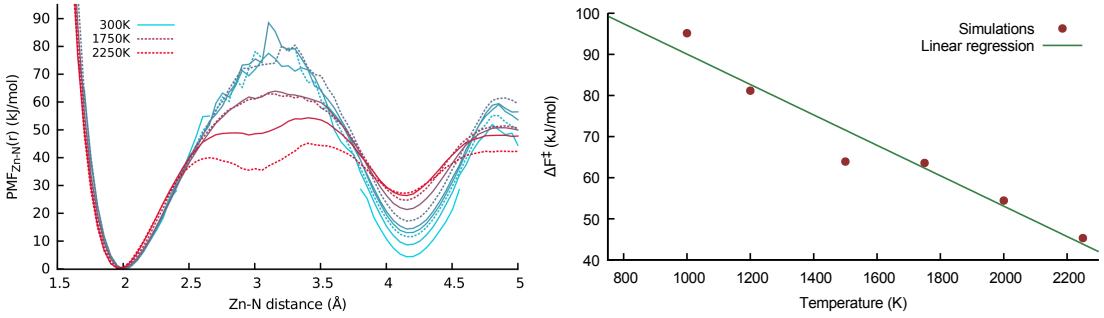

Figure 18 : À gauche : Potentiels de force moyenne le long de la coordonnée Zn–N à différentes températures. À droite : graphe de van 't Hoff des énergies libres extraites à partir du potentiel de force moyenne.

gures 19a et b la distribution du nombre de coordination du zinc en fonction de la température. Jusqu'à 1200 K la coordination tétraédrique est majoritaire et les défauts de coordination peuvent être considérés comme des défauts. La concentration de ces défauts se trouve être de la forme $n_\mathrm{d} \propto \exp(-\varepsilon/k_\mathrm{B}T)$, où $\varepsilon \approx 56$ kJ.mol^{-1} est l'énergie d'activation de formation de défaut. Ces défauts agissent alors comme des sites de nucléation pour la fusion. La Figure 19d montre des configurations pendant un échange de ligand autour d'un zinc à 1500 K. À partir d'un zinc initialement coordonné quatre fois, un ligand s'éloigne et est remplacé par un autre imidazolate. La Figure 19c montre le comportement moyen des distances entre le zinc et les

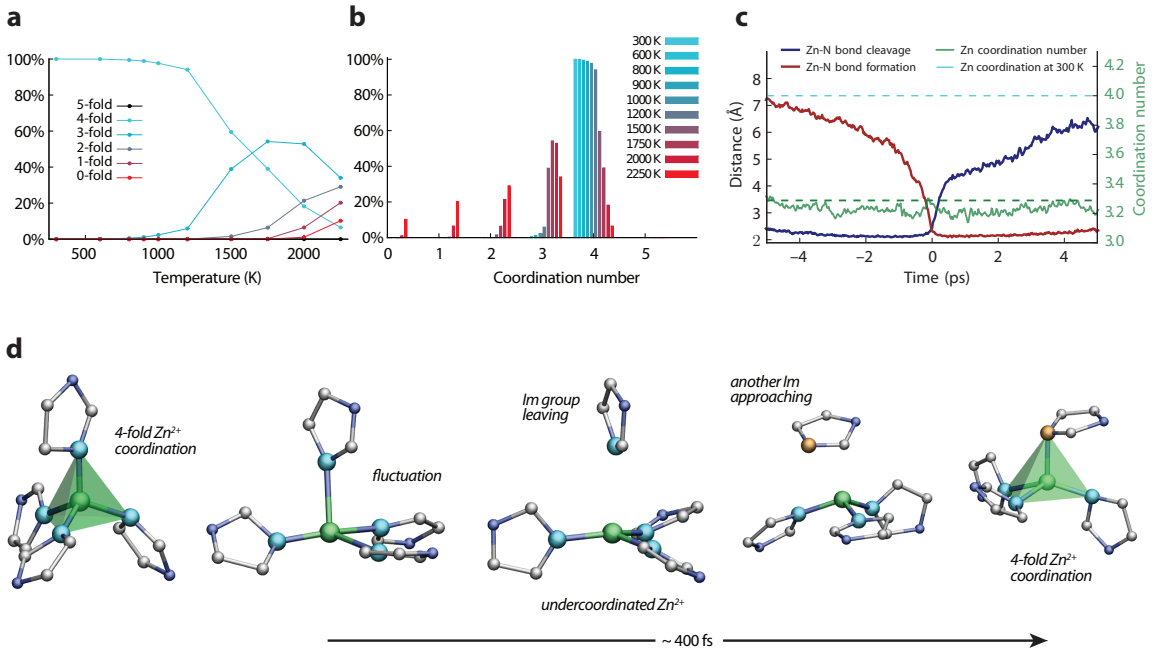

Figure 19 : (**a**) Distribution des nombres de coordination du zinc en fonction de la température. (**b**) Évolution thermique de chaque degré de coordination du zinc de 300 K (bleu clair) à 2250 K (rouge). (**c**) Comportement moyen durant un échange d'un atome d'azote par un autre dans la première sphère de coordination d'un zinc. (**d**) Visualisation d'un évènement d'échange représentatif. N (initialement coordonné) : bleu clair, N : bleu, N (coordonné après échange) : orange.

deux azotes concernés : on remarque un mécanisme concerté pour un échange durant moins de 2 ps. On retrouve un comportement similaire à celui de l'eau liquide avec des échanges de liaisons hydrogène : dans les deux cas il s'agit de liquides fortement associés formant des réseaux dynamiques avec des associations tétraédriques préférentielles.

Les Figures 20a et b montrent les déplacements carrés moyens des atomes de zinc et des centres de masse des imidazolates. Au-delà de 1200 K, j'observe une diffusion libre pour les deux espèces avec des coefficients de diffusion similaires, comme dans les liquides ioniques classiques. L'évolution du volume poreux total (calculé avec une sonde sphérique de rayon 1,2 Å) en fonction de la température est montrée sur la Figure 20c. Malgré un élargissement thermique attendu, le volume poreux total moyen reste globalement constant, en ne baissant que de 10% à la plus haute température comparée à 300 K. De plus, l'analyse du volume poreux accessible (i.e. excluant les cavités non connectées) montre qu'une grande partie de la porosité de la ZIF liquide est de la porosité accessible (allant de 74% dans le cristal à 300 K à 95% dans le liquide à 1500 K). Ainsi, à haute température la ZIF-4 forme un « liquide poreux » hybride. Cette observation est en adéquation avec les données expérimentales rapportées sur le volume poreux des verres de ZIFs. [214]

Dans cette étude, mes coauteurs et moi-même, [60] avons introduit le terme « MOF liquide », pour un liquide formé par la fusion d'un MOF dont la configuration chimique reste inchangée et dont les modes de coordination sont maintenus dans la phase liquide.

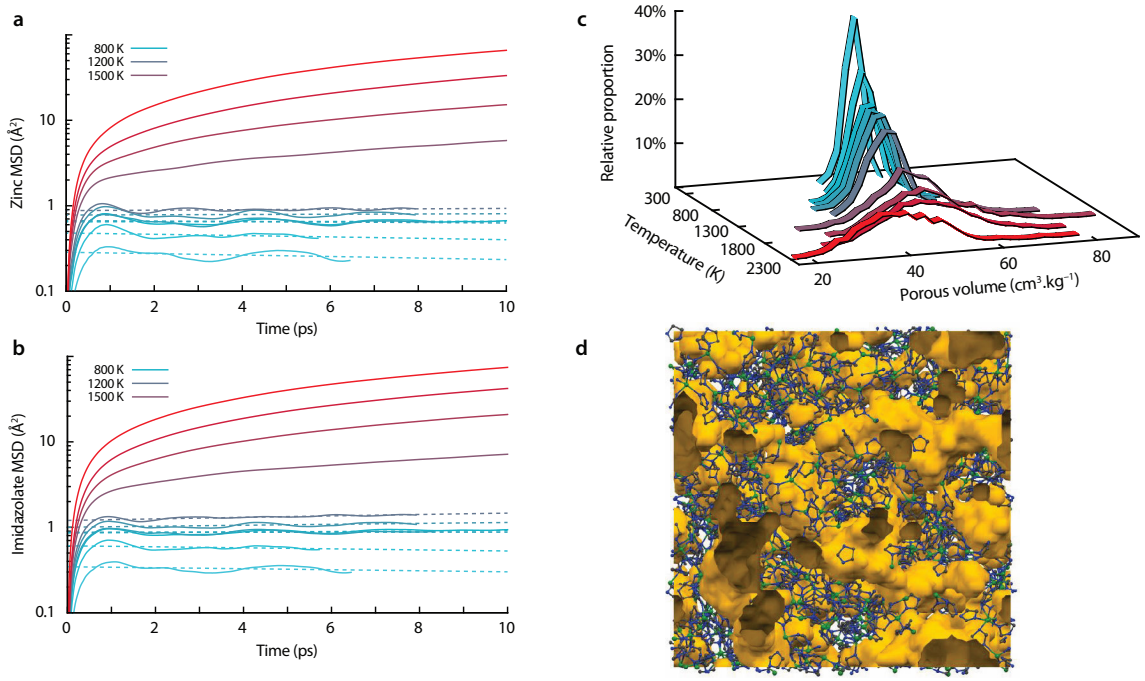

Figure 20 : Structure et dynamique de la ZIF liquide. Figure tirée de [60].

La généralisation de ce phénomène dépend d'un équilibre complexe entre la température de fusion et la température de décomposition. Cette dernière est dépendante d'une multitude de facteurs tels que l'atmosphère de travail, la vitesse de chauffe et la taille des particules. Cela dépend également de la chimie, avec des espèces comme les nitroimidazoles qui se décomposent du fait de la rupture des liaisons C–NO_2.

Dans la sous-partie suivante, je résume l'étude que j'ai mené sur ZIF-8, ZIF-zni et SALEM-2 pour étudier l'influence de la topologie et de la chimie sur la capacité de fusion d'un MOF et son comportement lors de celle-ci.

Influence de la topologie et de la chimie sur la fusion

Je résume tout d'abord la comparaison entre les trois structures existantes, ZIF-8, ZIF-4 et ZIF-zni, avant d'énoncer les résultats pour SALEM-2. Le ratio de Lindemann, qui caractérise la fusion lorsque sa valeur dépasse 15%, est représenté sur le panneau gauche de la Figure 21 en fonction de la température pour les trois ZIFs. La fusion a lieu entre 1200 K et 1500 K pour ZIF-4, entre 1500 K et 1750 K pour ZIF-zni, et au-delà pour ZIF-8. Ainsi je peux définir un ordre des températures de fusion : $T_m(\text{ZIF-4}) < T_m(\text{ZIF-zni}) < T_m(\text{ZIF-8})$.

De même, lorsqu'on s'intéresse au déplacement carré moyen par atome par rapport à la structure initiale et sur une durée de référence ($\tau = 75$ ps) (cf. panneau droit de la Figure 21), on voit que la diffusion ne commence qu'entre 1250 K et 1500 K pour ZIF-4 et seulement au-dessus de 1500 K pour ZIF-8. La diffusion au sein de la ZIF-zni semble être empêchée par sa structure dense, qualitativement différente des structures poreuses de ZIF-4 et ZIF-8.

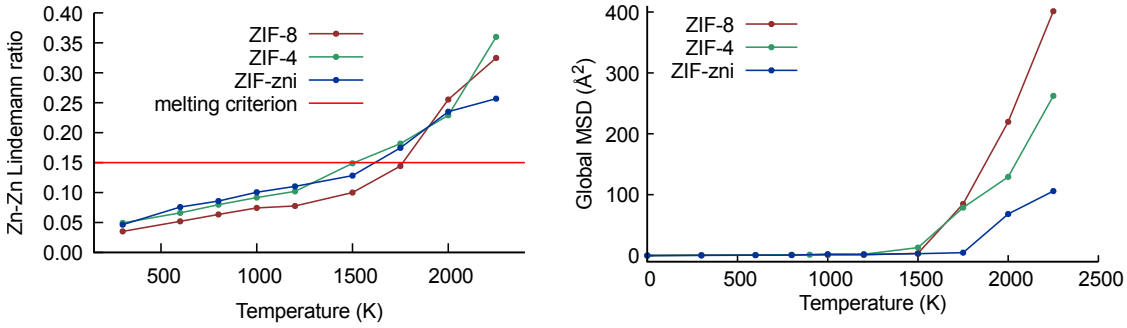

Figure 21 : À gauche : Comparaison de l'évolution du ratio de Lindemann pour les 3 ZIFs. À droite : Déplacement carré moyen global en fonction de la température pour ZIF-8 (en rouge), ZIF-4 (en vert) et ZIF-zni (en bleu).

Tout comme pour ZIF-4, la fusion dans ZIF-8 et ZIF-zni a lieu grâce à un processus activé menant à des évènements rares de rupture de liaisons de coordination. [207] C'est-à-dire que la fusion se passe à la limite de stabilité de la phase solide, mais à un point où elle est encore métastable. Le tableau 2 montre les enthalpies et entropies libres d'activation pour les liaisons Zn–N et Zn–Im.

	$\Delta U^{\ddagger}$	$\Delta S^{\ddagger}$	$\Delta F^{\ddagger}(865K)$
ZIF-8 (Zn–N)	145	48	103 ($\simeq 14kT$)
ZIF-8 (Zn–Im)	207	77	140 ($\simeq 20kT$)
ZIF-4 (Zn–N)	127	37	95 ($\simeq 13kT$)
ZIF-4 (Zn–Im)	123	36	92 ($\simeq 13kT$)
ZIF-zni (Zn–N)	126	38	93 ($\simeq 13kT$)
ZIF-zni (Zn–Im)	128	39	94 ($\simeq 13kT$)

Tableau 2 : Première colonne : enthalpie d'activation (en kJ/mol), deuxième colonne : entropie d'activation (en $J{\cdot}mol^{-1}{\cdot}K^{-1}$), troisième colonne : énergie libre d'activation à la température de fusion expérimentale de ZIF-4 (865 K) (en kJ/mol).

La comparaison entre les potentiels de force moyenne pour la coordonnée Zn–Im permet de distinguer les différences entre les trois structures. De fait, là où pour ZIF-4 et ZIF-zni la différence des thermes enthalpiques et entropiques pour les coordonnées Zn–N et Zn–Im sont négligeables, ZIF-8 montre un comportement bien différent. Les deux termes sont effet bien plus élevés pour ZIF-8 (+43% pour l'enthalpie et +60% pour l'entropie entre Zn–N et Zn–Im). Les valeurs plus élevées pour ZIF-8 selon les deux coordonnées de réaction vont bien dans le sens d'une difficulté accrue de provoquer la fusion. De plus, la différence de comportement entre ZIF-8 et les deux autres structures vis-à-vis de l'équivalence entre Zn–N et Zn–Im comme coordonnées de réaction ne peut trouver sa source uniquement dans la force des liaisons Zn–N, mais plutôt dans la topologie du réseau de coordination.

En terme de porosité, laissant de côté ZIF-zni qui est non poreuse, le comportement thermique de ZIF-8 est très différent de celui de ZIF-4 (cf. Figure 22). Contrairement au cas de ZIF-4, où la porosité du cristal est en grande partie maintenue dans la phase liquide, ZIF-8

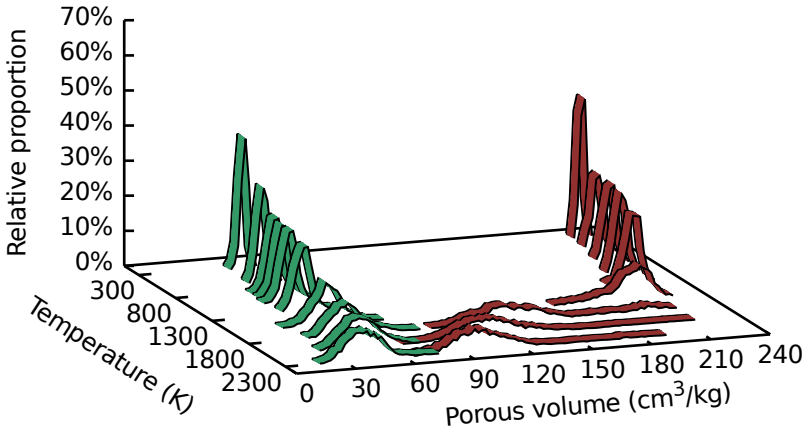

Figure 22 : Comparaison de l'évolution thermique du volume poreux total entre la ZIF-4 (vert) et la ZIF-8 (rouge).

perd plus de la moitié de sa porosité au cours de la fusion.

J'ai montré que le mécanisme de fusion est similaire dans les trois structures, mais que la ZIF-8 ne pourrait fondre qu'au-delà de sa température de décomposition, l'excluant des candidats à la fusion. Je formule l'hypothèse que cela est dû à la grande porosité de ZIF-8 : tandis que pour des ZIFs plus denses, comme ZIF-4 et ZIF-zni, le mouvement des ligands les laisse proche des autres ligands et se stabilisent par interactions de dispersion, dans ZIF-8 le détachement d'un ligand le laisse très isolé dans l'état intermédiaire, impliquant une barrière énergétique plus élevée.

La comparaison avec la structure SALEM-2 peut être résumée par la Figure 23. Le panneau gauche présente l'énergie libre d'activation nécessaire pour casser une liaison Zn–N et sa décomposition en partie enthalpique et entropique par la loi de van 't Hoff. Les valeurs obtenues sont nettement plus proches de celles de ZIF-8 que de celles de ZIF-4. De plus, le panneau de droite montre l'évolution du ratio de Lindemann pour les quatre ZIFs et on observe bien que SALEM-2 ne fond qu'à une température au moins aussi élevée que ZIF-8.

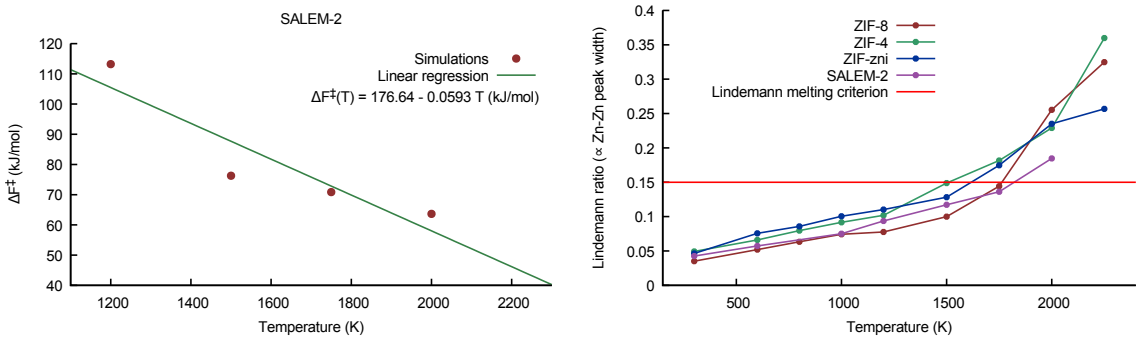

Figure 23 : À gauche : graphe de van 't Hoff plot des énergies libres d'activation associées à la rupture de la liaison de coordination Zn–Im pour SALEM-2. À droite : ratios de Lindemann en fonction de la température.

Ces comparaisons semblent en ligne avec la conclusion de [50] selon laquelle les ZIFs ont

un point de fusion proche de leur équivalent inorganique et donc que la topologie joue un rôle prépondérant dans la capacité d'une structure à fondre ou non. Dans le cas de ZIF-8 et SALEM-2, la température de fusion de la sodalite étant de 1557 K, leur fusion est très peu probable (impossible pour ZIF-8).

Il est encore nécessaire d'étudier d'autres ZIFs, en combinant des méthodes expérimentales et théoriques, afin de confirmer cette hypothèse sur le rôle prépondérant de la topologie et tenter d'établir un critère général sur la capacité de fusion à température relativement basse de ces matériaux. Pour cela, il sera nécessaire d'étudier des ZIFs avec des ligands organiques et des topologies différents, mais aussi des cations différents (comme le cadmium) [184] qui peuvent influencer la force de l'interaction métal–imidazolate. Le but serait de créer des MOFs liquides poreux avec des propriétés chimiques et physiques ajustables, comme c'est déjà le cas pour les structures cristallines de MOFs qui peuvent être construites en vue d'applications spécifiques. De tels matériaux pourraient être intéressants pour des séparations en phase liquide, de la catalyse homogène et du transport ionique. Ils pourraient aussi servir d'intermédiaires à l'obtention de verres de MOFs mécaniquement et thermiquement stables.

Caractérisation des verres obtenus par trempe

Systèmes et méthodes

Afin de réaliser des simulations de trempe des liquides obtenus par simulation de ZIF-4, ZIF-8 et SALEM-2 à 1500 K j'ai pris comme point de départ 10 configurations de chaque trajectoire à 1500 K. En effet, la petite taille de la maille élémentaire que j'ai considérée m'oblige à multiplier les simulations pour avoir une vue représentative de ce que serait la structure moyenne du verre résultant de la trempe. ZIF-8 ne fondant pas expérimentalement, les simulations de trempe pour cette structure ont servi à comparer les effets respectifs de changements de ligands (entre SALEM-2 et ZIF-8) et de topologies (entre ZIF-4 et SALEM-2).

Pour chaque configuration de chaque structure, j'ai donc lancé des simulations de dynamique moléculaire *ab initio* consécutives d'une durée de 4 ps aux températures de 1300 K, 1100 K, 900 K, 700 K, 500 K et 300 K. La Figure 24 montre un exemple de température instantanée au cours du temps pour une des 10 simulations de trempe de ZIF-4 liquide. Malgré un taux de refroidissement inaccessible expérimentalement les configurations vitreuses résultantes peuvent être analysées comme physiquement sensées de par la petite taille et l'échelle de temps considérées. Cette procédure a notamment été utilisée dans le passé sur des verres de silice avec de bons résultats. [220]

Des verres différents à partir de cristaux différents

Les propriétés que j'ai calculées pour les configurations vitreuses ont été moyennées sur les 10 trajectoires pour chaque structure. Dans la suite je dénote a_gZIF-4, a_gZIF-8 et a_gSALEM-2 le verre « moyen » obtenu pour ZIF-4, ZIF-8 et SALEM-2 respectivement.

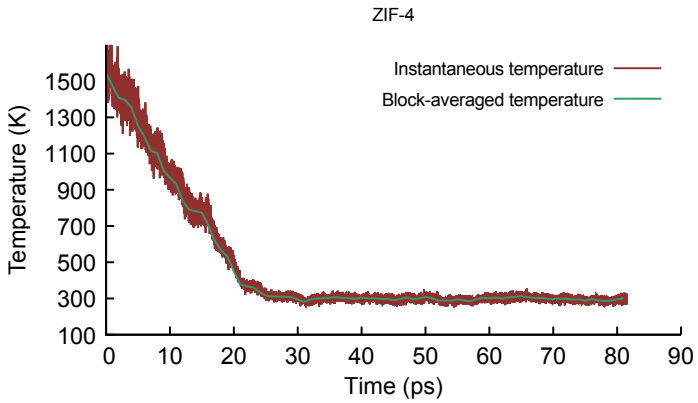

Figure 24 : Exemple de température instantanée résultant du déclin de température imposé. La température instantanée est en rouge et sa valeur moyennée par blocs de 1 ps (constante de temps du thermostat) est en vert.

La Figure 25 montre les distributions de nombres de coordination pour les atomes de zinc coordonnés aux atomes d'azote. On y voit une confirmation du mécanisme de reconstruction présent pour la ZIF-4, comme suggéré dans [50]. En effet, la proportion de zincs tétracoordonnés passe de 60% à 93% durant la trempe, revenant à un nombre moyen de coordination de 3,93 (comparé à la valeur de 4 dans le cristal). Cette augmentation est plus faible pour SALEM-2 et encore plus pour ZIF-8, avec des comportements très similaires entre ZIF-8 et SALEM-2 comparés à ZIF-4.

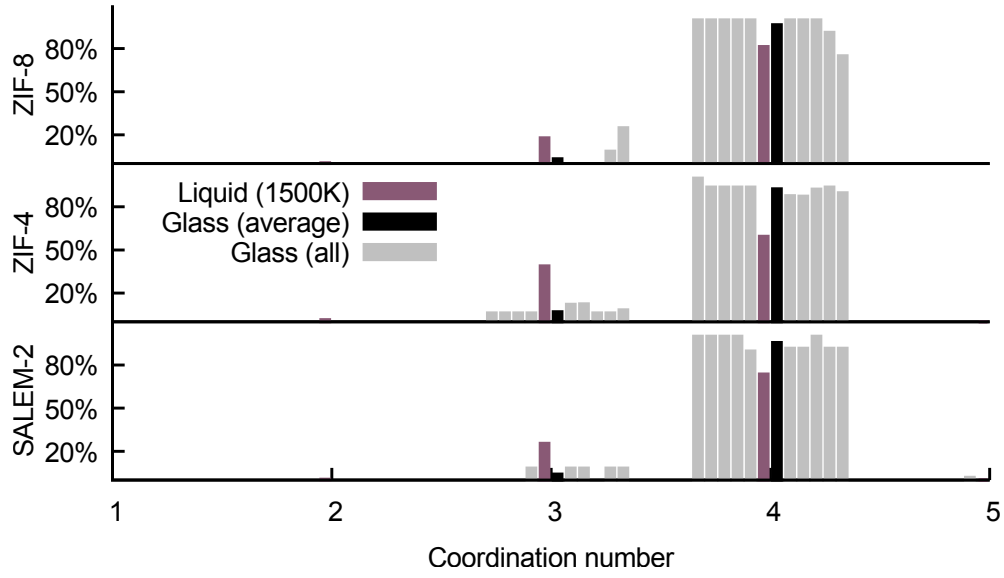

Figure 25 : Distributions des nombres de coordination zinc-azote.

Comme pour la fusion, j'ai étudié la porosité de ces structures après trempe. Ici encore, la topologie semble jouer le rôle prépondérant. En effet, pour ZIF-4 le volume poreux moyen est 29% supérieur dans le verre comparé à la phase cristalline alors qu'il est quasiment inchangé pour ZIF-8 (-3.5%) et pour SALEM-2 (+1%). De plus, les valeurs obtenues pour SALEM-2 et ZIF-8, bien que proches des valeurs dans les cristaux, sont tempérées par une proportion

importante de configurations ne présentant aucune porosité (20% pour ZIF-8 et 30% pour SALEM-2). La différence est encore plus prononcée pour les volumes poreux accessibles à une sonde de type hélium (cf. tableau 3). Pour ZIF-8 et SALEM-2, le volume poreux accessible est le même que le volume poreux, donc quasiment inchangé. Cependant, pour ZIF-4, la fusion semble ouvrir des canaux plus grands que dans le cristal en moyenne, menant à une augmentation de 64% du volume poreux accessible. Le fait de ne pas prendre en compte la densification de ZIF-4 durant la fusion et la trempe exacerbe sûrement cet effet, mais cela est cohérent avec les mesures de spectroscopie par annihilation de positron (*Positron annihilation lifetime spectroscopy* ou *PALS* en anglais) qui confirment l'ouverture de cavités dans le verre plus grandes que dans le cristal. [214]

	ZIF-8	ZIF-4	SALEM-2
Cristal	258	39	372
Verre	249	64	377

Tableau 3 : Volume poreux accessibles moyens (en cm^3/kg) pour les trois structures dans la phase cristalline et la phase vitreuse.

La comparaison entre les structures vis-à-vis des caractéristiques des verres obtenus par trempe indique que la substitution des cycles imidazolates et la topologie initiale jouent toutes deux un rôle. Néanmoins, la topologie de ZIF-4, permettant un réarrangement structural pendant la fusion et une reconstruction pendant la trempe, semble jouer un grand rôle dans la stabilisation de cette structure lors de ces deux processus. En effet, bien que SALEM-2 soit chimiquement identique à ZIF-4, son réseau de coordination s'effondre lors de la fusion et reste très altéré après trempe.

Un développement théorique possible serait de simuler directement, à l'aide de méthodes classiques, les structures vitreuses obtenues par modélisation de type *reverse* Monte Carlo. Cela permettrait d'avoir plus d'informations sur la structure et la dynamique des verres à plus grande échelle pour avoir une meilleure vision sur le désordre statistique et la thermodynamique de ces nouveaux matériaux. La simulation avec des méthodes classiques de la fusion et de la trempe serait aussi envisageable, mais avec un effort important de développement d'un champ de force adapté au préalable.

Remplissage de ZIF-4 par du CO_2 : influence sur la fusion

Je résume ici une étude exploratoire en cours sur la fusion de ZIF-4 dans laquelle j'ai introduit précédemment des molécules de CO_2 par simulations de type Monte Carlo dans l'ensemble grand canonique. Cette étude s'inscrit dans la même veine que celle publiée par Corradini et al. en 2016 sur la solvatation et le mécanisme de transport du CO_2 dans les carbonates fondus. [90] Elle est aussi cohérente avec l'usage des MOFs amorphes pour le piégeage de substances. [179]

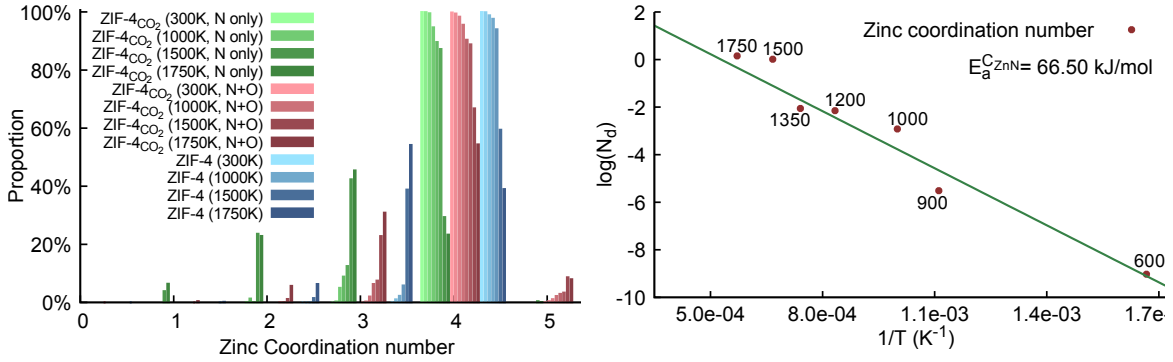

Figure 26 : À gauche : en vert : coordination Zn–N, en rouge : coordination Zn–N + Zn–O (une tétracoordination pour l'histogramme rouge peut par exemple être le résultat de trois azotes et un oxygène coordonnés au même zinc), en bleu : situation sans CO_2. À droite : graphe de van 't Hoff de la formation de défauts de coordination Zn–N ($E_a^{C_{ZnN}}$ étant l'énergie d'activation associée).

Coordination du dioxyde de carbone au zinc

Comme le montre le panneau gauche de la Figure 26, avant la fusion et jusqu'à 1350 K, la coordination de l'oxygène au zinc est extrêmement faible avec 0,09 oxygène par zinc à 1350 K (et 3,9 azotes). Cependant, dans la phase liquide à 1500 K, ce nombre croît à 0,85 oxygène par zinc tandis que la coordination zinc–azote décroît à 3,0 azotes par zinc. D'autre part, l'énergie d'activation associée à la création de défaut de coordination Zn–N grimpe de 28% comparé à la situation sans CO_2, ce qui peut être interprété comme une plus grande difficulté à créer des défauts à basse température. Ceci signifie en fait que la transition d'un régime où la tétracoordination Zn–N est majoritaire à un régime dans lequel elle représente moins de 50% arrive à une température plus basse avec du CO_2 (entre 1350 K et 1500 K) que sans (au-delà de 1500 K).

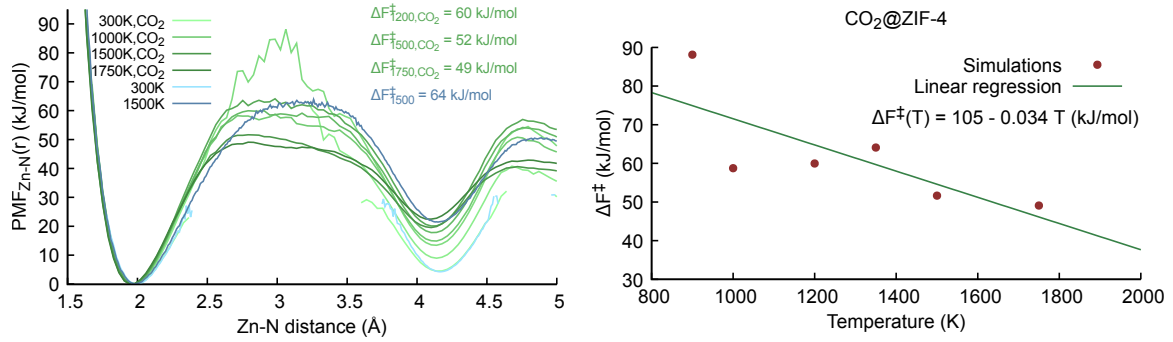

Figure 27 : À gauche : potentiel de force moyenne le long de la coordonnée zinc–azote (en vert) (situation sans CO_2 à 300 K et 1500 K en bleu). À droite : graphe de van 't Hoff montrant l'énergie libre d'activation nécessaire à la rupture d'une liaison Zn–N à différentes températures.

La considération des potentiels de force moyenne selon la coordonnée zinc–azote est instructive (cf. Figure 27). En effet, l'enthalpie d'activation associée à la rupture de cette liaison

est de 105 kJ/mol, soit nettement moins que dans le cas sans CO_2 (127 kJ/mol). Ceci semble indiquer que le dioxyde de carbone a un rôle de facilitateur dans le processus de fusion, qui dépend beaucoup de cette enthalpie d'activation.

Un certain nombre d'analyses peuvent encore être menées sur ces simulations pour étudier la coordination du CO_2 à la structure et son rôle dans la réduction éventuelle de la température de fusion. J'ai déjà pu voir que la présence de CO_2 abaisse l'énergie nécessaire à la rupture de liaisons Zn–N et augmente la diffusion des ions zinc. Une analyse topologique plus avancée serait intéressante pour comprendre la différence de comportement de fusion. De plus, cette étude étant purement théorique, des expériences devraient être menées pour épauler mes conclusions théoriques.

Conclusion

Grâce à des simulations au niveau quantique j'ai pu montrer que les propriétés mécaniques des zéolithes sont des propriétés très sensibles, qui sont difficilement appréhendées par des méthodes classiques. J'ai également montré que les méthodes d'apprentissage statistique offraient une manière de créer des prédicteurs rapides et fiables, comme je l'ai fait pour le ratio de Poisson et ses extrema.

L'étude de la fusion et de la trempe des ZIFs a mis en lumière l'influence cruciale de la topologie par rapport aux caractéristiques chimiques du ligand sur la capacité d'une ZIF à fondre. Grâce à cette étude, j'ai également découvert le mécanisme microscopique sous-jacent de la fusion des ZIFs. De nombreux efforts, à la fois expérimentaux et théoriques, sont encore nécessaires pour confirmer mes hypothèses en comparant des structures avec différents ligands, cations et topologies. Les nouveaux verres ainsi générés pourraient servir à piéger des substances dangereuses ou polluantes ou comme des verres actifs optiquement ou électroniquement par l'incorporation de telles fonctionnalités dans le MOF cristallin.

En définitive, les questions ouvertes par cette thèse sont toutes reliées aux liens entre les caractéristiques structurales et les propriétés physico-chimiques des matériaux microporeux. De nombreuses perspectives sont à présent ouvertes, que ce soit pour les zéolithes ou les MOFs, et en particulier les MOFs amorphes.

La principale question pour l'étude des propriétés mécaniques des zéolithes et les liens avec les caractéristiques structurales est l'influence des changements chimiques sur ces liens. De fait, en étudiant des structures zéolithiques avec différents éléments chimiques, non seulement l'aluminium, mais aussi le gallium ou le germanium par exemple, et différents cations extra-charpentes, il serait possible de dégager ce qui est inhérent à la topologie du réseau et ce qui dépend intimement de ses détails chimiques dans la détermination des propriétés mécaniques. Je me suis intéressé essentiellement à l'auxéticité, mais d'autres propriétés anomales demandent à être étudiées plus avant comme la compressibilité linéaire négative ou, pour prendre une propriété reliant thermique et mécanique, l'expansion thermique négative.

Au-delà du criblage de zéolithes possédant des structures intéressantes vis-à-vis d'une propriété particulière, la question de leur faisabilité reste non résolue. Ce problème, appelé le

zeolite conundrum en anglais, a résisté à de nombreuses études théoriques et expérimentales, malgré de récentes avancées expérimentales, avec la création du processus de synthèse de zéolithes « infaisables » ADOR. [225, 226] Certaines de ces nouvelles structures ont été étudiées sur le plan théorique. [227] Une voie qui reste largement à explorer et qui pourrait amener une meilleure compréhension théorique sur la faisabilité de ces structures serait de modéliser le processus de synthèse lui-même pour comprendre quelles sont les forces à l'œuvre. Cela pourrait permettre de concevoir des zéolithes pour des applications spécifiques, dont les propriétés auraient été prédites au préalable.

Dans le royaume des MOFs amorphes, comme je l'ai précédemment écrit, beaucoup de choses sont encore à éclaircir. Une des perspectives ouvertes par mon travail de thèse est de déterminer des critères précis pour la capacité d'une structure à fondre en se basant sur la nature du métal, la composition du ligand et les caractéristiques de la topologie. Une idée intéressante pour répondre à cette interrogation serait d'entraîner des champs de force réactifs sur des données de dynamiques moléculaires ab initio de la fusion de différents MOFs pour être ensuite capable de simuler et de comprendre le processus de fusion de façon moins coûteuse numériquement. Pour aller plus loin que les conditions standards, l'étude de l'influence de paramètres physiques sur la fusion, comme l'augmentation de pression, pourrait ouvrir de nouvelles possibilités, par exemple en rendant possible la fusion d'une structure ne fondant pas à pression ambiante. Dans un second temps, des modèles physiques plus simples pourraient être proposés pour réduire encore la dimensionnalité du problème et identifier les facteurs clés amenant à un comportement particulier lors de la fusion. Par exemple, comme j'ai vu que la topologie jouait un rôle important, une question intéressante serait : quels éléments de la topologie (symétrie, connectivité, topologie de l'interaction métal-ligand) importent le plus ? Avec de tels critères et une meilleure connaissance de la faisabilité expérimentale des structures considérées nous pourrions arriver à une véritable démarche de design rationnel de nouveaux liquides et verres poreux.

Résumé

Durant ma thèse j'ai réalisé des études en utilisant les méthodes de simulation moléculaire pour étudier des matériaux déjà utilisés industriellement, comme les zéolithes, ou qui pourraient l'être dans le futur, tels que les matériaux poreux à charpente organométallique appelés *Metal-Organic Frameworks* (MOFs).
Les zéolithes, connues depuis 1756 et synthétisées depuis les années 40, n'ont vu leur comportement mécanique étudié sur le plan théorique que récemment. Or certains de ces aluminosilicates poreux présentent des propriétés mécaniques dites anomales, tel que l'auxéticité. À l'aide d'une base de données structurales, j'ai relié les propriétés structurales de ces matériaux à leurs propriétés mécaniques et j'ai développé une méthodologie permettant de prédire l'auxéticité dans ces matériaux.
Les MOFs ont essentiellement été étudiés sous leur forme cristalline. Or leur amorphisation présente un intérêt tant sur le plan des processus que de part le potentiel d'applications des phases amorphes obtenues. Je me suis intéressé à la fusion et à la trempe de certains de ces matériaux. À l'aide de simulations moléculaires quantiques, j'ai montré quel était le mécanisme à l'œuvre lors de la fusion, caractérisé la nature du liquide et les liens existant entre la topologie initiale du matériau, son comportement lors de la fusion et le verre. J'ai aussi modélisé le remplissage d'un de ces matériaux par du dioxyde de carbone, son influence sur la fusion et la façon dont il pourrait être piégé dans la phase amorphe.

Mots Clés

Simulation moléculaire, Zéolithes, Metal-organic Frameworks, Matériaux poreux, Design rationnel.

Abstract

During my PhD I conducted studies based on molecular simulation methods to study two types of materials: zeolites, already used industrially and Metal-Organic Frameworks (MOFs), which present a lot of potential for applications, though their commercial use is still to be developed.
Zeolites, known since 1756 and synthesized since the 40s, have not been much studied in terms of their mechanical behaviour until less than 15 years ago. Yet some of these porous aluminosilicates have fascinating mechanical properties called anomalous properties, such as negative linear compressibility or auxeticity. Using a large structural database of hypothetical zeolites, I linked their structural descriptors and mechanical properties and developed a methodology allowing to screen this type of materials looking for auxeticity.
MOFs have essentially been studied as crystalline materials. Yet their amorphization is very interesting whether to study its mechanism or for potential applications of the amorphous phases obtained. I have been interested in characterizing the melting and quenching of some of these materials. In particular, using quantum molecular simulations, I unraveled the mechanism behind the melting, characterized the nature of the liquid phase and showed the links between the initial topology, the melting behaviour and the resulting glass-like phase. I also modelled the filling of one of these materials with carbon dioxide, its influence on the melting and the way it could be trapped inside the amorphous phase.

Keywords

Molecular simulation, Zeolites, Metal-organic Frameworks, Porous materials, Rational design.